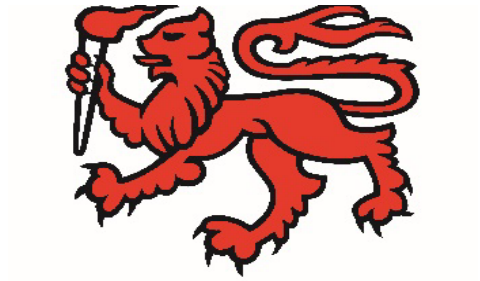

UNIVERSITY *of* TASMANIA

THE ORIGIN AND EVOLUTION OF INTRUSIVE AND EXTRUSIVE CARBONATITES

Naomi J. Potter

Bsc. University of Western Australia,

Bsc. (Hons) University of Tasmania

School of Natural Sciences (Earth Sciences)

Submitted in fulfilment of the requirements for the degree of

Doctor of Philosophy

University of Tasmania

May 2019

TABLE OF CONTENTS

LIST OF FIGURES AND TABLES

LIST OF APPENDICES

Abstract

Carbonatites are among the most volumetrically insignificant igneous rocks found at the earth's surface, and over the past century, a general picture has emerged on the composition, origin and evolution of carbonatitic magmas, however much remains to be done to fully understand them. Carbonatites are characterised by high concentrations of several strategic elements, including rare-earth elements, niobium, tantalum, phosphorous, copper, iron and fluorine. Carbonatites are mostly considered to be derived from a common parental magma, yet the different types of carbonatites are genetically distinct as they form at different depths in the upper mantle and are the result of partial melting, fractional crystallization or liquid immiscibility. Carbonatites have also been largely accepted to be associated with suites of alkaline igneous rocks and not as single rock units. Understanding the relationship between carbonatites and associated silicate rocks is an important aspect in interpreting the mantle to crust evolution of carbonatite complexes. Silicate-carbonate immiscibility is currently the leading mechanism for the association of coexisting carbonatites and alkaline silicate rocks. The advances in microanalytical techniques means that sophisticated mineralogy and melt inclusions methods that have been at the centre of many recent petrological and geochemical discoveries can now be applied to these complexes and provide important clues to the nature of the magmas that give rise to the genesis of carbonatites and the associated economic deposits within alkaline-ultramafic and carbonatitic complexes.

The thesis involves case studies on the 1993 carbonatitic eruption at Oldoinyo Lengai and perovskite ore from the Afrikanda alkaline-ultramafic complex. The studies build on, and expand, the use of petrography and mineralogy of carbonatites and associated alkaline silicate rocks to further the understanding of the genesis of carbonate-silicate melts and seeks to address petrological, geochemical and economic enigmas of extrusive and intrusive carbonatitic magmas. The goals of this thesis are to (1) understand the differentiation processes involved in the evolution of the carbonatites (2) determine the composition of the melt prior to emplacement and during magma ascent and (3) understand the genesis of the Oldoinyo Lengai lava and the perovskite ore in the Afrikanda alkaline-ultramafic complex. These goals are addressed by investigating the petrology and geochemistry of minerals and melt inclusions in the carbonatites and associated silicate rocks.

The rarity and difficulty in capturing definitive evidence of liquid immiscibility within magmas has posed a challenge for researchers, as intrusive carbonatite rocks are commonly affected by crystallisation and post-magmatic alteration. Liquid immiscibility is currently understood to be the underlying process for the generation of carbonatite magmas from a parental alkaline silicate magma at

crustal depth, and is possibly the only magmatic process that can explain the association of coexisting carbonatites and alkaline silicate rocks. Therefore, petrological and mineralogical studies on extrusive carbonatites, like Oldoinyo Lengai, are necessary to understand the genetic history of carbonatitic magmatism. The texture and mineralogy of the 1993 lava presents evidence of immiscibility between silicate, carbonate, chloride, and fluoride melt phases through textural features preserved in the silicate spheroids, melt inclusions, and carbonatite groundmass. The melt inclusions and silicate spheroids present evidence of silicate-carbonate and carbonate-carbonate immiscibility, while the groundmass shows evidence of carbonate-carbonate and carbonate-halide immiscibility. The rapid quenching of the lava facilitates the preservation of the end products of these immiscibility processes within the groundmass. The mineralogy and melt inclusion study at Oldoinyo Lengai provides confirmation that liquid immiscibility is responsible for the formation of natrocarbonatites. Textural evidence (at both macro- and micro-scales) also indicates that the formation of this natrocarbonatite lava did not occur as a simple single-stage process, and that multi-stage liquid immiscibility is a major factor in the petrogenesis of the lava. Therefore, although immiscibility is a common phenomenon in silicate magmas, we can identify evidence of unmixing through melt inclusion and groundmass studies of preserved extrusive carbonatites. The identification of carbonate-carbonate and carbonate-halide immiscibility within the natrocarbonatite lava shows that different types of liquid immiscibility, other than silicate-silicate and silicate-carbonate, can occur in natural magmas.

The Afrikanda alkaline-ultramafic complex is one of the smallest intrusions in the Devonian Kola Alkaline Province (KAP). The KAP in NW Russia is one of the largest carbonatite provinces in the world and hosts more than twenty plutonic and subvolcanic bodies, including alkaline, ultramafic, carbonatite, and melilitolite suites. Many of these complexes host ore deposits, with active mines at Kovdor (apatite-magnetite ore), Lovozero (loparite-ore) and Khibiny (nepheline-apatite ore). The concentric internal structure of the Afrikanda complex hosts olivinites and clinopyroxenites, cross-cut by minor intrusions of carbonatitic rocks with the ultramafic rocks hosting large stock-like bodies of perovskite-titanomagnetite ores. Perovskite-rich segregations are only found in alkaline-ultramafic complexes. Understanding the formation of the perovskite-rich segregations at Afrikanda is important for understanding the source and early history of the silicate and carbonatitic magmas. Afrikanda is assumed to be a magmatic complex, with the intrusive ultramafic rocks derived by partial melting of a metasomatised lithospheric source to produce a Ca-rich melanephelinitic magma, and the later carbonatites from an alkaline silica-rich carbonatitic magma that intruded the earlier-formed ultramafic rocks. The study investigates the mechanisms responsible for the development of the perovskite-rich segregations through a detailed textural and chemical analysis of the perovskite and perovskite- and magnetite-hosted inclusions within the ultramafic rocks (olivinites and clinopyroxenites) and carbonatites of the Afrikanda alkaline-ultramafic complex. Additionally, U-Pb geochronology was combined with major and trace element geochemistry to support the contemporaneous emplacement of

the various rock types in the Afrikanda complex. Across the perovskite-rich lithologies, we classified perovskite into three types (T1-T3) based on crystal morphology, inclusion abundance, composition, and zonation. Perovskite in olivinites and some clinopyroxenites is represented by clusters and networks of fine-grained, equigranular grains with abundant polymineralic inclusions (T1). In contrast, perovskite in other clinopyroxenites and some silicocarbonatites are coarse-grained with rare polymineralic inclusions with interlocked (T2) and massive (T3) textures. The polymineralic inclusions in perovskite and magnetite contain a variety of silicate, hydrous silicate, carbonate, oxide, sulphide and phosphate minerals. The unexpected mineralogy of the polymineralic inclusions raised several questions about the genesis of the alkaline complex. The difficulty in explaining the presence and composition of the inclusions in perovskite is associated with the occurrence of both magmatic and recrystallization processes in the complex. The study of the perovskite textures and perovskite- and magnetite-hosted inclusions revealed that perovskite has a magmatic origin but the formation of the polymineralic inclusions and the development of massive ore textures is associated with post-magmatic processes. Therefore, a non-magmatic model has been developed to explain the genesis of perovskite-rich segregations in the Afrikanda alkaline-ultramafic complex.

In this model, we propose that the polymineralic inclusions in perovskite formed by trapping the surrounding material between perovskite grains during post-magmatic coalescence at subsolidus temperatures. The continuation of the sintering process resulted in the coarsening of inclusion-rich subhedral perovskite into inclusion-poor anhedral and massive perovskite. Initial crystallisation of perovskite from the magma results in disseminated euhedral crystals enclosed by larger silicate, carbonate and oxide minerals. During subsolidus cooling these small, randomly orientated grains accumulate together and develop into loosely packed aggregates of perovskite. As these grains coalesce, varying amounts of interstitial material are trapped between the inclusion-free grains. These densely-packed perovskite grains undergo textural equilibration to form aggregates of perovskite with the external and internal appearance of a single crystal with internal inclusions. Therefore, the development of polymineralic inclusions is associated with the magmatic crystallisation of perovskite, textural re-equilibration and sintering. These perovskite grains then link together and form clusters and chains, with the granoblastic-polygonal texture associated with T1 perovskite. The progressive transition of T1 perovskite to T2 and T3 perovskite involves grain rotation and coalescence of these small equilibrated T1 polygonal clusters and results in the formation of larger anhedral polycrystalline mosaics (T2). In some areas, the continued consolidation and coarsening transforms the large polycrystalline perovskite into massive perovskite. Thus, the progressive development of clusters and networks of fine-grained perovskite crystals (T1) to mosaics of coarse-grained and massive perovskite (T2 and T3) in the ultramafic rocks is due to post-magmatic textural re-equilibration and re-crystallisation.

A combination of characteristic features identified in the Afrikanda perovskite (equigranular crystal mosaics, interlocked irregular-shaped grains, massive textures, grain coarsening and the loss of

polymineralic inclusions) are observed in chromite and magnetite layers in various igneous complexes, such as Bushveld, Fiskenaesset, Oman and Panzhihua, mantle-derived lherzolites and magnesian-ilmenite xenolith in kimberlites. No conclusive model has been proposed to explain the ore distributions and textural transformations observed in these oxide mineral deposits. Traditionally, the formation of oxide-rich seams, bands, stringers and layers has been linked to magmatic processes. Perovskite, chromite and magnetite deposits share textural features that could imply that their development involved similar mechanisms. The comprehensive study completed on the perovskite-rich zones in the three primary rock types at the Afrikanda alkaline-ultramafic complex, as well as additional evidence provided by studies on oxide deposits we can propose that the initial crystallisation of oxide minerals (whether magmatic or not) is followed by their textural re-equilibration at subsolidus temperatures. This re-equilibration produces perceptible changes in the morphology, size, orientation and compositional homogeneity of oxide mineral grains. From an exploration standpoint, the most important outcome of these processes is the accumulation of early-formed crystals into high-density oxide-rich zones and their coarsening and "purification" to form high-grade mineralized zones.

The study of carbonatites and associated silicate rocks at Oldoinyo Lengai and Afrikanda has shown the diversity in the genesis of carbonatites and the impact of different magmatic and post-magmatic processes on carbonatites. The mineralogy, textures and melt inclusions at Oldoinyo Lengai have shown that liquid immiscibility can be responsible for the formation of extrusive natrocarbonatites and can occur between multiple phases are different stages during a single eruption. The identification of carbonate-carbonate and carbonate-halide immiscibility within the lava supports that different types of liquid immiscibility, other than silicate-carbonate, can occur in carbonatites. The study at Afrikanda highlighted the textural and mineralogical complexity of carbonatites associated with silicate rocks in alkaline-ultramafic complexes, and provides a new perspective on the genesis of rare perovskite ore within carbonatite complexes. Textural similarities observed between perovskite ore from Afrikanda and oxide layers in various igneous complexes suggests that post-magmatic processes proposed for the development of perovskite may have facilitated the development of monomineralic layers in other oxide deposits around the world.

Statements and Declarations

Declaration of originality

This thesis contains no material which has been accepted for a degree or diploma by the University or any other institution, except by way of background information and duly acknowledged in the thesis, and to the best of my knowledge and belief no material previously published or written by another person except where due acknowledgement is made in the text of the thesis, nor does the thesis contain any material that infringes copyright.

Signed: **Dated:** 22/05/2019

Authority of access

This thesis may be made available for loan and limited copying and communication in accordance with the Copyright Act 1968.

Signed: **Dated:** 22/05/2019

Statement regarding published work contained in this thesis

The publishers of the papers comprising Chapters 2, 3, and 4 hold the copyright for that content and access to the material should be sought from the respective journals. The remaining non-published content of the thesis may be made available for loan and limited copying and communication in accordance with the Copyright Act 1968.

Signed: **Dated:** 22/05/2019

Statement of Co-Authorship

List of Authors

The following people and institutions contributed to the publications of work undertaken as part of this thesis:

Candidate: Naomi J. Potter, Department of Earth Sciences and CODES, University of Tasmania

Author 1: Vadim S. Kamenetsky, Supervisor, Department of Earth Sciences and CODES, University of Tasmania

Author 2: Karsten Goemann, Supervisor, Central Science Laboratory, University of Tasmania

Author 3: Antonio Simonetti, Department of Civil and Environmental Engineering and Earth Sciences, University of Notre Dame

Author 4: Matthew R.M. Ferguson, Department of Earth Sciences and CODES, University of Tasmania

Author 5: Anton Chakhmouradian, Department of Geological Sciences, University of Manitoba

Author 6: Victor Sharygin, V.S. Sobolev Institute of Geology and Mineralogy, Siberian Branch Russian Academy of Sciences

Author 7: Jay M. Thompson, Department of Earth Sciences and CODES, University of Tasmania

Author 8: Maya B Kamenetsky, Supervisor, Department of Earth Sciences and CODES, University of Tasmania

Author 9: Thomas Rodemann, Central Science Laboratory, University of Tasmania

Proportion of work undertaken towards papers:

Paper 1: Different types of liquid immiscibility in carbonatite magmas: A case study of the Oldoinyo Lengai 1993 lava and melt inclusions

Located in Chapter 2 (Published in *Chemical Geology*)

Candidate was the primary author and with authors 1 and 2 contributed to the conception and design of the research. Candidate and authors 1 and 2 collected new data included in the paper. Author 3 contributed to the interpretation of the research data. The paper was written by the candidate with revisions from authors 1, 2 and 3.

Candidate contributed approximately 95% to the planning, preparation, and execution of the work for the paper.

Paper 2: Textural evolution of perovskite in the Afrikanda alkaline-ultramafic complex, Kola Peninsula, Russia

Located in Chapter 3 (Published in *Contributions to Mineralogy and Petrology*)

Candidate was the primary author and with author 1 contributed to the conception and design of the research. Candidate and authors 1, 2 and 7 collected new data included in the paper. Candidate and authors 1, 4, 5 and 6 contributed to the interpretation of the research data. Candidate wrote the paper with revisions by author 1 and 4.

Candidate contributed approximately 90% to the planning, preparation, and execution of the work for the paper.

Paper 3: Polymineralic inclusions in oxide minerals of the Afrikanda alkaline-ultramafic complex: Implications for the evolution of perovskite mineralisation

Location in Chapter 4 (Submitted to *Contributions to Mineralogy and Petrology*)

Candidate was the primary author and with authors 1 and 8 contributed to the conception and design of the research. Candidate and authors 1, 2 and 9 collected new data included in the paper. Candidate and authors 1 and 5 to interpretation of the research data. Candidate wrote the paper with revisions by author 1 and 5.

Candidate contributed approximately 90% to the planning, preparation, and execution of the work for the paper.

We the undersigned agree with the above stated “proportion of work undertaken” for each of the above published (or submitted) peer-reviewed manuscripts contributing to this thesis:

Signed:	_____	_____
	Vadim Kamenetsky	Sebastien Meffre
	Supervisor	Head of Discipline
	School of Earth Science	School of Earth Science
	University of Tasmania	University of Tasmania
Date:	22/05/2019	23/05/2019

List of publications in this thesis

Journal articles:

Potter, N.J., Kamenetsky, V.S., Simonetti, A., Goemann, K., 2017. Different types of liquid immiscibility in carbonatite magmas: A case study of the Oldoinyo Lengai 1993 lava and melt inclusions, Chemical Geology, Volume 455, Pages 376-384.

Potter, N.J., Ferguson, M.R., Kamenetsky, V.S., Chakhmouradian, A.R., Sharygin, V.V., Thompson, J.M., Goemann, K. 2018. Textural evolution of perovskite in the Afrikanda alkaline–ultramafic complex, Kola Peninsula, Russia: Contributions to Mineralogy and Petrology. Volume 173. Pages 100-120.

Potter, NJ. Kamenetsky, VS., Chakhmouradian, AR., Kamenetsky, MB., Goemann, K., Rodemann, T. 2019. Polymineralic inclusions in oxide minerals of the Afrikanda alkaline-ultramafic complex: Implications for the evolution of perovskite mineralisation. Submitted to *Contributions to Mineralogy and Petrology*.

Conference abstracts:

Potter, N.J., Kamenetsky, V.S., Simonetti, A., 2015. Immiscibility of Silicate, Carbonate, Fluoride and Chloride Melt at Oldoinyo Lengai. Prague, Czech Republic. Goldschmidt. 16-21 August. Goldschmidt Abstract no. 2158.

Potter, N.J., Kamenetsky, V.S., Simonetti, A., 2015. Salt of the Earth: The cradle of humankind, University of Tasmania Graduate Research Conference. 3-4 September.

Potter, N.J., Ferguson, M.R., Kamenetsky, V.S., Chakhmouradian, A.R., Goemann, K., 2017. Inclusions in perovskite-magnetite-silicate rocks from Afrikanda, Russia: Clues to the early history of carbonatites? 11th International Kimberlite Conference. 18-22 September. Extended Abstract No. 11IKC-4539.

Potter, N.J., Kamenetsky, V.S., 2019. The development of perovskite mineralisation in the ultramafic rocks of the Afrikanda complex: Implications for chromite and magnetite monomineralic deposits. Magmatism of the Earth and Related Strategic Metal Deposits. 23-26 May. Extended Abstract.

Acknowledgements

I would like to express my gratitude to those who have supported me in completing this thesis and learning what was needed to reach this point. I would like to thank my three wonderful supervisors Professor Vadim Kamenetsky, Dr. Maya Kamenetsky, and Dr. Karsten Goemann. Thank you all for your insightful comments and continuous encouragement throughout my PhD. I would especially like to thank Dima for his ongoing support, patience, and willingness to share his knowledge. The joy and enthusiasm he has for research is contagious and consistently helped to motivate me during the research and writing of this thesis. I appreciate the time, ideas, and funding that were contributed to make my PhD experience productive and stimulating.

I'd also like to express my sincere thanks to co-authors and reviewers who helped to improve the quality of the publications. Thank you to my fellow students and staff at UTAS who contributed immensely to my personal and professional experience in Tasmania. Specific acknowledgment goes to Matt, Laura and Alex who have been a consistent source of friendship, advice and collaboration, and Adam, for being my conference travel companion. Additional thanks to Karsten, Sandrin and Thomas at the CSL and the support staff in the geology department, who keep things running smoothly

To all the friends that I made at College in Hobart please know that my time in Tasmania was so great because of the adventures and experiences we shared. I am especially grateful to Anika - thank you for all the great memories and for helping me during the stressful times.

Lastly, I would like to thank my parents for supporting me throughout the process of writing this thesis and in all my other pursuits. Your continuous encouragement has made this journey possible.

CHAPTER 1

INTRODUCTION

Carbonatites are among the most volumetrically insignificant igneous rocks found at the Earth's surface, yet they provide critical information and insight on the chemical evolution of the subcontinental upper mantle, that is rivalled by few other rock types (Bell, 2001). Carbonatites are defined as igneous rocks containing more than 50% carbonate minerals (Streckeisen, 1980). These rocks range in age from Archean to present day (Woolley and Kjarsgaard, 2008) and are mostly located within stable, intra-plate settings, often found in the peripheral regions of orogenic belts that have an apparent link to plate separation or orogenic events (Bell et al., 1998; Le Bas, 1987; Veizer et al., 1992). carbonatites are dominated by carbonate minerals, yet over 280 minerals are found in carbonatites worldwide highlighting the exotic diversity in the composition of carbonatites. Many are characterised by high concentrations of incompatible elements, distinctive igneous isotopic ratios and late-stage rare-earth element and fluorite mineralization. Late-stage mineralisation can enrich carbonatites in key elements of economic interest, including rare-earth elements, niobium, uranium and tantalum (Ingrid, 1998; Richardson and Birkett, 1996).

The origin and genesis of carbonatitic magmas has been a matter of discussion for many decades. Isotopic studies and the presence of mantle debris in carbonatites have established that parental magmas are ultimately derived from the mantle (Woolley, 2003; Woolley and Church, 2005). But, the main ongoing debate is whether they originate as a direct product of partial melting of mantle material, such as a carbonate-bearing peridotite (Bailey, 1993; Dalton and Wood, 1993; Ghosh et al., 2009; Woolley, 2003; Wyllie, 1989; Ying et al., 2004), or from a series of magmatic differentiation processes at shallow depths, such as silicate-carbonate liquid immiscibility or fractional crystallisation (Brooker and Kjarsgaard, 2011; Church and Jones, 1995; Dawson, 1998; Freestone and Hamilton, 1980; Lee and Wyllie, 1998; Wyllie, 1988).

Liquid immiscibility is widely recognised as one of the processes that generate carbonatites from silica undersaturated parental magmas at crustal depth, and is possibly the only magmatic process that can explain the association of coexisting carbonatites and alkaline silicate rocks (Barker, 1989; Kjarsgaard and Hamilton, 1989a; Le Bas, 1989; Wyllie, 1989; Wyllie et al., 1990). Liquid immiscibility involves the simultaneous removal of carbonate liquid and silicate minerals from the parent magma

(Kjarsgaard and Hamilton, 1988; Le Bas, 1989). Experimental studies have established that immiscibility between sodium-rich carbonatite and silicate magmas can occur over a wide range of pressures (Freestone and Hamilton, 1980; Hamilton and Kjarsgaard, 1993; Kjarsgaard and Hamilton, 1989b; Van Groos, 1975; Wyllie et al., 1990). The onset of liquid immiscibility is determined by the initial carbonate content of the parent magma (Ray, 1998). Changes to the temperature and pressure alters the composition of the carbonate liquid during separation from the alkaline silicate liquid, as observed in experimental work by Hamilton et al. (1979). Gittins (1989) argues that fractional crystallisation is unable to produce the high Nb, REE and other incompatible trace element characteristics of carbonatites, and that there is not enough CO_2 in the parental silicate melts to enable the volume associated with carbonatites. There have been several experimental studies that propose that crystal-liquid fractionation coupled with liquid immiscibility is capable of generating a spectrum of silicate magmas, from parental melilitite to differentiated phonolite, that coexist with immiscible carbonatite melts, ranging from sovite to natrocarbonatites (Brooker and Hamilton, 1990; Kjarsgaard and Hamilton, 1989a; Kjarsgaard and Hamilton, 1988, 1989b).

There are over 280 minerals known to occur in the various types of carbonatites identified all over the world, reflecting the exotic diversity of carbonatite compositions. According to the IUGS Subcommission on the Systematics of Igneous Rocks (Le Maitre, 2002, p. 10) the variety of carbonatites are separated into four main types based on the chemical classification and dominant carbonate component. 1. Calciocarbonatites, where the main carbonate is calcite, also known as calcite-carbonatite or sövite (if the rock is coarse-grained) or alvikite (if the rock is medium- to fine-grained). 2. Magnesiocarbonatites, where the main carbonate is dolomite, also known as dolomite-carbonatite. 3. Ferrocarbonatites, where the main carbonate is iron-rich. 4. Natrocarbonatites, where the rock is composed almost entirely of sodium, potassium and calcium carbonates. An additional classification of carbonatite is the silicocarbonatite, where the SiO_2 content of the rock is more than 20 percent (Le Maitre, 2002).

Calciocarbonatites represent the highest proportion of carbonatites found at the Earth's surface and are identified in extrusive and intrusive environments, with plutonic calciocarbonatites being more common (Woolley and Kjarsgaard, 2008). Calciocarbonatites are likely generated through various differentiation processes (Bailey, 1993). Magnesiocarbonatites are interpreted to be directly from the mantle, based on the entrained peridotite xenoliths and the absence of associated silicate magmas (Bailey, 1993). Ferrocarbonatites are rare and the origin of these carbonatites is still unknown, Kjarsgaard and Hamilton (1988) proposed that ferrocarbonatites reflect residual liquids that remained after crystal fractionation at low oxygen fugacities, enabling the iron to concentrate in the melt. Natrocarbonatites are the youngest manifestation of carbonatitic igneous activity and are chemically distinct from other lava compositions by their enrichment in Na_2O and K_2O (~40 wt.%), high fluoride and chloride contents (4-5 wt.%) but relatively low Ca, Mg and Fe contents (Dawson, 1962; Nielsen

and Veksler, 2002). The differences in these carbonatite compositions shows that the origin of each carbonatite must be judged on their own characteristics.

The evolution of carbonatitic magmas in the crust is known to be the most complex of all magma types. The wide array of carbonatite compositions and geological settings question the likelihood that all carbonatites originate from the same place (e.g. mantle or lithosphere) or result from the same petrogenetic process (e.g. liquid immiscibility or crystal fractionation). Over the past century, a general picture has emerged on the composition, origin and evolution of carbonatitic magmas, however much remains to be done to fully understand them.

1.1 Extrusive carbonatites

Extrusive carbonatites are composed of soluble carbonates that are easily weathered and rarely preserved in the geological record. Yet, fresh or preserved natrocarbonatites (e.g. recent volcanic eruptions) can provide significant genetic information about carbonatite magmatism that cannot be obtained by intrusive carbonatites due to post-magmatic alteration. The only active extrusive carbonatite volcano on Earth is Oldoinyo Lengai, situated in the Gregory Rift Valley in northern Tanzania. Oldoinyo Lengai has been steadily erupting alkali-rich natrocarbonatites for over 50 years.

Oldoinyo Lengai natrocarbonatites provided the first indication of a genetic link between carbonatites and alkaline silicate magmas, due to the transition of Oldoinyo Lengai from alkaline nephelinitic magmas to carbonatitic magmas (Clarke and Roberts, 1986; Dawson, 1998; Dawson et al., 1996; Deans and Roberts, 1984; Kjarsgaard et al., 1995). Liquid immiscibility is the proposed mechanism responsible for the generation of carbonatitic magma from a parental silicate magma at crustal depth, and is the most likely magmatic process that can explain the association of coexisting carbonatites and alkaline silicate rocks in intrusive and extrusive settings (Barker, 1989; Kjarsgaard and Hamilton, 1989a; Le Bas, 1989; Wyllie, 1989; Wyllie et al., 1990). The formation of carbonatites through silicate-carbonate immiscibility has been observed in experimental studies (Brooker, 1998; Brooker and Hamilton, 1990; Kjarsgaard and Hamilton, 1989b; Minarik, 1998) and petrographic and geochemical studies in natural samples (Le Bas, 1977; Panina and Motorina, 2008; Potter et al., 2017; Shastry and Kumar, 1995). Experimental studies established that immiscibility between sodium-rich carbonatites and silicate magmas can occur over a wide range of pressures and temperatures (Freestone and Hamilton, 1980; Hamilton and Kjarsgaard, 1993; Kjarsgaard and Hamilton, 1989b; Van Groos, 1975; Wyllie et al., 1990). However, definitive evidence is limited in natural samples to support liquid immiscibility within magmas, as carbonatites are commonly affected by crystallisation and post-magmatic alteration. Consequently, the process of liquid immiscibility in carbonatites and its role in magmatic differentiation has been overlooked.

Oldoinyo Lengai natrocarbonatites may not be as unique, with the weathered remnants of natrocarbonatite lavas and tuffs uncovered in the east African Rift (Deans and Roberts, 1984; Hay, 1983; Clarke and Roberts, 1986; Guzmics et al., 2011; Turner, 1988; Zaitsev and Keller, 2006) and Catanda in western Angola (Campeny et al., 2015; Giuliani et al., 2017). Natrocarbonatite lavas and tuffs at these locations have been leached by meteoric water, causing the alkalis to be removed and the original platy nyerereite to be replaced by calcite, which then metasomatises the surrounding wall rocks (fenitization) (Bailey, 1993; Baker and Nixon, 1989). The identification of these occurrences throughout the geological record indicates that natrocarbonatite volcanos like Oldoinyo Lengai have existed and that natrocarbonatites may represent a parental magma for other carbonatites. The post-magmatic alteration of intrusive carbonatite complexes means that limited evidence has been found of a genetic relation between the natrocarbonatite chemistry and the calcite-rich carbonates observed in volcanic and subvolcanic complexes around the world (Keller and Zaitsev, 2006). It is unlikely that the world's only active carbonatite volcano is unrelated to all other carbonatites in the geological record, and more likely that in the past carbonatite volcanoes like Oldoinyo Lengai have been altered and weathered and no longer resemble natrocarbonatites. A greater understanding of the link between intrusive and extrusive carbonatites is necessary to determine whether natrocarbonatites are a parental magma to other extrusive and intrusive carbonatite complexes around the world.

1.2 Intrusive alkaline-ultramafic and carbonatite complexes

Intrusive carbonatites are often spatially associated with a large range of silica-undersaturated alkaline igneous rocks (e.g. ijolite, melteigite, melilitolite, urtite, nepheline syenite and pyroxenite), mostly in concentrically zoned alkaline complexes, with some forming isolated dykes and sills, small plugs and lavas. As previously mentioned, chemical similarities between silicate phases in carbonatites and the associated silicate rocks have been used in the past to support a genetic relationship between carbonatites and silicate melts through liquid immiscibility (Cooper and Reid, 1998; Kjarsgaard and Hamilton, 1988; Kogarko et al., 1995) and crystal fractionation (Simonetti and Bell, 1994; Peterson, 1989). A wide variety of commodities have been exploited from carbonatites and associated alkaline rocks including rare earth elements, niobium, phosphate, iron, titanium, vermiculite, barite, fluorite, copper, calcite, and zirconium. Other elements enriched in these deposits are manganese, strontium, tantalum, thorium, vanadium, and uranium. Multiple stages of igneous activity and metasomatic replacement are often necessary to produce the localized ore mineral concentrations (Chakhmouradian and Zaitsev, 2012; Verplanck et al., 2014; Wall and Mariano, 1995; Xie et al., 2009). Provinces of alkaline rocks with clustered carbonatite intrusions are found in eastern Canada, northern Scandinavia, southern Brazil, East African Rift zones and the Kola Alkaline Province in Russia.

The Kola Alkaline Province (KAP) in NW Russia and eastern Finland hosts more than twenty alkaline-ultramafic rock complexes and is one of the largest carbonatite provinces in the world (Fig. 1.1; Kramm et al., 1993). The timing of alkaline and carbonatitic magmatism of the KAP has been studied extensively and is within the range of 410-362 Ma (Kramm and Sindern, 2004; Reguir et al., 2010). Many aspects of the geology of the KAP continue to generate impassioned scientific debates. A current dispute is the genesis and evolution of Ca-rich silicate rocks that are associated with carbonatites. The study of Ca-rich silicate rocks in the alkaline-ultramafic complexes could provide insight to the unknowns concerning the source and evolution of the carbonatitic magmas.

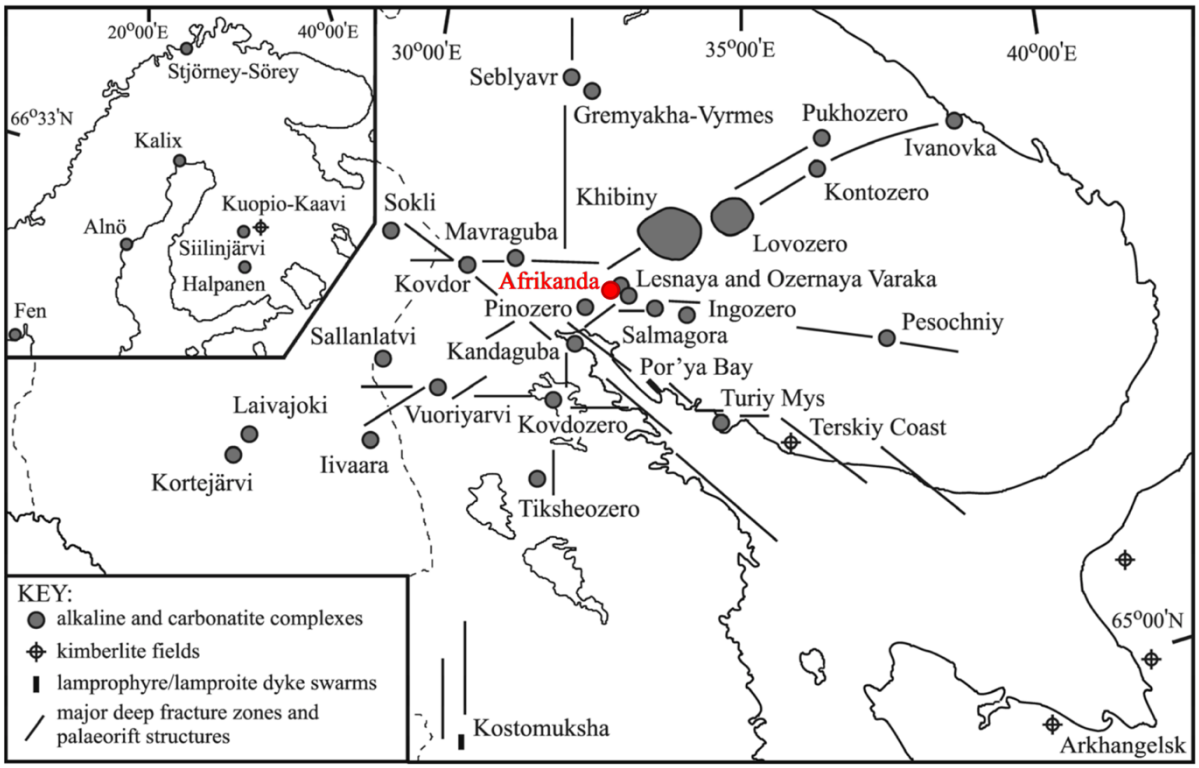

Figure 1. 1 Map of the Kola Peninsula showing the distribution of the alkaline and carbonatite complexes, kimberlite, lamproites and lamprophyres. (after Bell and Rukhlov, 2004 and Zaitsev et al., 2014).

The Afrikanda alkaline-ultramafic complex is the smallest complex in the KAP and is composed of texturally and modally diverse olivinites and clinopyroxenites, cross-cut by intrusions of carbonatitic and foiditic rocks. Afrikanda is largely assumed to be a magmatic complex, with the intrusive ultramafic rocks derived by partial melting of a metasomatised lithospheric source to produce a Ca-rich melanephelinitic magma, and the later carbonatites derived from an alkaline silica-rich carbonatitic magma that intruded the earlier-formed ultramafic rocks (Chakhmouradian and Zaitsev, 2004). The sodic alkaline nature of the carbonatite magmatism at Afrikanda and the similarities in the compositional and evolutionary trends of the plutonic ultramafic rocks at Afrikanda and Oldoinyo Lengai, have led to the hypothesis that the currently exposed lopolith at Afrikanda may have served as a feeder for a natrocarbonatite volcano similar to Oldoinyo Lengai (Chakhmouradian and Zaitsev,

2004). This comparison makes the complex an important location for understanding the link between intrusive and extrusive volcanism.

The ultramafic rocks in the Afrikanda complex host large stock-like bodies of perovskite-titanomagnetite ores enriched in rare earth elements (Yudin and Zak, 1971) and characterized by high amounts of titanium-oxide (8.5-18 %) and total iron (11-18 %) (Herz, 1976). Many complexes in the KAP host ore deposits, with active mines at Kovdor (apatite-magnetite ore), Khibiny (nepheline-apatite ore) and Lovozero (loparite-ore). However, the Afrikanda alkaline-ultramafic complex along with Powderhorn, USA and Tapira, Brazil are the only known titanium deposits where the primary titanium-bearing mineral is perovskite. All three are alkaline-carbonatite complexes hosting pyroxenites that contain perovskite-rich segregations and dikes (Armbrustmacher, 1981; Brod et al., 2013; Yudin and Zak, 1971). The rarity of perovskite ore deposits has prevented an understanding of their genesis due to the limited attention from the academic community. Understanding the formation of the perovskite-rich segregations at Afrikanda is important for understanding the source and early history of the silicate and carbonatitic magmas.

1.3 Research aims

The thesis involves case studies on the 1993 carbonatitic eruption at Oldoinyo Lengai and perovskite ore from the Afrikanda alkaline-ultramafic complex. The studies build on, and expand, the use of petrography and mineralogy of carbonatites and associated alkaline silicate rocks to further the understanding of the genesis of carbonate-silicate melts and seeks to address petrological, geochemical and economic enigmas of extrusive and intrusive carbonatitic magmas. To do this the following aims are addressed:

(1) Identify the mineral constituents and the major and trace element compositions of the minerals and melt inclusions in the rocks, using various microanalytical techniques, such as SEM, electron microprobe and LA-ICPMS.

(2) Determine the differentiation processes involved in the evolution of the carbonatites and understand the impact these processes had on the genesis of the alkaline complexes.

(3) Gain an insight into the composition of the melt prior to emplacement and the evolution of the melt during magmatic ascent.

(4) Integrate the petrological, mineralogical and geochemical data into a model regarding the genesis of Oldoinyo Lengai carbonatites and provide a new perspective on the genesis of the perovskite ore in the Afrikanda alkaline-ultramafic complex.

1.4 Thesis structure

Following the introductory chapter, the results are presented in three research chapters focusing on the processes involved in the formation of carbonatite lavas and mineralisation in carbonatite related-ore deposits. The chapters are presented as papers that have been published or currently under review in peer-reviewed scientific journals. The papers have been reformatted for this thesis but the content has not been altered from the published form. A summary of the research chapters and their relevance to the overall aims of this study are as follows:

Chapter 2

Potter, NJ. Kamenetsky, VS. Simonetti, A. Goemann, K. 2017. Different types of liquid immiscibility in carbonatite magmas: A case study of the Oldoinyo Lengai 1993 lava and melt inclusions. Chemical Geology. 455. 376-384.

The study investigates the texture and mineralogy of the June 1993 lava at Oldoinyo Lengai, and presents petrographic evidence of liquid immiscibility between silicate, carbonate, chloride, and fluoride melt phases. The data and textural observations (at both the macro- and micro-scales) indicate that the formation of this natrocarbonatite lava did not occur as a simple single-stage process, and that the silicate, carbonate, and halogen phases of the lava unmixed at different stages of evolution in the magmatic system. Several textural features are preserved in the silicate spheroids, melt inclusions, and carbonatite groundmass that exhibit evidence of silicate-carbonate, carbonate-carbonate and carbonate-halide immiscibility. The paper highlights that the rapid quenching of the lava facilitated the preservation of the liquid immiscibility end products within the groundmass. This work improves the understanding of the formation of natrocarbonatites as well as the behaviour of liquid immiscibility during the magmatic evolution of carbonatites.

Chapter 3

Potter, NJ. Ferguson, MR. Kamenetsky, VS. Chakhmouradian, AR. Sharygin, VV. Thompson, JM. Goemann, K. 2018. Textural evolution of perovskite in the Afrikanda alkaline–ultramafic complex, Kola Peninsula, Russia: Contributions to Mineralogy and Petrology. 173. p.100-120

The paper investigates the mechanisms responsible for the development of the perovskite-rich segregations within the ultramafic rocks and carbonatites of the Afrikanda alkaline-ultramafic complex. The detailed textural and chemical analysis of the three main lithologies at Afrikanda presents evidence

for the transformation of perovskite in the ultramafic rocks from clusters and networks of small, euhedral grains into large anhedral and massive grains. U-Pb geochronology was combined with major and trace element geochemistry to investigate the timing of the monomineralic perovskite ore layers developed in the different rock types at Afrikanda. The textural transformation suggests that the development of perovskite ore in the ultramafic rocks is a result of post-magmatic textural re-equilibration and recrystallization. Several distinct textural features identified in the Afrikanda perovskite are observed in other oxide ore deposits (e.g. chromite and magnetite) and indicates that the same sub-solidus amalgamation processes may be responsible for some of the coarse-grained and massive textures observed in other oxide deposits. The findings of the study have implications for the development of mineralisation in alkaline-carbonatite complexes worldwide.

Chapter 4

Potter, NJ. Kamenetsky, VS. Chakhmouradian, AR. Kamenetsky, MB. Goemann, K. Rodemann, T. Polymineralic inclusions in oxide minerals of the Afrikanda alkaline-ultramafic complex: Implications for the evolution of perovskite mineralisation. Submitted to Contributions to Mineralogy and Petrology.

This study conducts a detailed mineralogical examination of the polymineralic inclusions hosted in perovskite and magnetite from the ultramafic and carbonatitic rocks in the Afrikanda complex revealed important conclusions about the origin and evolution of the perovskite segregations in this alkaline-ultramafic complex. The unusual mineralogy and extreme variation in the inclusion assemblages ruled out a magmatic origin for the polymineralic inclusions, with the observed textures and compositions suggesting the polymineralic inclusions are formed by the entrapment of interstitial material during subsolidus sintering. A model has been developed that illustrates the post-magmatic development of perovskite from small disseminated magmatic perovskite to accumulations of massive inclusion-free perovskite. The recrystallization, sintering and grain growth processes at subsolidus temperatures are responsible for the difference in the distribution and abundance of inclusions between T1, T2 and T3 perovskite in olivinites, clinopyroxenites and silicocarbonatites at Afrikanda. The ongoing similarities identified between perovskite from Afrikanda and chromite and magnetite layers in various igneous complexes indicates that similar post-magmatic coarsening processes are involved in the formation of polymineralic inclusions in oxide minerals and ultimately the textural development of oxide ore deposits with monomineralic layers.

Chapter 5

The final chapter is a synthesis that summarises the progress made towards achieving the aims of this study and explores the limitations and significance of the research. The thesis is concluded by

highlighting new research questions that have arisen from this study and identifies future research directions for carbonatites and oxide deposits.

1.5. References

Armbrustmacher, T.J., 1981. The Complex of Alkaline Rocks at Iron Hill, Powderhorn district, Gunnison County, Colorado. New Mexico Geological Society, pp. 293-296.

Bailey, D.K., 1993. Carbonate magmas. Journal of the Geological Society, London, 150: 637-651.

Barker, D.S., 1989. Field relations of carbonatites. In: Bell, K. (Ed.), Carbonatites. Genesis and evolution. Unwin Hyman, London, pp. 38-68.

Bell, K., 2001. Carbonatites: Relationships to mantle plume activity. Mantle Plumes: Their Identification through Time(352): 267-290.

Bell, K., Kjarsgaard, B., Simonetti, A., 1998. Carbonatites - into the twenty-first century. Journal of Petrology, 39(11-12): 1839-1845.

Brod, J.A. et al., 2013. Decoupling of paired elements, crossover REE patterns, and mirrored spider diagrams: Fingerprinting liquid immiscibility in the Tapira alkaline–carbonatite complex, SE Brazil. Journal of South American Earth Sciences, 41: 41-56.

Brooker, R.A., 1998. The effect of CO_2 saturation on immiscibility between silicate and carbonate liquids: an experimental study. Journal of Petrology, 39(11/12): 1905-1915.

Brooker, R.A., Hamilton, D.L., 1990. Three-liquid immiscibility and the origin of carbonatites. Nature, 346(6283): 459-462.

Brooker, R.A., Kjarsgaard, B.A., 2011. Silicate-carbonate liquid Immiscibility and phase relations in the system SiO_2-Na_2O-Al_2O_3-CaO-CO_2 at 0.1-2.5 GPa with applications to carbonatite genesis. Journal of Petrology, 52: 1281-1305.

Campeny, M., Kamenetsky, V. S., Melgarejo, J. C., Mangas, J., Manuel, J., Alfonso, P., Kamenetsky, M. B., Bambi, A. C., and Gonçalves, A. O., 2015, Carbonatitic lavas in Catanda (Kwanza Sul, Angola): Mineralogical and geochemical constraints on the parental melt: Lithos, v. 232, p. 1-11.

Chakhmouradian, A.R., Zaitsev, A.N., 2004. Afrikanda: An association of ultramafic, alkaline and alkali-silica-rich carbonatitic rocks from mantle-derived melts. Phoscorites and carbonatites from mantle to mine: the key example of the Kola Alkaline Province, Mineralogical Society (UK) Series, 10: 247-291.

Chakhmouradian, A.R., Zaitsev, A.N., 2012. Rare earth mineralization in igneous rocks: sources and processes. Elements, 8(5): 347-353.

Church, A.A., Jones, A.P., 1995. Silicate-carbonate immiscibility at Oldoinyo Lengai. Journal of Petrology, 36: 869-889.

Clarke, M.G.C., Roberts, B., 1986. Carbonated melilitites and calcitized alkalicarbonatites from Homa Mountain, western Kenya: a reinterpretation. Geological Magazine, 123: 683-692.

Cooper, A.F., Reid, D.L., 1998. Nepheline sövites as parental magmas in carbonatite complexes: evidence from Dicker Willem, southwest Namibia. Journal of Petrology, 39(11-12): 2123-2136.

Dalton, J.A., Wood, B.J., 1993. The compositions of primary carbonate melts and their evolution through wallrock reaction in the mantle. Earth and Planetary Science Letters, 119(4): 511-525.

Dawson, J.B., 1962. The geology of Oldoinyo Lengai. Bulletin Volcanologique, 24: 349-387.

Dawson, J.B., 1998. Peralkaline nephelinite-natrocarbonatite relationships at Oldoinyo Lengai, Tanzania. Journal of Petrology, 39(11/12): 2077-2094.

Dawson, J.B., Pyle, D.M., Pinkerton, H., 1996. Evolution of natrocarbonatite from a wollastonite nephelinite parent: evidence from the June, 1993 eruption of Oldoinyo Lengai, Tanzania. The Journal of Geology: 41-54.

Deans, T., Roberts, B., 1984. Carbonatite tuffs and lava clasts of the Tinderet foothills, western Kenya: a study of calcified natrocarbonatites. Journal of the Geological Society, London, 141: 563-580.

Freestone, I.C., Hamilton, D.L., 1980. The role of liquid immiscibility in the genesis of carbonatites - an experimental study. Contributions to Mineralogy and Petrology, 73: 105-117.

Ghosh, S., Ohtani, E., Litasov, K.D., Terasaki, H., 2009. Solidus of carbonated peridotite from 10 to 20 GPa and origin of magnesiocarbonatite melt in the Earth's deep mantle. Chemical Geology, 262(1-2): 17-28.

Giuliani, A., Campeny, M., Kamenetsky, V. S., Afonso, J. C., Maas, R., Melgarejo, J. C., Kohn, B. P., Matchan, E. L., Mangas, J., and Gonçalves, A. O., 2017, Southwestern Africa on the burner: Pleistocene carbonatite volcanism linked to deep mantle upwelling in Angola: Geology, v. 45, no. 11, p. 971-974.

Guzmics, T., Mitchell, R. H., Szabó, C., Berkesi, M., Milke, R., and Abart, R., 2011, Carbonatite melt inclusions in coexisting magnetite, apatite and monticellite in Kerimasi calciocarbonatite, Tanzania: melt evolution and petrogenesis: Contributions to Mineralogy and Petrology, v. 161, p. 177-196.

Hamilton, D., Kjarsgaard, B., 1993. The immiscibility of silicate and carbonate liquids. South African journal of geology, 96(3): 139-142.

Hay, R.L., 1983. Natrocarbonatite tephra of Kerimasi volcano, Tanzania. Geology, 11(10): 599-602.

Ingrid, H.-K., 1998. Rare earth elements in sövitic carbonatites and their mineral phases. Journal of Petrology, 39(11-12): 2105-2121.

Kjarsgaard, B., Hamilton, D., Peterson, T., 1995. Peralkaline nephelinite/carbonatite liquid immiscibility: comparison of phase compositions in experiments and natural lavas from Oldoinyo Lengai, Carbonatite Volcanism. Springer, pp. 163-190.

Kjarsgaard, B.A., Hamilton, D.L., 1988. Liquid immiscibility and the origin of alkali-poor carbonatites. Mineralogical Magazine, 52: 43-55.

Kjarsgaard, B., Hamilton, D.L., 1989a. Carbonatite origin and diversity. Nature, 338(6216): 547-548.

Kjarsgaard, B.A., Hamilton, D.L., 1989b. The genesis of carbonatites by immiscibility. In: Bell, K. (Ed.), Carbonatites. Unwin Hyman, London, pp. 388-404.

Kogarko, L., Henderson, C., Pacheco, H., 1995. Primary Ca-rich carbonatite magma and carbonate-silicate-sulphide liquid immiscibility in the upper mantle. Contributions to Mineralogy and Petrology, 121(3): 267-274.

Kramm, U., Kogarko, L., Kononova, V., Vartiainen, H., 1993. The Kola Alkaline Province of the CIS and Finland: Precise Rb-Sr ages define 380–360 Ma age range for all magmatism. Lithos, 30(1): 33-44.

Kramm, U., Sindern, S., 2004. Timing of Kola ultrabasic, alkaline and phoscorite-carbonatite magmatism. Phoscorites and carbonatites from mantle to mine: the key example of the Kola Alkaline Province. Min Soc Great Britain & Ireland publication: 75-97.

Le Bas, M., 1989. Carbonatites: Genesis and evolution.

Le Bas, M.J., 1977. Carbonatite-nephelinite volcanism: an African case history. John Wiley & Sons.

Le Bas, M.J., 1987. Nephelinites and carbonatites. In: Fitton, J.G., Upton, B.G.J. (Eds.), Alkaline igneous rocks. Geological Society of London, pp. 53-83.

Lee, W.J., Wyllie, P.J., 1998. Processes of crustal carbonatite formation by liquid immiscibility and differentiation, elucidated by model systems. Journal of Petrology, 39(11-12): 2005-2013.

Le Maitre, R.W., 2002. Igneous rocks: a classification and glossary of terms: recommendations of the IUGS, Subcommission on the Systematics of Igneous Rocks. University Press.

Minarik, W.G., 1998. Complications to carbonate melt mobility due to the presence of an immiscible silicate melt. Journal of Petrology, 39(11-12): 1965-1973.

Nielsen, T., Troels F, Veksler, I.V., 2002. Is natrocarbonatite a cognate fluid condensate? Contributions to Mineralogy and Petrology, 142(4): 425-435.

Panina, L.I., Motorina, I.V., 2008. Liquid immiscibility in deep-seated magmas and the generation of carbonatite melts. Geochemistry International, 46: 448-464.

Potter, N.J., Kamenetsky, V.S., Simonetti, A., Goemann, K., 2017. Different types of liquid immiscibility in carbonatite magmas: A case study of the Oldoinyo Lengai 1993 lava and melt inclusions. Chemical Geology, 455: 376-384.

Ray, J.S., 1998. Trace element and isotope evolution during concurrent assimilation, fractional crystallization, and liquid immiscibility of a carbonated silicate magma. Geochimica et cosmochimica acta, 62(19): 3301-3306.

Reguir, E.P. et al., 2010. Trace-element study and uranium-lead dating of perovskite from the Afrikanda plutonic complex, Kola Peninsula (Russia) using LA-ICP-MS. Mineralogy and Petrology, 100(3-4): 95-103.

Richardson, D., Birkett, T., 1996. Carbonatite-associated deposits. Geology of Canadian Mineral Deposit Types, OR Ecstrand, WD Sinclair and RI Thorpe, Editors, Geological Survey of Canada, Geology of Canada(8): 541-558.

Shastry, A., Kumar, S., 1995. Petrogenesis of carbonatite veins and associated melanephelinite from Sarnu-Dandali Igneous Complex, Barmer, Rajasthan. NATIONAL ACADEMY SCIENCE LETTERS-INDIA, 18(7-8): 139-143.

Streckeisen, A., 1980. Classification and nomenclature of volcanic rocks, lamprophyres, carbonatites and melilitic rocks IUGS Subcommission on the systematics of igneous rocks. Geologische Rundschau, 69(1): 194-207.

Turner, D., 1988, Volcanic carbonatites of the Kaluwe complex, Zambia: Journal of the Geological Society, v. 145, no. 1, p. 95-106.

Van Groos, A.K., 1975. The effect of high CO2 pressures on alkalic rocks and its bearing on the formation of alkalic ultrabasic rocks and the associated carbonatites. American Journal of Science, 275(2): 163-185.

Veizer, J., Clayton, R., Hinton, R., 1992. Geochemistry of Precambrian carbonates: IV. Early Paleoproterozoic (2.25±0.25 Ga) seawater. Geochimica et Cosmochimica Acta, 56(3): 875-885.

Verplanck, P.L., Van Gosen, B.S., Seal II, R.R., McCafferty, A.E., 2014. A deposit model for carbonatite and peralkaline intrusion-related rare earth element deposits: Chapter J in Mineral deposit models for resource assessment. 2328-0328, US Geological Survey.

Wall, F., Mariano, A., 1995. Rare earth minerals in carbonatites: a discussion centred on the Kangankunde Carbonatite, Malawi. Mineralogical Society Series, 7: 193-226.

Woolley, A.R., 2003. Igneous silicate rocks associated with carbonatites: their diversity, relative abundances and implications for carbonatite genesis. Periodico di Mineralogia, 72: 17.

Woolley, A.R., Church, A.A., 2005. Extrusive carbonatites: A brief review. Lithos, 85(1-4): 1-14.

Woolley, A.R., Kjarsgaard, B.A., 2008. Paragenetic types of carbonatite as indicated by the diversity and relative abundances of associated silicate rocks: evidence from a global database. The Canadian Mineralogist, 46(4): 741-752.

Wyllie, P.J., 1988. Magma genesis, plate tectonics, and chemical differentiation of the Earth. Reviews of Geophysics, 26(3): 370-404.

Wyllie, P.J., 1989. Origin of carbonatites: evidence from phase equilibrium studies. In: Bell, K. (Ed.), Carbonatites. Genesis and evolution. Unwin Hyman, London, pp. 500-545.

Wyllie, P.J., Baker, M.B., White, B.S., 1990. Experimental boundaries for the origin and evolution of carbonatites. Lithos, 26: 3-19.

Xie, Y. et al., 2009. Continuous carbonatitic melt–fluid evolution of a REE mineralization system: Evidence from inclusions in the Maoniuping REE Deposit, Western Sichuan, China. Ore Geology Reviews, 36(1): 90-105.

Ying, J., Zhou, X., Zhang, H., 2004. Geochemical and isotopic investigation of the Laiwu–Zibo carbonatites from western Shandong Province, China, and implications for their petrogenesis and enriched mantle source. Lithos, 75: 413-426.

Yudin, B., Zak, S., 1971. Titanium deposits of northwestern USSR (eastern part of Baltic Shield). International Geology Review, 13(6): 864-872.

Zaitsev, A. N., and Keller, J., 2006, Mineralogical and chemical transformation of Oldoinyo Lengai natrocarbonatites, Tanzania: Lithos, v. 91, no. 1-4, p. 191-207.

CHAPTER 2

DIFFERENT TYPES OF LIQUID IMMISCIBILITY IN CARBONATITE MAGMAS: A CASE STUDY OF THE OLDOINYO LENGAI 1993 LAVA AND MELT INCLUSIONS

Chemical Geology 455 (2017) 376-384

2.0. Abstract

Oldoinyo Lengai is situated within the Gregory Rift Valley (northern Tanzania) and is the only active volcano erupting natrocarbonatite lava. This study investigates the texture and mineralogy of the June 1993 lava at Oldoinyo Lengai, and presents petrographic evidence of liquid immiscibility between silicate, carbonate, chloride, and fluoride melt phases. The 1993 lava is a porphyritic natrocarbonatite consisting of abundant phenocrysts of alkali carbonates, nyerereite and gregoryite, set in a quenched groundmass, composed of sodium carbonate, khanneshite, Na-sylvite and K-halite, and a calcium fluoride phase. Dispersed in the lava are silicate spheroids (<2 mm) with a cryptocrystalline silicate mineral assemblage wrapped around a core mineral. We have identified several textural features preserved in the silicate spheroids, melt inclusions, and carbonatite groundmass that exhibit evidence of silicate-carbonate, carbonate-carbonate and carbonate-halide immiscibility. Rapid quenching of the lava facilitated the preservation of the end products of these liquid immiscibility processes within the groundmass. Textural evidence (at both macro- and micro-scales) indicates that the silicate, carbonate, chloride and fluoride phases of the lava unmixed at different stages of evolution in the magmatic system.

2.1. Introduction

The petrogenetic evolution of silicate magmas is well known and extensively studied due to the preponderance of siliceous-type volcanism worldwide. In contrast, carbonate magmas are rarely observed in nature with the majority identified in intrusive settings and commonly altered post emplacement (Mitchell, 2005; Woolley, 2003). Oldoinyo Lengai (Tanzania) is the sole active volcano that erupts carbonatites and provides an unprecedented opportunity to better understand the magmatic evolution of this non-silicate type of Earth's magmatism.

The most commonly accepted mechanism proposed for the formation of natrocarbonatites is silicate-carbonate liquid immiscibility (Church and Jones, 1995; Dawson et al., 1996; Keller and Krafft, 1990; Kjarsgaard et al., 1995; Mitchell, 2009; Mitchell and Dawson, 2012; Peterson, 1990; Sharygin et al., 2012). Liquid immiscibility is defined as "*the coexistence of two or more liquid phases in equilibrium…[and]…occurs when the sum of the free energies of two melts in less than that of a mixture of them*" Freestone (1989). The rarity of and difficulty in capturing definitive evidence of liquid immiscibility within magmas has posed a challenge for researchers, as the rocks undergo crystallisation and post-magmatic alteration. For evidence to be preserved of the unmixing process, the liquids must either spatially separate or undergo no magmatic or weathering processes after unmixing. Consequently, the process of liquid immiscibility and its role in magmatic differentiation has been largely overlooked.

Melt inclusion and experimental studies are the primary methods used to support the identification of liquid immiscibility during the formation of magmatic rocks. Melt inclusions provide 'snapshots' of melts and fluids at the time of crystallisation and have recorded occurrences of liquid immiscibility in magmas from a variety of different tectonic settings (Kamenetsky and Kamenetsky, 2010; Mitchell, 2009; Panina and Motorina, 2008; Sekisova et al., 2015; Thompson et al., 2007). Experimental work endeavors to reproduce the sequence and composition of the phases appearing in natural rocks, offering theoretical conditions for these unmixing processes (Brooker and Kjarsgaard, 2011; Freestone and Hamilton, 1980; Kjarsgaard and Peterson, 1991; Moore, 2012; Veksler et al., 2012; Wyllie et al., 1990). The small size (<25 μm) and disequilibrium state within the melt inclusions, and the limited applicability of experimental studies to the natural environment renders some of the evidence and interpretations controversial.

Here we describe the texture and mineralogy of natrocarbonatite lava samples from the 1993 eruption at Oldoinyo Lengai and present both petrographic and melt inclusion evidence for the occurrence of liquid immiscibility between silicate, carbonate, chloride, and fluoride melt phases.

2.2. Geological setting and previous work

Oldoinyo Lengai, the only active natrocarbonatite volcano in the world, is situated within the Gregory Rift Valley in northern Tanzania. Between June 14 and June 25 1993, two of the most volumetrically largest lava flows erupted at Oldoinyo Lengai: the massive southern flow and the Chaos Crags flow (Dawson et al., 1994). These eruptions terminated a 10-year period that was dominated by the extrusion of low-volume, highly mobile carbonatite flows (Dawson et al., 1996). The samples investigated here are from the Chaos Crags flow, which is a particularly crystal-rich lava (79-91 % by volume), with a similar viscosity to rhyolite (Dawson et al., 1994). Several previous studies have investigated samples from the June 1993 lava and reported detailed descriptions of the eruption with

petrography and mineralogy of the lava (Church and Jones, 1995; Dawson et al., 1994; Dawson et al., 1996) and geochemical data (Simonetti et al., 1997).

2.3. Methodology

The samples were mounted in epoxy resin and polished using kerosene to prevent destruction of soluble minerals and melt inclusions. After exposure, samples were stored in a desiccator to minimise interaction with atmospheric moisture. All analytical work was performed at the Central Science Laboratory (CSL), University of Tasmania, Australia.

Mineral and melt inclusion compositions were determined by backscattered electron (BSE) imaging and energy dispersive X-ray spectrometry (EDS) using a Hitachi SU-70 field emission scanning electron microscope (SEM). Silicate and fluorapatite kernels were analysed using a Cameca SX100 electron microprobe equipped with a tungsten filament and five wavelength dispersive spectrometers (WDS) using 15 kV accelerating voltage, 30 and 20 nA beam current and a 5 and 20 μm beam diameter, respectively. Additional details are provided in Supplementary Methods. Electron backscattered diffraction (EBSD) on a Hitachi SU-70 SEM was used to evaluate the crystallographic orientation of the crystal microstructures. Ion-polishing for EBSD studies was done in Adelaide Microscopy. The EBSD analysis was performed using 20 kV acceleration voltage, around 3 nA beam current and an Oxford AZtec NordlysNano EBSD detector intergrated with the EDS system.

2.4. Results

The lava is a porphyritic natrocarbonatite composed of abundant euhedral to subhedral phenocrysts of alkali carbonates, nyerereite $Na_2Ca(CO_3)_2$ and gregoryite $(Na_2K_2Ca)CO_3$, surrounded by a quenched carbonatite groundmass (Fig. 2.1). Dispersed in the lava samples are silicate spheroids (<2 mm) characterised by a core kernel (>200 μm) enveloped in a cryptocrystalline assemblage composed of various silicate minerals. The lava has a low to moderate vesicularity (7-26 % vesicles), with a size distribution from <50 μm to 10 mm. Small vesicles have subspherical shapes, whereas the large vesicles are irregular and elongated, often showing signs of coalescence.

2.4.1. *Groundmass*

The carbonatite groundmass accounts for around 20% of the lavas' volume (excluding vesicles) and is mainly composed of sodium carbonate, khanneshite $(NaCa)_3(Ba,Sr,Ce,Ca)_3(CO_3)_5$, salt aggregates and a CaF phase (Fig. 2.2). Scattered throughout the carbonatite groundmass are anhedral to subhedral crystals (<20 μm) of apatite, cuspidine $Ca_4(Si_2O_7)(F,OH)_2$, nepheline $(Na,K)AlSiO_4$ and sulphides.

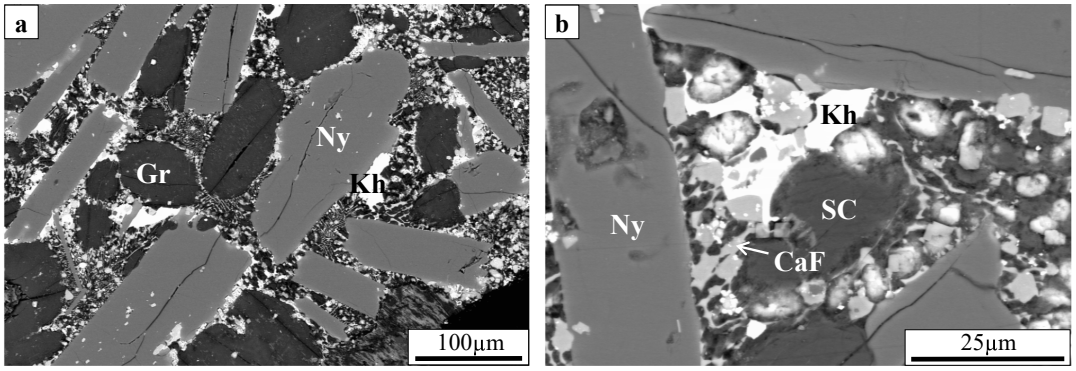

Figure 2. 1 (a) Back scattered electron (BSE) image of the 1993 lava, with nyerereite and gregoryite phenocrysts surrounded by the carbonatite groundmass. (b) BSE image of khanneshite in the carbonatite groundmass. Abbreviations: CaF – calcium fluoride, Gr – gregoryite, Kh – khanneshite, Ny – nyerereite, SC – sodium carbonate.

The primary constituent of the groundmass is a sodium-rich carbonate phase (Figs. 2.2, 2.3) that has a similar chemical composition to the gregoryite phenocrysts but contains slightly more Na (32% and 31%, respectively) and less Ca (5% and 7%, respectively). Another groundmass carbonate is Ba-rich (38-41 wt.% BaO), similar to khanneshite, distributed sporadically in the lava and has irregular, angular shapes (Fig. 2.1b). The salt aggregates are composed of two chloride end-members: potassium and sodium chloride, with both phases containing minor Na and K, respectively. Potassium chloride (Na-sylvite) is the primary component with sodium chloride (K-halite) dispersed inside, although there are areas composed of pure halite. Irrespective of their composition, all salt aggregates have spherical to irregular shapes (Fig. 2.3). The CaF phase exhibits linear, globular, symplectic, and graphic textures (Fig. 2.3), similar textures have been observed by Church and Jones (1995) and Dawson et al. (1996).

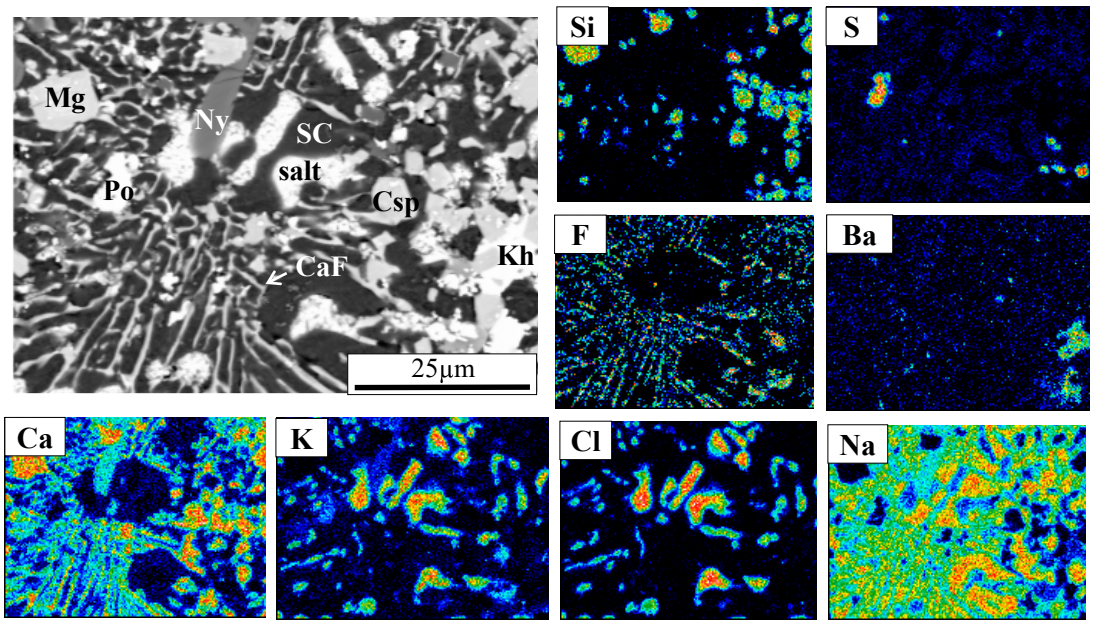

Figure 2. 2 BSE image and EDS element maps of the carbonatite groundmass. Abbreviations: CaF – calcium fluoride, Csp – cuspidine, Kh – khanneshite, Mg – magnetite, Ny – nyerereite, Po – pyrrhotite, salt – K-halite and Na-sylvite, SC – sodium carbonate.

The texture of the CaF phase varies throughout the samples and appears to be dependent on the surrounding phases, the most prevalent is the linear intergrowth texture (Fig. 2.3b). There are several crystallographic orientations observed for a given CaF phase (Figs. 2.4c, d). The variation in colour in Figures 2.4c and 2.4d indicates a difference in the orientation of the crystals, that is attributed to changes in the x, y and z axis. The stoichiometric composition is 44-47 wt.% F, 50-53 wt.% Ca and 1–4 wt.% Sr.

The sulphide minerals identified within the groundmass are pyrrhotite, Fe-alabandite MnS, Mn-sphalerite (Zn,Fe)S, djerfisherite $K_6Na(Fe,Cu,Ni)_{22}S_{26}Cl$ and galena. These sulphides mostly occur as small individual (<20 μm) anhedral crystals, as well as rare clusters (25-75 μm). The K-Fe-sulphide mineral has been identified as djerfisherite by the K:Fe:S ratio, despite the lack of Cu, Ni and Cl. The djerfisherite crystals occur as anhedral grains ranging in size from 5 μm to 100 μm, and contain 8-11%

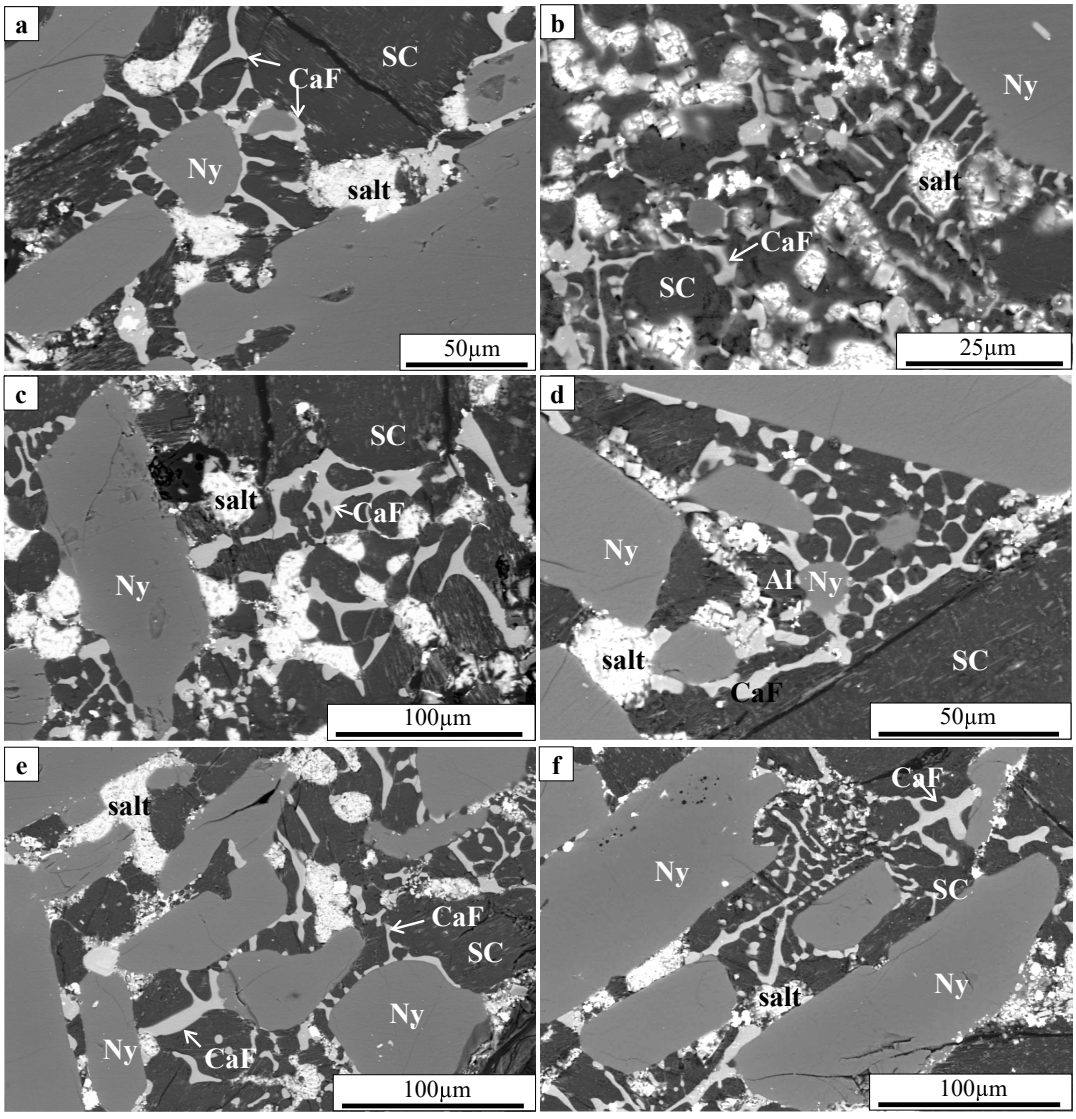

Figure 2. 3 BSE images of groundmass textures in the June 1993 lava. Abbreviations: Al – Fe-alabandite, CaF – calcium fluoride phase, Ny – nyerereite, salt – K-halite and Na-sylvite, SC – sodium carbonate.

K and 38-44% Fe. K-Fe-sulphide minerals have been observed in other natrocarbonatite lavas at Oldoinyo Lengai (Dawson et al., 1995; Jago and Gittins, 1999; Mitchell, 1997; Mitchell, 2006). The irregular distribution of the sulphide minerals throughout the groundmass and in phenocrysts suggests that they were present in the magma prior to eruption, as supported by Mitchell (1997) in the case of the 1995 eruption.

Other accessory minerals found in the groundmass are euhedral to subhedral crystals of fluorapatite, nepheline, cuspidine, and magnetite with an elevated concentration of Mn (1-4 wt. %). The cuspidine crystals (<20 µm) exhibit oscillatory zoning and contain numerous inclusions of Mn-magnetite. Other rare minerals include a potentially water-bearing potassium sulphate (<10 um) and an unknown Ba-K-Na-Mg fluoride mineral that forms small (<10 µm) anhedral grains. A similar fluoride

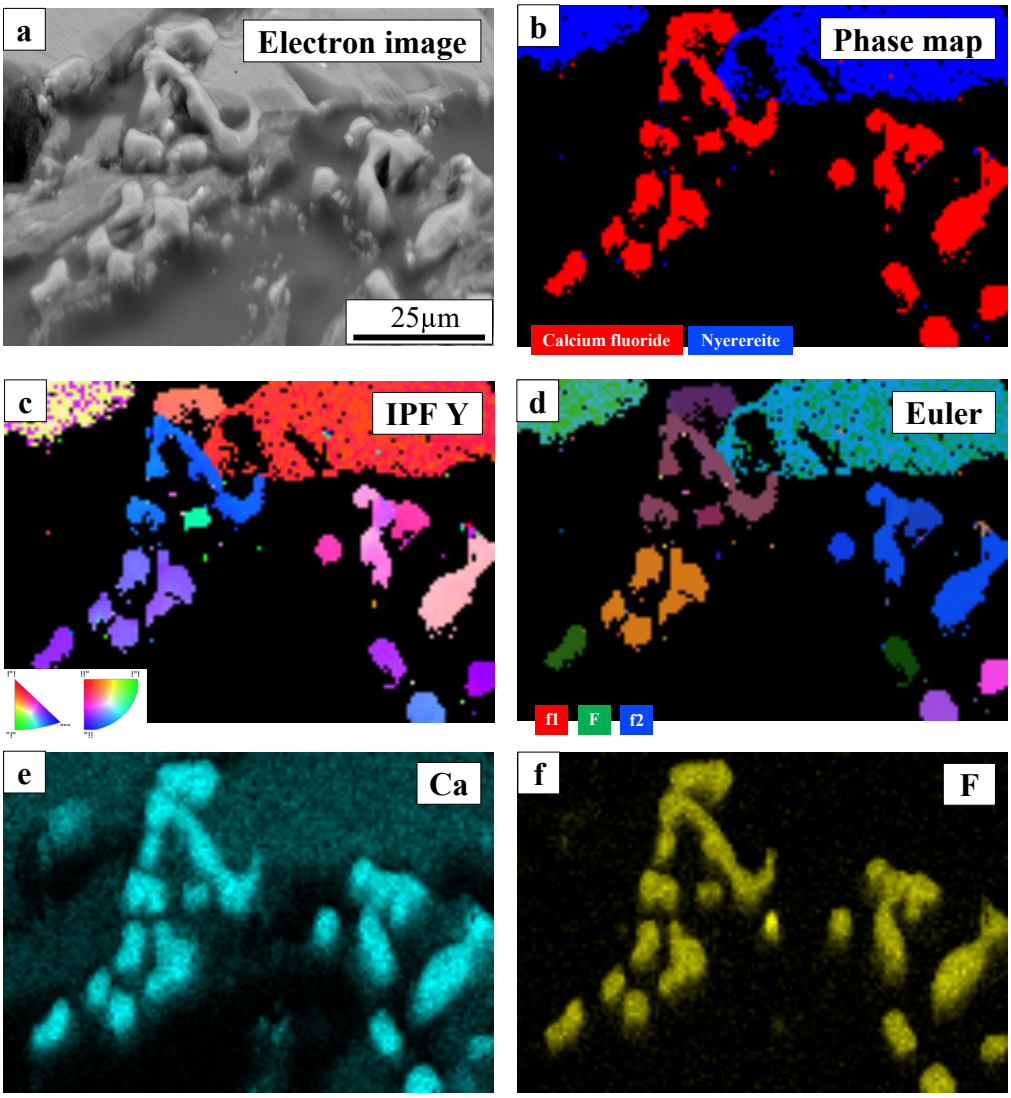

Figure 2. 4 (a) Electron image of the area mapped with a clear outline of the calcium fluoride (CaF) phase. (b) Phase map based on combined EDS and EBSD data showing the CaF phase. (c) Inverse pole figure (IPF) map in the Y direction showing varying crystal orientations in different colours. (d) Euler angle map using colours to denote the variety of crystal orientations in space using Euler angles: φ1-red φ-green, φ2-blue. (e-f) EDS compositional maps showing the uniform concentration of calcium and fluorine in the CaF phase.

mineral was identified by Mitchell (1997) as an intermediate member between neighborite and its potassium analogue, identified as K-neighborite (Na,K)MgF_3.

2.4.2. Silicate spheroids

The silicate spheroids (<2 mm) feature a central kernel (<1 mm) surrounded by a cryptocrystalline assemblage of clinopyroxene, garnet, nepheline, wollastonite, fluorapatite, magnetite, cuspidine and various sulphides (<20 μm; Fig. 2.5). There is a distinct boundary between the spheroids and the surrounding carbonatite groundmass, with nyerereite phenocrysts oriented around the spheroids (Fig. 2.5a). The amount of the silicate material around kernels varies from a thin coating (Fig 2.5d) to a much greater thickness that can fluctuate around the kernel (Figs. 2.5a, c). The kernel is usually a single euhedral crystal, or less commonly two or more crystal species either isolated or as a crystal aggregate (Figs. 2.5a-d). These grains are typically nepheline, clinopyroxene, garnet, wollastonite and fluorapatite. A subspherical carbonate phase is present within the silicate mineral assemblage, ranging in size from 10 to 150 μm (Figs. 2.5e, f). Some have separated into two carbonate compositions, a Na-rich phase (30-40 wt.% Na_2O), and a Ca-rich phase (23-28 wt.% CaO, 7-8 wt.% K_2O), both have irregular shapes, usually with the Ca-rich phase enveloped by the Na-rich phase.

2.4.2.1. Kernels

The majority of the nepheline grains have a homogeneous composition (Fig. 2.5b) with a small number exhibiting minor zonation with antithetic variations in FeO and K_2O concentrations (0.9-2.4 wt. % and 6-7.3 wt. %, respectively). The wollastonite grains are lath-shaped and have homogeneous compositions. Garnet grains belong to the andradite-schorlomite solid solution series and are identified as schorlomite end-members due to their high TiO_2 contents (10-15 wt. %; Fig. 2.5c). This mineral is referred to as Ti-andrandite by Dawson et al. (1996) and melanite by Church and Jones (1995). Clinopyroxene grains have predominantly low-Al, low-Ti compositions and display irregular oscillatory zoning with varying Mg and Fe contents that are readily observed in the BSE images (higher and lower Mg/Fe ratios correspond to darker and lighter areas, respectively; Fig 2.5d). The fluorapatite grains have high F contents (2-3 wt. %) and are less common than the previously mentioned silicate minerals. All kernels contain inclusions (10–50 μm) of other minerals including wollastonite, schorlomite, nepheline, clinopyroxene, titanite, and pyrrhotite. The chemical compositions of the kernels are provided in Supplementary Table S2.1. Detailed descriptions of the kernels in the silicate spheroids are given in Church and Jones (1995), Dawson et al. (1994) and Dawson et al. (1996).

2.4.3. Alkali carbonate phenocrysts

The nyerereite phenocrysts are primarily euhedral lath-shaped crystals (Fig. 2.1) with homogeneous compositions and inclusions (<50 μm) of fluorapatite, unknown Ba-K-Na-Mg fluoride, and small clusters (<50 μm) of cuspidine and djerfisherite crystals (<10 μm). The gregoryite phenocrysts have mostly rounded shapes with no well-defined crystal faces (Fig. 2.1) and occasionally contain inclusions (5-20 μm) of nyerereite, magnetite and djerfisherite. These crystals differ in their degree of chemical and textural alteration, some phenocrysts have homogenous compositions, while others have perthitic textures with variation in the Na and K content across each phenocryst (4-39 wt. % and 14-33 wt. %, respectively). Some altered phenocrysts display simple lamellar textures, whereas irregular, patchy textures with disseminated halite or K-halite are dominant. The lamellar textures suggest the breakdown of the gregoryite solid solution (Dawson et al., 1995). Also, the rims of the chemically altered gregoryite phenocrysts are more texturally uneven than the homogeneous phenocrysts.

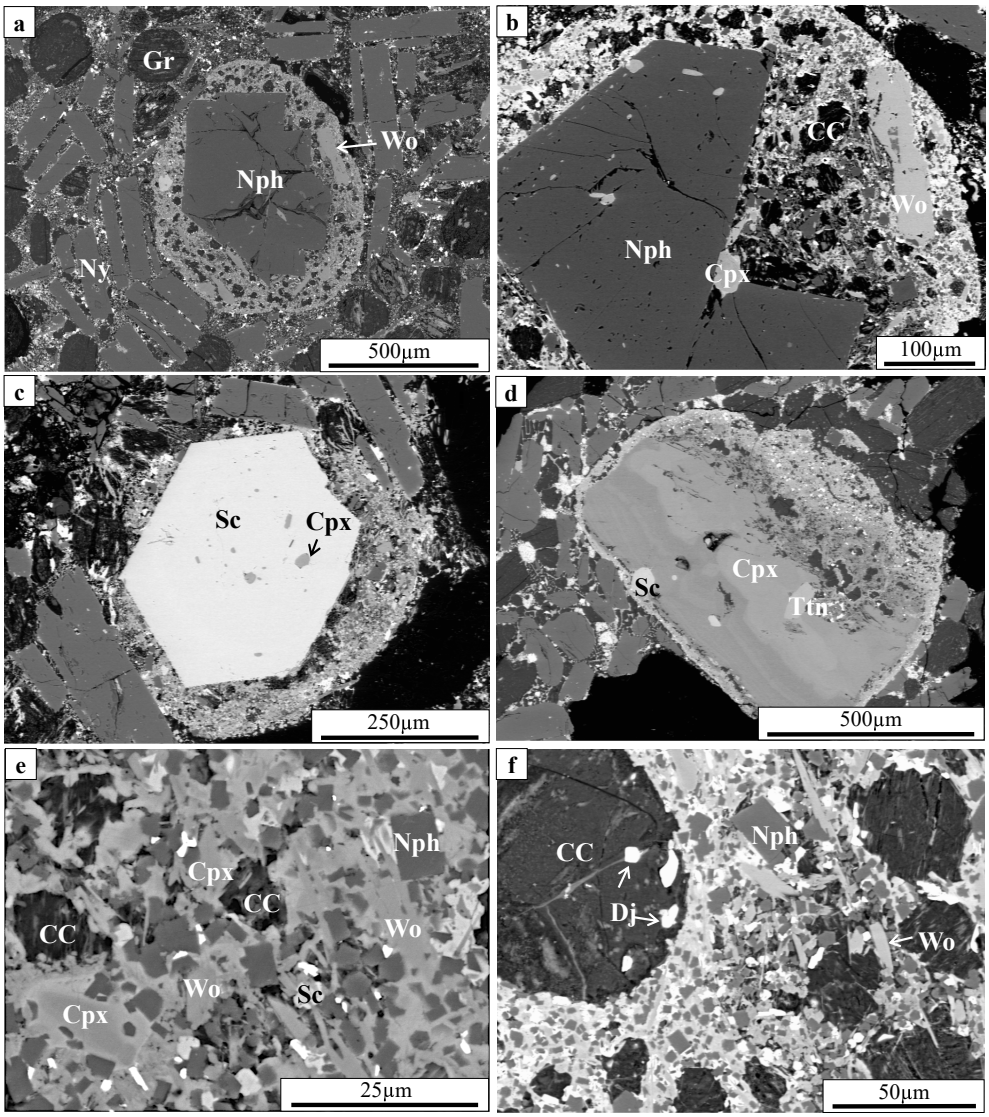

Figure 2. 5 BSE images of silicate spheroids in the June 1993 lava. (a, b) Nepheline kernel surrounded by a silicate mineral assemblage. (c) Schorlomite kernel surrounded by a silicate mineral assemblage. (d) Clinopyroxene kernel surrounded by a thin coating of the silicate mineral assemblage. (e, f) Close up of the silicate mineral assemblage within the silicate spheroids. Abbreviations: CC – carbonate component, Cpx – clinopyroxene, Dj – djerfisherite, Gr – gregoryite, Nph – nepheline, Ny – nyerereite, Sc – schorlomite, Ttn – titanate, Wo – wollastonite.

The chemical compositions of the nyerereite and gregoryite phenocrysts do not differ significantly from those documented in other natrocarbonatite lavas, except for the nyerereite phenocrysts which have high BaO contents (up to 3 wt. %; Supplementary Table S2.2). More details on the composition and textures of nyerereite and gregoryite phenocrysts from other eruptions are described in Mitchell and Kamenetsky (2012), Peterson (1990) and Zaitsev et al. (2009).

2.4.4 Melt inclusions

The exposed silicate and carbonate melt inclusions have a negative crystallographic shape and are randomly distributed throughout the crystals (Fig. 2.6). These are primary melt inclusions and represent the melt composition at the time of entrapment, but may not represent the bulk composition as all phases may not have been observed.

2.4.4.1. Silicate spheroids

The silicate melt inclusions (10 to 50 μm) are identified in all the silicate kernel minerals (nepheline, wollastonite, clinopyroxene and schorlomite; Figs. 2.6a-e). The glasses are silica-undersaturated and highly enriched in alkali elements (Supplementary Table S2.3). The majority of the silicate melt inclusions contain small Na-rich carbonate globules (2-10 μm) and occasionally enclose small crystals (2-5 μm) of apatite, clinopyroxene, magnetite and pyrrhotite. The wollastonite-hosted melt inclusions are also characterised by the presence of annite (10 to 30 vol.%; Fig. 2.6c).

The clinopyroxene and schorlomite phenocrysts contain both silicate and silicate-carbonate melt inclusions. The silicate-carbonate melt inclusions contain Na-rich carbonate globules along with a polycrystalline carbonate globule (5-20 μm) composed of a fine-grained aggregate of Na-rich and Ca-rich carbonate phases, similar to the carbonate component in the silicate spheroids (Figs. 2.6d, e).

2.4.4.2. Alkali carbonate and fluorapatite phenocrysts

Primary carbonate melt inclusions (5-25 μm) have been identified in nyerereite, gregoryite and fluorapatite phenocrysts (Figs 2.6f-i). These melt inclusions are scarce in comparison to the silicate melt inclusions as nyerereite and gregoryite typically lack melt inclusions. The carbonate melt inclusions have comparable chemical compositions to the carbonatite groundmass. The fluorapatite-hosted carbonate melt inclusions contain Na-rich carbonate globules and inclusions of apatite and calcite (Fig. 2.6f). Some of the melt inclusions have separated into an alkali carbonate and khanneshite, with daughter phases of cuspidine, nepheline, magnetite, and an unk own Ba-K-Na-Mg fluoride (Fig. 2.6g). Rare melt inclusions hosted in gregoryite contain a single nyerereite crystal in a heterogeneous carbonate-Na-sylvite matrix (Fig. 2.6h). In contrast, the nyerereite phenocrysts contain abundant melt inclusions,

composed of sodium carbonate, CaF and Na-sylvite with trapped crystals of cuspidine, apatite, and magnetite (Fig. 2.6i).

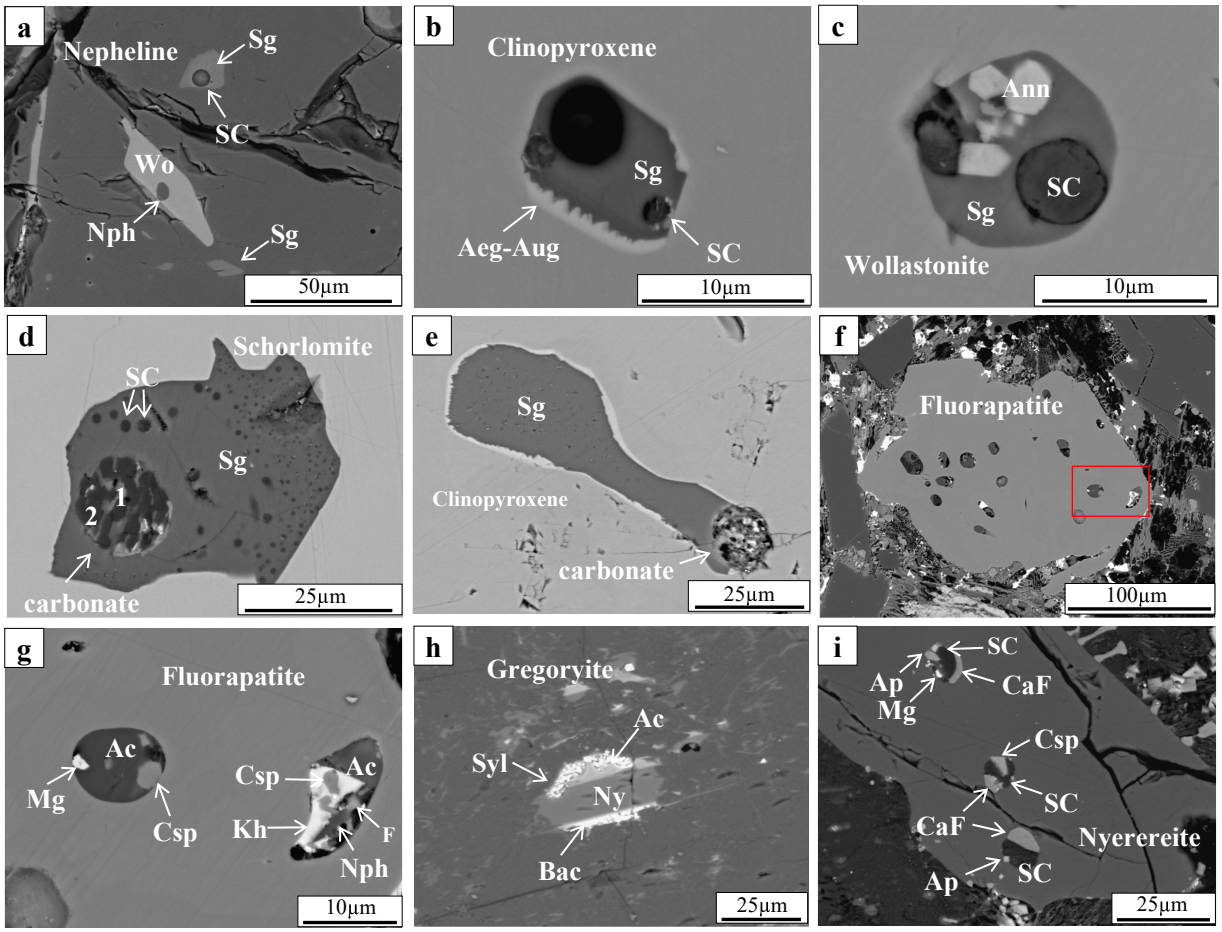

Figure 2. 6 BSE images of silicate and carbonate melt inclusions. (a) Nepheline kernel with silicate melt inclusions. (b) Clinopyroxene-hosted silicate melt inclusion with an intermediate reaction rim of aegirine-augite. (c) Wollastonite-hosted silicate melt inclusion. (d) Schorlomite-hosted silicate melt inclusion with a carbonate globule. (e) Clinopyroxene-hosted silicate melt inclusion with a carbonate globule. (f) Fluorapatite phenocryst in the carbonatite groundmass with numerous carbonate melt inclusions. (g) A close up of a carbonate melt inclusions in the figure 6f fluorapatite phenocryst. (h) Gregoryite-hosted carbonate melt inclusion. (i) Nyerereite-hosted carbonate melt inclusion. Abbreviations: Ac – alkali-carbonate, Aeg – aegirine, Ann – annite, Ap – apatite, Aug – augite, Bac – barium-rich carbonate, CaF – calcium fluoride phase, Csp – cuspidine, F – unknown Ba-K-Na-Mg fluoride, Kh - khanneshite, Mg – magnetite, Nph – nepheline, Ny – nyerereite, SC – sodium carbonate, Sg – silicate glass, Syl – Na-sylvite, Wo – wollastonite, 1 - calcium-rich phase, 2 - sodium-rich phase.

2.5. Discussion

2.5.1. Silicate-carbonate immiscibility

Occurrences of silicate-carbonate liquid immiscibility are widespread in nature and have been well documented in several alkaline carbonate-bearing complexes (Guzmics et al., 2011; Guzmics et al.,

2012; Lloyd and Stoppa, 2003; Mitchell, 2009; Mitchell and Dawson, 2012; Nielsen et al., 1997; Panina, 2005; Sharygin et al., 2012; Zaitsev et al., 2009). In our study, textural features of the silicate spheroids, melt inclusions and carbonatite groundmass provide evidence of silicate-carbonate immiscibility. The main textural evidence that supports liquid immiscibility in the lava is the distinct boundaries between different compositions in the melt inclusions and groundmass.

As textural evidence for liquid immiscibility is rarely preserved in rocks, melt inclusions are fundamental for the identification of unmixing in natural systems. The onset of silicate-carbonate immiscibility in carbonate-rich magmatic systems is an area of ongoing research, and there have been several heating experiments on synthetic and natural samples to determine the temperature and pressure of unmixing (Freestone and Hamilton, 1980; Kjarsgaard et al., 1995; Koster van Groos and Wyllie, 1966; Sharygin et al., 2012).

The silicate spheroids are identified as immiscible droplets of nephelinitic composition, which is consistent with previous interpretations (Church and Jones, 1995; Dawson et al., 1994; Dawson et al., 1996). The distinct boundary between the spheroids and the surrounding carbonatite, the rounded shape of the spheroids, the orientation of the nyerereite phenocrysts around the spheroids and the absence of penetration by these phenocrysts (Figs. 2.5a, b), all support the idea that silicate-carbonate liquid immiscibility enabled the formation of the silicate spheroids. These textures also suggest that the silicate spheroids were molten when first enveloped by the carbonate melt, enabling a subspherical shape. The silicate spheroids subsequently cooled and solidified prior to the crystallisation of the surrounding carbonate melt preventing the carbonate melt from penetrating the spheroids, an interpretation first proposed by Dawson et al. (1996).

The presence of the carbonate component within the silicate mineral assemblage in the spheroids (Figs. 2.5e, f) suggests that silicate-carbonate immiscibility proceeds with changes in temperature and pressure in the magmatic system. The carbonate components have comparable chemical compositions, however, some have separated into Ca-rich and Na-rich phases similar to the carbonate globules in the silicate-carbonate melt inclusions (e.g. Fig. 2.6d), suggesting that the carbonate melt had a comparable chemical composition during unmixing. Dawson et al. (1994) suggested "*the presence of carbonatite phases in the glasses entrapped in both the spheroid silicate phenocrysts and the spheroid matrix indicates that the spheroids are exhibiting multiple episodes of separation of carbonatite from a silicate melt*". The timing of separation of the carbonate component from the surrounding silicate melt remains unknown. However, we suggest that liquid immiscibility during magmatic ascent and cooling could have enabled the separation of the carbonate component from the surrounding silicate melt. Another possiblility could be that the carbonate component was trapped in the silicate melt when the silicate spheroids were first incorporated into the natrocarbonatite magma at the top of the magma chamber.

The kernels in the silicate spheroids do not represent phenocrysts in the natrocarbonatite magma, but they crystallised from the nephelinitic melt in the magma chamber. The kernels host silicate melt inclusions that are interpreted to represent the parental peralkaline nephelinitic magma in the magma chamber. The coexsistence of silicate and silicate-carbonate melt inclusions in the clinopyroxene and schorlomite kernels is the evidence for onset of silicate-carbonate liquid immiscibility, with the separation of the melt into two coexisting silicate and carbonate liquids.

The presence of cuspidine, nepheline and tilleyite in the groundmass is evidence that silica was present in the natrocarbonatite magma during crystallisation (Fig. 2.2; Dawson et al., 1996). The crystallisation of cuspidine is enabled by the significant concentration of fluorine in the natrocarbonatite magma.

2.5.1.1. Petrogenesis of silicate spheroids

The presence of silicate spheroids has not been reported in other natrocarbonatite lavas at Oldoinyo Lengai. The petrogenic model envisaged for the formation of these silicate spheroids in the 1993 lava is an adaptation of the processes suggested by Church and Jones (1995), Dawson et al. (1994) and Dawson et al. (1996), and is summarised here (Fig. 2.7). Prior to the 1993 eruption an injection of peralkaline nephelinitic magma intruded into the magma chamber (Fig. 2.7b). The intrusion disrupted the carbonate crystal mush at the top of the magma chamber that contains a high modal abundance of nyerereite and gregoryite phenocrysts (Dawson et al., 1994; Dawson et al., 1996). This enabled the incorporation of silicate kernels into the natrocarbonatite magma, with a silicate melt surrounding the kernels (Fig. 2.7c). The elevated viscosity of the 1993 natrocarbonatite magma (i.e. nyerereite and gregoryite crystal mush; Dawson et al., 1994; Dawson et al., 1996) prevented the silicate spheroids from settling back into the nephelinitic magma (Fig. 2.7c).

2.5.2. Carbonate-carbonate immiscibility

Two carbonate phases have been identified within the groundmass of the June 1993 lava: sodium carbonate and khanneshite. Dawson et al. (1996) also identified two carbonate groundmass phases, a gregoryite-like phase and a Ba-rich carbonate phase referred to as witherite. The Ba-rich carbonate phase has a variety of compositions in other natrocarbonatite lavas, most likely caused by the different chemical compositions of the carbonate melt (Dawson et al., 1996; Mitchell, 1997; Mitchell, 2006; Peterson, 1990). The identification of two different carbonate phases in these natrocarbonatite lavas points to unmixing of carbonates as a common feature of lavas at Oldoinyo Lengai.

We suggest that carbonate-carbonate immiscibility occurred during quenching. The separation produced khanneshite and a homogeneous Na-K-rich carbonate phase containing fluorine and chlorine, which subsequently separates into sodium carbonate, CaF, and salt. The immiscible separation of these two carbonate phases was supported by Mitchell (1997), whereas Dawson et al. (1996) attributed the

presence of two carbonate phases rather than one homogeneous carbonate phase (Phase X) and the coarser grain size of the "*sylvite and fluorite*" is due to slower cooling of the June 1993 lava.

2.5.3. Carbonate-halide immiscibility

We interpret the intergrown textures and chemical compositions of the groundmass phases: sodium carbonate, khanneshite, CaF and salt, and the presence of these same phases within the carbonate melt inclusions, to be evidence for carbonate-halide immiscibility in the June 1993 eruption at Oldoinyo Lengai. The presence of multiphase carbonate-halide immiscibility is identified by textural relationships between the carbonate, chloride, and fluoride phases in the groundmass and within the carbonate- and apatite-hosted melt inclusions. The melt inclusions have similar chemical compositions and textures as the carbonatite groundmass, which indicates that the same unmixing processes occurred on both macro- and micro-scales (Figs. 2.3, 2.6g-i). Subspherical to irregular shapes of the mixed Na-sylvite and K-halite aggregates are common in the groundmass of natrocarbonatites (Church and Jones, 1995; Dawson et al., 1995; Dawson et al., 1996; Keller and Krafft, 1990; Mitchell, 1997; Mitchell, 2006) and are most likely caused by sporadic unmixing of the chloride liquid (Fig. 2.3). The CaF phase has been identified in other natrocarbonatite lavas as "*intergrown fluorite with a gregoryite-like mineral*" (Church and Jones, 1995; Dawson et al., 1996; Mitchell, 1997; Mitchell, 2006). The EBSD data shows that the CaF phase has relatively homogeneous crystalline structures (Fig. 2.4), but has a distinctive texture that is typical of a liquid occurring interstitially to solid phases (e.g. nyerereite in this case; Fig. 2.3). The high crystal content of the lava, and thus inferred high degree of crystallisation, could have led to high concentrations of fluorine and chlorine in the residual melt, prompting unmixing of halide liquids on quenching. The process of liquid immiscibility during quenching and related textures are best depicted in experimental works with carbonate-silicate compositions, where the melt components form 'immiscibility' textures, and *bona fide* crystallographic shapes do not have time to develop (Brooker and Kjarsgaard, 2011; Kamenetsky and Yaxley, 2015). Immiscible carbonate-halide intergrowths have been described in other natrocarbonatite lavas with different proportion and composition of the unmixed components (Mitchell, 1997; Mitchell, 2006; Peterson, 1990). The rapid quenching of the lava facilitated the preservation of the end products of these immiscibility processes within the groundmass.

2.5.4. Multistage immiscibility

The mineralogical and textural features of the studied samples support the following origin of the 1993 natrocarbonatite lava at Oldoinyo Lengai (Fig. 2.7). The unmixing of the silicate, carbonate, chloride and fluoride components can be separated into different stages of evolution in the magmatic system and represent both high- and low-pressure immiscibility.

The first stage of liquid immiscibility is recorded by the silicate spheroids and the silicate melt inclusions within the central kernels. The observation of sodium carbonate globules and fine-grained carbonate aggregates in the silicate melt inclusions indicates that the onset of silicate-carbonate liquid

immiscibility happened prior to the crystallisation of the silicate minerals in the magma chamber. This immiscibility resulted in the spatial separation of the carbonate melt from the parental peralkaline nephelinitic melt in the magma chamber (Fig. 2.7a; Dawson et al., 1992; Mitchell, 1997; Sharygin et al., 2012). Our interpretations support that the separation happened at a shallow level within the magma plumbing system at Oldoinyo Lengai (Freestone and Hamilton, 1980; Keller and Zaitsev, 2012; Kervyn et al., 2008; Kjarsgaard et al., 1995).

The second stage of immiscibility occurred during eruption, as the decreasing temperature and pressure promotes unmixing in the carbonate melt, generating a heterogeneous mix of four immiscible phases. These fractions are represented by the two carbonate phases: sodium carbonate and khanneshite, and the two halide phases: CaF and Na-sylvite and K-halite salt aggregates.

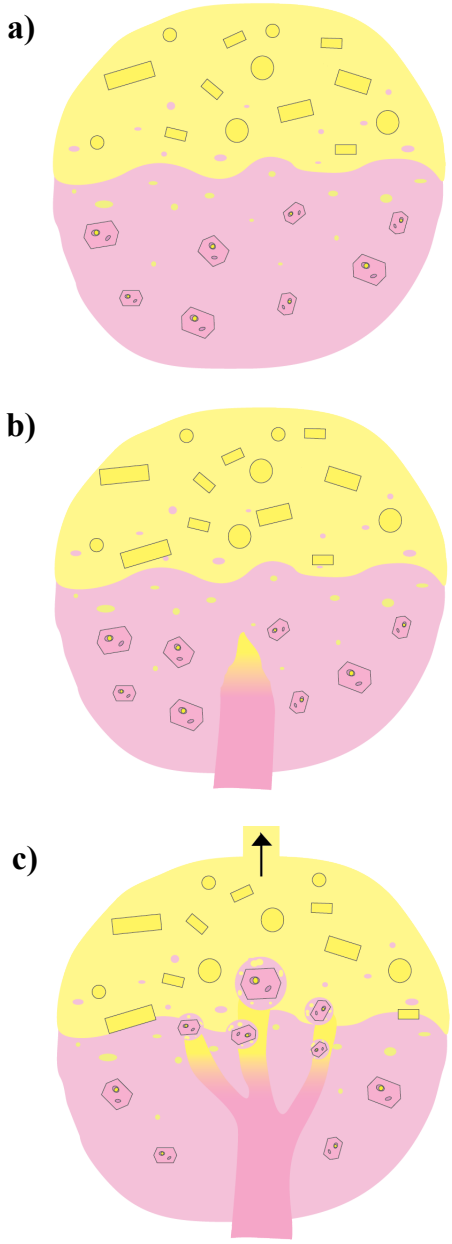

Figure 2. 7(a) Stratified magma chamber with an emulsion of nephelinitic magma overlain by natrocarbonatite magma. The stratification is a result of silicate-carbonate immiscibility. The high modal abundance of gregoryite and nyerereite phenocrysts in the lava indicates that there was a high crystal content in the natrocarbonatite magma prior to eruption, identified as a carbonate crystal mush (Dawson et al., 1994; Dawson et al., 1996). (b) A new injection of nephelinitic magma intrudes into the magma chamber. As the intrusion rises and cools, it undergoes immiscibility and partially separates into carbonate and silicate melts, with the carbonate segregation accumulating at the top of the intrusion. (c) The carbonate head of the intrusion disrupts the carbonate crystal mush at the top of the magma chamber, and pushes silicate minerals into the carbonate crystal mush. The high density of crystals enabled these silicate spheroids to become trapped within the surrounding natrocarbonatite magma (Church and Jones, 1995; Dawson et al., 1994; Dawson et al., 1996). The intrusion of new ascending melt may also cause mixing within the surrounding magma. It cannot be specified whether the silicate spheroids came from the intrusion or the surrounding nephelinitic magma.

2.6. Conclusions

1. The evidence presented suggests that liquid immiscibility occurred between silicate, carbonate, chloride, and fluoride melt phases in the June 1993 natrocarbonatite, and show that multi-stage liquid immiscibility is a major factor in the petrogenesis of this lava at Oldoinyo Lengai.
2. The identification of carbonate-carbonate and carbonate-halide immiscibility within the natrocarbonatite lava shows that different types of liquid immiscibility, other than silicate-silicate and silicate-carbonate, can occur in natural magmas. The identification of these diverse unmixed phases at both the macro- and micro-scale presents clear evidence that several types of liquid immiscibility happen during evolution of a single melt, both in the magma plumbing system and during eruption.
3. Liquid immiscibility is rarely observed in the rock record due to masking effects of crystallisation and alteration, but can be observed in melt inclusion and experimental studies. The identification of unmixing in the lavas' groundmass has the potential to provide a new avenue for studying liquid immiscibility in natural magmas.

2.7. References

Brooker, R.A., Kjarsgaard, B.A., 2011. Silicate-carbonate liquid immiscibility and phase re- lations in the system SiO_2-Na_2O-Al_2O_3-CaO-CO_2 at 0.1-2.5 GPa with applications to carbonatite genesis. J. Petrol. 52, 1281–1305.

Church, A.A., Jones, A.P., 1995. Silicate-carbonate immiscibility at Oldoinyo Lengai. J. Petrol. 36, 869–889.

Dawson, J.B., Pinkerton, H., Norton, G.E., Pyle, D.M., Browning, P., Jackson, D., Fallick, A.E., 1995. Petrology and geochemistry of Oldoinyo Lengai lavas extruded in November 1988: magma source, ascent and crystallization. In: Bell, K., Keller, J. (Eds.), Carbonatite Volcanism. Springer, pp. 47–69.

Dawson, J.B., Pinkerton, H., Pyle, D.M., Nyamweru, C., 1994. June 1993 eruption of Oldoinyo Lengai, Tanzania: exceptionally viscous and large carbonatite lava flows and evidence for coexisting silicate and carbonate magmas. Geology 22, 799–802.

Dawson, J.B., Pyle, D.M., Pinkerton, H., 1996. Evolution of natrocarbonatite from a wollas- tonite nephelinite parent: evidence from the June 1993 eruption of Oldoinyo Lengai, Tanzania. J. Geol. 41–54.

Dawson, J.B., Smith, J.V., Steele, I.M., 1992. 1966 ash eruption of the carbonatite volcano Oldoinyo Lengai: mineralogy of lapilli and mixing of silicate and carbonate magmas. Mineral. Mag. 56, 1–16.

Freestone, I.C., 1989. Liquid Immiscibility, Petrology. Springer, pp. 281–283. Freestone, I.C.,

Hamilton, D.L., 1980. The role of liquid immiscibility in the genesis of carbonatites - an experimental study. Contrib. Mineral. Petrol. 73, 105–117.

Guzmics, T., Mitchell, R.H., Szabó, C., Berkesi, M., Milke, R., Abart, R., 2011. Carbonatite melt inclusions in coexisting magnetite, apatite and monticellite in Kerimasi calciocarbonatite, Tanzania: melt evolution and petrogenesis. Contrib. Mineral. Petrol. 161, 177–196.

Guzmics, T., Mitchell, R.H., Szabó, C., Berkesi, M., Milke, R., Ratter, K., 2012. Liquid immiscibility between silicate, carbonate and sulfide melts in melt inclusions hosted in co- precipitated minerals from Kerimasi volcano (Tanzania): evolution of carbonated nephelinitic magma. Contrib. Mineral. Petrol. 164, 101–122.

Jago, B.C., Gittins, J., 1999. Mn- and F-bearing rasvumite in natrocarbonatite at Oldoinyo Lengai volcano, Tanzania. Mineral. Mag. 63, 53–55.

Kamenetsky, V.S., Kamenetsky, M.B., 2010. Magmatic fluids immiscible with silicate melts: examples from inclusions in phenocrysts and glasses, and implications for magma evolution and metal transport. Geofluids 10, 293–311.

Kamenetsky, V.S., Yaxley, G.M., 2015. Carbonate–silicate liquid immiscibility in the mantle propels kimberlite magma ascent. Geochim. Cosmochim. Acta 158, 48–56.

Keller, J., Krafft, M., 1990. Effusive natrocarbonatite activity of Oldoinyo Lengai, June 1988. Bull. Volcanol. 52, 629–645.

Keller, J., Zaitsev, A.N., 2012. Geochemistry and petrogenetic significance of natrocarbonatites at Oldoinyo Lengai, Tanzania: Composition of lavas from 1988 to 2007. Lithos 148, 45–53.

Kervyn, M., Ernst, G.G.J., Klaudius, J., Keller, J., Kervyn, F., Mattsson, H.B., Belton, F., Mbede, E., Jacobs, P., 2008. Voluminous lava flows at Oldoinyo Lengai in 2006: chronology of events and insights into the shallow magmatic system. Bull. Volcanol. 70, 1069–1086.

Kjarsgaard, B., Peterson, T., 1991. Nephelinite-carbonatite liquid immiscibility at Shombole volcano, East Africa: petrographic and experimental evidence. Mineral. Petrol. 43, 293–314.

Kjarsgaard, B.A., Hamilton, D.L., Peterson, T.D., 1995. Peralkaline nephelinite/carbonatite liquid immiscibility: comparison of phase compositions in experiments and natural lavas from Oldoinyo Lengai. In: Bell, K., Keller, J. (Eds.), Carbonatite Volcanism. Springer, pp. 163–190.

Koster van Groos, A.F., Wyllie, P.J., 1966. Liquid immiscibility in the system Na_2O-Al_2O_3- SiO_2-CO_2 at pressures up to 1 kilobar. Am. J. Sci. 264, 234–235.

Lloyd, F.E., Stoppa, F., 2003. Pelletal lapilli in diatremes—some inspiration from the old masters. Geolines 15, 65–71.

Mitchell, R.H., 1997. Carbonate-carbonate immiscibility, neighborite and potassium iron sulphide in Oldoinyo Lengai natrocarbonatite. Mineral. Mag. 61, 779–789.

Mitchell, R.H., 2005. Carbonatites and carbonatites and carbonatites. Can. Mineral. 43, 2049–2068.

Mitchell, R.H., 2006. Sylvite and fluorite microcrysts, and fluorite-nyerereite intergrowths from

natrocarbonatite, Oldoinyo Lengai, Tanzania. Mineral. Mag. 70, 103–114.

Mitchell, R.H., 2009. Peralkaline nephelinite–natrocarbonatite immiscibility and carbonatite assimilation at Oldoinyo Lengai, Tanzania. Contrib. Mineral. Petrol. 158, 589–598.

Mitchell, R.H., Dawson, J.B., 2012. Carbonate-silicate immiscibility and extremely peralkaline silicate glasses from Nasira cone and recent eruptions at Oldoinyo Lengai volcano, Tanzania. Lithos 152, 40–46.

Mitchell, R.H., Kamenetsky, V.S., 2012. Trace element geochemistry of nyerereite and gregoryite phenocrysts from natrocarbonatite lava, Oldoinyo Lengai, Tanzania: Impli- cations for magma mixing. Lithos 152, 56–65.

Moore, K.R., 2012. Experimental study in the Na_2O–CaO–MgO–Al_2O_3–SiO_2–CO_2 system at 3 GPa: the effect of sodium on mantle melting to carbonate-rich liquids and implica- tions for the petrogenesis of silicocarbonatites. Mineral. Mag. 76, 285–309.

Nielsen, T.F.D., Solovova, I.P., Veksler, I.V., 1997. Parental melts of melilitolite and origin of alkaline carbonatite: evidence from crystallised melt inclusions, Gardiner complex. Contrib. Mineral. Petrol. 126, 331–344.

Panina, L.I., 2005. Multiphase carbonate-salt immiscibility in carbonatite melts: data on melt inclusions from the Krestovskiy massif minerals (Polar Siberia). Contrib. Miner- al. Petrol. 150, 19–36.

Panina, L.I., Motorina, I.V., 2008. Liquid immiscibility in deep-seated magmas and the gen- eration of carbonatite melts. Geochem. Int. 46, 448–464.

Peterson, T.D., 1990. Petrology and genesis of natrocarbonatite. Contrib. Mineral. Petrol. 105, 143–155.

Sekisova, V.S., Sharygin, V.V., Zaitsev, A.N., Strekopytov, S., 2015. Liquid immiscibility dur- ing crystallization of forsterite-phlogopite ijolites at Oldoinyo Lengai volcano, Tanza- nia: study of melt inclusions. Russ. Geol. Geophys. 56, 1717–1737.

Sharygin, V.V., Kamenetsky, V.S., Zaitsev, A.N., Kamenetsky, M.B., 2012. Silicate– natrocarbonatite liquid immiscibility in 1917 eruption combeite–wollastonite neph- elinite, Oldoinyo Lengai Volcano, Tanzania: Melt inclusion study. Lithos 152, 23–39.

Simonetti, A., Bell, K., Shrady, C., 1997. Trace-and rare-earth-element geochemistry of the June 1993 natrocarbonatite lavas, Oldoinyo Lengai (Tanzania): Implications for the origin of carbonatite magmas. J. Volcanol. Geotherm. Res. 75, 89–106.

Thompson, A.B., Aerts, M., Hack, A.C., 2007. Liquid immiscibility in silicate melts and relat- ed systems. Rev. Mineral. Geochem. 65, 99–127.

Veksler, I.V., Dorfman, A.M., Dulski, P., Kamenetsky, V.S., Danyushevsky, L.V., Jeffries, T., Dingwell, D.B., 2012. Partitioning of elements between silicate melt and immiscible fluoride, chloride, carbonate, phosphate and sulfate melts, with implications to the origin of natrocarbonatite. Geochim. Cosmochim. Acta 79, 20–40.

Woolley, A.R., 2003. Igneous silicate rocks associated with carbonatites: their diversity, relative

abundances and implications for carbonatite genesis. Periodico di Mineralogia 72, 17.

Wyllie, P.J., Baker, M.B., White, B.S., 1990. Experimental boundaries for the origin and evo- lution of carbonatites. Lithos 26, 3–19.

Zaitsev, A.N., Keller, J., Spratt, J., Jeffries, T.E., Sharygin, V.V., 2009. Chemical composition of nyerereite and gregoryite from natrocarbonatites of Oldoinyo Lengai volcano, Tanza- nia. Geol. Ore Deposits 51, 608–616.

Appendix 2.1 Methodology

Scanning electron microscopy (SEM) and electron probe microanalysis (EPMA)

Samples were coated with around 20nm of carbon using a Ladd 40000 carbon evaporator. Mineral and melt inclusion compositions were determined by backscattered electron (BSE) imaging and energy dispersive X-ray spectrometry (EDS) using a Hitachi SU-70 field emission scanning electron microscope (SEM) equipped with an Oxford XMax80 AZtec 3 EDS system at 15 kV accelerating voltage and around 2.5 nA beam current. A list of the standards used for calibration is given in the table below.

Element	Line series	Standard	Source
Na	K	Anorthoclase Kakanui NMNH 133868	1
Mg	K	Olivine San Carlos NMNH 111312/444	1
Al	K	Plagioclase Lake County NMNH 115900	1
Si	K	Clinopyroxene Delegate	2
P	K	Apatite Durango NMNH 104021	1
S	K	Celestite	3
Cl	K	Tugtupite	3
K	K	Microcline NMNH 143966	1
Ca	K	Clinopyroxene Delegate	2
Ti	K	Rutile	3
Mn	K	Bustamite	3
Fe	K	Hematite	3
Sr	L	Celestite	3
Ba	L	Baryte	3

1 E. Jarosewich et al. 1980, Geostand. Newslett. 4, 43.

2 UTas in house

3 Astimex Standards Ltd, Toronto

Silicate and fluorapatite phenocrysts were analysed using a Cameca SX100 electron microprobe equipped with a tungsten filament and five wavelength dispersive spectrometers (WDS) using 15 kV accelerating voltage, 30 and 20 nA beam current and a 5 and 20 µm beam diameter, respectively. The Probe for EPMA software (Probe Software Inc.) was used for acquisition and data reduction. For apatite, a time dependent intensity correction was performed for F, Cl, K, and Na. Spectral interference corrections were performed within the iterative quantification of the data. Additional settings are given in the tables below.

Silicate phenocryst settings:

Element / Line	**Crystal**	**Inter-ference correc-tions**	**Counting times peak / background, seconds**	**Detection limit, wt%, 99% confidence**	**Precision, wt%, 1 sigma**	**Standard**	**Source**
F Kα	PC0	Fe	20 / 20	0.031	0.016	Apatite Durango NMNH 104021	1
Na Kα	TAP		20 / 2x10	0.017	0.026	Jadeite, Tawmaw, Burma, BM1913.451	2
Mg Kα	TAP		20 / 2x10	0.009	0.015	Periclase, natural	3
Al Kα	TAP		20 / 2x10	0.009	0.016	Plagioclase Lake County NMNH 115900	1
Si Kα	TAP		10 / 2x3	0.019	0.064	Augite-Cr Ney County NMNH 164905	1
P Kα	LPET		20 / 10	0.011	0.005	Apatite Durango NMNH 104021	1
S Kα	LPET		20 / 2x10	0.007	0.003	Celestine $SrSO_4$ Yate, England	2
Cl Kα	LPET		20 / 2x10	0.007	0.003	Tugtupite AS5625-AB	4
K Kα	PET		29 / 2x10	0.011	0.011	Orthoclase, Lucerne, Switzerland	2
Ca Kα	PET		20 / 2x10	0.013	0.051	Wollastonite, natural	3
Ti Kα	PET		30 / 2x15	0.012	0.012	Rutile, synthetic 99.999%	2
Cr Kα	LLiF		30 / 2x15	0.014	0.007	Eskolaite, synthetic 99.99%	2
Mn Kα	LLiF	Cr	30 / 28	0.016	0.011	Rhodonite, Broken Hill, Australia	2
Fe Kα	LLIF		20 / 2x10	0.021	0.044	Magnetite Minas Gerais NMNH 114887	1

1 E. Jarosewich et al. 1980, Geostand. Newslett. 4, 43.

2 P&H Developments Ltd., UK

3 UTas in house

4 Astimex Standards Ltd, Toronto

Fluorapatite phenocryst settings:

Element / Line	Crystal	Inter-ference correc-tions	Counting times peak / background, seconds	Detection limit, wt%, 99% confidence	Precision, wt%, 1 sigma	Standard	Source
F K ✔	PC0	Fe, Ce	20 / 20	0.048	0.050	Apatite Durango NMNH 104021	1
Na K ✔	TAP		20 / 2x10	0.018	0.013	Jadeite, Tawmaw, Burma, BM1913.451	2
Mg K ✔	TAP		20 / 2x10	0.012	0.005	Periclase, natural	3
Al K ✔	TAP		20 / 2x10	0.010	0.005	Plagioclase Lake County NMNH 115900	1
Si K ✔	TAP		20 / 2x10	0.011	0.009	Wollastonite, natural	3
P K ✔	LPET		20 / 10	0.014	0.076	Apatite Durango NMNH 104021	1
S K ✔	LPET		20 / 2x10	0.008	0.004	Celestine $SrSO_4$ Yate, England	2
Cl K ✔	LPET		20 / 2x10	0.009	0.005	Tugtupite AS5625-AB	4
K K ✔	PET		29 / 2x10	0.012	0.006	Orthoclase, Lucerne, Switzerland	2
Ca K ✔	PET		10 / 2x3	0.034	0.156	Apatite Durango NMNH 104021	1
Ti K ✔	PET		20 / 2x10	0.019	0.009	Rutile, synthetic 99.999%	2
Mn K ✔	LLiF		20 / 18	0.024	0.012	Rhodonite, Broken Hill, Australia	2
Fe K ✔	LLIF		20 / 2x10	0.036	0.018	Magnetite Minas Gerais NMNH 114887	1
Sr L ✔	LPET		60 / 2x30	0.020	0.021	Celestine $SrSO_4$ Yate, England	2
La L ✔	PET	Nd	50 / 2x25	0.037	0.019	$LaPO_4$, synthetic	5
Ce L ✔	LLIF		30 / 2x15	0.053	0.032	$CePO_4$, synthetic	5
Nd L ✔	LLIF	Ce	30 / 2x15	0.048	0.026	$NdPO_4$, synthetic	5

1 E. Jarosewich et al. 1980, Geostand. Newslett. 4, 43.

2 P&H Developments Ltd., UK

3 UTas in house

4 Astimex Standards Ltd, Toronto

5 D.J. Cherniak et al. 2004, Amer. Mineral. 89, 1533

Appendix 2.2 Representative composition tables

Table S2. 1 *Representative compositions of silicate kernels in silicate spheroids and carbonate globules.*

Wt.%	Cpx	Cpx	Schorlo	Nph	Woll	Ap	Carbonate globule[1]	Carbonate globule[2]
	EPMA	EPMA	EPMA	EPMA	EPMA	EPMA	SEM-EDS	SEM-EDS
SiO_2	50.67	51.63	29.25	41.87	51.12	0.79	<DL	<DL
TiO_2	0.38	0.51	11.72	<0.012	0.07	<0.019	<DL	<DL
Al_2O_3	0.95	1.18	0.80	33.24	<0.009	<0.01	<DL	<DL
Cr_2O_3	<0.014	<0.014	<0.014	<0.014	<0.014	n.a.	<DL	<DL
FeO	19.77	11.85	21.47	1.77	1.19	0.14	<DL	<DL
MnO	0.64	0.39	0.31	<0.016	0.45	0.04	<DL	<DL
MgO	5.58	10.75	0.72	0.02	0.19	0.02	<DL	<DL
CaO	18.38	22.38	31.61	0.11	46.37	54.75	27.55	7.23
Na_2O	3.39	1.46	0.32	16.09	0.05	0.29	11.90	30.90
K_2O	0.02	0.02	<0.011	6.24	0.01	0.04	7.86	3.10
P_2O_5	<0.011	0.02	0.02	<0.011	0.03	40.03	<DL	2.02
SO_3	0.01	0.01	<0.007	<0.008	<0.009	0.05	0.90	3.37
SrO	n.a.	n.a.	n.a.	n.a.	n.a.	0.79	2.22	<DL
BaO	n.a.	n.a.	n.a.	n.a.	n.a.	n.a.	0.93	<DL
La_2O_3	n.a.	n.a.	n.a.	n.a.	n.a.	0.18	n.a.	n.a.
Ce_2O_3	n.a.	n.a.	n.a.	n.a.	n.a.	0.31	n.a.	n.a.
Nd_2O_3	n.a.	n.a.	n.a.	n.a.	n.a.	0.16	n.a.	n.a.
Cl	0.01	0.01	<0.007	0.01	0.01	0.02	0.23	0.63
F	<0.031	<0.031	<0.031	<0.031	<0.031	2.14	n.a.	n.a.
O=Cl, F	0.01	0	0.01	0.02	0.01	-0.90		
Total	99.80	100.22	96.24	99.37	99.50	98.85	51.59	47.24

n.a. - not analysed, <DL - below detection limit, [1] Ca-rich phase, [2] Na-rich phase

Table S2. 2 *Representative compositions of alkali carbonate phenocrysts, all analysed by SEM-EDS.*

Wt.%	Ny	Ny	Ny	Gr	Gr
Na2O	11.27	15.12	9.25	31.41	31.68
P2O5	0.46	<DL	0.50	2.66	2.77
SO3	0.92	0.82	0.82	3.47	3.72
Cl	0.26	0.31	0.18	0.55	0.52
K2O	7.75	7.48	7.13	3.17	3.04
CaO	28.35	23.35	28.85	7.07	7.25
SrO	2.27	1.94	2.38	0.72	0.89
BaO	<DL	1.74	1.50	<DL	0.66
Total	51.28	50.77	50.61	49.04	50.52

Table S2. 3 *Representative compositions of silicate melt inclusions, all analysed by SEM-EDS.*

Wt.%	Woll	Neph	Cpx	Schorlo
SiO_2	50.40	52.8	49.70	50.5
TiO_2	0.6	1.20	<DL	<DL
Al_2O_3	13.36	8.97	20.86	13.60
FeO	5.85	7.54	2.35	8.56
MnO	<DL	0.34	<DL	0.48
MgO	<DL	0.35	<DL	0.71
CaO	1.23	4.21	0.95	0.70
Na_2O	13.90	11.66	9.30	12.08
K_2O	6.32	6.71	10.65	7.28
SO_3	0.52	0.40	0.40	0.40
Cl	0.34	0.32	0.15	0.19
Total	92.48	94.48	94.36	94.46

Appendix 2.3 Mineral EMPA and EDS data – see digital appendix

Appendix 2.4 EDS and EBSD textural images – see digital appendix

CHAPTER 3

TEXTURAL EVOLUTION OF PEROVSKITE IN THE AFRIKANDA ALKALINE-ULTRAMAFIC COMPLEX, KOLA PENINSULA, RUSSIA

Contributions to Mineralogy and Petrology

3.0. Abstract

Perovskite is a common accessory mineral in a variety of mafic and ultramafic rocks, but perovskite deposits are rare and studies of perovskite ore deposits are correspondingly scarce. Perovskite is a key rock-forming mineral and reaches exceptionally high concentrations in olivinites, diverse clinopyroxenites and silicocarbonatites in the Afrikanda alkaline-ultramafic complex (Kola Peninsula, NW Russia). Across these lithologies, we classify perovskite into three types (T1-T3) based on crystal morphology, inclusion abundance, composition, and zonation. Perovskite in olivinites and some clinopyroxenites is represented by fine-grained, equigranular, monomineralic clusters and networks (T1). In contrast, perovskite in other clinopyroxenites and some silicocarbonatites has fine- to coarse-grained interlocked (T2) and massive (T3) textures. Electron backscatter diffraction reveals that some T1 and T2 perovskite grains in the olivinites and clinopyroxenites are composed of multiple subgrains and may represent stages of crystal rotation, coalescence and amalgamation. We propose that in the olivinites and clinopyroxenites, these processes result in the transformation of clusters and networks of fine-grained perovskite crystals (T1) to mosaics of more coarse-grained (T2) and massive perovskite (T3). This interpretation suggests that sub-solidus processes can lead to the development of coarse-grained and massive perovskite. A combination of characteristic features identified in the Afrikanda perovskite (equigranular crystal mosaics, interlocked irregular-shaped grains, and massive zones) are observed in other oxide ore deposits, particularly in layered intrusions of chromitites and intrusion-hosted magnetite deposits and suggests that the same amalgamation processes may be responsible for some of the coarse-grained and massive textures observed in oxide deposits worldwide.

3.1. Introduction

Oxide deposits formed by a range of magmatic, metamorphic and sedimentary processes (Borrok et al. 1998; Force 1991; Hou et al. 2017; Irvine 1977; Latypov et al. 2017) are important sources of economically-critical elements, like Cr, Fe, V, Ti and platinum group metals. Perovskite ($CaTiO_3$) is not currently mined but could be a significant future titanium resource. This mineral is a typical accessory phase in a range of ultramafic and silica-undersaturated alkaline rocks, such as kimberlites, melilitolites, foidolites and carbonatites (Campbell et al. 1997; Chakhmouradian and Mitchell 1997; Nielsen 1980). In rare cases, perovskite is an abundant rock constituent, such as bebedourites in the Salitre alkaline complex, Brazil (Barbosa et al. 2012), dunites in the Gardiner carbonatite complex, Greenland (Campbell et al. 1997; Nielsen et al. 1997), and Benfontein kimberlite sills in South Africa (Dawson and Hawthorn 1973). However, perovskite deposits of significant tonnage and grade are exceptionally rare; the few examples, where the economic potential of the perovskite mineralisation has been explored are structurally and texturally complex alkaline-ultramafic intrusions at Afrikanda in northwestern Russia (Herz 1976), Tapira in southeastern Brazil (Brod 1999), and Powderhorn in Colorado, USA (Armbrustmacher 1981). It remains uncertain how the perovskite accumulated to ore-grade levels in these settings.

Scarcity of perovskite ore deposits has not entailed many genetic studies. Several scenarios have been proposed to account for perovskite-rich zones, the most common involves magmatic layering due to gravitational settling (Brod 1999; Dawson and Hawthorn 1973). On the other hand, perovskite-rich segregations show textural similarities to other oxide deposits, so genetic models for oxide ores may be pertinent to the genesis of perovskite accumulations. Relevant models include *in situ* crystallisation (Charlier et al. 2006; Latypov et al. 2013; Pang et al. 2007; Vukmanovic et al. 2013), magma mixing (Eales et al. 1990; Irvine 1977; Kinnaird et al. 2002), liquid immiscibility (Kolker 1982; Lister 1966; McDonald 1965; Zhou et al. 2005), mobilization of cumulate suspension from staging magma reservoirs (Eales and Costin 2012; Mondal and Mathez 2006), and a range of postmagmatic ore-forming processes, including post-cumulus growth (Vidyashankar and Govindaiah 2009; Yudovskaya and Kinnaird 2010) and deposition from hydrothermal fluids (Cawthorn 2011; Harlov et al. 2016; Knipping et al. 2015; Pushkarev et al. 2015). The current array of contrasting genetic models for the formation of oxide deposits suggests that sources of metals and mechanisms of their accumulation are not exclusive and should not be pigeonholed.

Our study of perovskite from the Afrikanda alkaline-ultramafic complex targets the understanding of mechanisms responsible for the development of related massive ore textures. We describe the mineral assemblages and textures of the main Afrikanda lithologies and define three key perovskite textural types and associated chemical trends. We discuss the stages of perovskite textural

development in the ultramafic rocks at Afrikanda, and the possibility of similar processes operating in other oxide deposits worldwide.

3.2. Geological background

The Afrikanda alkaline-ultramafic complex is one of the smallest intrusions in the Devonian (~380 Ma) Kola Alkaline Province that hosts more than twenty plutonic and subvolcanic bodies, including alkaline, ultramafic, carbonatite, and melilitolite suites (Kukharenko et al. 1965). The Afrikanda complex is a multiphase intrusion emplaced into Archaean gneisses of the Belomorian Mobile Belt during rifting of the Fennoscandian Shield (Chakhmouradian and Zaitsev 1999; Kramm et al. 1993). The complex has a ~11.5 km^2 circular shape at the current level of erosion, identified with gravimetric data as a 5 km thick ellipsoidal composite body with a NW-dipping conduit (Arzamastsev et al. 2000; Chakhmouradian and Zaitsev 2004). The complex has a concentric internal structure (Afanasyev, 2011; Kukharenko et al. 1965) and hosts texturally and modally diverse olivinites and clinopyroxenites, cross-cut by minor intrusions of carbonatitic and foidolitic rocks (Chakhmouradian and Zaitsev 2004).

The olivinites and minor melilite-bearing olivinites are found as xenoliths (up to 7 m) in the clinopyroxenites, implying that the former rocks represent the earliest intrusive phase at Afrikanda (Chakhmouradian and Zaitsev 1999). The term “olivinites” is used to emphasize that magnetite and perovskite, not chromite, are the major opaque minerals and to maintain consistency with previously published work on Afrikanda and other complexes in the Kola Alkaline Province and petrogenetically similar igneous provinces elsewhere in Russia. Most of the intrusion is composed of texturally and compositionally diverse clinopyroxenites (Chakhmouradian and Zaitsev 2004). These clinopyroxenites are coarse-grained in the centre and transition outwards from fine-grained to nepheline-bearing along the margins, before grading to melteigites. The perovskite ore and perovskite-bearing rocks are hosted in the coarse-grained clinopyroxenites, referred to in the Russian literature as “ore pyroxenites”, located in the central part of the complex. The ultramafic rocks often exhibit alternating oxide- and silicate-rich layers that are considered to represent igneous layering (Chakhmouradian and Zaitsev 2004). The oxide layers are primarily composed of perovskite and titanomagnetite and are enriched in rare earth elements (REE) (Chakhmouradian and Zaitsev 2004; Yudin and Zak 1971).

A carbonatitic suite, also known as calcite-amphibole-clinopyroxene rocks, occurs in the central part of the complex as branching veins (2 cm to 2 m thick) and seemingly irregular (in outcrop) bodies that cross-cut the ultramafic series (Chakhmouradian and Zaitsev 1999). According to the field, geochemical and mineralogical evidence, carbonatitic rocks are distinct from the clinopyroxenites, despite the abundance of diopside and perovskite in both. The carbonatitic rocks are mostly massive and coarse-grained to pegmatitic with modal proportions that change considerably over a short distance, producing a succession from silicocarbonatites to calcite carbonatites (Chakhmouradian et al. 2008;

Chakhmouradian and Zaitsev 2004; Pekov et al. 1997). The silicocarbonatites show a widespread mineralogical variability on a small spatial scale (Chakhmouradian et al. 2008; Chakhmouradian and Zaitsev 1999; Chakhmouradian and Zaitsev 2002; Chakhmouradian and Zaitsev 2004; Zaitsev and Chakhmouradian 2002). Alkaline feldspathoidal rocks appear to be the last intrusive phase and are principally represented by the melteigite–urtite series. The bulk of these rocks is associated with the nepheline-bearing clinopyroxenites in the eastern part of the complex, but pegmatoid ijolites comprising major nepheline, magnetite, perovskite and, locally, biotite also occur in the core as dikes cross-cutting the ultramafic and carbonatitic rocks (Chakhmouradian and Zaitsev 1999).

The Afrikanda perovskite-magnetite deposit is confined to the central part of the complex, dominated by coarse-grained clinopyroxenites (>50%) that host blocks of olivinites and are cross-cut by carbonatitic and feldspathoidal rocks. The ore comprises 15-35 vol.% Ti-rich magnetite and 10-36 vol.% perovskite, and shows wide variations in the abundance of silicate minerals and calcite, reflecting extreme petrographic heterogeneity of this deposit. The measured reserves, delineated to a depth of 300 m, include 34.3 Mt of ore averaging 12.5 wt.% Fe and 8.3 wt.% TiO_2 (Afanasyev, 2011).

3.3. Methodology

All instruments used for the characterisation of samples are housed at the University of Tasmania, Australia. Polished samples were analysed by backscattered electron (BSE) imaging, energy dispersive X-ray spectrometry (EDS) and electron backscatter diffraction (EBSD) using a Hitachi SU-70 field emission scanning electron microscope (SEM) in the Central Science Laboratory. The SEM is fitted with an Oxford XMax80 EDS detector and an HKL Nordlys Nano EBSD camera. Major and trace element and U-Pb isotope analyses of perovskite and titanite were conducted using an Agilent 7900 quadrupole ICPMS, coupled to a Coherent COMPex Pro 193 nm ArF excimer laser system equipped with a Laurin Technic (Resolution S155) constant geometry ablation cell at the School of Earth Sciences. Additional details are provided in Appendix 3.1.

3.4. Petrography of rock units

3.4.1. Melilite-bearing olivinites

Melilite-bearing olivinites are fine- to medium-grained, inequigranular rocks composed of forsterite (0.3 to 2 mm), åkermanite (0.6 to 2.7 mm), perovskite (50 to 550 μm) and magnetite (0.2 to 1.5 mm), and cut by calcite and wollastonite veinlets. Inclusions of euhedral perovskite (30-200 μm) are also found in all other minerals. Perovskite grains are physically separated by serpentine. The preferential orientation of elongate forsterite and magnetite grains and ubiquitous serpentine in the same orientation defines a weak planar fabric in the rock. The interconnected networks and clusters of smaller euhedral

perovskite grains enclose and distort the anhedral åkermanite, forsterite and magnetite grains generating intergrown, irregular and concave shapes (Fig. 3.1a). Åkermanite is sodium-rich (2-3 wt.% Na_2O) with thin rims of monticellite (11-12 wt.% FeO) surrounding some crystals. The forsterite crystals (~Fo_{86-88}) contain up to 1 wt.% CaO and are partially replaced and cross-cut by serpentine with magnetite infill. Ferroan monticellite lamellae are observed within a few olivine grains (Fig. 3.2a). Magnetite is compositionally homogeneous with high Ti, Mg and Al contents (4-7, 1-2 and 1-2 wt.% respective oxides).

3.4.2. Clinopyroxenites

The examined clinopyroxenites are fine- to medium-grained, inequigranular rocks mainly composed of clinopyroxene, perovskite and magnetite with minor calcite, richterite, phlogopite, magnesiohastingsite, titanite, chlorite and various REE minerals (Fig. 3.1b). Diopside (0.2 to 1 mm) is zoned with titanomagnetite and magnesiohastingsite lamellae (Fig. 3.2b) and inclusions of calcite, phlogopite and titanite. Diopside is partially replaced by magnesiohastingsite, biotite and clinochlore. Perovskite shows a range in grain sizes (0.05 to more than 2 mm), shapes (rounded to irregular) and zonation (homogeneous to complexly zoned), and varies from chains of euhedral crystals to large areas of interlocking grains. Magnetite grains are rounded (0.3 to 1.3 mm, with rare grains up to 10 mm) and contain variable Ti, Mg and Al contents (<4, 3 and 2 wt. % respective oxides). Magnetite also contains lamellae of Mg-rich ilmenite (Fig. 3.2c), trellis-like and irregular patches of ferroan spinel (<25 μm) and Mn- and Mg-rich ilmenite (<50 μm). The Mg-rich ilmenite lamellae contain small crystals of ferroan Ti-rich spinel (1 to 3 μm) and baddeleyite (<1 μm) (Fig. 3.2d). REE phases are observed as inclusions in other minerals, with ancylite-(Ce) in richterite, cerite-(Ce) in calcite, and ancylite-(Ce), cerite-(Ce) and loparite-(Ce) in titanite.

3.4.3. Silicocarbonatites

The examined silicocarbonatite samples are extremely inequigranular (fine- to coarse-grained) and predominantly composed of calcite, diopside, perovskite, magnetite, magnesiohastingsite and titanite. In perovskite-rich areas, calcite occurs as veinlets (up to 5 mm in width), euhedral crystals (0.3 to >4 mm across) and interstitial to perovskite (0.3 to 2 mm), and is the most abundant mineral in the samples (up to 50 vol. %). Titanite and cerite (less common) are observed at the peripheral areas of the calcite veinlets. Titanite is the most abundant interstitial mineral, with REE-minerals such as cerite-(Ce), loparite-(Ce) and ancylite-(Ce) found enclosed in the titanite. Magnetite has low Ti, Mg and Al contents (less than 1 wt. %, respectively) and contains lamellae of Mn- and Mg-rich ilmenite and irregular grains of Zn- and Fe-rich spinel. Perovskite shows a range of grain sizes (0.05 to more than 2 mm), shapes (rounded to irregular), and zonation (homogeneous to complexly zoned), and varies from small

interlocking grains to large areas of massive perovskite (Fig. 3.1c). Perovskite also occurs as clusters with accessory titanite, calcite, loparite-(Ce) and rare fluorapatite. For more detailed descriptions of the mineralogy and textures of silicocarbonatites the reader is referred to publications by Chakhmouradian and Zaitsev (1999; 2002; 2004) and Zaitsev and Chakhmouradian (2002).

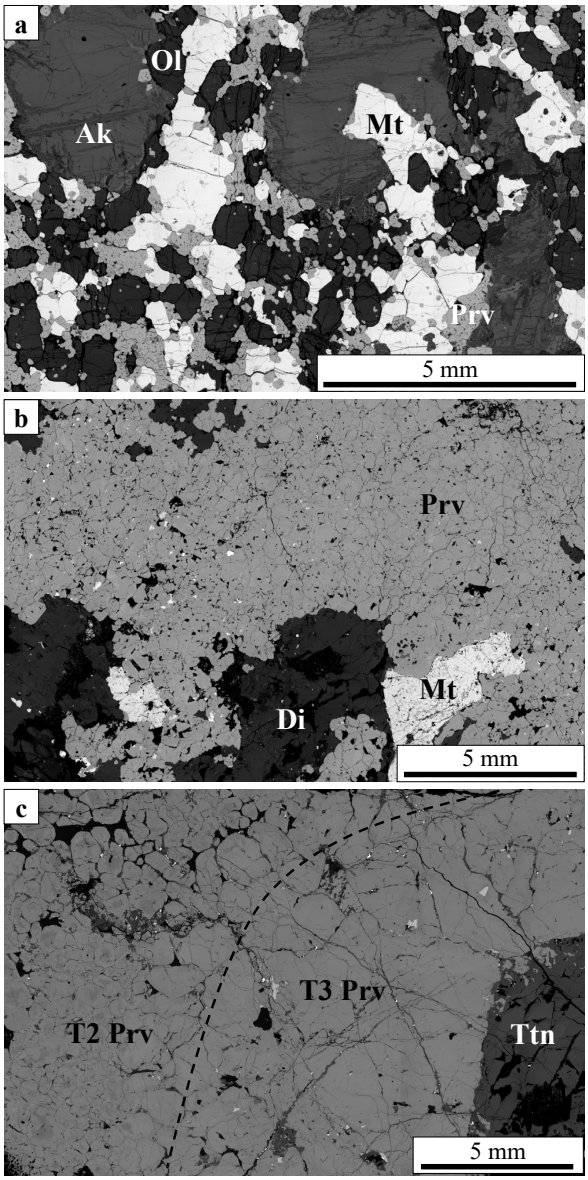

Figure 3. 1 Backscattered electron (BSE) images of characteristic textures and mineralogy of the three main Afrikanda rock types. (a) Olivinites composed of large akermanite, olivine and magnetite grains enclosed by smaller perovskite grains. (b) Clinopyroxenite composed of diopside, magnetite and smaller perovskite grains. (c) Silicocarbonatite composed of perovskite, calcite and titanite. Abbreviations: Ak – akermanite, Ttn – titanite, Prv – perovskite, Mt – magnetite, Ol – olivine, Di – diopside.

3.5. Perovskite textures

Three distinct perovskite textures are identified in the three main rock types at Afrikanda. These types are defined by their morphology, composition, zoning patterns and abundance of multiphase inclusions (Figs. 3.3a-f).

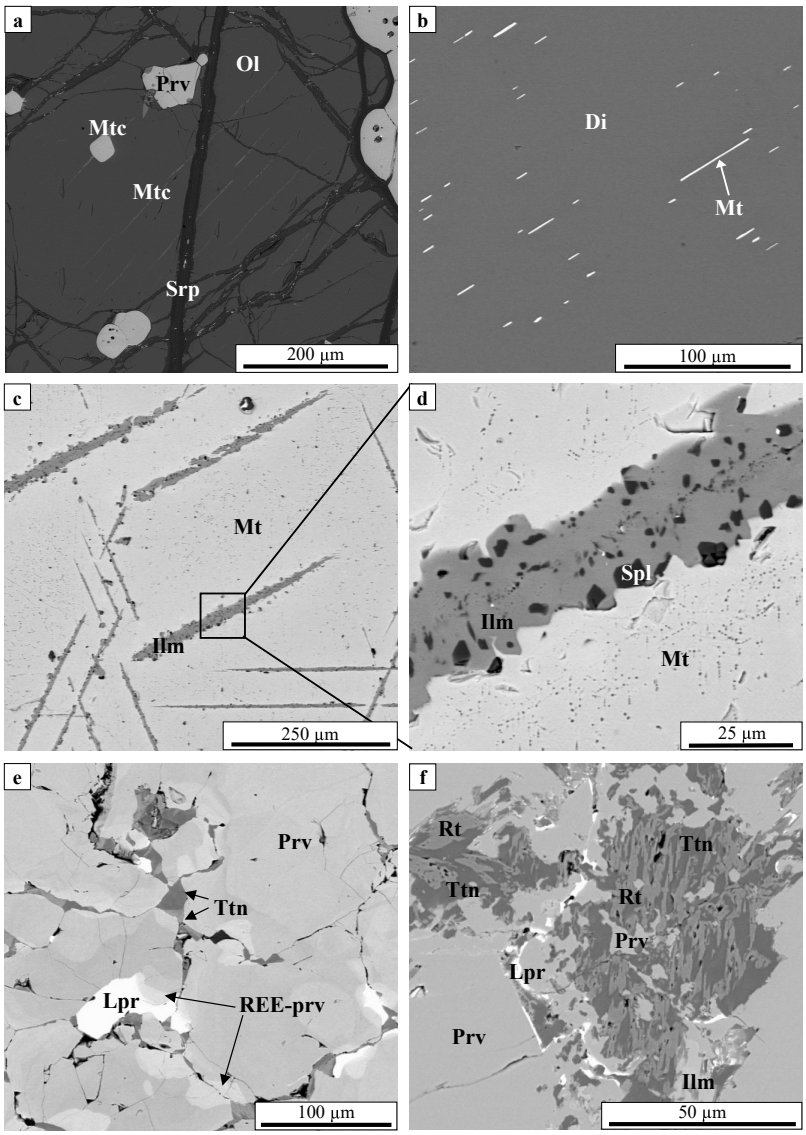

Figure 3. 2 BSE images of textural features in the Afrikanda rocks. (a) Ferroan monticellite lamellae in olivine from olivinites. (b) Titanomagnetite lamellae in diopside from clinopyroxenite. (c) Mg-rich ilmenite lamellae in magnetite from clinopyroxenite. (d) Close up of (c) with small crystals of ferroan Ti-rich spinel and baddeleyite (white specs) in the Mg-rich ilmenite lamellae. (e) Titanite, REE-perovskite and loparite at T2 perovskite grain margins from clinopyroxenite. (f) Symplectite-like intergrowths of titanite, rutile and ilmenite in T2 perovskite from silicocarbonatite. Abbreviations: Ttn – titanite, Lpr – loparite, Prv – perovskite, Ilm – ilmenite, REE-prv – REE-rich perovskite, Mt – magnetite, Spl – spinel, Di – diopside, Mtc – monticellite, Rt – rutile, Srp – serpentine, Ol – olivine.

Type one (T1) perovskite is observed in the olivinites and clinopyroxenites, characterised by interconnected polygonal crystal clusters and networks. The euhedral pseudo-octahedral perovskite grains (50-550 μm) have straight boundaries with widespread 120° triple-junctions (Fig. 3.3a). Multiphase inclusions are abundant in grain cores. The number of inclusions is dependent on grain size, with a general trend of more inclusions with increasing grain size. Most of the perovskite grains exhibit no detectable zoning in BSE images, while a small number of grains along the zone of contact with magnetite grains have a lower-AZ rim (AZ = average atomic number). Perovskite T1 in the clinopyroxenites has a greater number of grains with a low-AZ rim along their contact with both adjacent perovskite and magnetite grains. The perovskite grains neighboured by magnetite can also exhibit oscillatory zoning with multiple narrow bands along the grain boundaries (Fig. 3.3b). The grain

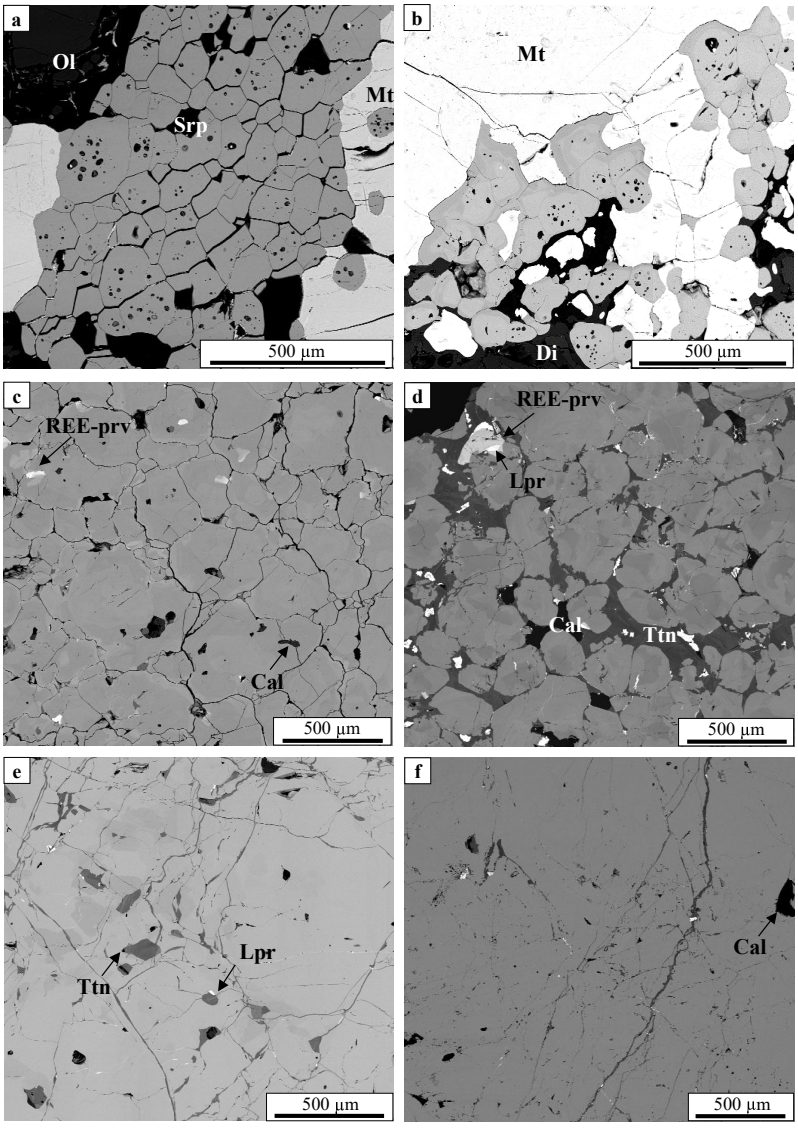

Figure 3. 3 Representative BSE images of the various perovskite textures. (a) T1 in olivinites. (b) T1 in clinopyroxenite. (c) T2 in clinopyroxenite. (d) T2 in silicocarbonatite. (e) T3 in clinopyroxenite. (f) T3 in silicocarbonatite. Abbreviations: Cal – calcite, Di – diopside, Lpr - loparite, Mt - magnetite, Ol – olivine, Srp – serpentine, REE-prv – REE-perovskite, Ttn – titanite.

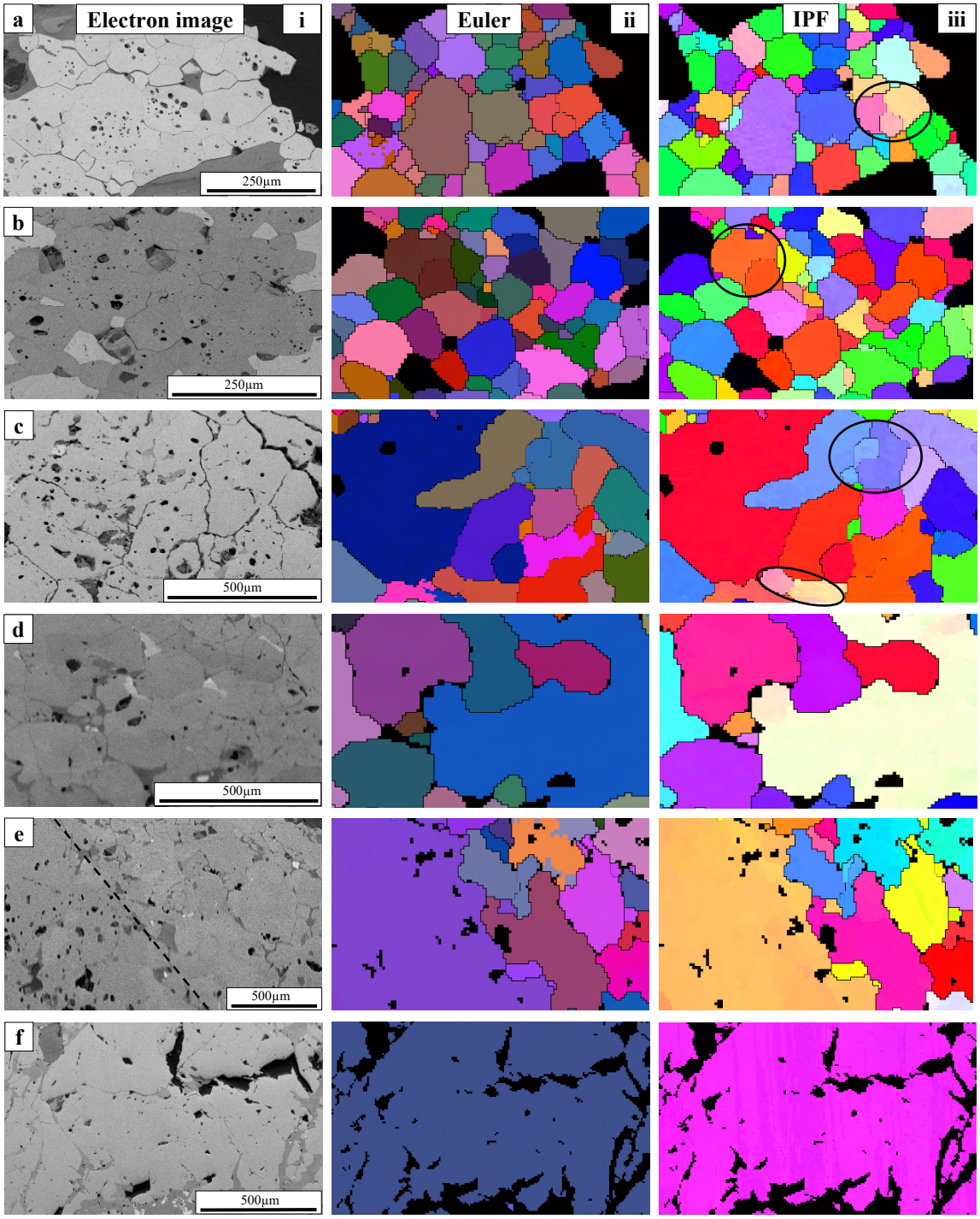

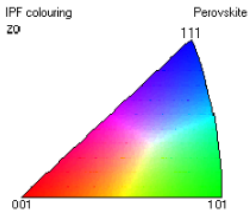

Figure 3. 4 Structural analysis and crystallographic orientation of perovskite grains in the different textures. (a) T1 in olivinites. (b) T1 in clinopyroxenite. (c) T2 in clinopyroxenite. (d) T2 in silicocarbonatite. (e) T2 (right) and T3 (left) in silicocarbonatite. (f) T3 in clinopyroxenite. (i) BSE image of the area mapped with EBSD shows perovskite grain boundaries. (ii) EBSD map representing the orientation of neighbouring perovskite grains in Euler space using colours to denote the variety of crystal orientations in space using Euler angles: φ1-red φ-green, φ2-blue. **iii** Inverse pole figure (IPF) map in the X or Z direction showing the variation in crystal orientation using colours. Black ovals show grains that are composed of subgrains with different crystallographic orientations.

boundaries between perovskite are straight, whereas boundaries with other minerals are curvilinear. The perovskite grain boundaries in the melilite olivinites and clinopyroxenites are clearly visible, however, EBSD revealed that some of these grains are a composite of several subgrains, each with slight deviations in crystal orientation (Figs. 3.4a_{iii}, b_{iii}).

Type two (T2) perovskite in the clinopyroxenites is represented by an intricate mosaic of interlocking anhedral grains (0.1 to 1 mm; Figs. 3.1b, 3.3c) and in the silicocarbonatites, by rounded grains (0.2 to >2 mm) surrounded by interstitial material (Figs. 3.1c, 3.3d). Triple junctions are observed between adjacent perovskite grains in the clinopyroxenites, at approximately 120°. Multiphase and monomineralic inclusions of phlogopite, magnetite, loparite-(Ce), calcite, titanite and fluorapatite vary from rare to abundant among the examined samples. Perovskite in the silicocarbonatites contains a greater proportion of monomineralic inclusions and fewer multiphase inclusions than that in the clinopyroxenites. Zoning is prominent in all perovskite grains and can be highly complex in some areas or individual grains. Large grains commonly display less compositional complexity than the smaller

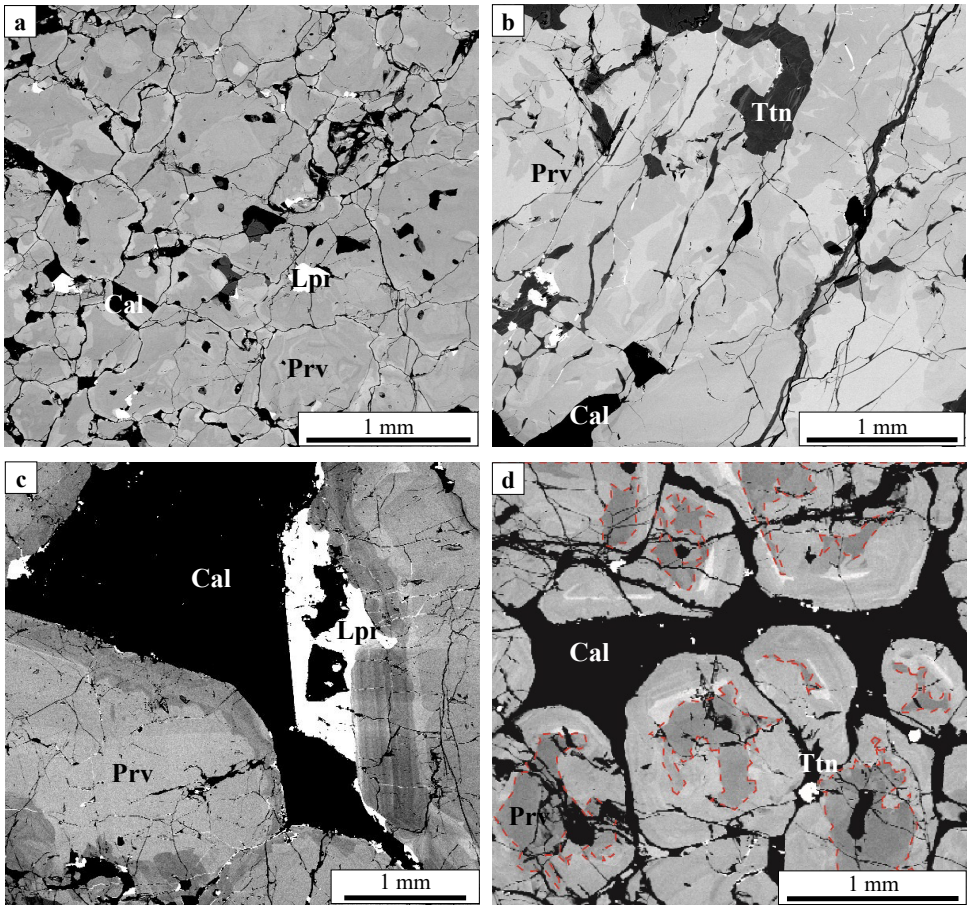

Figure 3. 5 BSE images of zoning patterns in T2 and T3 perovskite (enhanced contrast in c, d). (a) Complex zoning crossing grain boundaries in T2 clinopyroxenite. (b) Irregular zoning pattern in T3 clinopyroxenite. (c) The rims are enriched in REE (rare earth elements) and the cores are depleted in REEs in T2 perovskite in silicocarbonatites. The red dashed lines show the internal extent of zoning. (d) Dark rim (depleted in REE) in contact with calcite and loparite in silicocarbonatite. Abbreviations: Lpr – loparite, Ttn – titanite, Prv – perovskite, Cal – calcite, REE-prv – REE-perovskite.

grains. The zoning in the core is challenging to decipher due to compositional changes occurring along the grain boundaries and fractures (Figs. 3.5a, 3.3d). In BSE images, most grains have a darker core and comparatively lighter rim caused by differences in concentration of Na, light rare earth elements (LREE), and Nb (Fig. 3.5d). The changes in composition at the rims are not systematic, often showing irregular, embayed patterns (Fig. 3.5a). In some samples, perovskite has darker rim in areas where perovskite is in direct contact with magnetite or calcite (Fig. 3.5c).

Distinct areas of perovskite with elevated LREE contents (up to 20 wt. %), reflected in their high AZ, are referred to here as REE-perovskite. The mineral ranges in size from 20 μm to 1.5 mm and can exhibit irregular zoning due to differences in Na, LREE and Nb contents (Fig. 3.3d). The REE-perovskite forms irregular, cuspate shapes as halos around loparite-(Ce) in perovskite and at perovskite rims that are commonly in contact with interstitial loparite-(Ce) and titanite (Fig. 3.2e). Type 2 perovskite coexists with titanite, calcite and loparite-(Ce); rare fluorapatite was also found in the silicocarbonatites. Titanite is zoned and forms irregular wedge-shaped crystals between perovskite, thin rims around perovskite and intergrown with interstitial ilmenite (0.2-1 mm). REE-perovskite and loparite-(Ce) associated with T2 perovskite are more abundant in the silicocarbonatites, which also contain a larger proportion of interstitial minerals. Perovskite grain boundaries can be difficult to distinguish in BSE images, especially in the silicocarbonatites, however in the Euler images the boundaries are clearly visible (Figs. 3.4c_{ii}, d_{ii}). The Euler patterns also show that in the clinopyroxenites, most large irregularly shaped grains have only one crystallographic orientation, while the smaller more-rounded grains still have differences in orientation that indicate the presence of subgrains (Fig. 3.4c_{iii}). The irregular grain boundaries of large perovskite crystals suggest they developed from multiple smaller grains (Fig. 3.4c_{ii}). In the silicocarbonatites, the small and large perovskite grains have only one orientation (Fig. 3.4d_{iii}).

Type 3 (T3) in the clinopyroxenites and silicocarbonatites is represented by massive perovskite with patches of irregular zoning and rare multiphase inclusions. The intensity of the zoning varies across the samples, some areas are almost homogeneous and others exhibit complex patterns due to extreme variations in Na, LREE and Nb contents (Fig. 3.5b). Chakhmouradian and Zaitsev (1999) also reported small-scale order-of-magnitude variations in Th in REE-perovskite and loparite-(Ce) mantling T3. These authors also described oscillatory growth patterns truncated by Na-REE (±Nb,Th)-rich areas in euhedral cubo-octahedral crystals. Mineral inclusions of titanite, calcite, loparite-(Ce) and cerite are dispersed throughout massive perovskite and between perovskite grains. Generally, areas of perovskite with interstitial minerals contain fewer mineral inclusions, and vice versa. Interstitial titanite can be intergrown with ilmenite and form large patches up to 1 mm containing scattered ilmenite and perovskite. Symplectite-like intergrowths of titanite, rutile and ilmenite (200-500 μm) are typical in some silicocarbonatites (Fig. 3.2f). Type 3 perovskite lacks easily distinguishable grain boundaries. The

Euler images show that perovskite is massive, with the same crystallographic orientation for large areas of perovskite (Figs. 3.4e_{ii}, f_{ii}).

3.6. Multiphase inclusions in perovskite

The perovskite-hosted multiphase inclusions in the three rock types show rounded, elongated and irregular shapes, and range from <5 µm to 50 µm across. The inclusions are all identified as primary based on their random/unsystematic distribution within the grains and the lack of association with secondary features, such as healed fractures. The inclusions typically contain three to ten mineral phases and include anhydrous and water-bearing silicates, carbonates, oxides, sulphides and phosphates. The abundance of multiphase inclusions and their mineralogical complexity decrease from the olivinites to clinopyroxenites and then silicocarbonatites. A detailed analysis and discussion on these multiphase inclusions will be presented in a subsequent publication.

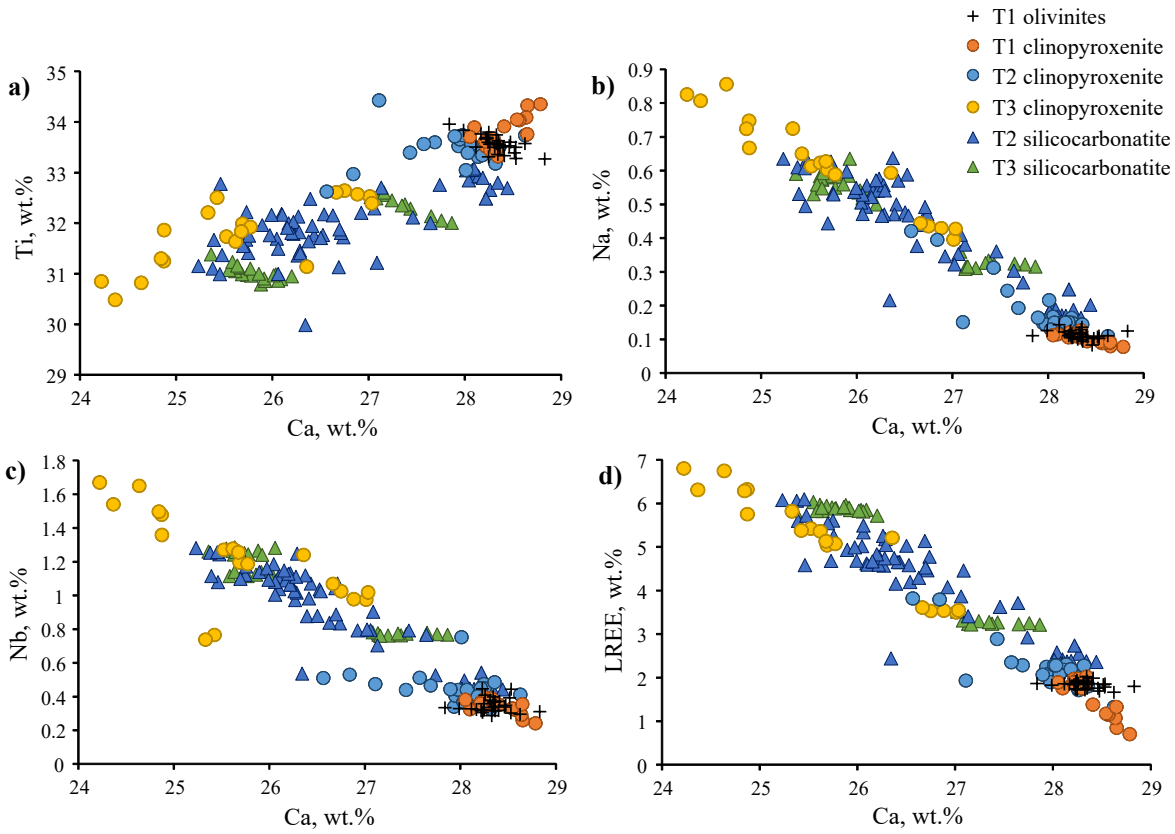

Figure 3. 6 Bivariate plots of LA-ICPMS major- and trace-element chemistry of the perovskites. Symbols correspond to the four perovskite textures found in the Afrikanda rock types: olivinites (crosses), clinopyroxenites (circles) and silicocarbonatites (triangles).

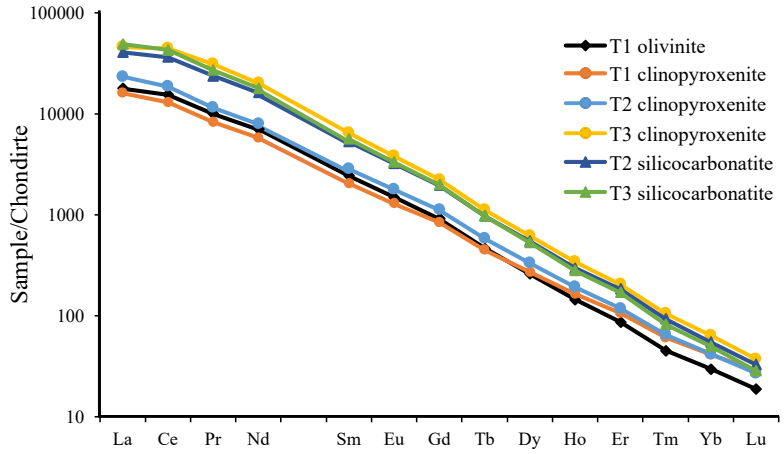

Figure 3. 7 Chondrite-normalised REE diagram of the average composition of T1 to T3 perovskite in the Afrikanda complex.

3.7. Perovskite compositions

The textural types of perovskite in the three rock types vary in major and trace element compositions. The substituent elements show a negative correlation with Ca and Ti and a positive correlation with each other (Figs. 3.6a-d). Type 1 perovskite has the lowest abundances of substituent elements and a limited range of compositions, notably up to 2 wt.% REE and less than 1 wt.% Fe (Fig. 3.6d). The range in element concentrations is greater in T2 and T3 perovskite due to their complex zoning patterns, with the most compositional scatter observed in T2 perovskite from the silicocarbonatites and T3 perovskite from the clinopyroxenites (Fig. 3.6). Type 2 perovskite contains 1-7 wt.% REE and up to 1.5 wt.% Nb and Fe, while T3 perovskite has 4-7 wt.% REE, 1-2 wt.% Nb, and up to 1.5 wt.% Na and Fe.

The REE budget of perovskite is dominated by cerium with the abundances of other lanthanides decreasing with increasing atomic number [La>Nd>Pr>Sm; $(La/Yb)_{CN}$= 140-2300]. Chondrite-normalised REE patterns for all textural types exhibit a negative slope (Fig. 3.7). Overall, the chondrite profiles show a relative enrichment in all REE from T1 to T3, with a greater increase in light REE for T2 and T3 compared to T1. The complete set of LA-ICPMS data is presented in the Appendix 3.2.

3.8. U-Pb geochronology

Fifteen in situ U-Pb isotopic measurements were obtained for perovskite from the olivinites, 45 from the clinopyroxenites and 124 from the silicocarbonatites. All but one analyses were used in age calculations. Perovskite contains abundant common Pb and so concordia intercept ages using the Tera-Wasserburg plot are reported. The Pb isotope composition of calcite was analysed and used as a common-Pb anchor for the concordia intercept ages because this mineral has high Pb/U ratios. The measured $^{207}Pb/^{206}Pb$ value of calcite is 0.8277 ± 0.0039 and, thus, differs from the two-stage Pb evolution model of Stacey and Kramers (1975) for 380 Ma. Perovskite from all lithologies gives a concordia intercept age of 368.3 ± 1.2 +/- 7.48 Ma (including systematic uncertainties) with an MSWD

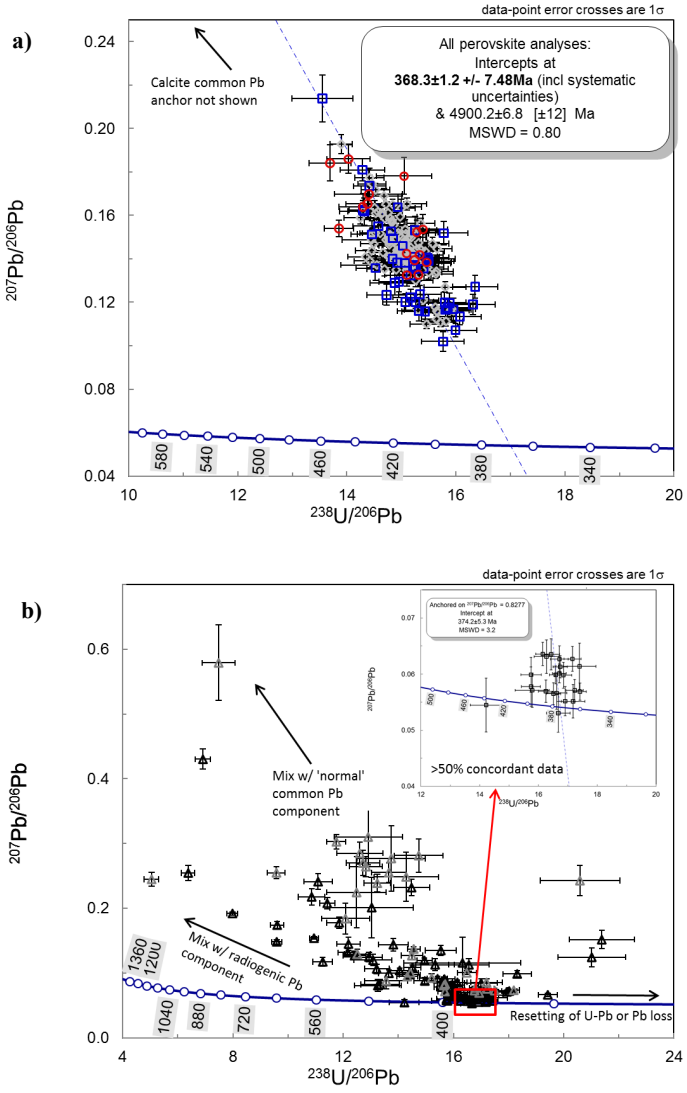

Figure 3. 8 Tera-Wasserburg concordia plot for (a) perovskite and (b) titanite analyses. Symbols: red circles are olivinites, blue squares are clinopyroxenites, grey diamonds are silicocarbonatites, grey and black triangles represent titanite around perovskite in the T3 and T4 silicocarbonatites, respectively. Error crosses are 1 sigma, while concordia intercept ages are 2 sigma. Systematic error component includes uncertainty in decay constants, uncertainty in primary calibration material and excess uncertainty factor of Horstwood et al. (2016).

of 0.80 and a probability-of-fit of 0.98 (Fig. 3.8a). Perovskite ages for each of the analysed lithologies are reported in Table 3.1.

One hundred and eleven in situ U-Pb isotope analyses of titanite were obtained from the silicocarbonatites. Significant scatter and discordance in the U-Pb system is present. A concordia intercept age of 374.2 ± 5.3 Ma +/- 7.5 Ma (including systematic uncertainties) was calculated for data points, whose concordance was greater than 50%, using the calcite common-Pb anchor (see above; Fig. 3.8b). The complete set of U-Pb geochronology results are presented in the Appendix 3.3.

Rock type	Mineral	Age (Ma)	MSWD	POF
Olivinite	Perovskite	370.4±5.4 / ±9.8	1.3	0.19
Clinopyroxenite	Perovskite	368.9±2.9 / ±7.9	0.84	0.76
Silicocarbonatite	Perovskite	368.1±1.3 / ±7.5	0.74	0.98
Silicocarbonatite	Titanite	374.2±5.3 / ±7.5	3.2	0.0

Table 3. 1 Summary of U-Pb ages of perovskite and titanite from samples of olivinites, clinopyroxenites and silicocarbonatites. Uncertainties are 2 sigma absolute and include uncertainties derived from random sources followed by uncertainties from random plus systematic sources of uncertainty calculated according to Horstwood et al. (2016). POF = probably of fit.

3.9. Discussion

3.9.1. Age of the Afrikanda complex

The Palaeozoic igneous complexes in the Kola Alkaline Province were emplaced during a relatively short time during the Late Devonian (380-360 Ma) with no reliably post-Devonian magmatic events recorded to date (Arzamastsev et al. 2000). The Afrikanda complex was emplaced at ~380 Ma with

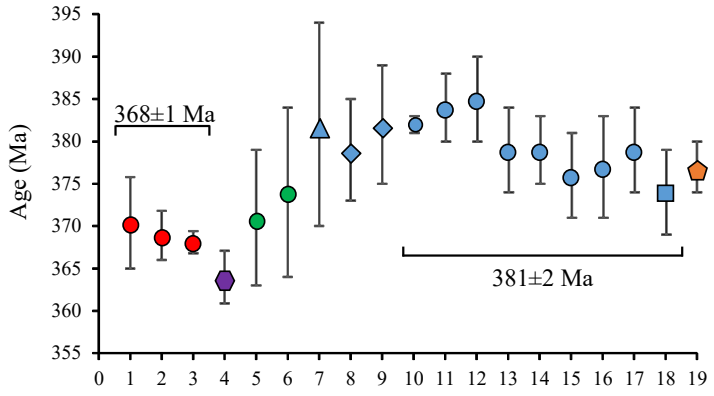

Figure 3. 9 Age summary of the alkaline ultramafic rocks in the Afrikanda complex. **1-3** Perovskite (circles) analysed in this paper. **4** Whole rock analysis (hexagon) in Kramm et al. (1993). **5-6** Perovskite data in Reguir et al. (2010). **7-9** Calzirtite (triangle) and zirconolite (diamond) data in Wu et al. (2010). **10-18** Perovskite and baddeleyite (square) data in Wu et al. (2013). **19** Schorlomite (pentagon) analysis in Salnikova et al. (2018).

other alkaline-ultramafic complexes, including Kovdor, Turiy Mys, Lesnaya Varaka and Ozernaya Varaka (Arzamastsev and Wu 2014).

Our geochronological study of perovskite from the melilite olivinites, clinopyroxenites and silicocarbonatites yielded similar ages of 370.4 ± 5.4, 368.9 ± 2.9, 368.1 ± 1.3, respectively (Table 3.1). Our average perovskite age of 368.3 ± 1.2 Ma (Fig. 3.8a) is in good agreement with most of the previously published U-Pb ages for this intrusion (Fig. 3.9), including: 364 ± 3 Ma and 374 ± 10 for perovskite from clinopyroxenite (Kramm et al. 1993; Reguir et al. 2010), 371 ± 8 Ma for perovskite from silicocarbonatite (Reguir et al. 2010), and 377 ± 3 Ma for schorlomite from silicocarbonatite (Salnikova et al. 2018). Somewhat older ages were reported by Wu et al. (2010; 2013) for perovskite from clinopyroxenite, calcite-bearing perovskite ore and ijolite–melteigite (376-385 Ma, averaging 381±2 Ma), and for calzirtite and zirconolite from clinopyroxenites (Wu et al. 2010). Several factors could be responsible for the slight age discrepancies between our data and the data of Wu et al. (2010; 2013), including the choice of U-Pb calibration material, susceptibility of some analytical techniques to matrix effects, and the choice of a common-Pb anchor. Our study supports the contemporaneous emplacement of the various rock types (olivinites, clinopyroxenites and silicocarbonatites) in the Afrikanda complex, as indicated by the identical ages of the perovskite from the different lithologies (Fig. 3.9). Evidence for the relatively rapid emplacement of the Afrikanda deposit comes primarily from the homogeneity of the perovskite U-Pb ages (MSWD of 0.80 for all perovskite analyses), at least at the precision attainable with the LA-ICPMS system used. Additionally, our study presents new insights into the common-Pb isotopic composition of the Afrikanda perovskite and shows that the initial Pb isotopic composition of its parental magma is significantly more radiogenic than predicted by the two-stage model of Stacey and Kramers (1975).

U-Pb age data have not been previously reported for titanite from the Afrikanda complex. Significant scatter in the U-Pb system for titanite is a result of either Pb movement within the titanite structure after crystallisation, or the incorporation of radiogenic and common Pb. Lead loss or partial re-setting of the U-Pb system during later re-crystallisation events could also be responsible for some of the scatter (Fig. 3.8b). Using data whose concordance is better than 50%, an age of 374.2 ± 5.3 Ma was calculated and is consistent with the perovskite results discussed above (Table 3.1). However, a range of younger titanite ages that are more discordant due to Pb loss suggest there may have been a re-setting or titanite crystallization event.

3.9.2. Development of perovskite textures

The detailed textural and chemical examination of perovskite in the olivinites, clinopyroxenites and silicocarbonatites revealed three perovskite types distinguished by morphology, zonation, inclusion abundance and chemical composition. The olivinites host T1 perovskite (Figs. 3.1a, 3.3a), whereas the clinopyroxenites contain T1-3 perovskite (Figs. 3.1b, 3.3b-d) and similar T2 and T3 textures are

observed in the silicocarbonatites. We have separated the geological interpretation of the ultramafic rocks (discussed below) from that of the silicocarbonatites. The focus here is primarily on the textural evolution of the olivinites and clinopyroxenites, because perovskite textures in the silicocarbonatites have been discussed previously by Chakhmouradian and Zaitsev (1999; 2004).

3.9.3. Olivinites and clinopyroxenites

Textures of rocks are the sum of all processes involved from the initial formation through maturation, and can be used to understand the sequence and nature of each of the evolutionary stages. However, the process of textural equilibration can effectively obscure features related to earlier developmental phases, so we can only speculate from the existing textures about the nature of a rock prior to recrystallization (Pike and Schwarzman 1977). In the case of the Afrikanda rocks, T1 perovskite forms chains and clusters and may suggest that at some point in the early history of the rock individual euhedral grains of perovskite were disseminated and then clumped together to form clusters and chains (Figs. 3.1a, 3.3a, b). However, we cannot provide clues on the origin of these individual perovskite grains due to the subsequent overprinting events. Therefore, we focus here on development of the Afrikanda perovskite ore by reconstructing the later stages of mineral amalgamation and recrystallization.

3.9.3.1. Textural equilibration

The T1 perovskite aggregates consist of closely packed equigranular crystals with pseudo-octahedral shapes, forming straight boundaries that converge at ~120° triple junctions. This arrangement resembles granoblastic-polygonal textures (Figs. 3.3a, 3.10a), as observed in monomineralic cumulates, mantle-derived ultramafics and massive metamorphic rocks such as granofelses (Figs. 3.10a, b; Higgins 2011; Holness et al. 2005; Holness et al. 2006; Hunter 1987; Kretz 1966; Wandji et al., 2009). Therefore, we suggest the granoblastic-polygonal texture of T1 perovskite indicates that the host rocks have experienced dynamic textural equilibration. The granoblastic-polygonal texture of T1 perovskite in olivinites and clinopyroxenites differs marginally due to the variable abundance and distribution of the surrounding minerals, with perovskite in the olivinites clumped together forming aggregates, but dispersed in clinopyroxenites forming chains. Textural equilibration is a well-known phenomenon in natural systems (e.g., Higgins 2015; Higgins 2017; Holness et al. 2006), but the bulk of empirical data, computer simulations and models come from materials research, especially alloys, ceramics and thin films (e.g., Holm et al. 2016). Thus, our current understanding of textural equilibration is limited to relatively simple systems (from a geologist's standpoint) that differ both chemically and mechanically from oxide-silicate assemblages described in the present work. Another challenge in adopting materials

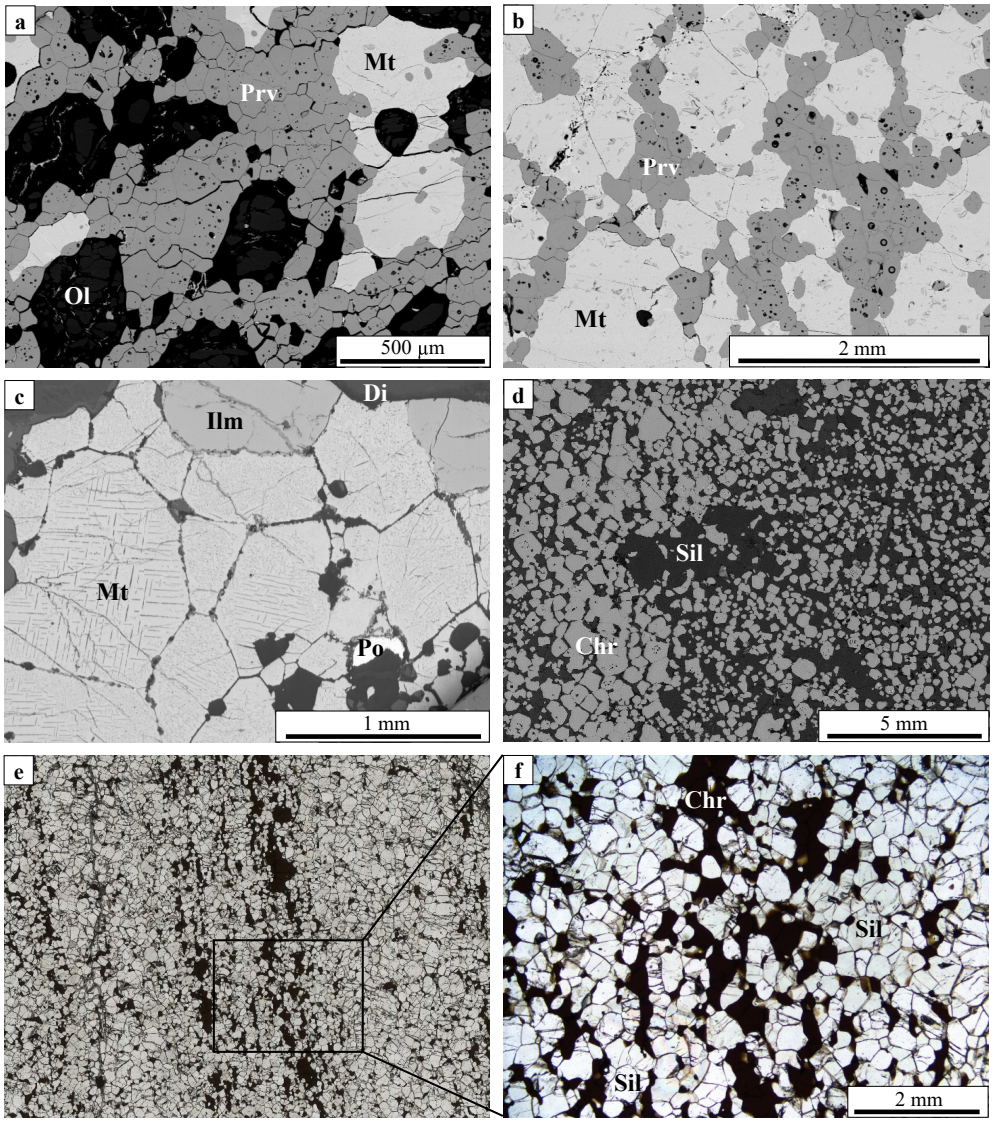

Figure 3. 10 BSE images of granoblastic textures (a-d) SEM (e, f) Plane-polarized light. (a) Equigranular mosaic of T1 perovskite from olivinite in the Afrikanda complex with straight boundaries and 120^{o} triple junctions. (b) Perovskite chains of T1 perovskite from clinopyroxenite in the Afrikanda complex. (c) Polygonal grains of Ti-magnetite in an Fe-Ti oxide ore layer at Panzhihua, China. (d) Disseminated equigranular euhedral chromite, with some chains and aggregates from Merensky Reef, South Africa. (e) Chains of chromite grains in a xenolith hosted in a tertiary basalt from the Snowy Mountains, Australia. (f) Close up of (e). Abbreviations: Chr – chromite, Sil – silicate minerals, Prv – perovskite, Ilm – ilmenite, Mt – magnetite, Di – diopside, Po – pyrrhotite.

science theories to rocks is terminology; for example, their use of the term "recrystallization" is essentially restricted to deformation-induced phenomena, whereas processes addressed in this paper would be described as "grain growth due to annealing" (e.g., Chapter 11 in Humphreys and Hatherly (2004)). According to previously published experimental evidence, the degree and style of textural equilibration depend on many parameters, notably temperature, pressure, grain distribution, modal homogeneity of the precursor, high-temperature phase transitions, the presence of structural defects, and such kinetic factors as cooling rate (Clark et al. 1977; Humphreys and Hatherly 2004; Kreitcberg

et al. 2017; McCloy et al. 2009; Syrenko and Klinishev 1973). Because we observe no evidence for postmagmatic metamorphism at Afrikanda, and the subsolidus mineral assemblages common in the silicocarbonatites record a temperature range of 200-400 °C (Chakhmouradian and Williams 2004; Chakhmouradian and Zaitsev 2004), we assume the documented textural changes arose during cooling. The process involved grain-boundary migration, boundary-angle adjustment, dislocation movement, loss of inclusions, and ultimately, coarsening of the grains to minimise their internal and surface energies (Hunter 1987). We suggest that after perovskite accumulation, slow cooling of the ultramafic rocks enabled the transformation of many small, randomly oriented and possibly irregularly-fitted perovskite grains into the observed polygonal mosaics (Figs. 3.1a, 3.3a, 3.10a).

3.9.3.2. Perovskite coalescence and coarsening

Grain coalescence and coarsening are important processes in the late stages of textural equilibration (Doherty et al. 1997; Hunter 1987). In this section, we discuss grain growth during subsolidus evolution of the ultramafic rocks at Afrikanda as a continuation of the previously recognised textural equilibration. The development of larger grains can either occur by grain boundary migration, i.e. through the dissolution of small crystals and simultaneous growth of larger crystals, or by grain coalescence, where adjacent grain boundaries are eliminated as similarly oriented crystals coalesce (Higgins 2011; Li 1962). The application of EBSD in our study of perovskite enables us to identify and differentiate between these two types of grain growth (Humphreys 2001). Some large grains in T1 and T2 perovskite are composed of subgrains with slightly different crystallographic orientations (circled in Figs. 3.4a-c). These subgrains within larger perovskite grains suggest the dominant mechanism of grain growth was grain rotation and coalescence. Experimental evidence has shown that coalescence is favoured over grain boundary migration at lower temperatures (Rios et al. 2005; Sandström et al. 1978; Varma and Willits 1984; Walter and Koch 1963). This further supports that the observed perovskite textures and their inferred transformation represent a postmagmatic environment.

The process of grain coarsening occurs via diffusion of vacancies in the crystal lattice, in an effort to eliminate or homogenise high angle, irregular, and large area boundaries (Li 1962). These disequilibrium features are removed as adjacent crystals adopt similar crystallographic orientations and grain boundaries are eliminated as similarly oriented grains coalesce into one larger crystal; this process is exemplified by T1 and T2 perovskite (circled in Figs. 3.4a-c) (Jones et al. 1979; Li 1962; Rios et al. 2005). These larger grains can continue to grow at low-angle boundaries with neighbouring small grains (Li 1962). Also during coalescence, the new grain boundaries straighten, removing 120° triple junctions by adjusting the dihedral angles of the adjacent grains. This process alters the morphology of the newly coalesced grain and neighbouring grains (see Fig. 4 in Rios et al. (2005)). Triple junctions are typical in T1 perovskite, while less common triple junctions in T2 are no longer strictly at 120° due to the boundary migration associated with grain coalescence (Fig. 3.3c; Vernon 1970). Type 2 perovskite shows the best examples of grain coalescence, with EBSD images capturing grain coalescence “in

progress" (like T1) and at completion. Larger T2 perovskite grains in the clinopyroxenites have some remaining triple junctions and are composed of multiple misoriented subgrains of similar sizes to T1 perovskite (Fig. 3.4c_{iii}). We suggest the large grains initially resembled T1 perovskite clusters prior to coalescence and have not completely adopted a uniform orientation. Further, we interpret the textural equilibration in the Afrikanda perovskite samples to indicate that coalescence and coarsening of small equilibrated polygonal clusters (T1) enabled the development of a mosaic of larger T2 polycrystalline grains with interlocking grain boundaries and smaller areas of massive T3 perovskite.

3.9.4. Effects of recrystallization

The coarsening of accumulated perovskite during recrystallization in the Afrikanda complex is supported by the complex chemical zoning patterns in perovskite and exsolution lamellae in the associated minerals.

3.9.4.1. Perovskite chemical zoning

Perovskite-group minerals serve as sensitive indicators to changes in parental environments through complex substitutions of multiple elements in their structure (Chakhmouradian et al. 2013; Mitchell et al. 2017). The variation in the composition and zoning of perovskite from T1 to T3 records the chemical evolution of its crystallization environment under open- or closed-system conditions. Zoning patterns can be caused by chemical fluctuations in the parental medium, changes in the physical conditions during crystal growth, or solid-state redistribution of elements (Dowty 1976a; Dowty 1976b).

Perovskite in T1 is distinguished from T2 and T3 perovskite by the state of textural equilibration and significant differences in chemical composition. Importantly, T1 grains have no internal zoning, consistently low REE values and minor compositional variation localized to the rims of some grains in contact with magnetite (Figs. 3.3b, 3.6a-d). Perovskite in the clinopyroxenite shows far more compositional variation, with simple zoning along perovskite grain contacts and oscillatory patterns at the contacts adjacent to magnetite (Fig. 3.3b). We interpret the internal compositional homogeneity to record textural equilibration of perovskite grains, and the minor zoning to arise from later metasomatic processes.

In contrast, T2 and T3 perovskite are significantly more complex with non-systematic and discontinuous zoning (Figs. 3.5a, b). Their composition is highly variable, particularly with respect to REE contents (Fig. 3.6d) and is linked with the irregular and complex zoning patterns. Zoning in T2 and T3 perovskite could be associated with the development of local chemical gradients during grain coalescence, where the differential diffusion of cations creates compositional complexity and irregularity superposed over the existing grain morphology (Fig. 3.6d). Perovskite in T3 is massive and most of T3 is relatively homogeneous, with some areas still displaying convoluted zoning with no clear pattern (Figs. 3.3e, f). We suggest these homogeneous areas re-equilibrated through solid-state diffusion removing the complex zoning and physical impurities such as multiphase inclusions. Areas that are

texturally heterogeneous underwent limited textural re-equilibration, however the zoning is still less complex or abundant than in T2 perovskite.

3.9.4.2. Controls on perovskite compositions

The composition of T1 perovskite is fairly homogeneous, while T2 and T3 vary significantly, reflecting changes in the availability of such elements as REE, Nb and Th (Figs. 3.6c, d). In T2 perovskite, these elements are primarily concentrated at the rims and along the grain boundaries (Figs. 3.2e, 3.5a, c, d). This type of zoning can be produced by selective cation diffusion during re-equilibration of perovskite with a fluid phase. This process has been invoked to explain perovskite zoning in some kimberlites (Chakhmouradian et al. 2013) and loparite-(Ce) replacement by cation-deficient phases in some alkaline rocks (Chakhmouradian et al. 1999). We suggest the high-REE rims in the Afrikanda T2 perovskite are probably associated with the progressive infiltration of REE and other substituent elements into perovskite from a fluid percolating along grain boundaries and fractures (Fig. 3.2e). The formation of T3 perovskite was a continuation from T2 polycrystalline grains, and resulted in higher levels of REE (on average) in T3 relative to T2 perovskite from the same rock type (Fig. 3.7). This enrichment in REE possibly required input of these elements from an external source (e.g., carbonatitic or alkaline magma; Chakhmouradian and Mitchell 1997). We envisage that continuous flux of REE through the ultramafic intrusion under open-system conditions produced the compositional variations.

The presence of REE-perovskite and loparite-(Ce) as discontinuous rims and overgrowths on T2 and T3 perovskite (Figs. 3.2e, 3.5a, b) is also undoubtedly linked to the infiltration of a REE-rich fluid in an open system. We agree with Chakhmouradian and Mitchell (1997) that these minerals developed due to infiltration of REE-rich CO_2-rich fluid, which facilitated both fracturing and the uptake of REE (± Th ± Nb) in the perovskite structure. The infiltration of REE into the crystal structure produces a diffuse marginal zone of REE-perovskite (Fig. 3.2e), whose width is controlled by the kinetics of diffusion and the relative diffusivity of differently charged cations (Chakhmouradian et al. 2013). Similar perovskite-loparite-(Ce) reaction rims and mantles have been reported in other carbonatite complexes and, less commonly, in evolved kimberlites (Chakhmouradian et al. 1999; Chakhmouradian and Mitchell 1997; Chakhmouradian and Mitchell 2000).

3.9.4.3. Exsolution lamellae

Exsolution lamellae are a common feature in minerals that have undergone re-equilibration to rid their crystal structure of impurities through solid-state diffusion (Putnis 2009). Exsolution textures in the olivinites and clinopyroxenites include monticellite lamellae in forsterite (Fig. 3.2a), magnetite and magnesiohastingsite lamellae in diopside (Fig. 3.2b), and inclusions of spinel and ilmenite in Ti-rich magnetite (Figs. 3.2c, d).

Calcium is generally a minor constituent in forsterite, with concentrations lower than 1 wt.% (Jurewicz and Watson 1988; Simkin and Smith 1970). The rare occurrence of Ca-rich exsolution phases, such as

diopside and monticellite-kirschsteinite, have been reported as a product of postmagmatic transformation of olivine in terrestrial rocks (Gaeta 1996; Markl et al. 2001; Xiong et al. 2017; Yufeng et al. 2008) and meteorites (McKay et al. 1998; Mikouchi et al. 1995). We interpret the textures in the Afrikanda samples to have formed by exsolution of Fe-rich monticellite during postmagmatic equilibration of Ca-rich forsterite. Elongate lamellae of oxide phases in pyroxenes are observed in mafic igneous and metamorphic rocks (Fleet et al. 1980; Garrison and Taylor 1981). Based on petrographic evidence, we suggest that exsolution of Ti-rich magnetite and magnesiohastingsite from the diopside host at Afrikanda also occurred during subsolidus equilibration.

Magnetite is observed in both rock types, but the composition and homogeneity (i.e., the nature and relative abundance of exsolution lamellae) differs between the examined olivinite and clinopyroxenite samples. Exsolution textures in Ti-rich magnetite are common in mafic plutonic rocks and have been the subject of much research (Haggerty 1991; Price 1980; Ramdohr 2013). Exsolution textures reflect the chemical composition and cooling history of the precursor magnetite (Buddington and Lindsley 1964; Howarth et al. 2013; Von Gruenewaldt et al. 1985). The magnetite in the olivinites has the highest concentrations of Ti, Mg and Al and does not exhibit any exsolution lamellae. Magnetite in the clinopyroxenite samples has much lower levels of these elements due to preferential partitioning of Ti and Mg into ilmenite, and Mg and Al into spinel inclusions (Fig. 3.2d). The variation in magnetite texture between the two rock types supports the suggestion that they underwent different degrees of subsolidus re-equilibration.

3.9.5. Perovskite textures in the silicocarbonatites

3.9.5.1. Chemical composition and zoning

Perovskite zoning in the silicocarbonatites is more complex than in the clinopyroxenites. The T2 perovskite has oscillatory zoning in the cores and irregular zoning at the rims (Fig. 3.5d) and in T3 massive perovskite has areas with oscillatory or irregular zoning, as well as homogeneous areas. The oscillatory zoning in T2 and T3 perovskite is a primary magmatic feature. The irregular complex zoning juxtaposed over primary growth patterns in these perovskite varieties was caused by progressive infiltration of REE, Na and locally also Nb and Th into the structure during postmagmatic fluid-driven alteration (Chakhmouradian and Zaitsev 1999). This process culminated with the deposition of REE-perovskite and loparite-(Ce) locally along the margin of, and fractures within, perovskite crystals (Figs. 3.3d, 3.5c, d). Titanite crystallized after these minerals, indicating either an increase in silica activity, or a decrease in fluid temperature (Chakhmouradian 2004). The formation of symplectitic intergrowths of titanite with rutile and ilmenite (Fig. 3.2f) implies increasing fluid acidity or, more likely, a further decrease in temperature, which would expand the stability fields of both rutile and ilmenite at a given pH, $p(CO_2)$ and $a(Fe^{2+})$ (Chakhmouradian 2004; Chakhmouradian and Mitchell 2002).

Occasional grains of T2 perovskite rimmed by low-REE material are much less common and could be produced by the inverse process, i.e. extraction of REEs from perovskite by percolating fluids (Fig. 3.5c). The compositionally homogeneous sections in T3 perovskite probably re-equilibrated through solid-state diffusion, which erased such primary textural characteristics as growth zoning and multiphase inclusions.

3.9.5.2. Textural development

In the silicocarbonatites, we observe irregularly shaped crystals with continuous crystallographic orientation, similar to the clinopyroxenites; however, the small perovskite grains also have a single crystallographic orientation and are not a composite of subgrains (Fig. 3.4d_{iii}). The absence of EBSD evidence of subgrain coalescence and the preservation of oscillatory zoning in T2 and T3 perovskite suggests that the coarse-grained perovskite did not undergo the same coalescence and amalgamation processes as those observed in the ultramafic rocks. However, the similarities in chemical composition, zoning patterns and associated minerals (e.g., titanite, REE-perovskite and loparite-(Ce)) indicate that the perovskite from both the ultramafic rocks and silicocarbonatites experienced the same fluid-driven alteration. We propose that the silicocarbonatites did not undergo perovskite recrystallization due to the lower solidus temperature of the silicocarbonatites compared to the ultramafic rocks. Also, the perovskite was initially fine-grained in the olivinites and clinopyroxenites but coarse-grained in the silicocarbonatites, so the difference in initial grain size may have impeded perovskite recrystallisation in the silicocarbonatites.

3.9.6. Textural similarities with other oxide deposits

Several textural features that support the process of perovskite amalgamation and re-equilibration in the Afrikanda complex are observed in other oxide-rich igneous systems, namely chromite and magnetite deposits (Charlier et al., 2006; Dill, 2010; Mungall, 2014), as well as mantle-derived lherzolites and dunites (Wandji et al., 2009), apatite in carbonatites (Chakhmouradian et al., 2017; Kamenetsky et al., 2015), recrystallized nepheline syenites (Chakrabarty et al., 2016; Ulbrich, 1993) and magnesian-ilmenite xenolith/xenocrysts in kimberlites and basanites (Mitchell, 1973; Leblanc et al. 1982). These features include granoblastic mosaics, massive textures, grain coarsening and the transition from inclusion-rich to inclusion-free grains (Christiansen 1985; Ghisler 1976; Yudovskaya and Kinnaird 2010). Understanding the mechanisms responsible for the development of these features in disseminated and massive ore bodies within chromitite and magnetitite layers remains ambiguous.

3.9.6.1. Granoblastic mosaics and massive textures

For comparison, we have chosen typical examples of ophiolite dunites, podiform chromitites and ultramafic xenoliths. Chains of connected euhedral chromite crystals observed in ultramafic xenoliths, igneous complexes like Bushveld (South Africa) and Fiskenaesset (Greenland) and the Oman ophiolite resemble networks of T1 perovskite (Fig. 3.10e). Granoblastic textures in peridotitic xenoliths from the

subcontinental lithospheric mantle are highlighted by the equigranular, euhedral olivine with interspersed linear chromite chains (Figs. 3.10e, f). The latter are similar to the T1 perovskite chains at Afrikanda (Fig. 3.10b). The xenolith textures reflect metamorphic stresses that caused mineral grains to recrystallize into granoblastic mosaic textures with straight margins and 120° triple junctions (Pike and Schwarzman 1977). At Bushveld and Fisknaesset, small chromite grains are generally euhedral to subhedral and form elongate chains, also reminiscent of T1 perovskite (Ghisler 1970; Sampson 1932; Yudovskaya and Kinnaird 2010). Silicate mineral inclusions are common and mostly restricted to grain cores.

Chromitites in the Oman ophiolite belt demonstrate an increasing grain size with deformation (Christiansen 1986). Christiansen (1985) described three morphological types of chromite (A, B and C) that are comparable to the three textural types of perovskite (T1, T2 and T3), respectively in the present study. Type A consists of closely packed subhedral to euhedral chromite grains that mostly range between 0.5 and 1 mm across and regularly host silicate inclusions. Type B is closely packed, subhedral to anhedral chromite grains between 0.1 mm and 4.5 mm in size with occasional silicate inclusions. Type C is composed of massive, closely packed and interlocking anhedral chromite grains with indiscernible boundaries and an estimated size larger than A- and B-type grains. Christiansen (1985; 1986) proposed that the coarsening of chromite occurred during recrystallization and was driven by strain-induced grain boundary migration and/or grain growth driven by interfacial energy gradient. We suggest that a similar mechanism was responsible for the textural evolution of perovskite in the Afrikanda ultramafic rocks.

Chains of connected crystals with granoblastic-polygonal textures are also observed in disseminated magnetite ore from the Panzhihua layered mafic intrusion, China. In this intrusion, magnetite mostly forms net-textures with densely packed clusters of polygonal grains with straight boundaries and 120° interfacial angles (Fig. 3.10c) that resemble the granoblastic texture of T1 perovskite (Figs. 3.1a, 3.3a, 3.10a; Pang et al. 2007; Zhou et al. 2005).

The presence of both inclusion-rich euhedral grains and inclusion-poor anhedral grains is also observed in chromitite layers from the Oman ophiolite belt and the Fiskenaesset and Bushveld complexes (Christiansen 1985; Ghisler 1976; Yudovskaya and Kinnaird 2010). The transition between these textures can be associated with late post-magmatic processes including re-equilibration, post-cumulus growth and contact metamorphism. The development of these inclusion-free grains and the associated massive textures at Afrikanda and other oxide deposits will be discussed in a subsequent publication.

No conclusive and/or unifying model has been proposed to explain the ore distributions and textural transformations observed in the aforementioned mineral deposits. Traditionally, the formation of oxide-rich seams, bands, stringers and layers has been linked to magmatic processes. Perovskite,

chromite and magnetite deposits share textural features that could imply that their development involved similar mechanisms. As we suggest for perovskite in the Afrikanda alkaline-ultramafic complex, the initial crystallisation of oxide minerals (whether magmatic or not) is followed by their textural re-equilibration at subsolidus temperatures. This re-equilibration produces perceptible changes in the morphology, size, orientation and compositional homogeneity of oxide mineral grains. From an exploration standpoint, the most important outcome of these processes is the accumulation of early-formed crystals into high-density oxide-rich zones and their coarsening and "purification" to form high-grade mineralized zones.

3.10. Conclusions

The textural and chemical examination of perovskite from the olivinites, clinopyroxenites and silicocarbonatites in the Afrikanda alkaline-ultramafic complex revealed three types of perovskite (T1 to T3) and lead to the following conclusions:

1. Perovskite from olivinites, clinopyroxenite and silicocarbonatite yielded similar ages, with an average of 368.3±1.2 Ma. The perovskite and titanite ages support the contemporaneous emplacement of these lithologies at Afrikanda. The ages are slightly younger than previously published ages and could be due to discrepancies associated with the technique or reflect the timing of recrystallization.
2. In ultramafic rocks (olivinites and clinopyroxenites) the progressive coarsening of perovskite from small, euhedral, disseminated grains into large anhedral and massive grains, and the various textures and zoning patterns is evidence of post-magmatic recrystallization and textural re-equilibration. We propose the post-magmatic development of perovskite involved three stages: (1) textural equilibration enabling the development of perovskite clusters and chains after initial perovskite crystallisation; (2) grain rotation and coalescence of the small equilibrated polygonal clusters to form larger anhedral polycrystalline mosaics; (3) in some areas the continued consolidation and coarsening transforms the large polycrystalline perovskite into massive perovskite.
3. The textural similarities between perovskite from Afrikanda and chromite and magnetite layers in various igneous complexes suggest similar post-magmatic coarsening processes are also involved in the development of other oxide ore deposits with monomineralic layers.

3.11. References

Afanasyev, B.V., 2011. Mineral resources of the alkaline–ultramafic massifs of the Kola Peninsula. Roza Vetrov, St. Petersburg, pp 224 (in Russian).

Armbrustmacher, T.J., 1981. The Complex of Alkaline Rocks at Iron Hill, Powderhorn district, Gunnison County, Colorado. New Mexico Geological Society, pp. 293-296.

Arzamastsev, A., Wu, F.-Y., 2014. U-Pb geochronology and Sr-Nd isotopic systematics of minerals from the ultrabasic-alkaline massifs of the Kola province. Petrology, 22(5): 462-479.

Barbosa, E.S.R. Brod, J.A., Junqueira-Brod, T.C., Dantas, E.L., de Oliveira Cordeiro, P.F., Gomide, C.S. 2012. Bebedourite from its type area (Salitre I complex): a key petrogenetic series in the Late-Cretaceous Alto Paranaíba Kamafugite–Carbonatite–Phoscorite association, Central Brazil. Lithos, 144: 56-72.

Borrok, D.M., Kelser, S.E., Boer, R.H., Essene, E.J., 1998. The Vergenoeg magnetite-fluorite deposit, South Africa; support for a hydrothermal model for massive iron oxide deposits. Economic Geology, 93(5): 564-586.

Brod, J.A., 1999. Petrology and geochemistry of the Tapira alkaline complex, Minas Gerais State, Brazil, Durham University.

Buddington, A., Lindsley, D., 1964. Iron-titanium oxide minerals and synthetic equivalents. Journal of Petrology, 5(2): 310-357.

Campbell, L.S., Henderson, P., Wall, F., Nielsen, T.F., 1997. Rare earth chemistry of perovskite group minerals from the Gardiner Complex, East Greenland. Mineralogical Magazine, 61(2): 197-212.

Cawthorn, R., 2011. Geological interpretations from the PGE distribution in the Bushveld Merensky and UG2 chromitite reefs. Journal of the Southern African Institute of Mining and Metallurgy, 111(2): 67-79.

Chakhmouradian, A., Mitchell, R., Pankov, A., Chukanov, N., 1999. Loparite and 'metaloparite' from the Burpala alkaline complex, Baikal Alkaline Province (Russia). Mineralogical Magazine, 63(4): 519-519.

Chakhmouradian, A., Williams, C., 2004. Mineralogy of high-field-strength elements (Ti, Nb, Zr, Ta, Hf) in phoscoritic and carbonatitic rocks of the Kola Peninsula, Russia. Phoscorites and carbonatites from mantle to mine: the key example of the Kola Alkaline Province, 10: 293-340.

Chakhmouradian, A.R., 2004. Crystal chemistry and paragenesis of compositionally unique (Al-, Fe-, Nb-, and Zr-rich) titanite from Afrikanda, Russia. American Mineralogist, 89(11-12): 1752-1762.

Chakhmouradian, A.R., Cooper, M.A., Medici, L., Hawthorne, F.C., Adar, F., 2008. Fluorine-rich hibschite from silicocarbonatite, Afrikanda complex, Russia: crystal chemistry and conditions of crystallization. The Canadian Mineralogist, 46(4): 1033-1042.

Chakhmouradian, A.R., Reguir, E. P., Zaitsev, A. N., Couëslan, C., Xu, C., Kynický, J., Mumin, A. H., and Yang, P., 2017. Apatite in carbonatitic rocks: Compositional variation, zoning, element partitioning and petrogenetic significance. Lithos, 274: 188-213.

Chakhmouradian, A.R., Mitchell, R.H., 1997. Compositional variation of perovskite-group minerals from the carbonatite complexes of the Kola Alkaline Province, Russia. The Canadian Mineralogist, 35(5): 1293-1310.

Chakhmouradian, A.R., Mitchell, R.H., 2000. Occurrence, alteration patterns and compositional variation of perovskite in kimberlites. The Canadian Mineralogist, 38(4): 975-994.

Chakhmouradian, A.R., Mitchell, R.H., 2002. New data on pyrochlore-and perovskite-group minerals from the Lovozero alkaline complex, Russia. European Journal of Mineralogy, 14(4): 821-836.

Chakhmouradian, A.R., Reguir, E.P., Kamenetsky, V.S., Sharygin, V.V., Golovin, A.V., 2013. Trace-element partitioning in perovskite: implications for the geochemistry of kimberlites and other mantle-derived undersaturated rocks. Chemical Geology, 353: 112-131.

Chakhmouradian, A.R., Zaitsev, A.N., 1999. Calcite-amphibole-clinopyroxene rock from the Afrikanda complex, Kola Peninsula, Russia: mineralogy and a possible link to carbonatites. I. Oxide minerals. Canadian Mineralogist, 37: 177-198.

Chakhmouradian, A.R., Zaitsev, A.N., 2002. Calcite–amphibole–clinopyroxene rock from the Afrikanda complex, Kola Peninsula, Russia: mineralogy and a possible link to carbonatites. III. Silicate minerals. The Canadian Mineralogist, 40(5): 1347-1374.

Chakhmouradian, A.R., Zaitsev, A.N., 2004. Afrikanda: An association of ultramafic, alkaline and alkali-silica-rich carbonatitic rocks from mantle-derived melts. Phoscorites and carbonatites from mantle to mine: the key example of the Kola Alkaline Province, Mineralogical Society (UK) Series, 10: 247-291.

Charlier, B., Duchesne, J.-C., Vander Auwera, J., 2007. Magma chamber processes in the Tellnes ilmenite deposit (Rogaland Anorthosite Province, SW Norway) and the formation of Fe–Ti ores in massif-type anorthosites. Chemical Geology, 234(3-4): 264-290.

Christiansen, F.G., 1985. Deformation fabric and microstructures in ophiolitic chromitites and host ultramafics, Sultanate of Oman. Geologische Rundschau, 74(1): 61-76.

Christiansen, F.G., 1986. Deformation of chromite: SEM investigations. Tectonophysics, 121(2-4): 175-196.

Clark, B.R., Price, F.R., Kelly, W.C., 1977. Effects of annealing on deformation textures in galena. Contributions to Mineralogy and Petrology, 64(2): 149-165.

Dawson, J., Hawthorn, J., 1973. Magmatic sedimentation and carbonatitic differentiation in kimberlite sills at Benfontein, South Africa. Journal of the Geological Society, 129(1): 61-85.

Dill, H.G., 2010. The “chessboard” classification scheme of mineral deposits: Mineralogy and geology from aluminum to zirconium. Earth-Science Reviews, 100(1-4): 1-420.

Doherty, R., Hughes, D., Humphreys, F., Jonas, J., Jensen, D. J., Kassner, M., King, W., McNelley, T., McQueen, H., and Rollett, A., 1997. Current issues in recrystallization: a review. Materials Science and Engineering: A, 238(2): 219-274.

Dowty, E., 1976a. Crystal structure and crystal growth: I. The influence of internal structure on morphology. American Mineralogist, 61(5-6): 448-459.

Dowty, E., 1976b. Crystal structure and crystal growth: II. Sector zoning in minerals. American Mineralogist, 61(5-6): 460-469.

Eales, H., Costin, G., 2012. Crustally contaminated komatiite: primary source of the chromitites and Marginal, Lower, and Critical Zone magmas in a staging chamber beneath the Bushveld Complex. Economic Geology, 107(4): 645-665.

Eales, H., De Klerk, W., Teigler, B., 1990. Evidence for magma mixing processes within the Critical and Lower Zones of the northwestern Bushveld Complex, South Africa. Chemical Geology, 88(3-4): 261-278.

Fleet, M., Bilcox, G.A., Barnett, R.L., 1980. Oriented magnetite inclusions in pyroxenes from the Grenville Province. The Canadian Mineralogist, 18(1): 89-99.

Force, E.R., 1991. Geology of titanium-mineral deposits, 259. Geological Society of America.

Gaeta, M., 1996. Ca-Fe-rich exsolution lamellae from olivine in a wehrlitic xenolith, Monti Vulsini Volcanic District, Central Italy. Mineralogica et Petrologica Acta, 39: 159-167.

Garrison, J.R., Taylor, L.A., 1981. Petrogenesis of pyroxene-oxide intergrowths from kimberlite and cumulate rocks; co-precipitation or exsolution? American Mineralogist, 66(7-8): 723-740.

Ghisler, M., 1970. Pre-metamorphic folded chromite deposits of stratiform type in the early Precambrian of West Greenland. Mineralium Deposita, 5(3): 223-236.

Ghisler, M., 1976. The Geology, Mineralogy and Geochemistry of the-Pre-Orogenic Archaean Stratiform Chromite Deposits at-Fiskenaesset, West Greenland.

Haggerty, S.E., 1991. Oxide textures; a mini-atlas. Reviews in Mineralogy and Geochemistry, 25(1): 129-219.

Harlov, D.E., Meighan, C.J., Kerr, I.D., Samson, I.M., 2016. Mineralogy, chemistry, and fluid-aided evolution of the Pea Ridge Fe oxide-(Y+ REE) deposit, southeast Missouri, USA. Economic Geology, 111(8): 1963-1984.

Herz, N., 1976. Titanium Deposits in Alkalic Igneous Rocks. In Force, E. R., (Eds.), Geology and Resources of Titanium. Geological Survey Professional Paper 959. United States Government Printing Office, Washington, pp. 58-66.

Higgins, M.D., 2011. Textural coarsening in igneous rocks. International Geology Review, 53(3-4): 354-376.

Higgins, M.D., 2015. Quantitative textural analysis of rocks in layered mafic intrusions, Layered Intrusions. Springer, pp. 153-181.

Higgins, M.D., 2017. Quantitative investigation of felsic rock textures using cathodoluminescence images and other techniques. Lithos, 277: 259-268.

Holm, E., Farjami, S., Manohar, P., Rohrer, G., Rollett, A., Srolovitz, D., Weiland, H., 2016. Proceedings of the 6th International Conference on Recrystallization and Grain Growth (ReX&GG 2016).

Holness, M.B., Cheadle, M.J., McKenzie, D., 2005. On the use of changes in dihedral angle to decode late-stage textural evolution in cumulates. Journal of Petrology, 46(8): 1565-1583.

Holness, M.B., Nielsen, T.F., Tegner, C., 2006. Textural maturity of cumulates: a record of chamber filling, liquidus assemblage, cooling rate and large-scale convection in mafic layered intrusions. Journal of Petrology, 48(1): 141-157.

Horstwood, M.S., Košler, J., Gehrels, G., Jackson, S. E., McLean, N. M., Paton, C., Pearson, N. J., Sircombe, K., Sylvester, P., Vermeesch, P., 2016. Community-Derived Standards for LA-ICP-MS U-(Th-)Pb Geochronology–Uncertainty Propagation, Age Interpretation and Data Reporting. Geostandards and Geoanalytical Research, 40(3): 311-332.

Hou, B., Keeling, J., Van Gosen, B.S., 2017. Geological and Exploration Models of Beach Placer Deposits, Integrated from Case-Studies of Southern Australia. Ore Geology Reviews, 80: 437-459.

Howarth, G.H., Prevec, S.A., Zhou, M.-F., 2013. Timing of Ti-magnetite crystallisation and silicate disequilibrium in the Panzhihua mafic layered intrusion: Implications for ore-forming processes. Lithos, 170: 73-89.

Humphreys, F., 2001. Review grain and subgrain characterisation by electron backscatter diffraction. Journal of materials science, 36(16): 3833-3854.

Humphreys, F.J., Hatherly, M., 2004. Recrystallization and related annealing phenomena. Elsevier.

Hunter, R.H., 1987. Textural equilibrium in layered igneous rocks, Origins of igneous layering. Springer, pp. 473-503.

Irvine, T., 1977. Origin of chromitite layers in the Muskox intrusion and other stratiform intrusions: A new interpretation. Geology, 5(5): 273-277.

Jones, A., Ralph, B., Hansen, N., 1979. Subgrain coalescence and the nucleation of recrystallization at grain boundaries in aluminium. Proceedings of the Royal Society of London, 368: 345-357.

Jurewicz, A.J., Watson, E.B., 1988. Cations in olivine, Part 1: Calcium partitioning and calcium-magnesium distribution between olivines and coexisting melts, with petrologic applications. Contributions to Mineralogy and Petrology, 99(2): 176-185.

Kamenetsky, V.S., Mitchell, R.H., Maas, R., Giuliani, A., Gaboury, D., Zhitova, L., 2015. Chlorine in mantle-derived carbonatite melts revealed by halite in the St.-Honoré intrusion (Québec, Canada). Geology, 43: 687-690.

Kinnaird, J., Kruger, F., Nex, P., Cawthorn, R., 2002. Chromitite formation—a key to understanding processes of platinum enrichment. Applied Earth Science, 111(1): 23-35.

Knipping, J.L.. Bilenker, L. D., Simon, A. C., Reich, M., Barra, F., Deditius, A. P., Wälle, M., Heinrich, C. A., Holtz, F., and Munizaga, R., 2015. Trace elements in magnetite from massive iron oxide-apatite deposits indicate a combined formation by igneous and magmatic-hydrothermal processes. Geochimica et Cosmochimica Acta, 171: 15-38.

Kolker, A., 1982. Mineralogy and geochemistry of Fe-Ti oxide and apatite (nelsonite) deposits and evaluation of the liquid immiscibility hypothesis. Economic Geology, 77(5): 1146-1158.

Kramm, U., Kogarko, L., Kononova, V., Vartiainen, H., 1993. The Kola Alkaline Province of the CIS and Finland: Precise Rb-Sr ages define 380–360 Ma age range for all magmatism. Lithos, 30(1): 33-44.

Kreitcberg, A., Brailovski, V., Turenne, S., 2017. Effect of heat treatment and hot isostatic pressing on the microstructure and mechanical properties of Inconel 625 alloy processed by laser powder bed fusion. Materials Science and Engineering: A, 689: 1-10.

Kretz, R., 1966. Interpretation of the shape of mineral grains in metamorphic rocks. Journal of Petrology, 7(1): 68-94.

Kukharenko, A.A., Orlova, M. P., Bulakh, A. G., Bagdasarov, E. A., Rimskaya-Korsakova, O. M., Nefedov, E. I., Ilinskiy, G. A., Sergeev, A. S., and Abakumova, N. B., 1965. The Caledonian Complex of Ultrabasic and Alkaline Rocks and Carbonatites of the Kola Peninsula and Northern Karelia. Nedra, Leningrad, Russia, 722 pp.

Latypov, R., Chistyakova, S., Mukherjee, R., 2017. A Novel Hypothesis for Origin of Massive Chromitites in the Bushveld Igneous Complex. Journal of Petrology, 1: 41.

Latypov, R., O'Driscoll, B., Lavrenchuk, A., 2013. Towards a model for the in situ origin of PGE reefs in layered intrusions: insights from chromitite seams of the Rum Eastern Layered Intrusion, Scotland. Contributions to Mineralogy and Petrology, 166(1): 309-327.

Leblanc, M., Dautria, J.-M., Girod, M., 1982. Magnesian ilmenitite xenoliths in a basanite from Tahalra, Ahaggar (Southern Algeria). Contributions to Mineralogy and Petrology, 79: 347-354.

Li, J.C., 1962. Possibility of subgrain rotation during recrystallization. Journal of Applied Physics, 33(10): 2958-2965.

Lister, G.F., 1966. The composition and origin of selected iron-titanium deposits. Economic Geology, 61(2): 275-310.

Markl, G., Marks, M., Wirth, R., 2001. The influence of T, a SiO2, and f O2 on exsolution textures in Fe-Mg olivine: An example from augite syenites of the Ilimaussaq Intrusion, South Greenland. American Mineralogist, 86(1-2): 36-46.

McCloy, J., Korenstein, R., Zelinski, B., 2009. Effects of temperature, pressure, and metal promoter on the recrystallized structure and optical transmission of chemical vapor deposited zinc sulfide. Journal of the American Ceramic Society, 92(8): 1725-1731.

McDonald, J.A., 1965. Liquid immiscibility as one factor in chromitite seam formation in the Bushveld Igneous Complex. Economic Geology, 60(8): 1674-1685.

McKay, G., Miyamoto, M., Mikouchi, T., Ogawa, T., 1998. The cooling history of the Lewis Cliff 86010 angrite as inferred from kirschsteinite lamellae in olivine. Meteoritics & Planetary Science, 33(5): 977-983.

Mikouchi, T., Takeda, H., Miyamoto, M., Ohsumi, K., McKay, G.A., 1995. Exsolution lamellae of kirschsteinite in magnesium-iron olivine from an angrite meteorite. American Mineralogist, 80(5-6): 585-592.

Mitchell, R.H., 1973. Magnesian ilmenite and its role in kimberlite petrogenesis. The Journal of Geology, 81:301-311.

Mitchell, R.H., Welch, M.D., Chakhmouradian, A.R., 2017. Nomenclature of the perovskite supergroup: A hierarchical system of classification based on crystal structure and composition. Mineralogical Magazine, 81(3): 411-462.

Mondal, S.K., Mathez, E.A., 2006. Origin of the UG2 chromitite layer, Bushveld Complex. Journal of Petrology, 48(3): 495-510.

Mungall, J., 2014. Geochemistry of magmatic ore deposits, Treatise on Geohemistry, pp. 195-218.

Nielsen, T., 1980. The petrology of a melilitolite, melteigite, carbonatite and syenite ring dike system, in the Gardiner complex, East Greenland. Lithos, 13(2): 181-197.

Nielsen, T.F.D., Solovova, I.P., Veksler, I.V., 1997. Parental melts of melilitolite and origin of alkaline carbonatite: evidence from crystallised melt inclusions, Gardiner complex. Contributions to mineralogy and petrology, 126: 331-344.

Pang, K.-N., Zhou, M.-F., Lindsley, D., Zhao, D., Malpas, J., 2007. Origin of Fe–Ti oxide ores in mafic intrusions: evidence from the Panzhihua intrusion, SW China. Journal of Petrology, 49(2): 295-313.

Pekov, I., Petersen, O.V., Voloshin, A., 1997. Calcio-ancylite-(Ce) from Ilímaussaq and Narssârssuk, Greenland, Kola Peninsula and Polar Urals, Russia, ancylite-(Ce)-calcio-ancylite-(Ce) an isomorphous series. Neues Jahrbuch für Minerologie, Abhandlungen(171, 3): 309-322.

Pike, J.N., Schwarzman, E., 1977. Classification of textures in ultramafic xenoliths. The Journal of Geology, 85(1): 49-61.

Price, G., 1980. Exsolution microstructures in titanomagnetites and their magnetic significance. Physics of the Earth and Planetary Interiors, 23(1): 2-12.

Pushkarev, E., Kamenetsky, VS., Morozova, A., Khiller, V., Glavatskykh, S., Rodemann, T. 2015. Ontogeny of ore Cr-spinel and composition of inclusions as indicators of the pneumatolytic–hydrothermal origin of PGM-bearing chromitites from Kondyor massif, the Aldan Shield. Geology of Ore Deposits, 57(5): 352-380.

Putnis, A., 2009. Mineral replacement reactions. Reviews in mineralogy and geochemistry, 70(1): 87-124.

Ramdohr, P., 2013. The ore minerals and their intergrowths. Elsevier.

Reguir, E.P., Camacho, A., Yang, P., Chakhmouradian, A.R., Kamenetsky, V.S., Halden, N.M. 2010. Trace-element study and uranium-lead dating of perovskite from the Afrikanda plutonic complex, Kola Peninsula (Russia) using LA-ICP-MS. Mineralogy and Petrology, 100(3-4): 95-103.

Rios, P.R., Siciliano Jr, F., Sandim, H.R.Z., Plaut, R.L., Padilha, A.F., 2005. Nucleation and growth during recrystallization. Materials Research, 8(3): 225-238.

Salnikova, E., Stifeeva, M., Chakhmouradian, A., Glebovitsky, V., Reguir, E., 2018. The U–Pb System in Schorlomite from Calcite–Amphobole–Pyroxene Pegmatite of the Afrikanda Complex (Kola Peninsula). Doklady Earth Sciences, 478(2): 148-151.

Sampson, E., 1932. Magmatic chromite deposits in southern Africa. Economic Geology, 27(2): 113-144.

Sandström, R., Lehtinen, B., Hedman, E., Groza, I., Karlsson, S., 1978. Subgrain growth in Al and Al-1% Mn during annealing. Journal of Materials Science, 13(6): 1229-1242.

Simkin, T., Smith, J., 1970. Minor-element distribution in olivine. The Journal of Geology, 78(3): 304-325.

Stacey, J.S., Kramers, J.D., 1975. Approximation of terrestrial lead isotope evolution by a two-stage model. Earth and Planetary Science Letters, 26(2): 207-221.

Syrenko, A., Klinishev, G., 1973. Recrystallization of copper under hydrostatic pressure up to 15 kbar. Journal of Materials Science, 8(6): 765-769.

Ulbrich, M.N., 1993. Mineralogy of nepheline syenites from the Poços de Caldas alkaline massif SE Brazil: chemistry, X-ray data and microtextures of feldspars. Revista Brasileira de Geociências, 23:388-399.

Varma, S., Willits, B.L., 1984. Subgrain growth in aluminum during static annealing. Metallurgical Transactions A, 15: 1502-1503.

Vernon, R., 1970. Comparative grain-boundary studies of some basic and ultrabasic granulites, nodules and cumulates. Scottish Journal of Geology, 6(4): 337-351.

Vidyashankar, H., Govindaiah, S., 2009. Ore petrology of the V-Ti magnetite (lodestone) layers of the Kurihundi area of Sargur schist belt, Dharwar craton. Journal of the Geological Society of India, 74(1): 58-68.

Von Gruenewaldt, G., Klemm, D., Henckel, J., Dehm, R., 1985. Exsolution features in titanomagnetites from massive magnetite layers and their host rocks of the Upper Zone, Eastern Bushveld Complex. Economic Geology, 80(4): 1049-1061.

Walter, J., Koch, E., 1963. Substructures and recrystallization of deformed (100)[001]-oriented crystals of high-purity silicon-iron. Acta Metallurgica, 11(8): 923-938.

Wandji, P., Tsafack, J., Bardintzeff, J., Nkouathio, D., Dongmo, A.K., Bellon, H., Guillou, H., 2009. Xenoliths of dunites, wehrlites and clinopyroxenites in the basanites from Batoke volcanic cone

(Mount Cameroon, Central Africa): petrogenetic implications. Mineralogy and Petrolology, 96:81-98.

Wu, F.-Y., Arzamastsev, A.A., Mitchell, R.H., Li, Q.-L., Sun, J., Yang, Y.-H., Wang, R.-C. 2013. Emplacement age and Sr–Nd isotopic compositions of the Afrikanda alkaline ultramafic complex, Kola Peninsula, Russia. Chemical Geology, 353: 210-229.

Wu, F.-Y., Yang, Y.-H., Mitchell, R.H., Bellatreccia, F., Li, Q.-L., Zhao, Z.-F. 2010. In situ U–Pb and Nd–Hf–(Sr) isotopic investigations of zirconolite and calzirtite. Chemical Geology, 277(1): 178-195.

Xiong, F., Yang, J., Dilek, Y., Wang, C., 2017. Nanoscale Diopside and Spinel Exsolution in Olivine from Dunite of the Tethyan Ophiolites, Southwestern Turkey: Implications for the Multi-Stage Process. Journal of Nanoscience and Nanotechnology, 17(9): 6587-6596.

Yudin, B., Zak, S., 1971. Titanium deposits of northwestern USSR (eastern part of Baltic Shield). International Geology Review, 13(6): 864-872.

Zaitsev, A.N., Chakhmouradian, A.R., 2002. Calcite–amphibole–clinopyroxene rock from the Afrikanda complex, Kola Peninsula, Russia: mineralogy and a possible link to carbonatites. II. Oxysalt minerals. The Canadian Mineralogist, 40(1): 103-120.

Zhou, M.-F., Robinson, P.T., Lesher, C.M., Keays, R.R., Zhang, C.-J., Malpas, J. 2005. Geochemistry, petrogenesis and metallogenesis of the Panzhihua gabbroic layered intrusion and associated Fe–Ti–V oxide deposits, Sichuan Province, SW China. Journal of Petrology, 46(11): 2253-2280.

Appendix 3.1 Methodology

EDS and EBSD analysis

Backscattered electron (BSE) imaging, energy dispersive X-ray spectrometry (EDS) and electron backscatter diffraction (EBSD) were performed using a Hitachi SU-70 field emission scanning electron microscope (SEM). The instrument is fitted with a Hitachi photo-diode BSE detector and an Oxford AZTec 3 microanalysis system with XMax80 EDS detector and HKL Nordlys Nano EBSD camera.

For BSE-EDS analyses the samples were coated with around 20 nm of carbon using a Ladd 40000 carbon evaporator and analysed at 15 kV accelerating voltage and 2-3 nm beam current. Elements were calibrated on well characterised natural and synthetic standard reference materials. The intensity of the cobalt K x-ray peak series was determined at the start of each session on pure cobalt metal as an indirect beam current measurement to avoid normalisation of compositional data to 100% total.

For combined EDS-EBSD mapping the samples received an additional polishing step after conventional mechanical polishing using a Pace GIGA-0900 vibratory polisher with SIAMAT colloidal silica suspension (particle size 60nm, pH >9.5) and a thinner carbon coating of around 10 nm. The samples were analysed at 70º tilt from normal, 20 kV accelerating voltage, and 3 nm beam current. EBSD maps were processed using the HKL Channel5 Tango package.

Perovskite and titanate U-Pb analysis and data reduction

Perovskite and titanite U-Pb analyses were performed on an Agilent 7900 quadropole ICPMS, coupled to a Resolution S155 laser ablation system with a Coherent COMPex Pro 110 ArF Excimer laser operating at 193nm wavelength and ~20ns pulse width. Each analysis was pre-ablated with 5 laser pulses to remove any surface contamination. Blank gas was analysed for 8 s followed by 25 s of perovskite ablation with operating conditions of 5 Hz and ~2 J/cm^2 using a spot size of 32 µm. Helium carrier gas flowing at 0.35 l/min carried particles ablated by the laser out of the sample chamber and mixed with Ar gas before transfer to the plasma. For perovskite, the down hole fractionation, instrument drift and mass bias calibration for Pb/U and Pb/Th ratios were calculated using the 91500 zircon analysed throughout each analytical session with U-Pb isotopic values from (Horstwood et al., 2016). Isotopes measured for the perovskite dating included: ^{49}Ti, ^{56}Fe, ^{202}Hg, ^{204}Pb, ^{206}Pb, ^{207}Pb, ^{208}Pb, ^{232}Th and ^{238}U. Currently no widely available reference material for U-Pb exists for the mineral perovskite, so a fragment of perovskite from the Oka carbonatite complex was analysed each session to assess accuracy of the technique. Our results for perovskite from the Oka carbonatite gave a Concordia intercept age of 121.2±3.9 Ma +/- 4.59 Ma (incl. systematic uncertainties), well within uncertainty of

the Cox and Wilton (2006) age of 131±7Ma age for perovskite from the Oka carbonatite and consistent with apatite fission track ages for the complex (Cox and Wilton (2006) and references within). For titanite, the down hole fractionation, instrument drift and mass bias calibration for Pb/U and Pb/Th ratios were calculated using analyses of an in-house titanite reference material with un-published ID-MC-ICPMS U-Pb isotopic composition. Isotopes measured for the perovskite dating included: ^{49}Ti, ^{56}Fe, ^{202}Hg, ^{204}Pb, ^{206}Pb, ^{207}Pb, ^{208}Pb, ^{232}Th and ^{238}U. Accuracy of this calibration was done using several titanite reference materials for U-Pb including titanite from the Fish Canyon Tuff (FC-3), titanite from Mt Dromedary, and an in-house titanite (100606) with an ID-TIMS age published in Best (2012). All secondary reference titanite are well within uncertainty of their published ID-TIMS ages and the full data set is in the Electronic Supplement.

For both perovskite and titanite, calibration of the ^{207}Pb/^{206}Pb ratio was calculated using the NIST610 glass analysed throughout the sessions and corrected using the values recommended by Baker et al. (2004). Calibration of trace elements analysed along with the U-Pb isotopic data was done using the NIST610 glass as the calibration material using values from Jochum et al. (2011) and using ^{49}Ti as the internal standard element for both perovskite and titanite and assuming stoichiometric proportions (350,500 ppm and 181,600 ppm respectively). This trace element data was only used for assistance in interpreting geochronology data and was not used in further interpretations as there are significant substitutions for Ti in both minerals.

All data reduction calculations and error propagations were done within Microsoft Excel® via macros designed at the University of Tasmania, and using techniques summarised by Halpin et al. (2014) and Thompson et al. (2018). Interrogation of time-resolved signals allowed for identification of isotopic heterogeneity within the ablation volume. Time-resolved isotopic ratios for each analysis were scrutinised on U-Pb concordia diagrams to investigate the presence of common Pb and/or ancient Pb-loss and/or mixing of age zones; analyses (or parts of analyses) were excluded from the dataset where any of these trends was detected, utilising a similar approach to that of Petrus and Kamber (2012) . Uncertainties were calculated using similar techniques to those outlined by Halpin et al. (2014) and Horstwood et al. (2016). Tera-Wasserburg diagrams and age calculations were made using Isoplot v4.15 (Ludwig, 2012).

Trace element analyses

Major and trace element analyses of perovskite and titanite were performed on an Agilent 7900 quadropole ICPMS, coupled to a Resolution S155 laser ablation system with a Coherent COMPex Pro 110 ArF Excimer laser operating at 193nm wavelength and ~20ns pulse width. Each analysis was pre-ablated with 5 laser pulses to remove any surface contamination. Blank gas was analysed for 8 s followed by 25 s of perovskite ablation with operating conditions of 5 Hz and ~2 J/cm2 using a spot

size of 29 µm. Helium carrier gas flowing at 0.35 l/min carried particles ablated by the laser out of the sample chamber to be mixed with Ar gas before transfer to the plasma. The elements measured had typical detection limits that ranged from <1000 ppm for Si, <100 ppm for Ca and Ti, <50 ppm for Na, K, Fe, Ce, <5 ppm for Al, Mn, Sr, Nb, La, Nd, Sm and Th and <1ppm for Li, Mg, Sc, V, Ga, Rb, Zr, Ba, Pr, HREE, Hf, Ta, Pb and U.

Samples were analysed in runs of 12 bracketed by two spots of the primary standard at the start and end of each run. Additionally, one analysis of the BCR-2g and GSD-1g standards were included in each run as a secondary standard to monitor the accuracy of the measurements using the preferred values from the GeoReM website. Element abundances were calculated using the NIST610 glass as the primary calibration material using values from Jochum et al. (2011) and using ^{43}Ca as the internal standard element for perovskite and ^{49}Ti for titanite, with both minerals normalized to a 100% and 99% total for each mineral respectively. All data reduction calculations and error propagations were done within Microsoft Excel® via macros designed at the University of Tasmania, and using techniques summarised by Longerich et al. (1996).

Appendix 3.2 LAICPMS trace element perovskite data – see digital appendix

Appendix 3.3 U-Pb Chronology data – see digital appendix

Appendix 3.4 Additional EDS images – see digital appendix

CHAPTER 4

POLYMINERALIC INCLUSIONS IN OXIDE MINERALS OF THE AFRIKANDA ALKALINE-ULTRAMAFIC COMPLEX: IMPLICATIONS FOR THE EVOLUTION OF PEROVSKITE MINERALISATION

Submitted to Contributions to Mineralogy and Petrology

4.0. Abstract

The exceptional accumulation of perovskite in the alkaline-ultramafic Afrikanda complex (Kola Peninsula, Russia) led to the study of polymineralic inclusions hosted in perovskite and magnetite to understand the development of the perovskite-rich zones in the olivinites, clinopyroxenites and silicocarbonatites. The abundance of inclusions varies across the three perovskite textures, with numerous inclusions hosted in the fine-grained equigranular perovskite, fewer inclusions in the coarse-grained interlocked perovskite and rare inclusions in the massive perovskite. The inclusions are composed of a variety of silicate, carbonate, sulphide, phosphate and oxide phases. The bulk compositions of neighbouring inclusions are not comparable, signifying a heterogeneously trapped media. In the fine-grained euhedral perovskite, polymineralic inclusions were heated to 1000°C and did not homogenise, indicating the presence of minerals and melt/fluid at the time of trapping. These observations reveal the inclusions are not bona fide melt inclusions. We propose that the inclusions represent material trapped during subsolidus sintering of magmatic perovskite. The continuation of the sintering process resulted in the coarsening of inclusion-rich subhedral perovskite into inclusion-poor anhedral and massive perovskite. These findings advocate the importance of inclusion studies for interpreting the origin of oxide minerals and their associated economic deposits and suggest that the formation of large scale accumulations of minerals in other oxide deposits may be a result of annealing of individual disseminated grains.

4.1. Introduction

Oxide deposits are important sources of economically significant elements, like Cr, Fe, V, Ti and platinum group metals, and can be formed through a range of magmatic, metamorphic and sedimentary processes (Borrok et al. 1998; Force 1991; Hou et al. 2017; Irvine 1977; Latypov et al. 2017). For decades, oxide minerals, such as chromite and magnetite, have been the focus of numerous academic studies, yet Deposits of other oxide minerals, such as perovskite (ideally, $CaTiO_3$), have received little attention from the research community due to their rarity in nature. Perovskite is a common accessory mineral in a variety of alkaline and ultramafic rocks, including carbonatites and kimberlites (Campbell et al. 1997; Chakhmouradian and Mitchell 1997; Nielsen 1980) and in rarer cases, can be a major mineral in rocks such as bebedourites, dunites and melilitolites (Barbosa et al. 2012; Dawson and Hawthorn 1973; Nielsen et al. 1997). Only a few undersaturated alkaline complexes contain potentially economic quantities of perovskite, and only Powderhorn in Colorado, USA (Armbrustmacher 1981), Tapira in southeastern Brazil (Brod 1999), and Afrikanda in northwestern Russia (Afanasyev 2011), have been the focus of several published studies.

Melt and fluid inclusions are important tools used to decipher the origin and evolution of oxide mineral deposits. These small pockets of material allow genetic constraints to be placed on their host minerals, by enabling the parental composition to be identified and the physico-chemical conditions to be reconstructed. However, the opacity of many oxide minerals presents obvious challenges for inclusion studies by limiting our ability to discover inclusions and provide their three-dimensional characterisation. Nevertheless, studies of perovskite-hosted inclusions in plutonic alkaline-ultramafic complexes have been conducted to better understand the link between carbonatites and associated alkaline silicate rocks (Kogarko et al. 1991; Nielsen et al. 1997; Panina 2005; Veksler et al. 1998). In this work, we analysed perovskite- and magnetite-hosted inclusions in ultramafic and carbonate rocks from the Afrikanda complex to shed further light on their petrogenesis, and the development of this high-grade perovskite deposit (34.3 Mt at ~12 wt.% TiO_2: Afanasyev 2011).

The perovskite-rich segregations in the olivinites, clinopyroxenites and silicocarbonatites at the Afrikanda alkaline-ultramafic complex have been proposed to be magmatic (Chakhmouradian and Zaitsev 2004), yet a recent publication by Potter et al. (2018) identified textural features that indicated that the accumulation process involved post-magmatic recrystallization and textural re-equilibration. This idea was first put forth by Kukharenko et al. (1965), who suggested that large, crudely-shaped perovskite crystals at Afrikanda "formed by recrystallization of finer-grained material" (p. 331), but did not offer evidence in support of their interpretation. Potter et al. (2018) demonstrated that perovskite segregations were conceived and rendered by processes similar to those documented for several chromite and magnetite deposits around the world (Borisova et al. 2012; Lorand and Cottin 1987; McElduff and Stumpfl 1991; Yudovskaya and Kinnaird 2010). In the present paper, we build upon the textural study completed by Potter et al. (2018) by analysing perovskite- and magnetite-hosted

inclusions in representative rock types from the deposit. The mineralogical and chemical observations are used to determine the origin and development of the perovskite-rich segregations in the Afrikanda complex. Some implications for chromite and magnetite deposits are also discussed.

4.2. Geological background

The Afrikanda alkaline-ultramafic complex is one of the smallest intrusions in the Devonian (~380 Ma) Kola Alkaline Province (Kukharenko et al. 1965). The complex covers an area of ~11.5 km^2 and has a concentric internal structure comprising texturally and mineralogically diverse olivinites and clinopyroxenites, cross-cut by minor intrusions of carbonatites and feldspathoidal rocks (Fig. 4.1; Afanasyev 2011; Chakhmouradian and Zaitsev 2004; Downes et al. 2005; Kukharenko et al. 1965). These rock units do not show any evidence of deformation and preserve most of the primary structures and textures. Perovskite ore is confined to the central part of the complex measuring 0.77 sq. km and dominated by clinopyroxenites (>50 vol.%) that host blocks of olivinites and are cross-cut by carbonatitic and feldspathoidal rocks.

The examined olivinite samples are inequigranular, fine- to medium-grained, and composed of forsterite, åkermanite, perovskite and magnetite, with accessory monticellite developed between åkermanite and forsterite, and calcite and wollastonite confined to veinlets. Clinopyroxenite samples are fine- to medium-grained, inequigranular, and primarily composed of diopside, perovskite and

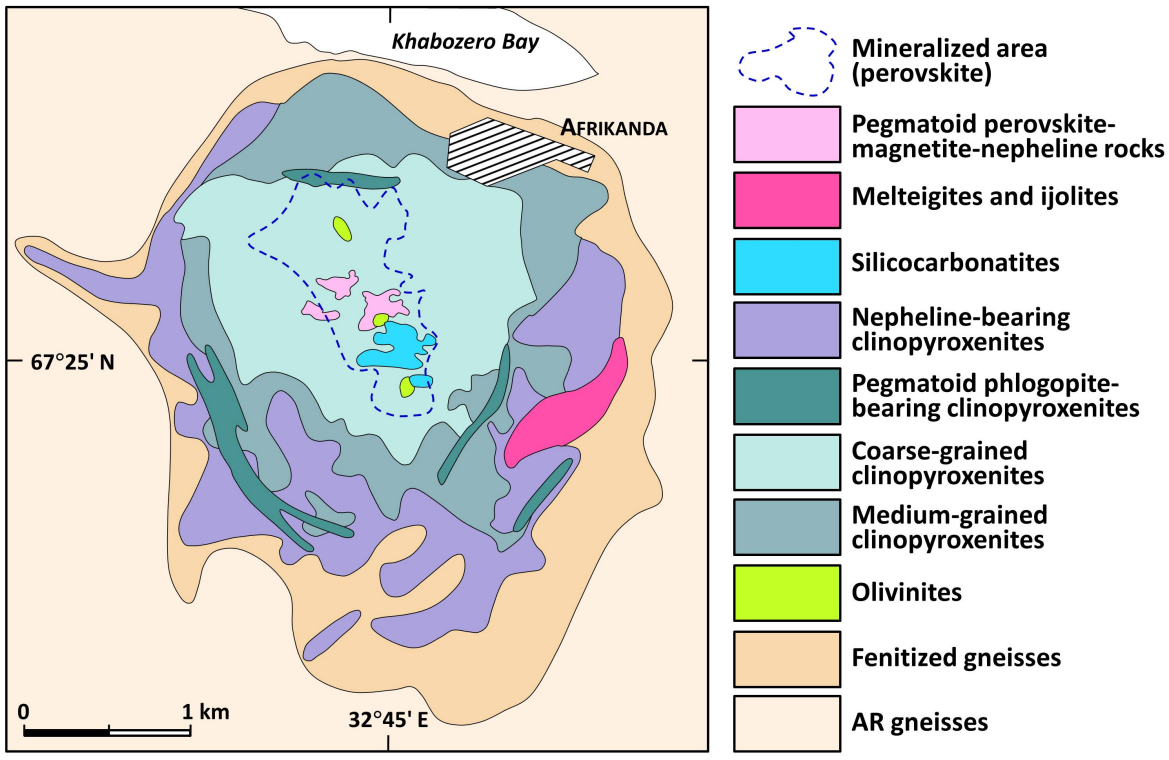

Figure 4. 1 Simplified geological map of Afrikanda in the Kola Peninsula showing the distribution of the silicate and alkaline rock units in the complex (modified after Afanasyev et al., 2011).

magnetite, with minor proportions of calcite, richterite, phlogopite, magnesiohastingsite, titanite, chlorite and loparite. Silicocarbonatite samples are fine- to coarse-grained, inequigranular and predominantly composed of calcite, diopside, perovskite, titanite and minor magnesiohastingsite and magnetite. All three samples came from the central part of the complex, where pilot-scale mining of perovskite ore occurred in the 1980s. In that area, measuring <0.05 km^2, the ultramafic and carbonatitic rocks are intimately associated and . Most of the minerals identified in the present work were reported from the Afrikanda rocks in previous studies (Chakhmouradian and Zaitsev 1999, 2002, 2004; Zaitsev and Chakhmouradian 2002; Kukharenko et al. 1965; Potter et al. 2018). For further details on the petrography and mineralogy of the Afrikanda complex, we refer the reader to Kukharenko et al. (1965), Chakhmouradian and Zaitsev (1999, 2004) and Afanasyev (2011).

4.3. Perovskite and magnetite textures

Three types of perovskite textures were identified in the studied olivinite, clinopyroxenite and silicocarbonatite samples (Potter et al. 2018). These textures are based on the crystal morphology, inclusion abundance, composition and zonation of perovskite. Olivinites and clinopyroxenites host type 1 (T1) perovskite, which is characterised by polygonal clusters and networks of small (50 to 550 μm) grains with abundant polymineralic inclusions (Figs. 4.2a-d). Types 2 (T2) and 3 (T3) are both observed in clinopyroxenites and silicocarbonatites. Type 2 perovskite is characterised by anhedral mosaics of large (0.2 to 2 mm) zoned grains that host sporadic polymineralic inclusions (Fig. 4.2e). Type 3 perovskite is very coarse-grained (>2 mm) and almost devoid of polymineralic inclusions (Fig. 4.2f).

Magnetite grains in the three rock types are euhedral to anhedral and range from 0.3 to 1.3 mm; rare grains are up to 10 mm; however, the textures and compositions vary significantly. In the olivinites, magnetite is texturally and compositionally homogeneous, whereas that in the clinopyroxenites and silicocarbonatites is heterogeneous with respect to the Ti, Mg and Al contents, and hosts lamellae of Mg-rich ilmenite and trellis-like and irregular patches of Fe-rich spinel (<25 μm), Mn- and Mg-rich ilmenite (<50 μm) and irregular grains of Zn-rich spinel (<20 μm). Magnetite-hosted inclusions were observed only in the silicocarbonatites. Only a few isolated inclusions were identified in other minerals, such as åkermanite, in the three rock types. For additional descriptions of the textures and compositions of perovskite and magnetite in these rocks, refer to Potter et al. (2018) and Chakhmouradian and Zaitsev (1999).

4.4. Methodology

perovskite and magnetite grains were mounted in epoxy and dry-polished with 800 μm grit paper to 1 μm oil-based diamond paste and cleaned with shellite (petroleum-based solvent). All grinding and polishing was carried out using kerosene as a lubricant to avoid damage to water-soluble phases

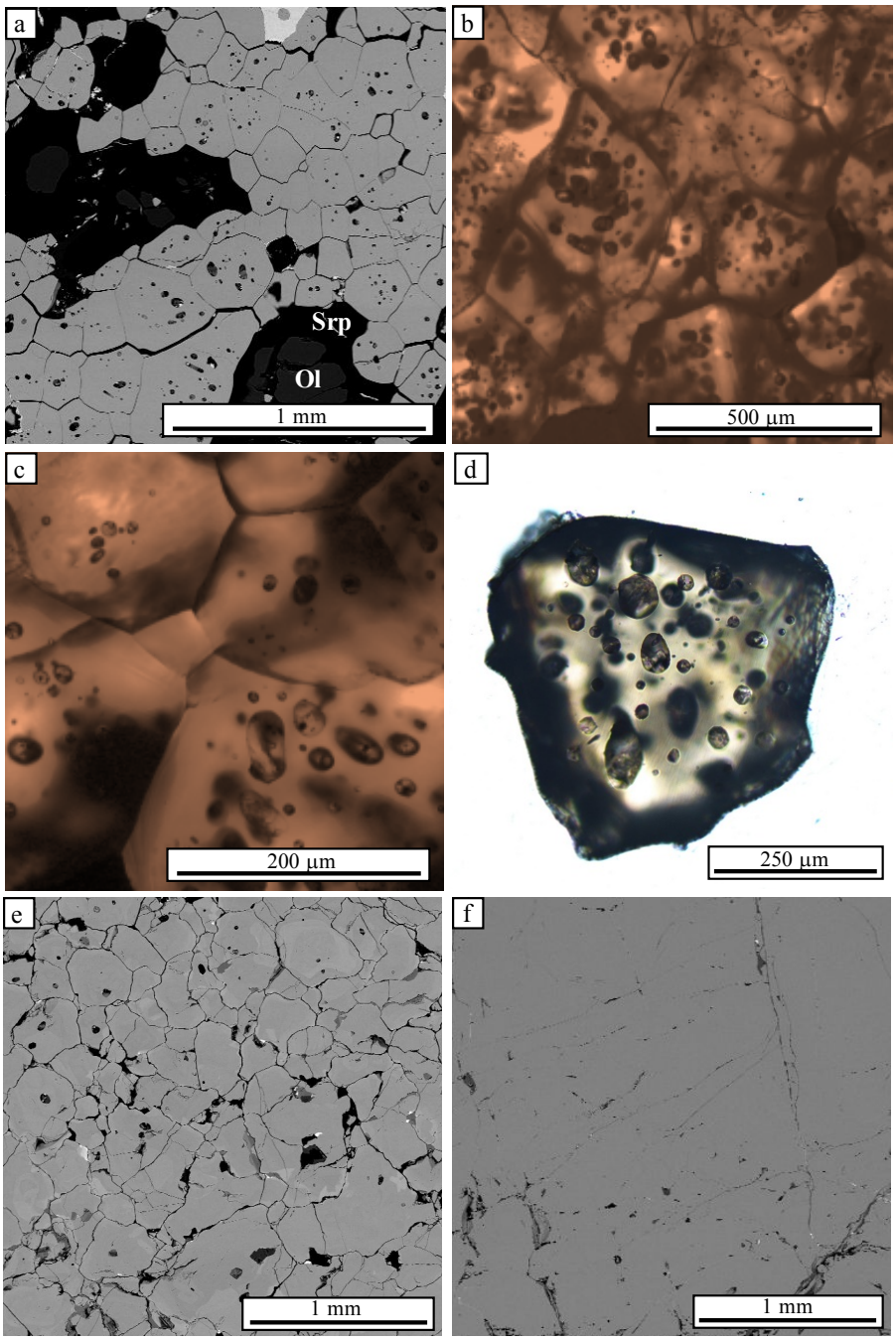

Figure 4. 2 Representative images of perovskite textures in backscattered electrons (a, e, f) and transmitted light (b-d) that show variations in inclusion abundance. Abundant multiphase inclusions in T1 perovskite from (a) olivinites and (b, c, d) clinopyroxenite; (e) less frequent multiphase inclusions in T2 perovskite from clinopyroxenite; (f) scarce multiphase inclusions in T3 perovskite from silicocarbonatite. Abbreviations: forsterite (Ol) and serpentine (Srp).

that could be present in the inclusions. Coarse-grained polishing paper was also avoided as the contrast in hardness between silicates, oxides and carbonates could result in the plucking of softer carbonates from the inclusions.

All instruments used for the examination of perovskite- and magnetite-hosted inclusions are located at the University of Tasmania, Australia. Samples were analysed with a Hitachi SU-70 field-emission scanning electron microscope (SEM) fitted with an Oxford AZtec Xmax80 energy-dispersive

X-ray spectrometer. High-resolution backscattered electron (BSE) images and energy-dispersive X-ray spectrometry (EDS) were used for element mapping and semi-quantitative analysis of inclusions and minerals.

Raman spectroscopy was applied to confirm the size, shape and composition of inclusions in T1 perovskite from a clinopyroxenite sample. Two perovskite-hosted inclusions were mapped with a Renishaw inVia Raman microscope equipped with a 532-nm laser operating at 225 μW. Individual spectra were acquired with 1s exposure and 10 accumulations, using a ×50 microscope objective and 1800 lines/mm diffraction grating to provide a spectral resolution of 1.75 cm^{-1}.

4.4.1. Composition of perovskite-hosted inclusions

Three methods were applied to measure the bulk composition of selected inclusions (>10 μm in size), with neighbouring inclusions analysed within the same zones of perovskite grains.

For method 1, EDS maps were collected from exposed inclusions to determine their overall bulk composition by combining analytical data from all mapped pixels in the inclusion. The outlines of the mapped areas were set to >1 μm from the boundary of the host mineral to minimise contributions to the analysis from electron excitation of the host mineral. The data were acquired with a focused beam at an accelerating voltage of 15 kV and a beam current of ~3 nA. The counting time was minimised to limit any compositional changes and volatile loss due to beam-induced damage. Inclusions with holes were avoided as much as possible in these analyses.

For method 2, the bulk composition of discrete inclusions was calculated using the compositions of their constituent minerals determined by EDS using the same operating conditions as above. To estimate relative contributions of each mineral, their area was measured in proportion to the area of the entire inclusion; it was assumed that these proportions are representative of the three-dimensional relations among the constituent minerals (Bussweiler et al. 2016; Hoshide and Obata 2012). Short counting times (10 seconds live time) and a scanned beam were employed to prevent excessive beam damage to carbonates and other easily volatilized phases. However, minor Na volatilization occurred during the analysis of Na-rich carbonates. Additionally, some inclusion-hosted minerals (e.g., åkermanite) are compositionally zoned, and thus minor discrepancies arise depending on the choice of EDS data for the calculation of bulk compositions in those cases. To minimize these uncertainties, the average composition of zoned minerals was used.

Both methods provide semi-quantitative results as the surface expression of individual inclusions is likely not representative of its three-dimensional anatomy, and the accuracy of analysis is limited by simultaneous electron excitation of multiple intimately intergrown phases, secondary X-ray fluorescence, and the use of bulk matrix-correction methods for heterogeneous mineral assemblages. Numerous inclusions were analysed by both methods to identify general trends in the dataset and the average bulk composition of inclusions in each rock type. To test the consistency of these results, both methods were employed for the same inclusions. Some inclusions gave dissimilar concentrations for

several elements, probably owing to errors in determining the relative contribution of each phase to the bulk composition in method 2. Therefore, method 1 was chosen as the primary approach to quantifying the bulk composition of inclusions in the present work.

LA-ICPMS was used to quantify the composition of entire inclusions by ablating them with a laser beam. This method limits any potential bias associated with the analysis of partially exposed inclusions (Halter et al. 2004; Pettke et al. 2004). A series of spot analyses were conducted on 10 inclusions located under the polished surface of perovskite. To ensure that the inclusions were ablated completely, the majority of analyses were done with a 29 μm laser beam, however some smaller inclusions (<15 μm) were ablated with a smaller spot size of 19 μm. Because the ablated volume must be larger than the inclusion, some of the host perovskite was included in the analysis. The known composition of the surrounding perovskite and the general absence of titanium in the inclusion compositions enabled the subtraction of the perovskite from the LA-ICPMS data. The resultant data are not quantified to obtain absolute abundances due to the absence of internal standards and therefore the data have been used for identifying trends in the element ratios of analysed inclusions.

4.4.2. Heating experiments

The mechanical and chemical stability of perovskite permits its rapid heating and cooling and prevents inclusions from decrepitating (Nielsen et al. 1997). These authors conducted their experiments at 1050-1100^{o}C and noted overheating, excessive reaction between the perovskite host and inclusions and incomplete melting, indicated by residual solid phases in the solidified melt. To reduce the risk of overheating, a maximum temperature of 1000^{o}C was chosen to observe the sequence of heat-induced phase transformations in inclusions. The relative opaqueness of the Afrikanda perovskite obstructed the visual control of phase transformations during heating. Consequently, bulk heating experiments were conducted in a custom-made vertical furnace without visual control. For this, a sample of clinopyroxenite was crushed to liberate perovskite grains with abundant inclusions. Grains ranging between 0.3 and 0.5 mm across were then wrapped in 0.5 mm thick platinum foil with a piece of graphite. Three different batches of perovskite grains were heated to 800 °C, 900 °C and 1000 °C, respectively, at 1 atmosphere for 10 minutes, then quenched in water. The grains were then mounted and polished using the technique described above.

4.5. Results

4.5.1. Perovskite-hosted polymineralic inclusions

Polymineralic inclusions are abundant in the cores of T1 perovskite from the olivinites and clinopyroxenites. In BSE images, some perovskite grains are crowded with inclusions, whereas other grains appear to lack them altogether (Fig. 4.2a). However, examination of these samples in a 130 μm-thick section in transmitted light shows that every grain contains tens to hundreds of inclusions (Figs.

4.2b, c). Our EDS data show that neighbouring inclusions rarely contain the same assemblage of minerals. Obviously, the orientation of an exposed polymineralic inclusion with respect to sample surface will affect the apparent abundance of its constituents, particularly when it comes to less-common minerals (Figs. 4.3b-e).

The inclusions vary from <5 μm to 100 μm in size. Small inclusions (<30 μm) are mostly globular, with more elongate and irregular shapes prevalent in larger inclusions. All inclusions are crystalline and contain anhydrous and hydrous silicate, carbonate, oxide, sulphide and phosphate minerals (Table 4.1). They also contain voids (up to 20% of the exposed surface) that may have contained soluble phases, fluids or gases lost at the sample-preparation stage.

4.5.1.1. Inclusions in olivinites

Inclusions in perovskite from the olivinite samples vary from <5 to 30 μm in diameter. Most inclusions are globular; however, large inclusions are elongate and irregular in shape. They contain three to ten minerals (Fig. 4.4), most common of which are (listed in order of decreasing abundance): phlogopite, pectolite, magnetite, åkermanite, nyerereite and cuspidine (Table 4.1, Fig. 4.4). Notably, cuspidine and rasvumite have not been previously reported from Afrikanda.

4.5.1.2. Inclusions in clinopyroxenites

Inclusions in large euhedral perovskite crystals from the silicocarbonatites are characteristically larger than those in the ultramafic rocks, and range from 10 to 100 μm in diameter. In addition, they are more elongate and irregular in shape than those from the olivinites or clinopyroxenites (Fig. 4.6). The inclusions commonly have two to three, but locally up to six, minerals exposed at the surface. The most

Anhydrous silicates	**Olvt**	**Cpxt**	**Sct**	**Hydrous silicates**	**Olvt**	**Cpxt**	**Sct**
Aegirine-augite $(Ca,Na)(Mg,Fe)Si_2O_6$	3	2	0	Clinochlore $Mg_5Al(AlSi_3O_{10})(OH)_8$	3	7	4
Åkermanite $(Ca_2MgSi_2O_7)$	16	5	0	Cuspidine $Ca_4Si_2O_7(F,OH)_2$	13	6	0
Andradite $Ca_3Fe^{3+}{}_2(SiO_4)_3$	2	1	0	Magnesiohastingsite $NaCa_2(Mg_4Fe^{3+})Si_6Al_2O_{22}(OH)_2$	2	1	0
Cancrinite $Na_6Ca_2(Al_6Si_6O_{24})(CO_3)_2$	13	20	0				
Forsterite Mg_2SiO_4	7	3	0	Pectolite $NaCa_2Si_3O_8(OH)$	18	19	15
Gittinsite $CaZrSi_2O_7$	1	1	0	Phlogopite $KMg_3(AlSi_3O_{10})(OH,F)_2$	26	27	16
Nepheline $Na_3K(AlSiO_4)_4$	7	2	13	**Sulphides**			
Sodalite $Na_8(Al_6Si_6O_{24})Cl_2$	12	7	5	Chalcopyrite $CuFeS_2$	2	1	0
Titanite $CaTiSiO_5$	2	19	19	Pyrrhotite $Fe_{1-x}S$	2	3	0
Wollastonite $CaSiO_3$	8	1	0	Rasvumite KFe_2S_3	3	1	0
Carbonates				**Phosphates**			
Calcite $CaCO_3$	8	7	12	Hydroxylapatite $Ca_5(PO_4)_3(OH)$	3	3	2
Burbankite $(Na,Ca)_3(Sr,Ba,REE)_3(CO_3)_5$	1	3	0	Fluorapatite $Ca_5(PO_4)_3F$	10	9	10
Nyerereite $Na_2Ca(CO_3)_2$	13	4	6	**Oxides**			
Shortite $Na_2Ca_2(CO_3)_3$	12	7	14	Magnetite $Fe^{2+}Fe^{3+}{}_2O_4$	16	8	8

Table 4. 1 Mineralogy of 50 perovskite-hosted polymineralic inclusions in the olivinites (Olvt), clinopyroxenites (Cpxt) and silicocarbonatites (Sct), listed alphabetically. The numbers indicate how many of the 50 inclusions host each mineral.

abundant phases are titanite, phlogopite, pectolite and shortite (Table 4.1, Fig. 4.6). No sulphides are observed in these inclusions. Some inclusions appear to be composed of calcite or titanite only; these may be either polymineralic inclusions with only one mineral exposed at the surface, or truly monomineralic.

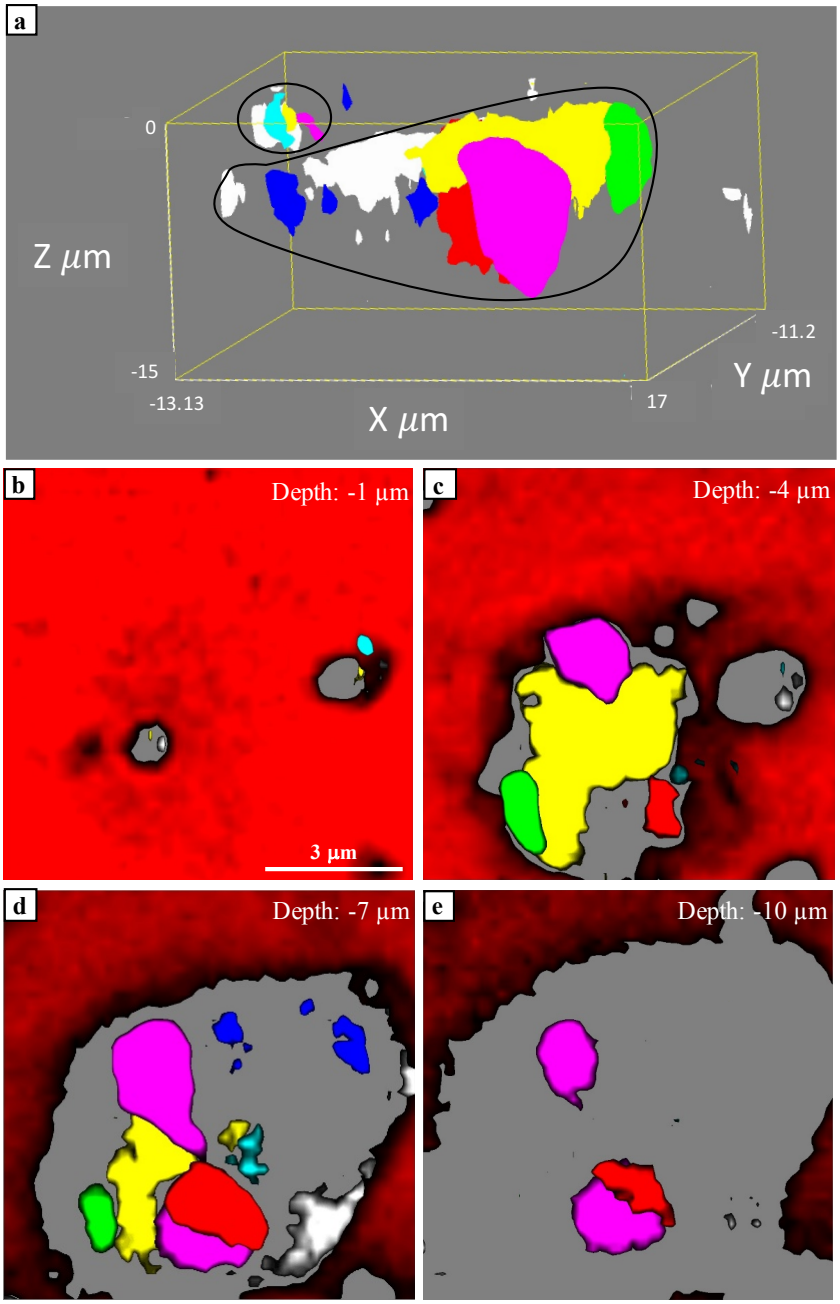

Figure 4. 3 Polymineralic inclusions in T1 perovskite from clinopyroxenite. (a) 3D Raman model; black rim indicates the size and location of inclusions. (b-e) Raman depth slices in the Z direction. Red shading is the host perovskite crystal, yellow – sodalite, pink – shortite, red – calcite, white – unidentified phase, light blue – magnetite, green – apatite, dark blue – diopside, grey – no spectral response.

4.5.1.3. Inclusions in silicocarbonatites

Inclusions in large euhedral perovskite crystals from the silicocarbonatites are characteristically larger than those in the ultramafic rocks, and range from 10 to 100 μm in diameter. In addition, they are more elongate and irregular in shape than those from the olivinites or clinopyroxenites (Fig. 4.6). The inclusions commonly have two to three, but locally up to six, minerals exposed at the surface. The most

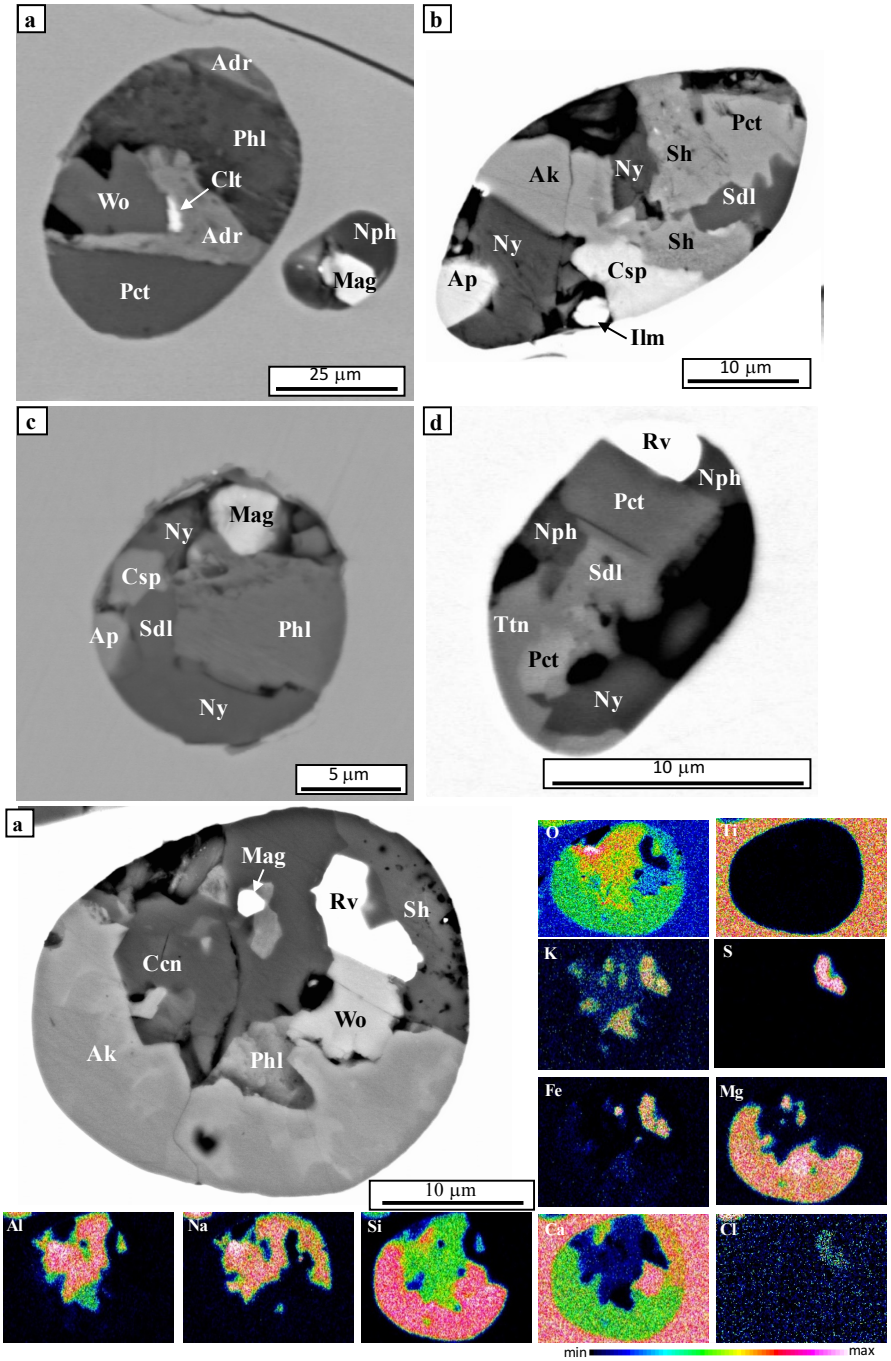

Figure 4. 4 Perovskite-hosted polymineralic inclusions in olivinites a-d BSE images e EDS elemental map showing the texture and mineralogy. Abbreviations: åkermanite (Ak), andradite (Adr), apatite (Ap), cancrinite (Ccn), celestine (Clt), cuspidine (Csp), Mg-rich ilmenite (Ilm), magnetite (Mag), nepheline (Nph), nyerereite (Ny), pectolite (Pct), phlogopite (Phl), rasvumite (Rv), shortite (Sh), sodalite (Sdl), titanite (Ttn), wollastonite (Wo).

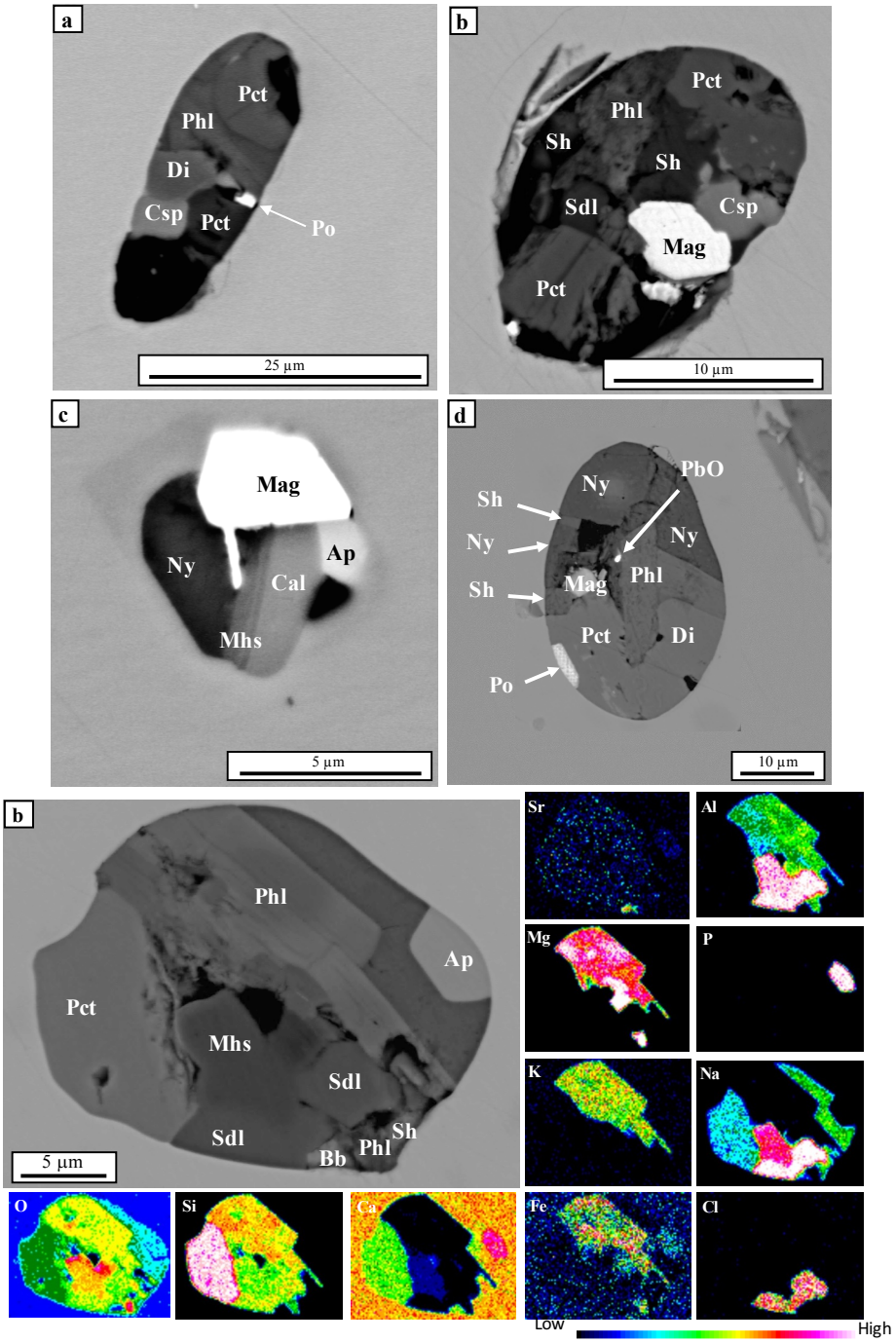

Figure 4. 5 Perovskite-hosted polymineralic inclusions in clinopyroxenites a-d BSE images e EDS elemental map showing the texture and mineralogy. Abbreviations: apatite (Ap), burbankite (Bb), calcite (Cal), cuspidine (Csp), lead-oxide (PbO), magnesiohastingsite (Mhs), magnesiohastingsite (Mhs), magnetite (Mag), nyerereite (Ny), pectolite (Pct), phlogopite (Phl), pyrrhotite (Po), shortite (Sh), sodalite (Sdl).

abundant phases are titanite, phlogopite, pectolite and shortite (Table 4.1, Fig. 4.6). No sulphides are observed in these inclusions. Some inclusions appear to be composed of calcite or titanite only; these

may be either polymineralic inclusions with only one mineral exposed at the surface, or truly monomineralic.

4.5.1.4. Mineral abundances and composition

A 3D model of two inclusions from the clinopyroxenite sample described above was created using Raman depth-profiling (Fig. 4.3a). The high refractive index, opacity of perovskite and limited Raman response prevented the identification of at least one mineral inside the largest inclusion. This phase produced no detectable Raman signature under the chosen measurement conditions, except for a significant reduction in the intensity of perovskite signal, and therefore could not be identified. Phase information is available only to a depth of ~10 μm, and the signal is lost for most minerals at ~8 μm (Fig. 4.3e).

The abundance of individual minerals varies appreciably with depth (Figs. 4.3b-e), and can be either over- or underestimated when a cross-section is analysed in polished samples. To improve the reliability of these data, the minerals in over 400 inclusions were analysed (200 in olivinites, 150 in clinopyroxenites and 50 in silicocarbonatites), and semi-quantitative bulk compositions were obtained

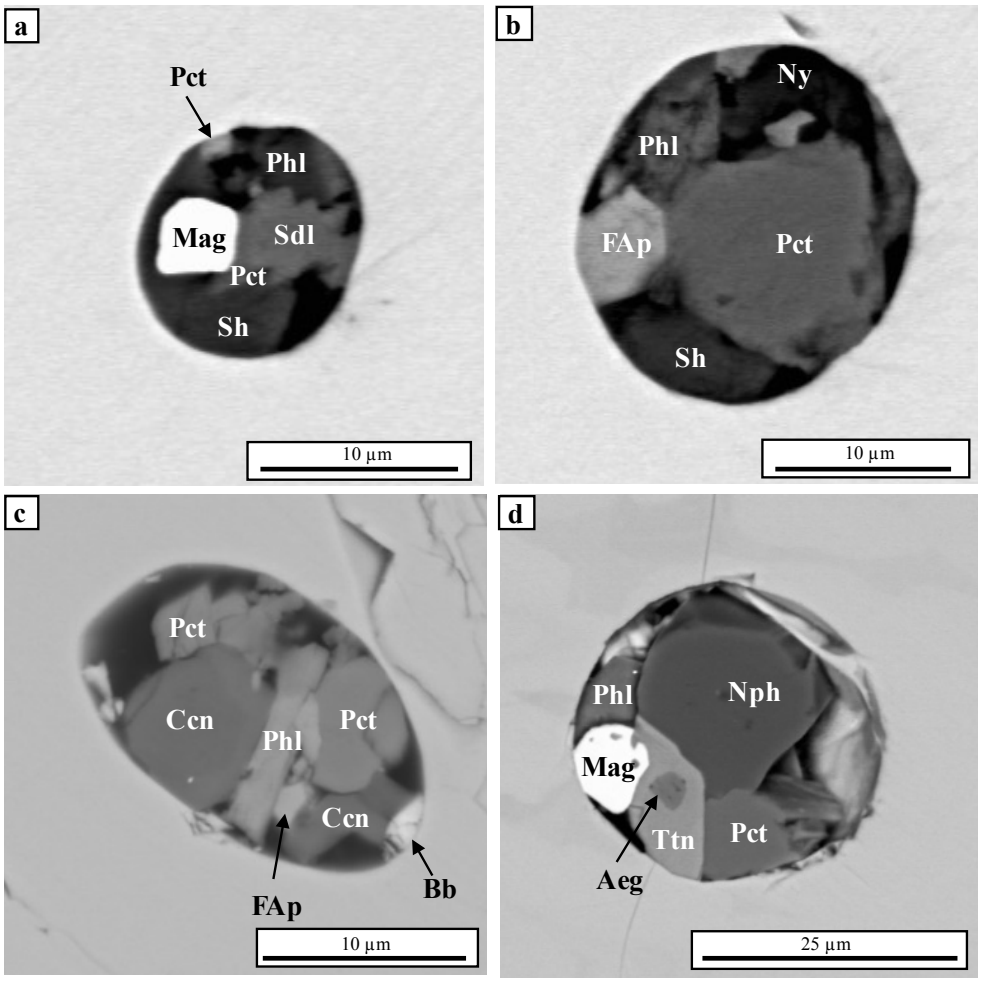

Figure 4. 6 BSE images of selected perovskite-hosted polymineralic inclusions in the silicocarbonatites. Abbreviations: aegirine-augite (Aeg), cancrinite (Ccn), fluorapatite (FAp), magnetite (Mag), nepheline (Nph), nyerereite (Ny), pectolite (Pct), phlogopite (Phl), shortite (Sh), sodalite (Sdl), titanite (Ttn).

using method 1 (Fig. 4.7a) for 184 inclusions (76 in olivinites, 74 in clinopyroxenites and 34 in silicocarbonatites).

Table 4.1 presents a list of the minerals observed in the analysed inclusions, along with the frequency each mineral is observed in 50 representative inclusions from each of the rock types. Minerals that were only observed once or twice (e.g., celestine shown in Fig. 4.4a), were left out of Table 4.1. Phlogopite is the only mineral that consistently shows a euhedral habit. Clinopyroxene, wollastonite, apatite and magnetite are euhedral in some inclusions, but more typically anhedral. All other minerals form irregular, anhedral grains. Compositions of the major constituent minerals are shown in Figure 4.7b (refer to Supplementary File 4A for details).

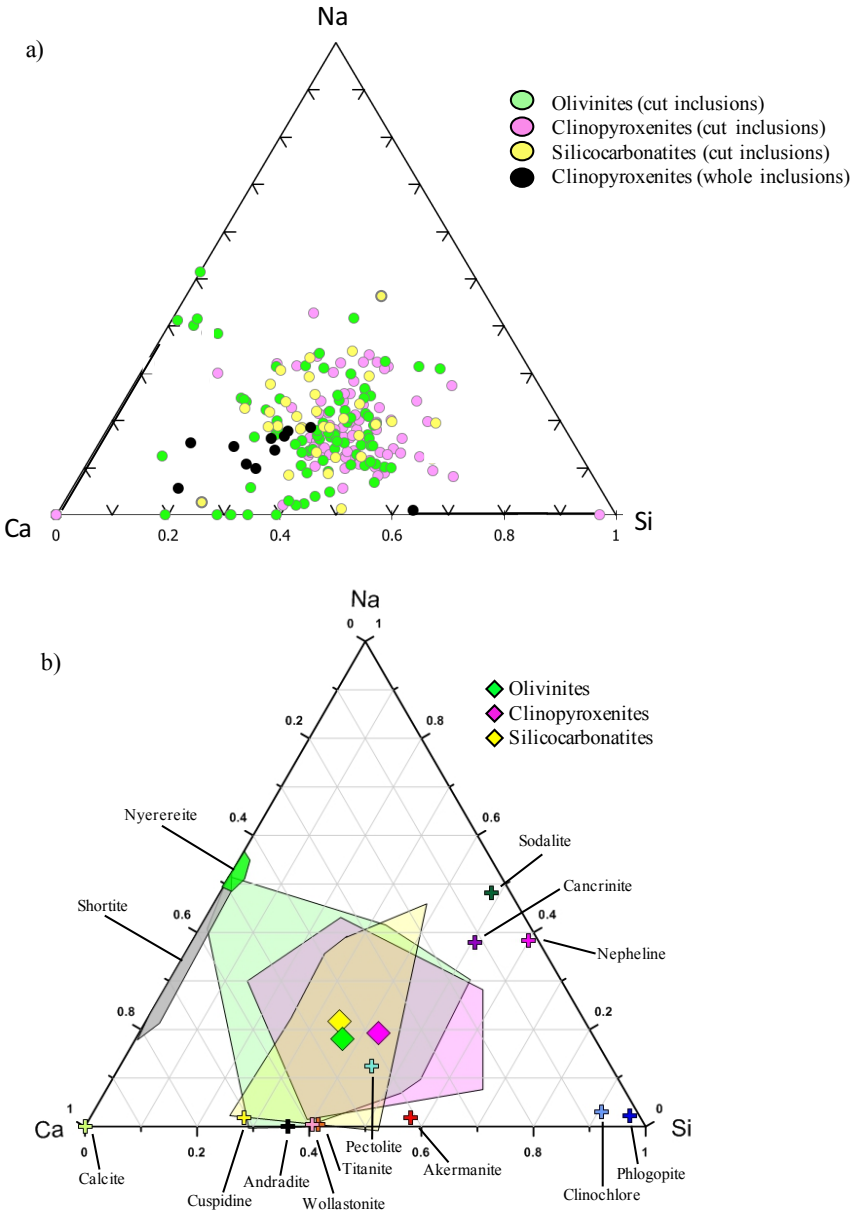

Figure 4. 7 Ternary diagrams showing compositional variations of perovskite-hosted polymineralic inclusions in olivinites, clinopyroxenites and silicocarbonatites, measured in weight percent (wt.%). (a) Bulk compositions of inclusions in the three rock types; (b) average mineral compositions, average bulk compositions and compositional fields for inclusions in each of the rock types.

Hydrous silicates are the most abundant minerals in the inclusions from all three rock types. The abundance of phlogopite, magnesiohastingsite and chlorite is similar in the samples from all three rock types (Table 4.1). Cuspidine and cancrinite are common in perovskite from the olivinites and clinopyroxenites, but were not observed in the silicocarbonatites. Phlogopite is the most abundant mineral and has variable composition (notably, its Mg# ranges from 35 to 100, and Na_2O may reach 6 wt.%). Chlorite is also variable in composition in the three rock types, but is identified as clinochlore (i.e., the Mg-dominant end-member) with Mg# ranging from 40 to 92 in all studied inclusions.

Anhydrous silicate minerals are most abundant in perovskite-hosted inclusions from the olivinites and decrease in abundance in the clinopyroxenites and silicocarbonatites. Among these minerals, the most abundant are clinopyroxene and cancrinite in the olivinites, titanite and cancrinite in the clinopyroxenites (observed in both T2 and T3 perovskite), and titanite and nepheline in the silicocarbonatites. Forsterite (Mg# = 56-88) is present in inclusions from the olivinites and clinopyroxenites. Nepheline is relatively common in perovskite from the silicocarbonatite, but not the other two rock types, and has a relatively constant composition (8 wt.% K_2O, 30 wt.% Al_2O_3, ≤2 wt.% FeO).

The abundance of carbonate minerals is similar in the olivinites and silicocarbonatites, and decreases in the clinopyroxenites. Nyerereite and shortite are the most abundant in perovskite from the olivinites. shortite and calcite occur with similar frequency in perovskite-hosted inclusions from the clinopyroxenites and silicocarbonatites. Calcite contains up to 2 wt.% Sr and shortite may have elevated K_2O contents (up to 5 wt.%), which explains some of the deviation away from the ideal composition in Figure 4.7a (the remainder is probably due to Na loss during EDS analysis).

The abundance of apatite is similar in inclusions from all three rock types. Both fluorapatite and hydroxylapatite were observed and fluorapatite contains up to 5 wt.% F and 2 wt.% Sr. Magnetite is the only prevalent oxide mineral present in the examined inclusions, with loparite [$(Na,Ce,Ca)(Ti,Nb)O_3$] observed in several of inclusions in the clinopyroxenites. Magnetite contains up to 2 wt.% MnO and differs significantly from the rock-forming magnetite in the three rock types, which invariably contains TiO_2, MgO and Al_2O_3 (from <2 to 13 wt.%).

4.5.1.5. Inclusions *after heating*

Heating of perovskite samples from clinopyroxenite to 800, 900 and 1000 °C shows that the polymineralic inclusions do not homogenise at these temperatures and that the mineralogy of neighbouring inclusions remains variable. Several factors may have contributed to the failure of the inclusions to homogenise: (1) different pressure and volatile regime at which inclusion entrapment occurred, relative to the ambient-pressure experiments in oxygen conducted in this study; (2) the inability of carbonate melts to quench to glass and (3) the entrapment of crystals within the inclusion when the inclusion initially formed. It is well-known that carbonate-silicate melt relations change appreciably with lithostatic pressure and $P(CO_2)$ (e.g., Brooker and Kjarsgaard 2011). The extent of

crustal unroofing at Afrikanda is estimated to have been as much as 8-11 km (Arzamastsev et al. 2000), i.e. it is feasible that perovskite crystallized at P = 2-3 kbar and encapsulated homogeneous material that does not form a single phase at ambient pressure. For a detailed study, we chose over 20 inclusions that remained uncompromised during the heating experiments at each temperature (i.e., did not fracture or leak). Our examination revealed the presence of bubble-free inclusions composed of a variety of minerals (Fig. 4.8).

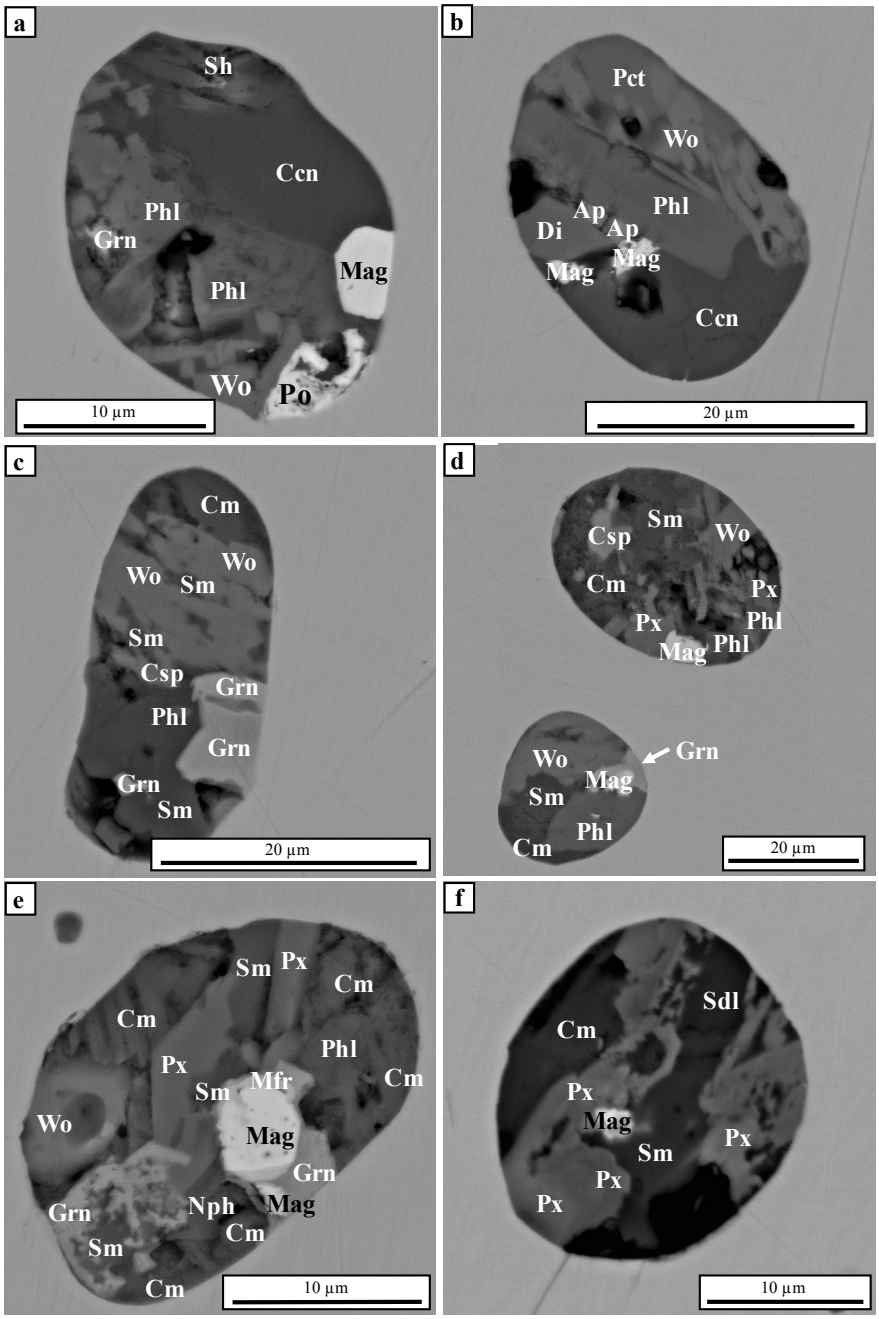

Figure 4. 8 BSE images showing the results of heating experiments at (a, b) 800 °C, (c, d) 900 °C and (e, f) 1000 °C. Abbreviations: cancrinite (Ccn), carbonate melt (Cm), cuspidine (Csp), diopside (Di), garnet (Grn), magnesioferrite (Mfr), magnetite (Mag), nepheline (Nph), pectolite (Pct), phlogopite (Phl), pyroxene (Px), pyrrhotite (Po), shortite (Sh), silicate melt (Sm), sodalite (Sdl), wollastonite (Wo).

At 800 °C, the inclusions contain alkali carbonates, nyerereite and shortite, as tabular crystals that are separated by a silicate melt. Silicate minerals, apatite and magnetite have compositions similar to those in the unheated inclusions. At 900 °C (Figs. 4.8c, d), clinopyroxene, wollastonite, apatite, calcite and cuspidine have similar compositions to the unheated precursors. The compositions of other phases, like cancrinite, clinochlore, nepheline, pectolite and sodalite differ slightly between the two types of inclusions. Additionally, silicate and carbonate melt phases are observed. At 1000 °C (Figs. 4.8e, f), the major constituent phases are wollastonite and clinopyroxene, along with silicate (nephelinitic) and carbonate melts. Other daughter minerals, including cancrinite, clinochlore, sodalite, schorlomite, nepheline and halite, were identified and found to have variable compositions.

Shortite and nyerereite were identified in the inclusions heated to 800 °C, but at higher temperatures, these phases disappear to yield a new carbonate phase. At 1000 °C, the latter is composed of 27 wt.% CaO, 19 wt.% Na_2O, 6 wt.% K_2O, 4 wt.% SiO_2, 1 wt.% F and up to 2 wt.% SO_3 and P_2O_5. The composition of the silicate melt becomes progressively potassic with temperature, as the Na_2O, CaO and Cl contents decrease (from 20 to 14, 7 to 3 and 0.5 to below detection, respectively), and the K_2O, FeO and MgO contents increase (from 1 to 8, 0 to 4 and 0.3 to 1 wt.%, respectively). Aluminium and Si values are consistent and show relatively little variation with temperature (14-16 and 12-20 wt.%, respectively).

Minerals such as halite, magnesioferrite and Ti-rich andradite are observed in the heated inclusions, but not in the unheated inclusions. Heated inclusions commonly host two magnetite or apatite crystals, rather than a single crystal, as observed in the unheated material (Fig. 4.8b). Garnet, formed at 900 °C and 1000 °C, has high TiO_2 contents (up to 9 wt.%) and is commonly adjacent to magnetite (Figs. 4.8d, e). Magnetite is the dominant oxide mineral at 800 °C, whereas magnesioferrite becomes more abundant at 900 °C and 1000 °C. In addition to high MgO (up to 20 wt.%), this mineral is enriched in Mn and, locally, CuO (up to 4 wt.% for both). aegirine-augite and wollastonite are more common in the heated inclusions than in the unheated samples (Table 4.1).

4.5.1.6. Bulk compositions

The bulk compositions of inclusions in each rock type are presented in Figure 4.7. The observed scatter clearly arises from variations in the abundance and composition of individual constituent minerals (Table 4.1; Fig. 4.7a). Average bulk compositions of inclusions exposed at the surface from each rock type have been calculated and are highlighted in Figure 4.7b. These compositions are comparable to one another for several elements, despite the observed mineralogical variations (Table 4.1; 8-9 wt.% Na_2O, 6-7 wt.% FeO, 6-8 wt.% Al_2O_3 and 1-2 wt.% K_2O). Inclusions in the olivinites have the highest CaO (24 wt.%) and lowest K_2O (2 wt.%) contents, whereas those in the clinopyroxenites have the highest MgO and SiO_2 (7 and 32 wt.%, respectively) and lowest TiO_2 (2 wt.%) contents. The inclusions from the silicocarbonatites are characterized by the highest K_2O and TiO_2 (2 and 8 wt.%, respectively) and the lowest levels of MgO and SiO_2 (3 and 28 wt.%, respectively).

The complete dataset shows an overall trend of decreasing K, Al, Mg and Fe with increasing Ca content from the olivinites to the clinopyroxenites to the silicocarbonatites. Inclusions in the olivinites and clinopyroxenites show an increase in Na as Si decreases, and those in the clinopyroxenites also show a negative correlation between Na and K.

4.5.2. Magnetite-hosted polymineralic inclusions

Magnetite-hosted polymineralic inclusions are observed only in the silicocarbonatites. They are uncommon, randomly distributed throughout the grains, and are similar in abundance to the perovskite-hosted inclusions in the silicocarbonatites. Their morphology is controlled by the isometric symmetry of the host crystal (i.e., polygonal), although some have a globular appearance (Fig. 4.9). The inclusions range from 10 to 80 μm in size and are composed of 2 to 6 minerals each, including hydrous and anhydrous silicates, carbonates, oxides, sulphides, halides and sulphates (Fig. 4.9). Some of the minerals identified in these inclusions (specifically, the Na-rich phases like sodalite, northupite, neighborite a

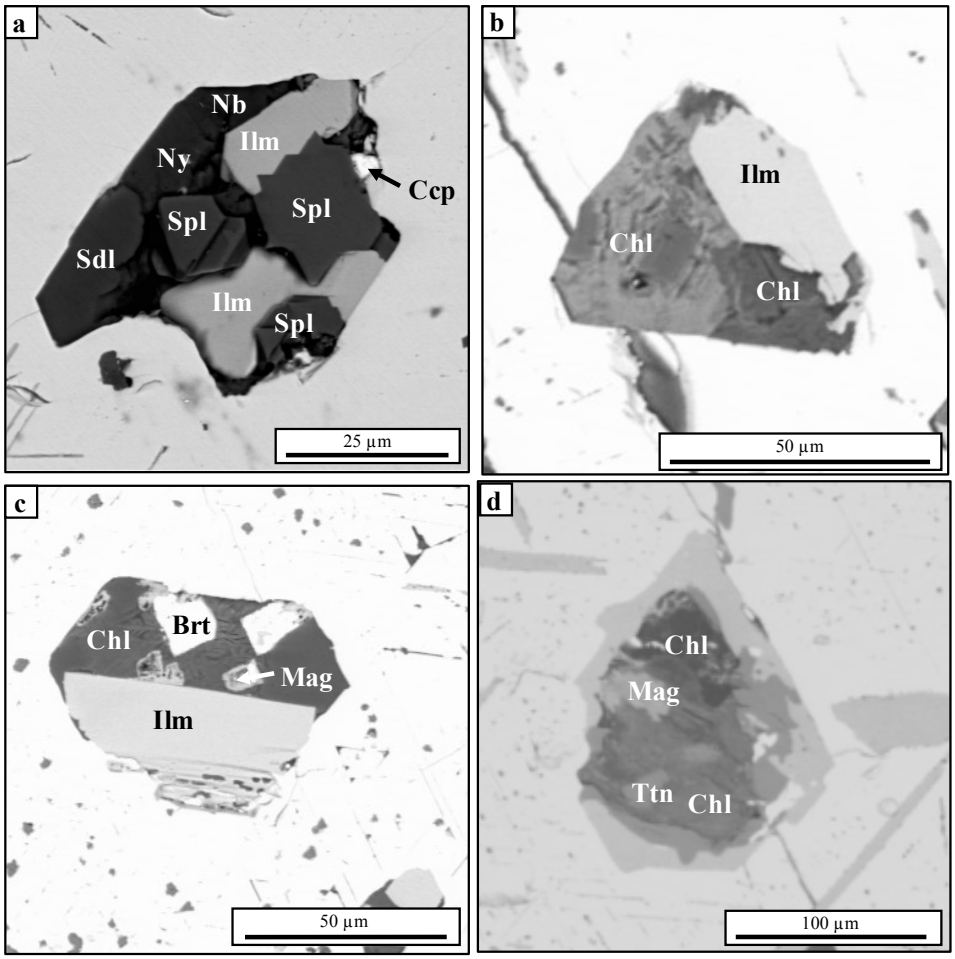

Figure 4. 9 BSE images of selected magnetite-hosted polymineralic inclusions in the silicocarbonatites. Abbreviations: barite (Brt), chalcopyrite (Ccp), chlorite (Chl), ilmenite (Ilm), magnetite (Mag), neighborite (Nb), nyerereite (Ny), sodalite (Sdl), spinel (Spl) and titanite (Ttn).

Oxides		**Silicates**	
Freudenbergite $Na_2Fe^{3+}{}_2Ti_6O_{16}$	3	Na-amphibole	3
Ilmenite $FeTiO_3$	7	Phlogopite $KMg_3(AlSi_3O_{10})(F,OH)_2$	4
Magnetite $Fe^{2+}Fe^{3+}{}_2O_4$	2	Clinochlore $Mg_5Al(AlSi_3)O_{10}(OH)_8$	3
Spinel $MgAl_2O_4$	13	Sodalite $Na_8(Al_6Si_6O_{24})Cl_2$	2
Zirconolite $(Ca,REE)Zr(Ti,Nb,Fe)_2O_7$	1	**Sulphates**	
Carbonates		Barite $BaSO_4$	1
Calcite $CaCO_3$	2	K-Fe-sulphate	1
Quinitinite $Mg_4Al_2(OH)_{12}CO_3*4(H_2O)$	1	**Sulfides**	
Na-Fe-carbonate	2	Chalcopyrite $CuFeS_2$	1
Northupite $Na_3Mg(CO_3)_2Cl$	1	Sphalerite $(Zn,Fe)S$	1
Nyerereite $Na_2Ca(CO_3)_2$	2	**Fluorides**	
Shortite $Na_2Ca_2(CO_3)_3$	1	Neighborite $NaMgF_3$	1

Table 4. 2 Mineralogy of 20 magnetite-hosted polymineralic inclusions in the silicocarbonatites, listed alphabetically. The numbers indicate how many of the 20 inclusions host each mineral.

4.6. Discussion

4.6.1. General comments

The examination of perovskite from the olivinites, clinopyroxenites and silicocarbonatites, and magnetite from the latter rock type, revealed the presence of peculiar polymineralic inclusions that differ in abundance and composition. Here, we focus on determining the origin of these inclusions to better understand the development of perovskite accumulations at Afrikanda and their relevance to similar monomineralic units in other oxide (e.g., chromite and magnetite) deposits around the world.

Polymineralic silicate inclusions are a notable feature in perovskite in ultramafic alkaline complexes (Kogarko et al. 1991; Nielsen et al. 1997; Panina 2005; Veksler et al. 1998), chromite in layered intrusions (Christiansen 1985; Spandler et al. 2005; Vukmanovic et al. 2013), anorthosite and ophiolite complexes (Ghisler 1976; Lorand and Ceuleneer 1989; Melcher et al. 1997; Prichard et al. 2018), and magnetite in carbonatite complexes (Afanasyev 2011; Chen et al. 2013; Kukharenko et al. 1965). In many of these settings, the oxide minerals are commonly identified as a cumulate magmatic phase, and the inclusions are interpreted as primary melt inclusions and consequently used to resolve the composition of their parental melts (Lorand and Ceuleneer 1989; Prichard et al. 2018; Rollinson et al. 2018; Spandler et al. 2005). At Afrikanda, the polymineralic inclusions in perovskite across all three rock types, and inclusions in magnetite in the silicocarbonatites, are identified as primary based on their randomly clustered distribution and the absence of secondary features (e.g., healed fractures: Figs. 4.2a-d). Therefore, we must determine whether these inclusions are primary melt inclusions or the consequence of post-magmatic re-equilibration that was proposed by Potter et al. (2018).

Melt inclusions are defined as small droplets of melt trapped in a mineral during its growth and subsequently re-equilibrated with the host, i.e. their bulk chemical composition can be used as a proxy for that of the parental melt (Kamenetsky and Kamenetsky 2010; Danyushevsky et al. 2002; Roedder 1984; Sobolev 1996; Sobolev and Kostyuk 1975). Therefore, true melt inclusions must meet specific petrological and mineralogical criteria. Firstly, the inclusion must be composed of a combination of entrapped melt (i.e., glass or devitrified glass in silicate systems and quench-textured carbonate aggregates in carbonatites) and products of its crystallisation and degassing, such as daughter crystals. Secondly, at specific temperatures and pressures, the inclusion contents can be homogenised to yield a single phase through the melting of every daughter phase and dissolution of a gas or fluid (Frezzotti 2001). Thirdly, melt inclusions in the same zone of the host mineral are expected to have the same composition. Lastly, melt inclusion compositions should correlate with the composition of their host mineral, thus reflecting melt-crystal equilibrium. The perovskite- and magnetite-hosted polymineralic inclusions studied in the present work do not meet these criteria, which raises questions about their validity as true melt inclusions. Below, we discuss the observed compositional and mineralogical features and attempt to decipher the origin of the polymineralic inclusions in the perovskite.

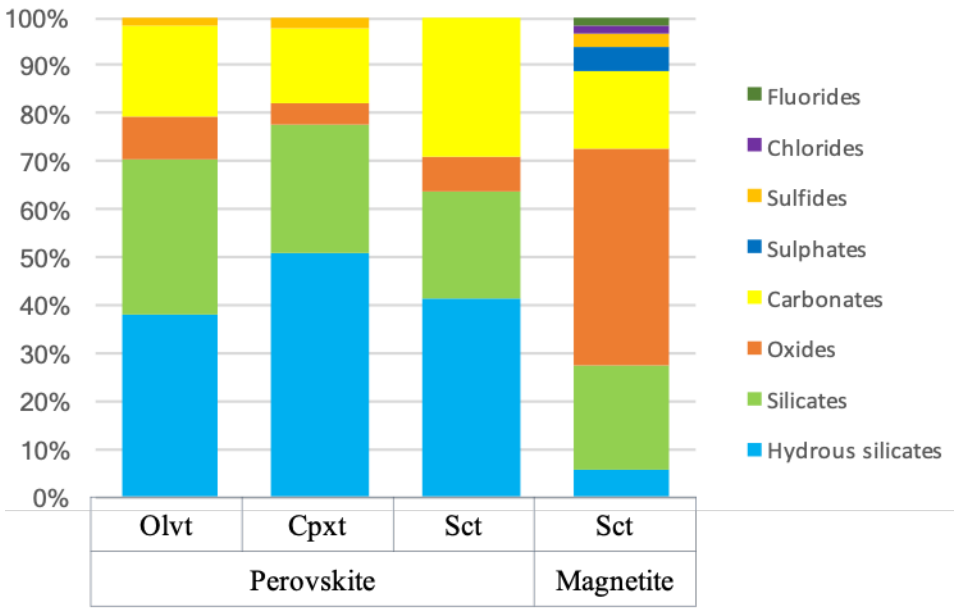

Figure 4. 10 Summary of main mineral phases observed in the perovskite and magnetite inclusions hosted in the three rock types.

4.6.2. Composition of polymineralic inclusions

The polymineralic inclusions are composed of a variety of phases, including silicates, carbonates, sulphides, phosphates and oxides (Fig. 4.10; Table 4.1). phases that are common in bona fide silicate melt inclusions, such as silicate glass, were not recorded in the present work. The dominant constituent minerals and the frequency of their occurrence can provide an insight into the composition of the surrounding media during their entrapment. Phlogopite is the most common constituent in the inclusions, closely followed by pectolite and one of the carbonate phases. The decreasing abundance of

silicates and increasing abundance of carbonates in the perovskite-hosted inclusions in olivinites and clinopyroxenites compared to the silicocarbonatites supports the transition from silicate- to carbonate-dominated compositions.

Perovskite-hosted inclusions in the olivinites in contrast to the clinopyroxenites and silicocarbonatites have a higher abundance of the Na-rich carbonate (nyerereite) than Ca-rich carbonates (calcite and shortite), whereas calcite and shortite are more abundant than nyerereite in the clinopyroxenites and silicocarbonatites (Fig. 4.10, Table 4.1). This chemical trend represents the transition from Na-rich to Ca-rich compositions.

Across the three rock types, several rare minerals and unusual mineral assemblages were identified in the inclusions. First, hydrous silicates like clinochlore and pectolite, whose stability is limited to ~800^{o}C are not expected to occur in unaltered melt inclusions (McOnie et al. 1975; Yagi et al. 1968). Titanite at Afrikanda is an abundant hydrothermal phase (Chakhmouradian 2004; Chakhmouradian and Zaitsev 2004), but has not been observed in any of the primary parageneses. Minerals, such as rasvumite and gittinsite, have not been previously documented as liquidus minerals in any magmatic environment. Other minerals, such as wollastonite and cancrinite, occur in both magmatic and metasomatic environments, but are overall more common in the latter (e.g., Dawson 1998; Martins et al. 2017; Pekov et al. 2011; Veksler et al. 1998). At Afrikanda, both these minerals are abundant inclusion constituents in the olivinites and clinopyroxenites (Figs. 4.4, 4.5, 4.6). Many of the other minerals listed in Table 4.1 (e.g., åkermanite, andradite, cuspidine, forsterite, magnesiohastingsite, titanite, magnetite and apatite) are not restricted to magmatic environments and are common in contact-metamorphic rocks as well (Aleksandrov and Troneva 2007; Beard and Drake 2007; Currie et al. 1992; Meinert 1992). Thus, the investigated inclusions appear to contain minerals that can be regarded as typically magmatic (e.g., nyerereite) with those that are not paragenetically constrained or are expected to occur in metamorphic or hydrothermal environments (e.g., chlorite and pectolite). Because the inclusions are encapsulated and protected by the host crystal, their post-entrapment transformation should have been independent of the physico-chemical changes affecting the host (Ferrero and Angel 2018). This "paragenetic isolation" can favour the formation and preservation of phases that differ from those in the surrounding rock. However, it does not explain how unquestionably hydrothermal phases, like chlorite and pectolite, could develop in a supposedly isolated micro-environment.

The majority of minerals identified in the present work have been previously reported from the Afrikanda rocks (Chakhmouradian and Zaitsev 1999, 2002, 2004; Zaitsev and Chakhmouradian 2002; Kukharenko et al. 1965). Some of these minerals (forsterite, åkermanite, nepheline, magnesiohastingsite, calcite, magnetite) are the principal primary phases in the igneous rocks, whereas the others are either characteristic products of their alteration (cancrinite, sodalite, wollastonite, pectolite, titanite, gittinsite and clinochlore), or have been reported exclusively in primary inclusions from the silicocarbonatites (Na-rich carbonates) (Chakhmouradian and Zaitsev 2004). Phlogopite is particularly common in the contact zone between the ultramafic and carbonatitic rocks and cross-cutting

alkaline-silicate veins, comprising predominantly altered nepheline, diopside and magnetite. Phlogopite appears to have formed metasomatically at the expense of primary ferromagnesian silicates and was subsequently replaced by clinochlore. Notably, however, previous workers identified minerals that are not particularly uncommon or exotic, which were not found in any of the inclusions; most notable examples include baddeleyite, calzirtite, zircon (primary constituents in the silicocarbonatites: Chakhmouradian and Zaitsev 1999, 2002), loparite and hydrogarnets (common late-stage phases across the different rock types (Kukharenko et al. 1965; Chakhmouradian et al. 2008; Potter et al. 2018). On the other hand, the Ca -silicate mineral cuspidine, which is common in perovskite-hosted inclusions from the ultramafic rocks (Table 4.1), has not been known from Afrikanda prior to this work.

4.6.3. Bulk composition of inclusions

Neighbouring inclusions that were analysed at the surface display significant chemical variability in their bulk composition (Fig. 4.7a), as can be expected from the observed mineralogical diversity (Table 4.1). Unexpectedly however, the average bulk compositions, calculated from their constituent phases (diamonds in Fig. 4.7b) are similar among the three rock types. The chemical variability in the bulk compositions of whole inclusions measured across perovskite grains confirms that neighbouring inclusions in the same perovskite grain are chemically diverse, as suggested by the chemical variability in the cut inclusions (Fig. 4.7a). The variability in the bulk compositions most likely results from the heterogeneous nature of the trapped perovskite-hosted inclusions and indicates they do not fit the definition of melt inclusions.

4.6.4. Transformations in inclusions during heating

Heating of perovskite-hosted inclusions to 800, 900 and 1000 °C failed to produce a homogeneous melt (Figs. 4.8e, f). Instead, we observed the preservation, melting and chemical alteration of the encapsulated minerals, along with the formation of new phases. These newly formed minerals (e.g., magnesioferrite, halite and Ti-rich andradite) and compositional changes in some of the minerals during heating imply chemical reactions among the precursor phases. These reactions were undoubtedly facilitated by the breakdown of hydrous silicates unstable above 800^{o}C (clinochlore and pectolite). Some of the reacting phases melted at a certain temperature to form carbonate and silicate liquids. However, in a bona fide melt inclusion these daughter phases should have melted without changing their composition or reacting to form new phases. The presence of crystals of apatite, clinopyroxene and garnet at 1000°C indicates that inclusions were composed of a mixture of co-trapped minerals and therefore are not typical melt inclusions (Figs. 4.8e, f).

The abundance of wollastonite is significantly higher in the heated inclusions than in their precursors. Reaction between Ca-silicate and carbonate phases during heating may have facilitated the formation of additional wollastonite (Figs. 4.8c-f), in a manner similar to wollastonite crystallization in skarns (Haldar 2013). Wollastonite is also common as kernels and a matrix mineral in silicate spheroids

in carbonatitic lava at Oldoinyo Lengai (Church and Jones 1995; Dawson et al. 1996; Potter et al. 2017) and could be the product of a similar reaction triggered by the interaction of silicate and carbonate melts in the magma chamber (Sharygin et al. 2012).

4.6.5. Differences and similarities between perovskite- and magnetite-hosted inclusions

Polymineralic inclusions in magnetite are only observed in the silicocarbonatites (Fig. 3.1). The reason for the abundance of inclusions in T1 perovskite in the olivinites and clinopyroxenites, and the absence of such inclusions from the magnetite and associated silicate minerals is unknown. Compared to the polymineralic inclusions in perovskite, the magnetite-hosted inclusions contain relatively abundant barite and freudenbergite, as well as less common, but identified in 10% of inclusions neighborite, northupite, halite, zirconolite and an unidentified K-Fe sulphate. The mineralogical differences between the perovskite- and magnetite-hosted inclusions (Tables 4.1, 4.2) suggests there is no close genetic links between the two types of inclusions. These differences further support the interpretation that the inclusions documented in the present study are not typical melt inclusions and therefore cannot be considered representative of the composition of parental melts. Even if the two minerals crystallised at different stages in the evolutionary history of the silicocarbonatites, as suggested by Chakhmouradian and Zaitsev (2004), the composition of melt inclusions in perovskite and magnetite would be expected to follow some coherent trend recording chemical changes in the evolving magma, which is not observed.

4.6.6. Abundance and Distribution of polymineralic inclusions

4.6.6.1 T1 perovskite

Randomly distributed inclusions are concentrated primarily in the cores of euhedral T1 perovskite in the olivinites and clinopyroxenites, whereas the rims are typically devoid of inclusions. This peculiar distribution pattern could be the result of magmatic or metamorphic processes. If the perovskite host represents an unmodified magmatic phase, then inclusions could have been entrapped during the initial stage of its crystallisation. The observed drop in inclusion abundance from core to rim could be due to a change in physico-chemical conditions or in perovskite growth rate (Roedder 1984). Slower growth rates would allow more time for local mass transfer and adjustment of grain boundaries, leading to fewer inclusions. Because inclusions' density does not correlate with compositional zoning, we can rule out changes in the physico-chemical conditions of the system. The relative scarcity of polymineralic inclusions in the rim could potentially result from a drop in the perovskite growth rate. Alternatively, the inclusions in T1 perovskite could have developed during its postmagmatic textural re-equilibration, involving an increase in grain size (Potter et al. 2018). This process has previously been suggested as a mechanism of inclusion entrapment in chromitites (Christiansen 1986; Hulbert and Von Gruenewaldt 1985; Lorand and Cottin 1987). During this process, any intergranular material would be entrapped in recrystallizing perovskite as inclusions.

4.6.6.2 T2 and T3 perovskite

The T1 perovskite in the olivinites and clinopyroxenites host abundant inclusions (Figs. 4.2a-d), whereas T2 and T3 crystals in the clinopyroxenites and silicocarbonatites contain occasional inclusions that are randomly distributed throughout the grains (Figs. 4.2e, f). Similar textural features are observed in primary oxide minerals at several other ore deposits: e.g., the Oman ophiolite, Fiskenaesset in Greenland and Bushveld in South Africa (Christiansen 1985; Ghisler 1976; Rollinson et al. 2018; Tanner et al. 2018; Vukmanovic et al. 2013; Yudovskaya and Kinnaird 2010). In these deposits, oxide minerals form layers composed of chains of euhedral crystals with plenty of inclusions, similar to T1 perovskite, and larger anhedral and massive grains with few inclusions, i.e. analogous to T2 perovskite in the clinopyroxenites. The transition from inclusion-rich euhedral oxide grains to inclusion-poor anhedral oxide grains is believed to be associated with non-magmatic processes, such as recrystallization, high-temperature deformation, post-cumulus growth and contact metamorphism (Butcher and Merkle 1987; Christiansen 1985; 1986; Ghisler 1976).

Potter et al. (2018) presents evidence for the recrystallization and sintering of perovskite in the ultramafic rocks at Afrikanda, leading to the transformation of the early-formed euhedral T1 crystals into coarse-grained aggregates of T2 and T3 perovskite. The grain coarsening triggered the removal of inclusions as adjacent crystals adopted similar crystallographic orientations, grain boundaries moved, and similarly oriented grains coalesced into one larger crystal (Jones et al. 1979; Li 1962; Rios et al. 2005). The result is an aggregate of grains with different orientations developing the external appearance of a single crystal (Potter et al. 2018).

4.6.7. Origin of polymineralic inclusions

The unusual assemblage of minerals in the polymineralic inclusions, and the observation that neighbouring inclusions have different modal and bulk compositions raises several questions about their formation. The most critical one is, how and when during the evolution of the complex did they form? Perovskite accumulations are rare (Armbrustmacher 1981; Brod 1999; Herz 1976), so studies on perovskite-hosted inclusions have been limited to accessory phases in kimberlites and various alkaline complexes (Campbell et al. 1997; Guzmics et al. 2012; Kogarko et al. 1995; Nielsen 1980; Panina 2005). Magmatic processes are favoured for the formation of perovskite-hosted inclusions in alkaline-ultramafic complexes, such as Gardiner in Greenland and Guli and Krestovsky in Siberia (Kogarko et al. 1991; Nielsen et al. 1997; Panina 2005; Veksler et al. 1998). Previously, inclusions hosted by perovskiteat Afrikanda were explained as crystallised silicate melts (Chakhmouradian and Zaitsev 2004). This interpretation should now be tested against alternative models on the basis of the newly acquired petrographic and mineralogical data.

4.6.7.1. Do Afrikanda inclusions represent trapped melts?

The inclusions exhibit several petrographic characteristics common to melt inclusions, such as negative crystal shapes imposed by the perovskite host (Figs. 4.4, 4.5, 4.6), well-developed crystals (Figs. 4.4e, 4.5e), random distribution of inclusions (Fig. 4.2d) and the lack of an obvious relationship with secondary textural features, such as fractures (Figs. 4.4, 4.5, 4.6). The ability of magmatic minerals to trap melt inclusions is dependent on several factors, including the growth rate of their host mineral, the abundance and composition of the melt surrounding the grains, and the type of chemical reactions occurring at the edge of the growing crystals (Roedder 1984). Primary melt inclusions in plutonic rocks are challenging to interpret as they do not "quench" to glass and characteristically form polymineralic assemblages.

A potential explanation for the formation of magmatic T1 perovskite with a diverse assemblage of daughter phases in neighbouring inclusions is that the magma was highly heterogeneous in terms of melt, crystal and fluid abundances. Thus, the compositional variability in the surrounding media during perovskite growth could produce variability across a population of closely spaced inclusions (Kogarko et al. 1991; Nielsen et al. 1997; Panina 2005; Veksler et al. 1998). Then, once the melt was trapped, individual inclusions represented isolated closed systems, and their evolution followed different crystallisation paths, producing different mineral assemblages (e.g., Panina 2005). However, the following features do not support the identification of these inclusions as crystallised droplets of primary melts. Firstly, perovskite is the only mineral with abundant inclusions. The associated oxide

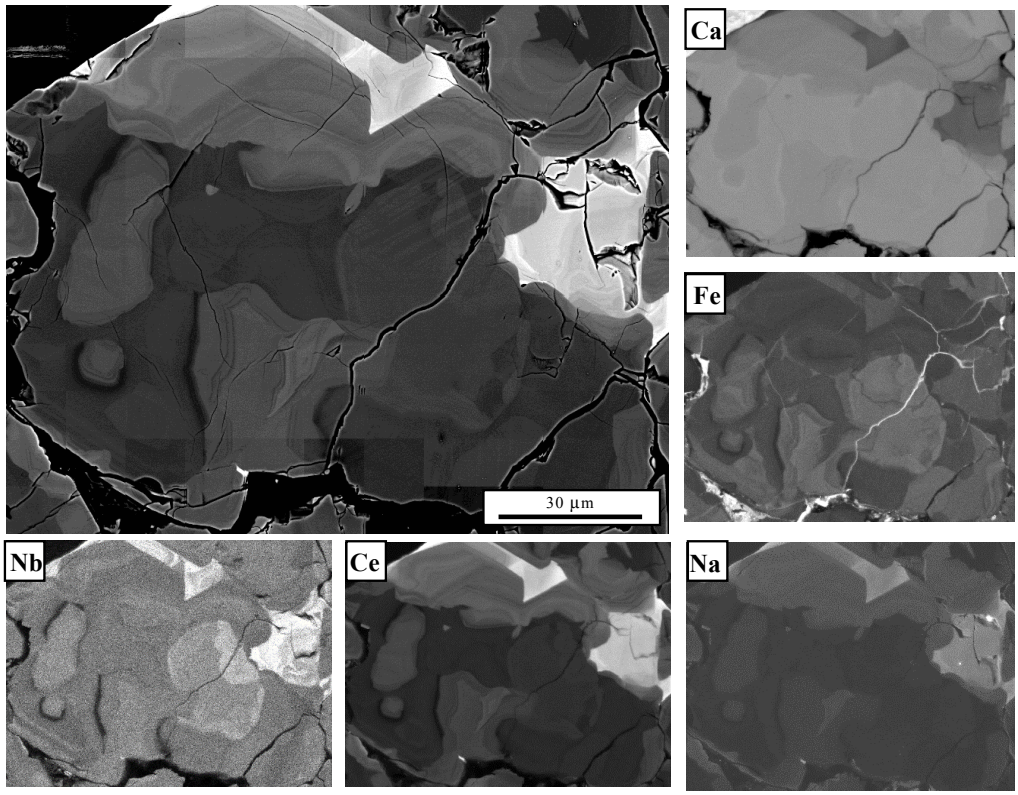

Figure 4. 11 BSE image of T2 perovskite grain and EDS elemental maps showing the complex zonation patterns within and between individual grains.

and silicate minerals, including those that compose the bulk of the host rocks, are typically devoid of inclusions (Potter et al. 2018). Secondly, many perovskite-hosted phases across all three rock types are clearly of non-magmatic origin and may require an aqueous fluid for their formation (Table 4.1). Thirdly, the bulk compositions of neighbouring inclusions vary significantly (Fig. 4.4a). Moreover, perovskite and magnetite in the silicocarbonatites contain very different inclusion assemblages (Tables 4.1, 4.2), whereas melt inclusions in associated minerals that crystallised from the same melt would be expected to have similar compositions or follow a distinguishable trend. Even if the inclusions were derived from a heterogeneous magmatic system, the co-existing minerals should be in equilibrium.

4.6.7.2. Can Afrikanda inclusions have a non-magmatic origin?

As a magmatic model cannot explain most of the previously discussed key features of the polymineralic inclusions, we propose an alternative non-magmatic model that involves the trapping of polymineralic inclusions during an extended period of post-magmatic activity at subsolidus temperatures. To ascertain the nature of these processes, we tap into the previously published mineralogical studies of Afrikanda (Kukharenko et al. 1965; Chakhmouradian and Zaitsev 1999, 2004) and of oxide deposits elsewhere (Borisova et al. 2012; Lorand and Cottin 1987; McElduff and Stumpfl 1991; Yudovskaya and Kinnaird 2010). Inclusions hosted within the oxide minerals in these complexes possess a similar texture to those hosted by perovskite and magnetite at Afrikanda. These inclusions are primary, polymineralic and contain various assemblages of minerals that differ from those in the matrix surrounding their host chromite grains. Several authors have linked the formation of these inclusions with postcumulus sintering or hydrothermal activity (Borisova et al. 2012; Hulbert and Von Gruenewaldt 1985; Lorand and Cottin 1987; McElduff and Stumpfl 1991).

The hydrous silicates observed in the present work are common late-stage phases in the ultramafic, feldspathoidal and carbonatitic rocks at Afrikanda (Kukharenko et al. 1965; Chakhmouradian and Zaitsev 2002, 2004; Chakhmouradian et al. 2008). Some of these minerals (e.g., phlogopite and magnesiohastingsite) are absent or rare in the ultramafic units, but increase in abundance dramatically near their contact with cross-cutting carbonatitic and feldspathoidal rocks. Other silicates containing volatiles are localised in areas affected by subsolidus re-equilibration with fluids. Clinochlore is an abundant hydrothermal mineral precipitated in fractures and developed after phlogopite and amphiboles; cancrinite and sodalite replace nepheline in the ijolites; pectolite was reported from hydrothermally altered alkaline rocks and silicocarbonatites. Cuspidine was observed in many perovskite-hosted inclusions in the olivinites and clinopyroxenites, but is not known to occur outside the inclusions. It is thus plausible that their trapping occurred after the development of chlorite and replacement of nepheline by volatile-bearing feldspathoids, but prior to the deposition of prehnite, zeolites and muscovite. This interpretation would be consistent with the crystallisation order of these minerals in the silicocarbonatites, where chlorite was deposited at $T \approx 200^{o}C$, and the hydrous (Na, Ca, K) aluminosilicates at lower T (Chakhmouradian and Zaitsev 2002, 2004). Any cuspidine present

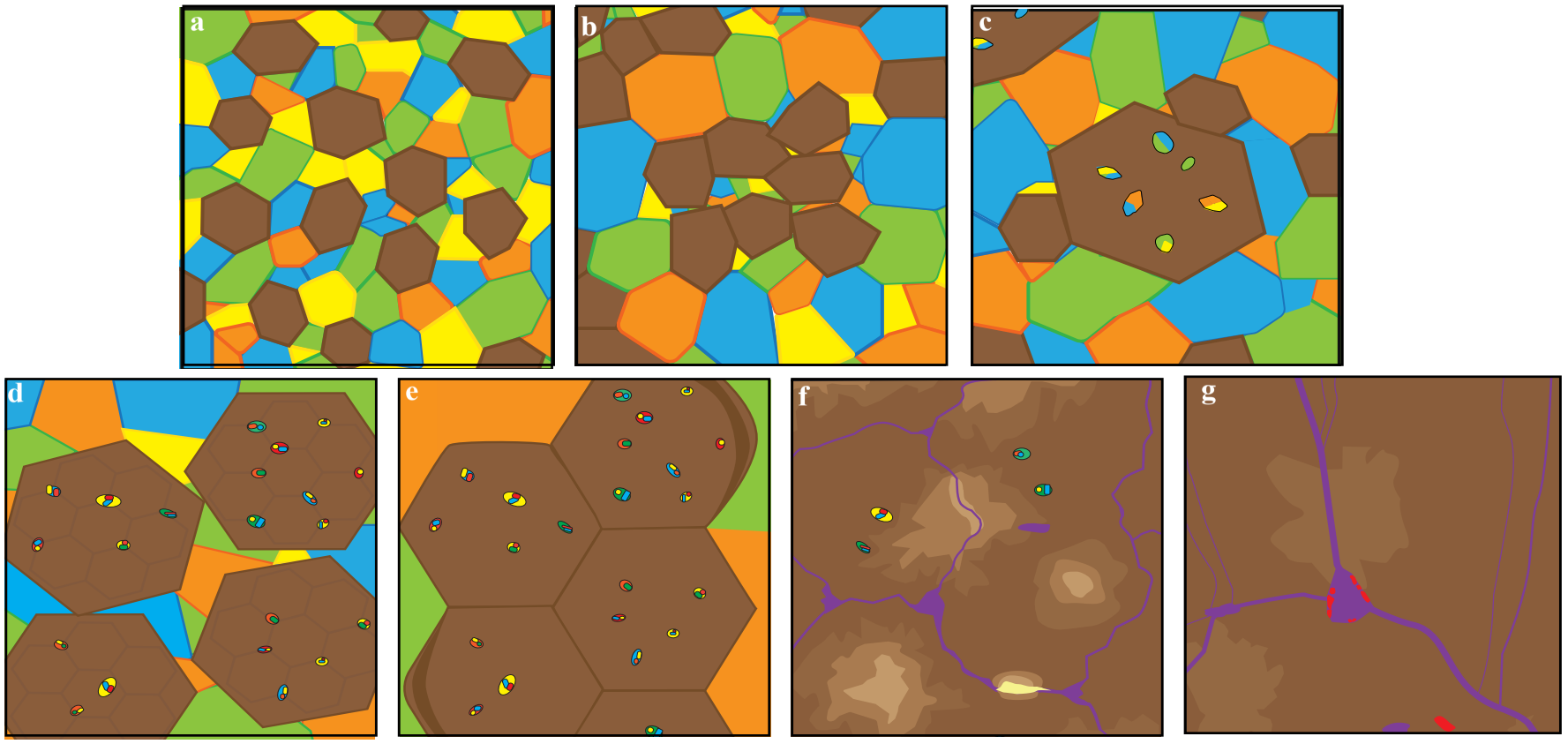

Figure 4. 12 A simplified sketch showing the processes involved in the origin of perovskite-hosted inclusions and textural transformation of T1 to T3 perovskite in ultramafic rocks: (a) disseminated inclusion-free perovskite, (b) coalescence and accumulation of small perovskite into coarser-grained aggregates with entrapped material between the grains, (c) re-adjustment of the perovskite outer boundaries to form pseudo-octahedral shapes with entrapped polymineralic inclusions, straight boundaries and 120° interfacial angles, (d) perovskite grains continue to coalesce and accumulate into pseudo-octahedral shapes (e) elimination of internal perovskite boundaries and collision with other equigranular polygonal perovskite grains forming clusters and chains surrounded by silicate and oxide minerals, (f) sintering of T1 perovskite results in the development of an intricate crystal mosaic of interlocked T2 perovskite grains, (g) continued sintering forming T3 massive perovskite with veins of titanite.

outside the perovskite-hosted inclusions was probably replaced with secondary minerals (most likely, prehnite) at that final evolutionary stage.

The model proposed here for the formation of polymineralic inclusions and development of perovskite aggregates at Afrikanda has been adopted from models by Hulbert and Von Gruenewaldt (1985) and Butcher and Merkle (1987). The model proposed by Hulbert and Von Gruenewaldt (1985) explains the formation of polymineralic inclusions and the densification of chromite at Bushveld, and suggests that the crystallisation and densification of chromite occurred *in situ*. Here, we propose that the trapping of the surrounding media and transition from T1 to T3 perovskite did not necessarily occur *in situ*, and may have involved perovskite movement during the post-magmatic accumulation and development of perovskite-rich zones.

We suggest that at least some of the polymineralic inclusions in perovskite represent the material that surrounded precursor individual perovskite grains, including magmatic phases (e.g., olivine, melilite, clinopyroxene, Na-carbonates) and minerals formed during reaction of these primary parageneses with subsequently emplaced melts and their derivative fluids (e.g., cancrinite, pectolite and clinochlore). This material was trapped by perovskite grains during post-magmatic sintering at subsolidus temperatures, which resulted in the coarsening of disseminated T1 into massive T3 perovskite. The textural transformation of T1 perovskite to massive T3 perovskite is outlined by Potter et al. (2018) so in this publication we only discuss the transitio n in relation to the inclusion morphology and composition.

Initially, perovskite crystallised as disseminated euhedral crystals interspersed with silicate, carbonate and oxide minerals (Fig. 4.12b). At this stage, the aggregates entrained small grains of associated minerals and were affected by fluid activity that gave rise to a variety of secondary minerals juxtaposed over the primary paragenesis (clinochlore, titanite, cancrinite etc.). The random trapping of interstitial material explains the observed mineralogical diversity and lack of correlation among neighbouring inclusions. As the perovskite aggregates underwent subsolidus sintering, coalescing grains trapped varying amounts of interstitial fine-grained material (Hulbert and Von Gruenewaldt 1985) as solitary inclusions that follow no crystallographic orientation with respect to their host crystal. The random trapping of interstitial material explains the observed mineralogical diversity and lack of correlation between neighbouring inclusions. It is possible that interstitial fluids were also trapped during this process (e.g., Johnson and Hollister 1995) and that their reaction with the solid phases in isolated inclusions further diversified their composition. The outer boundary of these densely-packed grains re-orientate to form pseudo-octahedral shapes with straight boundaries (Fig. 4.12c) and then clusters and chains of closely packed crystals with ~120° triple junctions (Figs. 4.2a-c, 4.12d). As discussed by Potter et al. (2018), the grains continued to coalesce to form larger anhedral T2 perovskite (Figs. 4.2e, 12e). As the adjacent crystals adopted similar crystallographic orientations and grain boundaries were eliminated, polymineralic inclusions were removed, and pre-existing growth zones

were merged into complex coalescent patterns (Figs. 4.11). The T2 perovskite eventually transformed into the inclusion-poor T3 variety (Figs. 4.2f, 12f).

The development of late-stage REE-rich perovskite and loparite-(Ce) as discontinuous rims and overgrowths on T2 and T3 perovskite (Fig. 4.11), and of titanite veins along grain boundaries (Fig. 4.12e) is linked to the infiltration of a REE-rich fluid (Chakhmouradian and Zaitsev 1999, 2004; Potter et al. 2018). The relative timing of this event is difficult to constrain at present because titanite was observed in the polymineralic inclusions, whereas loparite-(Ce) was not. Notably, none of the other REE minerals documented by Chakhmouradian and Zaitsev (1999, 2002, 2004) and Zaitsev and Chakhmouradian (2002) in the silicocarbonatites were observed in the present work either. This may indicate that these minerals precipitated after the sintering process was largely complete and in response to fluid infiltration from an unknown source (possibly, a new pulse of alkaline magma). The proposed model does not explain the formation of large (up to 5 cm across) pseudocuboctahedral perovskite crystals in the silicocarbonatites, which show oscillatory zoning and in fractures, host a distinct assemblage of minerals that were not observed in the T1, T2 or T3 perovskite (e.g., REE carbonates: Chakhmouradian and Zaitsev, 1999, 2002).

Our hypothesis encompasses the development of polymineralic inclusions and the transition from disseminated to massive perovskite at Afrikanda, and implies that igneous rocks of this type may experience extensive post-magmatic re-working. The textural similarities between the examined perovskite and oxide layers in various igneous complexes indicates that the post-magmatic processes outlined above may be applicable to a wide range of natural systems, and that oxide minerals serve as an ideal record-keeper of their evolutionary history.

4.7. Conclusion

The abundance and composition of perovskite- and magnetite-hosted inclusions varies across the three textural types in the olivinites, clinopyroxenites and silicocarbonatites at the Afrikanda complex. The investigation into the composition and texture of the inclusions showed that they have unusual mineral assemblages and differing chemical compositions between and within inclusions. We propose that these findings indicate the inclusions are not bona fide melt inclusions and represent homogeneous material that was trapped during the subsolidus sintering of magmatic perovskite. Once trapped the inclusions behave as isolated systems so reactions between the solid and fluid phases in the inclusions accounts for some of the variability in the mineralogy of the polymineralic inclusions in perovskite. The continuation of the sintering process resulted in the coarsening of inclusion-rich subhedral perovskite into inclusion-poor anhedral and massive perovskite. The development of polymineralic inclusions and transition from disseminated perovskite to massive perovskite at Afrikanda demonstrates that the ultramafic and carbonatitic rocks have experienced dynamic textural

equilibration and complex sintering and recrystallization during the evolution of the alkaline-ultramafic complex.

4.8. References

Afanasyev, B.V., 2011. Mineral resources of the alkaline–ultramafic massifs of the Kola Peninsula. Roza Vetrov, St. Petersburg, pp 224 (in Russian).

Armbrustmacher, T.J., 1981. The Complex of Alkaline Rocks at Iron Hill, Powderhorn district, Gunnison County, Colorado. New Mexico Geological Society, pp. 293-296.

Arzamastsev, A., Glaznev, V., Raevsky, A., Arzamastseva, L., 2000. Morphology and internal structure of the Kola Alkaline intrusions, NE Fennoscandian Shield: 3D density modelling and geological implications. Journal of Asian Earth Sciences, 18(2): 213-228.

Barbosa, E.S.R. Brod, J.A., Junqueira-Brod, T.C., Dantas, E.L., de Oliveira Cordeiro, P.F., Gomide, C.S. 2012. Bebedourite from its type area (Salitre I complex): a key petrogenetic series in the Late-Cretaceous Alto Paranaíba Kamafugite–Carbonatite–Phoscorite association, Central Brazil. Lithos, 144: 56-72.

Beard, A., Drake, S., 2007. A melilite-bearing high-temperature calcic skarn, Camasunary Bay, Isle of Skye Scottish. Journal of Geology, 43: 57-67.

Borrok, D.M., Kelser, S.E., Boer, R.H., Essene, E.J., 1998. The Vergenoeg magnetite-fluorite deposit, South Africa; support for a hydrothermal model for massive iron oxide deposits. Economic Geology, 93(5): 564-586.

Borisova, A.Y, Ceuleneer, G., Kamenetsky, V.S., Arai, S., Béjina, F., Abily, B., Bindeman, I.N, Polvé, M., De Parseval, P., Aigouy, T., 2012. A new view on the petrogenesis of the Oman ophiolite chromitites from microanalyses of chromite-hosted inclusions. Journal of Petrology, 53: 2411-2440.

Borrok, D.M., Kelser, S.E., Boer, R.H., Essene, E.J. 1998. The Vergenoeg magnetite-fluorite deposit, South Africa: Support for a hydrothermal model for massive iron oxide deposits. Economic Geology 93: 564-586.

Brod, J.A., 1999. Petrology and geochemistry of the Tapira alkaline complex, Minas Gerais State, Brazil, Durham University.

Brooker, R.A., Kjarsgaard, B.A., 2011. Silicate-carbonate liquid Immiscibility and phase relations in the system SiO_2-Na_2O-Al_2O_3-CaO-CO_2 at 0.1-2.5 GPa with applications to carbonatite genesis. Journal of Petrology, 52: 1281-1305.

Bussweiler, Y., Stone, R.S., Pearson, D.G., Luth, R.W., Stachel, T., Kjarsgaard, B.A., Menzies, A., 2016. The evolution of calcite-bearing kimberlites by melt-rock reaction: evidence from polymineralic inclusions within clinopyroxene and garnet megacrysts from Lac de Gras kimberlites, Canada. Contributions to Mineralogy and Petrology, 171: 65.

Butcher, A.R., Merkle, R.K., 1987. Postcumulus modification of magnetite grains in the upper zone of the Bushveld Complex, South Africa. Lithos, 20: 247-260.

Campbell, L.S., Henderson, P., Wall, F., Nielsen, T.F., 1997. Rare earth chemistry of perovskite group minerals from the Gardiner Complex, East Greenland. Mineralogical Magazine, 61(2): 197-212.

Chakhmouradian, A.R., Zaitsev, A.N. 2004. Afrikanda: An association of ultramafic, alkaline and alkali-silica-rich carbonatitic rocks from mantle-derived melts. In: Wall F, Zaitsev AN (ed) Phoscorites and carbonatites from mantle to mine: the key example of the Kola Alkaline Province. Mineralogical Society (UK) Series, London, pp 247-291.

Chakhmouradian, A.R., Cooper, M.A., Medici, L., Hawthorne, F.C., Adar, F., 2008. Fluorine-rich hibschite from silicocarbonatite, Afrikanda complex, Russia: crystal chemistry and conditions of crystallization. The Canadian Mineralogist, 46(4): 1033-1042.

Charlier, B. 2007. Petrogenesis of magmatic iron-titanium deposits associated with Proterozoic massif-type anorthosites. Dissertation. Liege University.

Charlier, B., Duchesne, J.-C., Vander Auwera, J., 2007. Magma chamber processes in the Tellnes ilmenite deposit (Rogaland Anorthosite Province, SW Norway) and the formation of Fe–Ti ores in massif-type anorthosites. Chemical Geology, 234(3-4): 264-290.

Chen, W., Kamenetsky, V.S., Simonetti, A., 2013. Evidence for the alkaline nature of parental carbonatite melts at Oka complex in Canada. Nature Communications 4: 2687.

Christiansen, F.G., 1985. Deformation fabric and microstructures in ophiolitic chromitites and host ultramafics, Sultanate of Oman. Geologische Rundschau, 74(1): 61-76.

Christiansen, F.G., 1986. Deformation of chromite: SEM investigations. Tectonophysics, 121(2-4): 175-196.

Church, A.A., Jones, A.P., 1995. Silicate-carbonate immiscibility at Oldoinyo Lengai. Journal of Petrology, 36: 869-889.

Currie, K., Knutson, J., Temby, P. 1992. The Mud Tank carbonatite complex, central Australia-an example of metasomatism at mid-crustal levels. Contributions to Mineralogy and Petrology 109: 326-339.

Danyushevsky, L.V., McNeill, A.W., Sobolev, A.V. 2002. Experimental and petrological studies of melt inclusions in phenocrysts from mantle-derived magmas: an overview of techniques, advantages and complications. Chemical Geology, 183: 5-24.

Dawson, J., Hawthorn, J., 1973. Magmatic sedimentation and carbonatitic differentiation in kimberlite sills at Benfontein, South Africa. Journal of the Geological Society, 129(1): 61-85.

Dawson, J.B., Pyle, D.M., Pinkerton, H., 1996. Evolution of natrocarbonatite from a wollastonite nephelinite parent: evidence from the June, 1993 eruption of Oldoinyo Lengai, Tanzania. The Journal of Geology: 41-54.

Dawson, J.B. 1998. Peralkaline nephelinite-natrocarbonatite relationships at Oldoinyo Lengai, Tanzania. Journal of Petrology 39:2077-2094

Dill, H.G. 2010. The “chessboard” classification scheme of mineral deposits: Mineralogy and geology from aluminum to zirconium. Earth-Science Reviews 100:1-420

Downes, H., Balaganskaya, E., Beard, A., Liferovich, R., Demaiffe, D., 2005. Petrogenetic processes in the ultramafic, alkaline and carbonatitic magmatism in the Kola Alkaline Province: A review. Lithos, 85: 48-75.

Eales, H., De Klerk, W., Teigler, B., 1990. Evidence for magma mixing processes within the Critical and Lower Zones of the northwestern Bushveld Complex, South Africa. Chemical Geology, 88(3-4): 261-278.

Ferrero, S., Angel, R.J., 2018. Micropetrology: Are inclusions grains of truth? Journal of Petrology, 59: 1671-1700.

Force, E.R., 1991. Geology of titanium-mineral deposits, 259. Geological Society of America.

Frezzotti, M-L., 2001. Silicate-melt inclusions in magmatic rocks: Applications to petrology. Lithos, 55: 273-299.

Ghisler, M., 1976. The Geology, Mineralogy and Geochemistry of the-Pre-Orogenic Archaean Stratiform Chromite Deposits at-Fiskenaesset, West Greenland. Monograph Series on Mineral Deposits, Greb. Borntraeger, pp 156.

Guzmics, T., Mitchell, R.H., Szabó, C., Berkesi, M., Milke, R., Ratter, K. 2012. Liquid immiscibility between silicate, carbonate and sulfide melts in melt inclusions hosted in co-precipitated minerals from Kerimasi volcano (Tanzania): evolution of carbonated nephelinitic magma. Contributions to Mineralogy and Petrology 164: 101-122.

Haldar, S.K., Tisljar, J., 2013. Mineral Deposits: Host Rocks and Origin. In: Haldar SK, Tisljar J (ed) Introduction to mineralogy and petrology. Elsevier, pp 261-279.

Halter, W.E., Pettke, T., Heinrich, C.A. 2004. Laser-ablation ICP- MS analysis of melt inclusions in an andesitic complex: I. Analytical approach and data evaluation. Contributions to Mineralogy and Petrology 147: 385-396.

Harlov, D.E., Meighan, C.J., Kerr, I.D., Samson, I.M., 2016. Mineralogy, chemistry, and fluid-aided evolution of the Pea Ridge Fe oxide-(Y+ REE) deposit, southeast Missouri, USA. Economic Geology, 111(8): 1963-1984.

Herz, N., 1976. Titanium Deposits in Alkalic Igneous Rocks. In Force, E. R., (Eds.), Geology and Resources of Titanium. Geological Survey Professional Paper 959. United States Government Printing Office, Washington, pp. 58-66.

Higgins, M.D., 2011. Textural coarsening in igneous rocks. International Geology Review, 53(3-4): 354-376.

Hoshide, T., Obata, M., 2012. Amphibole-bearing multiphase solid inclusions in olivine and plagioclase from a layered gabbro: origin of the trapped melts. Journal of Petrology, 53: 419-449.

Hou, B., Keeling, J., Van Gosen, B.S., 2017. Geological and Exploration Models of Beach Placer Deposits, Integrated from Case-Studies of Southern Australia. Ore Geology Reviews, 80: 437-459.

Hulbert, L., Von Gruenewaldt, G., 1985. Textural and compositional features of chromite in the lower and critical zones of the Bushveld Complex south of Potgietersrus. Economic Geology, 80: 872-895.

Irvine, T., 1977. Origin of chromitite layers in the Muskox intrusion and other stratiform intrusions: A new interpretation. Geology, 5(5): 273-277.

Johnson, E., Hollister, L. 1995. Syndeformational fluid trapping in quartz: determining the pressure-temperature conditions of deformation from fluid inclusions and the formation of pure CO2 fluid inclusions during grain-boundary migration. Journal of Metamorphic Geology 13: 239-249.

Jones, A., Ralph, B., Hansen, N., 1979. Subgrain coalescence and the nucleation of recrystallization at grain boundaries in aluminium. Proceedings of the Royal Society of London, 368: 345-357.

Kamenetsky, V.S., Kamenetsky, M.B. 2010 Magmatic fluids immiscible with silicate melts: examples from inclusions in phenocrysts and glasses, and implications for magma evolution and metal transport. Geofluids 10: 293–311.

Kinnaird, J., Kruger, F., Nex, P., Cawthorn, R., 2002. Chromitite formation—a key to understanding processes of platinum enrichment. Applied Earth Science, 111(1): 23-35.

Knipping, J.L.. Bilenker, L. D., Simon, A. C., Reich, M., Barra, F., Deditius, A. P., Wälle, M., Heinrich, C. A., Holtz, F., and Munizaga, R., 2015. Trace elements in magnetite from massive iron oxide-apatite deposits indicate a combined formation by igneous and magmatic-hydrothermal processes. Geochimica et Cosmochimica Acta, 171: 15-38.

Kogarko, L, Plant, D., Henderson, C., Kjarsgaard, B., 1991. Na-rich carbonate inclusions in perovskite and calzirtite from the Guli intrusive Ca-carbonatite, Polar Siberia. Contributions to Mineralogy and Petrology, 109: 124-129.

Kogarko, L., Henderson, C., Pacheco, H. 1995. Primary Ca-rich carbonatite magma and carbonate-silicate-sulphide liquid immiscibility in the upper mantle. Contributions to Mineralogy and Petrology 121: 267-274.

Krasnova, N.I. 2001. The Kovdor phlogopite deposit, Kola Peninsula, Russia. The Canadian Mineralogist 39: 33-44.

Kukharenko, A.A., Orlova, M. P., Bulakh, A. G., Bagdasarov, E. A., Rimskaya-Korsakova, O. M., Nefedov, E. I., Ilinskiy, G. A., Sergeev, A. S., and Abakumova, N. B., 1965. The Caledonian Complex of Ultrabasic and Alkaline Rocks and Carbonatites of the Kola Peninsula and Northern Karelia. Nedra, Leningrad, Russia, 722 pp.

Latypov, R., Chistyakova, S., Mukherjee, R., 2017. A Novel Hypothesis for Origin of Massive Chromitites in the Bushveld Igneous Complex. Journal of Petrology, 1: 41.

Latypov, R., O'Driscoll, B., Lavrenchuk, A., 2013. Towards a model for the in situ origin of PGE reefs in layered intrusions: insights from chromitite seams of the Rum Eastern Layered Intrusion, Scotland. Contributions to Mineralogy and Petrology, 166(1): 309-327.

Li, J.C., 1962. Possibility of subgrain rotation during recrystallization. Journal of Applied Physics, 33(10): 2958-2965.

Lorand, J., Ceuleneer, G., 1989. Silicate and base-metal sulfide inclusions in chromites from the Maqsad area (Oman ophiolite, Gulf of Oman): A model for entrapment. Lithos, 22(3): 173-190.

Lorand, J., Cottin, J., 1987. Na-Ti-Zr-H 2 O-rich mineral inclusions indicating postcumulus chrome-spinel dissolution and recrystallization in the Western Laouni mafic intrusion, Algeria. Contributions to Mineralogy and Petrology, 97(2): 251-263.

Martins, T., Kressall, R., Medici, L., Chakhmouradian, A.R., 2017. Cancrinite–vishnevite solid solution from Cinder Lake (Manitoba, Canada): crystal chemistry and implications for alkaline igneous rocks. Mineralogical Magazine, 81(5): 1261-1277.

McDonald, J.A., 1965. Liquid immiscibility as one factor in chromitite seam formation in the Bushveld Igneous Complex. Economic Geology, 60(8): 1674-1685.

McElduff, B., Stumpfl, E., 1991. The chromite deposits of the Troodos complex, Cyprus - Evidence for the role of a fluid phase accompanying chromite formation. Mineralium Deposita, 26(4): 307-318.

McOnie, A., Fawcett, J.J., James, R., 1975. The stability of intermediate chlorites of the clinochlore-daphnite series at 2 kbar PH2O. American Mineralogist: Journal of Earth and Planetary Materials, 60(11-12): 1047-1062.

McElduff, B., Stumpfl, E. 1991. The chromite deposits of the Troodos complex, Cyprus - Evidence for the role of a fluid phase accompanying chromite formation. Mineralium Deposita 26: 307-318.

Meinert, L.D., 1992. Skarns and skarn deposits. Geoscience Canada, 19(4).

Melcher, F., Grum, W., Simon, G., Thalhammer, T.V., Stumpfl, E.F., 1997. Petrogenesis of the ophiolitic giant chromite deposits of Kempirsai, Kazakhstan: A study of solid and fluid inclusions in chromite. Journal of Petrology, 38(10): 1419-1458.

Mitchell, R.H., 1986. Kimberlites: Mineralogy, geochemistry and petrology. Plenum Press, New York, 442 pp.

Nielsen, T., 1980. The petrology of a melilitolite, melteigite, carbonatite and syenite ring dike system, in the Gardiner complex, East Greenland. Lithos, 13(2): 181-197.

Nielsen, T.F.D., Solovova, I.P., Veksler, I.V., 1997. Parental melts of melilitolite and origin of alkaline carbonatite: evidence from crystallised melt inclusions, Gardiner complex. Contributions to mineralogy and petrology, 126: 331-344.

Pang, K-N., Zhou, M-F., Lindsley, D., Zhao, D., Malpas, J. 2007. Origin of Fe–Ti oxide ores in mafic intrusions: evidence from the Panzhihua intrusion, SW China. Journal of Petrology 49: 295-313.

Pang, K-N., Li, C., Zhou, M-F., Ripley, E.M. 2008. Abundant Fe–Ti oxide inclusions in olivine from the Panzhihua and Hongge layered intrusions, SW China: evidence for early saturation of Fe–Ti oxides in ferrobasaltic magma. Contributions to Mineralogy and Petrology 156: 307-321.

Panina, L.I., 2005. Multiphase carbonate-salt immiscibility in carbonatite melts: data on melt inclusions from the Krestovskiy massif minerals (Polar Siberia). Contributions to Mineralogy and Petrology, 150: 19-36.

Pekov, I.V., Olysych, L.V., Chukanov, N.V., Zubkova, N.V., Pushcharovsky, D.Y., Van, K.V., Giester, G., Tillmanns, E. 2011. Crystal chemistry of cancrinite-group minerals with an AB-type framework: A review and new data. I. Chemical and structural variations The Canadian Mineralogist 49: 1129-1150.

Pettke, T., Halter, W.E., Webster, J.D., Aigner-Torres, M., Heinrich, C.A. 2004. Accurate quantification of melt inclusion chemistry by LAICPMS: a comparison with EMP and SIMS and advantages and possible limitations of these methods. Lithos 78: 333–361.

Potter, N.J., Ferguson, M.R., Kamenetsky, V.S., Chakhmouradian, A.R., Sharygin, V.V., Thompson, J.M., Goemann, K., 2018. Textural evolution of perovskite in the Afrikanda alkaline–ultramafic complex, Kola Peninsula, Russia. Contributions to Mineralogy and Petrology 173: 100.

Potter, N.J., Kamenetsky, V.S., Simonetti, A., Goemann, K., 2017. Different types of liquid immiscibility in carbonatite magmas: A case study of the Oldoinyo Lengai 1993 lava and melt inclusions. Chemical Geology, 455: 376-384.

Prichard, H.M., Barnes, S.J., Godel, B., 2018. A mechanism for chromite growth in ophiolite complexes: Evidence from 3D high-resolution X-ray computed tomography images of chromite grains in Harold's Grave chromitite in the Shetland ophiolite. Mineralogical Magazine, 82(3): 457-470.

Reynolds, I.M., 1985. The nature and origin of titaniferous magnetite-rich layers in the upper zone of the Bushveld Complex: A review and synthesis. Economic Geology, 80(4): 1089-1108.

Rios, P.R., Siciliano Jr, F., Sandim, H.R.Z., Plaut, R.L., Padilha, A.F., 2005. Nucleation and growth during recrystallization. Materials Research, 8(3): 225-238.

Roedder, E., 1984. Volume 12: Fluid inclusions. Reviews in mineralogy. Mineralogical Society of America, Washington, 644 pp.

Rollinson, H., Mameri, L., Barry, T., 2018. Polymineralic inclusions in mantle chromitites from the Oman ophiolite indicate a highly magnesian parental melt. Lithos, 310: 381-391.

Sadykov, V., Bulgakov. N.N., Muzykantov, V.S., Kuznetsova, T.G., Alikina, G.M., Lukashevich, A.I., Potapova, Y.V., Rogov, V.A., Burgina, E.B., Zaikovskii, V.I., Moroz, E.M. 2004. Mobility and

reactivity of the surface and lattice oxygen of some complex oxides with perovskite structure. In: Mixed Ionic Electronic Conducting Perovskites for Advanced Energy Systems. Springer, 53-74.

Sharygin, V.V., Kamenetsky, V.S., Zaitsev, A.N., Kamenetsky, M.B., 2012. Silicate–natrocarbonatite liquid immiscibility in 1917 eruption combeite–wollastonite nephelinite, Oldoinyo Lengai Volcano, Tanzania: Melt inclusion study. Lithos, 152: 23-39.

Sobolev, A., 1996. Melt inclusions in minerals as a source of principle petrological information. Petrology, 4(3): 209-220.

Sobolev, V., Kostyuk, V., 1975. Magmatic crystallization based on a study of melt inclusions. Fluid Inclusion Research, 9: 182-253.

Spandler, C., Mavrogenes, J., Arculus, R., 2005. Origin of chromitites in layered intrusions: Evidence from chromite-hosted melt inclusions from the Stillwater Complex. Geology, 33(11): 893-896.

Tanner, D., McDonald, I., Harmer, R.J., Muir, D.D., Hughes, H.S., 2018. A record of assimilation preserved by exotic minerals in the lowermost platinum-group element deposit of the Bushveld Complex: The Volspruit Sulphide Zone. Lithos.

Veksler, I., Nielsen, T., Sokolov, S., 1998. Mineralogy of crystallized melt inclusions from Gardiner and Kovdor ultramafic alkaline complexes: Implications for carbonatite genesis. Journal of Petrology, 39(11-12): 2015-2031.

Vukmanovic, Z., Barnes, S.J., Reddy, S.M., Godel, B., Fiorentini, M.L., 2013. Morphology and microstructure of chromite crystals in chromitites from the Merensky Reef (Bushveld Complex, South Africa). Contributions to Mineralogy and Petrology, 165(6): 1031-1050.

Yagi, K., Kikuchi, T., Kakuta, H., 1968. Thermal decomposition of pectolite and its hydrothermal synthesis. Journal of the Faculty of Science, Hokkaido University. Series 4, Geology and mineralogy, 14(2): 123-134.

Yudovskaya, M.A., Kinnaird, J.A., 2010. Chromite in the Platreef (Bushveld Complex, South Africa): occurrence and evolution of its chemical composition. Mineralium Deposita, 45(4): 369-391.

Zhou, M.-F., Robinson, P.T., Lesher, C.M., Keays, R.R., Zhang, C.-J., Malpas, J. 2005. Geochemistry, petrogenesis and metallogenesis of the Panzhihua gabbroic layered intrusion and associated Fe–Ti–V oxide deposits, Sichuan Province, SW China. Journal of Petrology, 46(11): 2253-2280.

Appendix 4.1 Methodology

EDS analysis

Backscattered electron (BSE) imaging, energy dispersive X-ray spectrometry (EDS) were performed using a Hitachi SU-70 field emission scanning electron microscope (SEM). The instrument is fitted with a Hitachi photo-diode BSE detector and an Oxford AZTec 3 microanalysis system with XMax80 EDS detector and HKL Nordlys Nano EBSD camera.

For BSE-EDS analyses the samples were coated with around 20 nm of carbon using a Ladd 40000 carbon evaporator and analysed at 15 kV accelerating voltage and 2-3 nm beam current. Elements were calibrated on well characterised natural and synthetic standard reference materials. The intensity of the cobalt K x-ray peak series was determined at the start of each session on pure cobalt metal as an indirect beam current measurement to avoid normalisation of compositional data to 100% total.

Elemental analysis of perovskite-hosted inclusion

Major and trace element analyses of inclusions hosted in perovskite were performed on an Agilent 7900 quadropole ICPMS, coupled to a Resolution S155 laser ablation system with a Coherent COMPex Pro 110 ArF Excimer laser operating at 193nm wavelength and ~20ns pulse width. Blank gas was analysed for 8 s followed by 25 s of perovskite ablation with operating conditions of 5 Hz and ~2 J/cm^2 using a spot size of 15 or 29 μm. Helium carrier gas flowing at 0.35 l/min carried particles ablated by the laser out of the sample chamber and mixed with Ar gas before transfer to the plasma. The elements measured had typical detection limits that ranged from <1000 ppm for Si, <100 ppm for Ca and Ti, <50 ppm for Na, K, Fe, <5 ppm for Al, P, S, Cl, and Sr, and <1ppm for Mg, Rb and Ba.

Samples were analysed in runs of 12 bracketed by two spots of the primary standard at the start and end of each run. Additionally, one analysis of the BCR-2g and GSD-1g standards were included in each run as a secondary standard to monitor the accuracy of the measurements using the preferred values from the GeoReM website. Element abundances were calculated using the NIST610 glass as the primary calibration material using values from Jochum et al. (2011) and using ^{43}Ca as the internal standard element for perovskite and ^{49}Ti for titanite, with both minerals normalized to a 100% and 99% total for each mineral respectively. All data reduction calculations and error propagations were done within Microsoft Excel® via macros designed at the University of Tasmania, and using techniques summarised by Longerich et al. (1996).

References

Jochum, K. P., Weis, U., Stoll, B., Kuzmin, D., Yang, Q., Raczek, I., Jacob, D. E., Stracke, A., Birbaum, K., and Frick, D. A., 2011, Determination of reference values for NIST SRM 610–617 glasses following ISO guidelines: Geostandards and Geoanalytical Research, v. 35, no. 4, p. 397-429.

Longerich, H. P., Günther, D., and Jackson, S. E., 1996, Elemental fractionation in laser ablation inductively coupled plasma mass spectrometry: Fresenius' journal of analytical chemistry, v. 355, no. 5-6, p. 538-542.

Appendix 4.2 Perovskite-hosted inclusion data – see digital appendix

Appendix 4.3 Magnetite-hosted inclusion data – see digital appendix

Appendix 4.4 Heated perovskite-hosted inclusion data – see digital appendix

Appendix 4.5 Supplementary figures – see digital appendix

CHAPTER 5

SYNTHESIS

5.1 Introduction

The thesis aimed at the development of carbonatitic lava at Oldoinyo Lengai and the perovskite-rich segregations in the ultramafic and carbonatitic rocks at Afrikanda alkaline-ultramafic complex to advance the knowledge on the genesis of carbonatitic volcanism and carbonatite-related igneous complexes. The studies effectively build on and expand the use of petrography and mineralogy of carbonatites and associated alkaline silicate rocks to further the understanding of the genesis of extrusive and intrusive carbonatites. The projects make a significant contribution to the current literature on liquid immiscibility in non-silicate magmas, inclusion studies in oxide minerals and the complex mineralogy of carbonatites.

This chapter summarises the key results of the studies and reflects on their significance, based on scientific merit and their implications for carbonatites, alkaline-ultramafic complexes and oxide deposits. Section 7.1 summarises how each chapter has contributed to answering the research aims of this thesis. Section 7.2 presents how the findings fit into the spectrum of carbonatite research and the implications the research has on the broader academic community (e.g. oxide deposit research). Section 7.3 discusses the avenues for future research on carbonatites and associated economic deposits.

5.2 Summary and significance of the research

5.2.1. Chapter 2: Different types of liquid immiscibility in carbonatite magmas: a case study of the Oldoinyo Lengai 1993 lava and melt inclusions

This chapter investigates the texture and mineralogy of the June 1993 natrocarbonatite lava at Oldoinyo Lengai and presents petrographic evidence of liquid immiscibility between silicate, carbonate, chloride, and fluoride melt phases. The study demonstrates that multi-stage liquid immiscibility is a major factor in the petrogenesis of this lava at Oldoinyo Lengai. Several previous studies have investigated samples from the June 1993 lava and reported detailed descriptions of the eruption with petrography and

mineralogy of the lava (Church and Jones, 1995; Dawson et al., 1994; Dawson et al., 1996) and geochemical data (Simonetti et al., 1997). This work has built on these studies, with the identification of carbonate-carbonate and carbonate-halide immiscibility within the natrocarbonatite lava and has shown that different types of liquid immiscibility, other than silicate-silicate and silicate- carbonate, can occur in natural magmas. The genetic model for the 1993 natrocarbonatite lava involved the unmixing of several chemical components at different stages of evolution in the magmatic system. The first stage required a new injection of nephelinitic magma to intrude into the magma chamber. As the intrusion rises and cools, it undergoes silicate-carbonate immiscibility and partially separates into carbonate and peralkaline nephelinitic melts, with the carbonate segregation accumulating at the top of the intrusion. The carbonate head of the intrusion disrupts the carbonate crystal mush at the top of the magma chamber, and pushes silicate minerals into the carbonate crystal mush. The high density of crystals enabled these silicate spheroids to become trapped within the surrounding natrocarbonatite magma. The second stage of immiscibility occurred during the eruption, with the decreasing temperature and pressure generating a heterogeneous mix of four immiscible phases, with carbonate-carbonate and carbonate-halide immiscibility recorded in the groundmass. The identification of these diverse unmixed phases at both the macro- and micro-scale presents clear evidence that several types of liquid immiscibility occurred during the evolution of a single melt, both in the magma plumbing system and during the eruption, to produce a carbonatitic lava.

5.2.2 Chapter 3: Textural evolution of perovskite in the Afrikanda alkaline-ultramafic complex, Kola Peninsula, Russia

This chapter examines the textures and chemical composition of perovskite from the ultramafic and carbonatitic rocks in the Afrikanda alkaline-ultramafic complex and investigates the development of perovskite-rich segregations in these rocks. The scarcity of perovskite ore deposits has limited the number of genetic studies and prior to this study there was great uncertainty on how the perovskite accumulated to an ore-grade level in this setting. Our geochronological study of perovskite from the olivinites, clinopyroxenites and silicocarbonatites yielded similar ages to previous estimations (Arzamastsev et al., 2000). The perovskite and titanite ages support the contemporaneous emplacement of these lithologies at Afrikanda. Across the ultramafic and carbonatitic rocks, we identified three different perovskite textures, based on based on crystal morphology, inclusion abundance, composition, and zonation. The model for the textural development of perovskite-rich segregations in the Afrikanda alkaline-ultramafic complex combines the observed textures and findings from other oxide-rich complexes and deposits. Subsolidus sintering and re-crystallisation are commonly accepted processes for the densification of magnetite and chromite into monomineralic layers (Reynolds, 1985; Hulbert and Von Gruenewaldt, 1985; Ulmer and Gould, 1982). The textural transformation involved the progressive coarsening of clusters and networks of fine-grained perovskite crystals into mosaics of coarse-grained and massive perovskite in the ultramafic rocks due to post-magmatic recrystallization

and textural re-equilibration. The three stages of development in the perovskite-rich sections involved (1) textural equilibration enabling the development of fine-grained, equigranular, monomineralic clusters and networks after initial perovskite crystallisation (2) grain rotation and coalescence of the small equilibrated polygonal clusters to form fine- to coarse-grained interlocked anhedral polycrystalline mosaics (3) in some areas the continued consolidation and coarsening transforms the large polycrystalline perovskite into massive perovskite. We propose that the silicocarbonatites did not undergo perovskite recrystallization due to the lower solidus temperature of the silicocarbonatites compared to the ultramafic rocks. However, the perovskite from both the ultramafic rocks and silicocarbonatites experienced the same fluid-driven alteration. The findings show that the formation of the carbonatites in the complex is different from the formation of the ultramafic rocks.

5.2.3. Chapter 4*: Polymineralic inclusions in oxide minerals of the Afrikanda alkaline-ultramafic complex: Implications for the evolution of perovskite mineralisation*

This chapter presents a petrological and mineralogical examination of the polymineralic inclusions hosted in perovskite and magnetite from the ultramafic and carbonatitic rocks in the Afrikanda complex. The study provides support for the process of perovskite amalgamation and re-equilibration in the Afrikanda complex discussed in Chapter 3, with post-magmatic sintering proposed as the cause for the variable distribution and abundance of inclusions between the three types of perovskite in olivinites, clinopyroxenites and silicocarbonatites at Afrikanda. The non-magmatic model presented in this chapter illustrates the processes involved in the formation of inclusion-rich T1 perovskite, and the loss of inclusions and transition from small disseminated inclusion-free magmatic perovskite grains to equigranular, inclusion-rich grains in clusters and accumulations of massive perovskite. The first step is the magmatic precipitation of small disseminated inclusion-free perovskite grains enclosed by larger silicate, carbonate and oxide minerals. During subsolidus cooling, the randomly orientated grains accumulate together through grain rotation and collision at triple junctions to develop into loosely packed aggregates of perovskite with entrapped material between the grains. Coalescence of adjoining perovskite grains and re-adjustment of grain boundaries leads to the removal formation of pseudo-octahedral shapes with straight boundaries and polymineralic inclusions. The granbolastic-polyagonal texture of these grains is assigned to T1 perovskite. The collision of these equigranular polygonal T1 perovskite leads to the development of clusters and chains surrounded by silicate and oxide minerals. Sintering of T1 perovskite results in the development of an intricate crystal mosaic of interlocked anhedral T2 perovskite grains. In some areas, the continued consolidation and coarsening transforms the T2 perovskite into massive T3 perovskite. The findings show the importance of inclusion studies for interpreting the origin of oxide minerals and their associated economic deposits and that formation of polymineralic inclusions can be associated with non-magmatic processes.

5.3 Implications

5.3.1 Oldoinyo Lengai

The global literature encompasses a substantial quantity of information on the composition of the carbonatite lavas at Oldoinyo Lengai (Church and Jones, 1995; Dawson, 1962; Le Bas, 1981; Mitchell, 2005; Mitchell, 2009). However, details on the mineralogical and textural relationship between minerals in the lavas are lacking. This study on the mineralogy and melt inclusions at Oldoinyo Lengai has shown that liquid immiscibility can be responsible for the formation of natrocarbonatites and that liquid immiscibility can occur between multiple phases are different times during a single eruption. The identification of carbonate-carbonate and carbonate-halide immiscibility within the natrocarbonatite lava supports the theory that different types of liquid immiscibility, other than silicate-silicate and silicate-carbonate, can occur in natural magmas. Due to the rarity of and difficulty in capturing definitive evidence of liquid immiscibility within magmas, a large portion of the research on liquid immiscibility is experimental based (Groos and Wyllie, 1963; Kjarsgaard et al., 1995; Kjarsgaard and Peterson, 1991; Petibon et al., 1998). Therefore, this research contributes to the field of liquid immiscibility in natural samples and the identification of carbonate-carbonate and carbonate-halide unmixing in the lavas' groundmass has the potential to provide a new avenue for the study liquid immiscibility in natural magmas.

5.3.2 Afrikanda alkaline-ultramafic complex

In terms of global significance, very few studies have been completed on the Afrikanda alkaline-ultramafic complex, and the geochemical and textural information provided by the study adds substantially to existing information available on perovskite in the carbonatites and ultramafic rocks. The study at Afrikanda has highlighted the textural and mineralogical complexity of the alkaline-ultramafic complex and provides a new perspective on the genesis of the perovskite ore in the Afrikanda alkaline-ultramafic complex. The study also contributes to the understanding of how perovskite-rich segregations form, as there are a few other localities around the world where perovskite forms in high abundances but almost no studies have mentioned, let alone studied, them e.g. Tapira, Brazil and Powderhorn, USA. Understanding these perovskite-rich portions in the carbonatite complexes at these locations are important for understanding the formation of the carbonatite complex, and therefore this study provides a basis for future studies on these complexes.

It has been proposed by Anton and Chakhmouradian (2004) that the Afrikanda complex is the remnants of an exposed lopolith that served as a feeder of a natrocarbonatite volcano, like Oldoinyo Lengai. Therefore, it is undoubtedly plausible that liquid-immiscibility is responsible for the formation of the Afrikanda complex. The multi-stage process of the Oldoinyo Lengai volcano is comparable to the Afrikanda complex in regard to the silicate rocks crystallising prior to the formation of the carbonatites, as supported by textural and geochronological data. Additionally, The unexpected

identification of textural similarities between perovskite-rich segregations at Afrikanda and chromite and magnetite deposits in various igneous complexes has significant implications for oxide and perovskite deposit research in the future. Therefore, the detailed petrological and mineralogical study of perovskite-rich segregations at Afrikanda could also have implications for the development of monomineralic layers in oxide deposits. The limited number of studies conducted on polymineralic inclusions observed in chromite layers in oxide deposits opens a new avenue of study in chromite deposits, and may have implications for the current theories hypothesized for their formation.

Additionally, the benefit of utilising EBSD in mineral studies was supported by this study, with the identification of internal grain boundaries that were not visible in BSE images. Several other authors have shown the successful application of this technology (Humphreys, 2001; Mörk and Moen, 2007; Prior et al., 2009) and the addition of this study highlights the importance of EBSD to help determine the evolution of microstructures and textures during annealing in igneous, sedimentary and metamorphic settings.

5.3.3 Inclusion studies

Inclusion studies have expanded rapidly over the last decade, largely due to advances in microanalytical techniques, and have been at the centre of many recent petrological and geochemical discoveries. The study of melt and polymineralic inclusions at both complexes highlights the importance of these tiny parcels of melt in understanding numerous aspects of the rocks and their genesis. For the study of Oldoinyo Lengai, the identification of liquid-immiscibility within the inclusions of silicate and carbonate minerals enables the timing of immiscibility to be predicted. At Afrikanda, the study of the inclusions provided the opportunity to see past the later metamorphism and alteration to better understand the earliest stages of the complex development of the perovskite-rich deposits. Polymineralic inclusions are generally rare in magmatic environments, and the unusual compositions of this type of inclusion is not widely discussed in the literature, with the general assumption being that they are magmatic. The study of the perovskite at Afrikanda raises questions about the viability of perovskite being a magmatic mineral and presents several avenues for future research.

5.4 Future research

The contributions listed in the previous section indicate how much scientific information can be acquired from petrological and geochemical analyses of carbonatites and associated complexes. The studies have provided a multi-stage immiscibility model for the genesis of carbonatite lava and an insight into the complex history of perovskite in alkaline-ultramafic complexes, but there are still many questions about Oldoinyo Lengai and Afrikanda that have not been addressed. Therefore, these studies have provided a starting point for research focused on petrological and economical enigmas in

carbonatites and oxide-rich complexes. Key questions arising from the study that warrant further research include:

(1) How does perovskite from the Tapira and Powderhorn (aka Iron Hill) compare to Afrikanda?

One of the substantial implications of the findings from Chapter 3 is that the perovskite-rich segregations of the Afrikanda complex may not be formed solely through the magmatic processes. However, the unknowns associated with the other perovskite deposits at Tapira, Brazil and Powderhorn, USA limits the conclusions that can be drawn from our study. Powderhorn, USA and Tapira, Brazil, along with Afrikanda, Russia are the only known titanium deposits where the primary titanium-bearing mineral is perovskite (Armbrustmacher, 1981; Brod et al., 2013). Tapira and Powderhorn are also both carbonatite complexes, with the main theories for their formation associated with partial melting, fractional crystallization and liquid-liquid immiscibility. A limited number of studies have been conducted on these complexes, but none have conducted detailed investigations on the perovskite-rich segregations hosted in pyroxenites and perovskite-magnetite dykes in these complexes. At Tapira, the current theory is that these zones are indicative of the remobilisation of crystal-mush aggregates during the emplacement of partially-crystallised cumulate sequences (Brod et al., 2013) and at Powderhorn, the perovskite-rich layer is believed to have formed from multiple pulses of magma (Temple and Grogan, 1965; Van Gosen, 2009 – from thesis). Liquid immiscibility is also proposed to have played a role in the genesis of these units in the later stages of the Powderhorn complex. Therefore, we propose that a detailed textural and mineralogical investigation of the perovskite-rich segregations of Tapira and Powderhorn would provide a more complete understanding of the mechanisms involved in the textural development of perovskite in these complexes. The Afrikanda complex was thought to be purely magmatic prior to our study, and so may be the case with these complexes. The studies would also have implications for understanding the unusual nature of perovskite deposits and clarify whether these perovskite-rich segregations have been generated by a similar mechanism to those at Afrikanda.

(2) How do other alkaline-ultramafic carbonatite complexes compare to the Afrikanda complex?

The best way to improve our understanding of carbonatites and provide a more comprehensive view on the conditions required to generate carbonatite complexes is to identify and establish patterns and similarities between outcrops to help link and evaluate the different formation mechanisms. Therefore, the first complex recommended is the Guli pluton, the world's largest alkaline ultramafic carbonatite massif, mostly composed of dunites and peridotites. The complex is of Triassic age (240 Ma) and covers an area of 1500-1600 km^2. It is a polyphase pluton consisting of a variety of rock types intruded in the order: dunites, pyroxenites, melilitic rocks, melteigites, syenites and carbonatites (Kapustin, 1980). The complex will help to understand the relationship between the peridotites and carbonatites and to determine the differentiation processes that enabled the formation of the carbonatites in the complex. By conducting a detailed mineralogical study of carbonate-bearing melt inclusions in dunite from the

Guli complex, this would be one of the first melt inclusion studies to be conducted on carbonatites from the Guli complex and would provide an insight into the composition of the melt prior to emplacement and the evolution of the melt during magmatic ascent.

(3) What are the composition of inclusions in different units from chromite deposits that are texturally similar to Afrikanda?

Oxide ore deposits have been the focus of numerous academic studies, with a range of magmatic, metamorphic and sedimentary processes proposed for their formation (Borrok et al., 1998; Force, 1991; Hou et al., 2017; Irvine, 1977; Latypov et al., 2017). The ongoing similarities identified between perovskite from Afrikanda and chromite and magnetite layers in various igneous complexes indicates that similar post-magmatic coarsening processes are involved in the formation of polymineralic inclusions in oxide minerals and ultimately the textural development of oxide ore deposits with monomineralic layers. Many papers discuss the change from inclusion-rich to inclusion-free sections due to recrystallisation and sintering (Borisova et al., 2012; Christiansen, 1985; Vukmanovic et al., 2013; Yudovskaya and Kinnaird, 2010). However, very few consider the composition of these inclusions prior to their disappearance to better understand the formation of these inclusions and the environment that caused them to be trapped in the minerals. We propose inclusion studies be conducted on chromite-hosted inclusions in the Oman ophiolite belt and the Fiskenaesset and Bushveld complexes, to determine the distribution and composition of the inclusions, the timing of the trapped inclusions and ultimately place genetic constraints on the formation of chromite. In oxide ore deposits, many of the principal minerals contain inclusions suitable for visually controlled heating and other experimental studies (e.g. olivine, apatite, nepheline, clinopyroxene, and phlogopite), yet the primary oxide ore minerals (e.g. Cr-spinel and magnetite) are not. Although these minerals are opaque, their hardness, absence of cleavage and resistance to alteration enables their inclusions to preserve trapped melt compositions. The non-silicate and non-carbonate nature of the host oxide minerals allow confident recognition of trapped silicate and carbonate melt components, as the latter are unlikely to suffer from post-entrapment re-equilibration with the host. Yet inclusion studies in chromite deposits are rare. Many chromite deposits are thought to be magmatic based on the study of their mineralogy, however, the study of hosted inclusions can provide another level of evidence to further prove or disprove this idea. These studies would involve petrological and geochemical analyses and by extending the study of polymineralic inclusions to these deposits, would enable the validity of the implications of Chapter 3 and 4 to be verified. The unexpected discovery of polymineralic inclusions at Afrikanda and the limited number of published studies on polymineralic inclusions outside of ultra-high pressure complexes, indicates the importance of expanding this area of research. As without more data the ability to determine the relationship between these inclusions and the host minerals is severely restricted.

(4) Additional areas of future research

Other avenues that have been identified during the completion of this thesis include the crystallization of silicate minerals in carbonatites, as this has important implications on the composition of crustal carbonatites. Since carbonatite petrogenesis is still heavily debated in the scientific community any new information regarding the character and nature of carbonatite magmas is essential. Additionally, the conditions of formation of the various types of carbonates (e.g. dolomitic and calcitic) and their mutual association in carbonatite complexes is not well understood. Therefore, every new discovery of carbonatite or carbonate-bearing magmatic rock presents an opportunity for a better understanding of the complex processes leading to their formation and emplacement.

5.5 Final remarks

The wealth of knowledge about carbonatites shows how far the scientific community has come in the ability to identify and interpret these rocks and understand their formation. However, fundamental questions about the evolution of carbonatites from the mantle to the surface, caused by their potential to form through various magmatic and metamorphic mechanisms, need to be addressed. Therefore, through the persistent study of intrusive and extrusive carbonatites, we will continue to gain a well-rounded view on the different aspects of carbonatite complexes and better understand the processes that modify and control the evolution of carbonatites and their associated mineral deposits around the world.

5.6. References

Borisova, A.Y., Ceuleneer, G., Kamenetsky, V.S., Arai, S., Béjina, F., Abily, B., Bindeman, I.N, Polvé, M., De Parseval, P., Aigouy, T., 2012. A new view on the petrogenesis of the Oman ophiolite chromitites from microanalyses of chromite-hosted inclusions. Journal of Petrology, 53: 2411-2440.

Chakhmouradian, A.R., Zaitsev, A.N., 2004. Afrikanda: An association of ultramafic, alkaline and alkali-silica-rich carbonatitic rocks from mantle-derived melts. In: Wall F, Zaitsev AN (ed) Phoscorites and carbonatites from mantle to mine. The key example of the Kola Alkaline Province. Mineralogical Society (UK) Series, London: 247-291.

Groos, A.V., Wyllie, P., 1963. Experimental data bearing on the role of liquid immiscibility in the genesis of carbonatites. Nature, 199(4895): 801-802.

Kapustin, I.u.r.L., 1980. Mineralogy of carbonatites. Amerind Publishing Company.

Le Bas, M.J., 1981. Carbonatite Magmas. Mineralogical Magazine, 44(334): 133-140.

Mörk, M.B.E., Moen, K., 2007. Compaction microstructures in quartz grains and quartz cement in deeply buried reservoir sandstones using combined petrography and EBSD analysis. Journal of Structural Geology, 29(11): 1843-1854.

Petibon, C.M., Kjarsgaard, B.A., Jenner, G.A., Jackson, S.E., 1998. Phase relationships of a silicate-bearing natrocarbonatite from Oldoinyo Lengai at 20 and 100 MPa. Journal of Petrology, 39(11-12): 2137-2151.

Prior, D.J., Mariani, E., Wheeler, J., 2009. EBSD in the earth sciences: applications, common practice, and challenges, Electron backscatter diffraction in materials science. Springer, pp. 345-360.

PUBLISHED PAPERS

Chemical Geology 455 (2017) 376–384

Contents lists available at ScienceDirect

Chemical Geology

journal homepage: www.elsevier.com/locate/chemgeo

Different types of liquid immiscibility in carbonatite magmas: A case study of the Oldoinyo Lengai 1993 lava and melt inclusions

Naomi J. Potter [a,*], Vadim S. Kamenetsky [a], Antonio Simonetti [b], Karsten Goemann [c]

[a] School of Physical Sciences, University of Tasmania, Tasmania 7001, Australia
[b] Department of Civil and Environmental Engineering and Earth Sciences, University of Notre Dame, IN 46556, USA
[c] Central Science Laboratory, University of Tasmania, Tasmania 7001, Australia

ARTICLE INFO

Article history:
Received 31 May 2016
Received in revised form 13 September 2016
Accepted 26 September 2016
Available online 28 September 2016

Keywords:
Natrocarbonatite
Carbonatite
Oldoinyo Lengai
Melt inclusions
Liquid immiscibility

ABSTRACT

Oldoinyo Lengai is situated within the Gregory Rift Valley (northern Tanzania) and is the only active volcano erupting natrocarbonatite lava. This study investigates the texture and mineralogy of the June 1993 lava at Oldoinyo Lengai, and presents petrographic evidence of liquid immiscibility between silicate, carbonate, chloride, and fluoride melt phases. The 1993 lava is a porphyritic natrocarbonatite consisting of abundant phenocrysts of alkali carbonates, nyerereite and gregoryite, set in a quenched groundmass, composed of sodium carbonate, khanneshite, Na-sylvite and K-halite, and a calcium fluoride phase. Dispersed in the lava are silicate spheroids (<2 mm) with a cryptocrystalline silicate mineral assemblage wrapped around a core mineral. We have identified several textural features preserved in the silicate spheroids, melt inclusions, and carbonatite groundmass that exhibit evidence of silicate-carbonate, carbonate-carbonate and carbonate-halide immiscibility. Rapid quenching of the lava facilitated the preservation of the end products of these liquid immiscibility processes within the groundmass. Textural evidence (at both macro- and micro-scales) indicates that the silicate, carbonate, chloride and fluoride phases of the lava unmixed at different stages of evolution in the magmatic system.

1. Introduction

The petrogenetic evolution of silicate magmas is well known and extensively studied due to the preponderance of siliceous-type volcanism worldwide. In contrast, carbonate magmas are rarely observed in nature with the majority identified in intrusive settings and commonly altered post emplacement (Mitchell, 2005; Woolley, 2003). Oldoinyo Lengai (Tanzania) is the sole active volcano that erupts carbonatites and provides an unprecedented opportunity to better understand the magmatic evolution of this non-silicate type of Earth's magmatism.

The most commonly accepted mechanism proposed for the formation of natrocarbonatites is silicate-carbonate liquid immiscibility (Church and Jones, 1995; Dawson et al., 1996; Keller and Krafft, 1990; Kjarsgaard et al., 1995; Mitchell, 2009; Mitchell and Dawson, 2012; Peterson, 1990; Sharygin et al., 2012). Liquid immiscibility is defined as "*the coexistence of two or more liquid phases in equilibrium…[and]…occurs when the sum of the free energies of two melts in less than that of a mixture of them*" Freestone (1989). The rarity of and difficulty in capturing definitive evidence of liquid immiscibility within magmas has posed a challenge for researchers, as the rocks undergo crystallisation and post-magmatic alteration. For evidence to be preserved of the unmixing process, the liquids must either spatially separate or undergo no magmatic or weathering processes after unmixing. Consequently, the process of liquid immiscibility and its role in magmatic differentiation has been largely overlooked.

Melt inclusion and experimental studies are the primary methods used to support the identification of liquid immiscibility during the formation of magmatic rocks. Melt inclusions provide 'snapshots' of melts and fluids at the time of crystallisation and have recorded occurrences of liquid immiscibility in magmas from a variety of different tectonic settings (Kamenetsky and Kamenetsky, 2010; Mitchell, 2009; Panina and Motorina, 2008; Sekisova et al., 2015; Thompson et al., 2007). Experimental work endeavors to reproduce the sequence and composition of the phases appearing in natural rocks, offering theoretical conditions for these unmixing processes (Brooker and Kjarsgaard, 2011; Freestone and Hamilton, 1980; Kjarsgaard and Peterson, 1991; Moore, 2012; Veksler et al., 2012; Wyllie et al., 1990). The small size (<25 μm) and disequilibrium state within the melt inclusions, and the limited applicability of experimental studies to the natural environment renders some of the evidence and interpretations controversial.

Here we describe the texture and mineralogy of natrocarbonatite lava samples from the 1993 eruption at Oldoinyo Lengai and present both petrographic and melt inclusion evidence for the occurrence of liquid immiscibility between silicate, carbonate, chloride, and fluoride melt phases.

* Corresponding author.
E-mail address: pottern@utas.edu.au (N.J. Potter).

http://dx.doi.org/10.1016/j.chemgeo.2016.09.034
0009-2541/

2. Geological setting and previous work

Oldoinyo Lengai, the only active natrocarbonatite volcano in the world, is situated within the Gregory Rift Valley in northern Tanzania. Between June 14 and June 25, 1993, two of the most volumetrically largest lava flows erupted at Oldoinyo Lengai: the massive southern flow and the Chaos Crags flow (Dawson et al., 1994). These eruptions terminated a 10-year period that was dominated by the extrusion of low-volume, highly mobile carbonatite flows (Dawson et al., 1996). The samples investigated here are from the Chaos Crags flow, which is a particularly crystal-rich lava (79–91% by volume), with a similar viscosity to rhyolite (Dawson et al., 1994). Several previous studies have investigated samples from the June 1993 lava and reported detailed descriptions of the eruption with petrography and mineralogy of the lava (Church and Jones, 1995; Dawson et al., 1994; Dawson et al., 1996) and geochemical data (Simonetti et al., 1997).

3. Methodology

The samples were mounted in epoxy resin and polished using kerosene to prevent destruction of soluble minerals and melt inclusions. After exposure, samples were stored in a desiccator to minimise interaction with atmospheric moisture. All analytical work was performed at the Central Science Laboratory (CSL), University of Tasmania, Australia.

Mineral and melt inclusion compositions were determined by backscattered electron (BSE) imaging and energy dispersive X-ray spectrometry (EDS) using a Hitachi SU-70 field emission scanning electron microscope (SEM). Silicate and fluorapatite kernels were analysed using a Cameca SX100 electron microprobe equipped with a tungsten filament and five wavelength dispersive spectrometers (WDS) using 15 kV accelerating voltage, 30 and 20 nA beam current and a 5 and 20 μm beam diameter, respectively. Additional details are provided in Supplementary Methods. Electron backscattered diffraction (EBSD) on a Hitachi SU-70 SEM was used to evaluate the crystallographic orientation of the crystal microstructures. Ion-polishing for EBSD studies was done in Adelaide Microscopy. The EBSD analysis was performed using 20 kV acceleration voltage, around 3 nA beam current and an Oxford AZtec NordlysNano EBSD detector integrated with the EDS system.

4. Results

The lava is a porphyritic natrocarbonatite composed of abundant euhedral to subhedral phenocrysts of alkali carbonates, nyerereite $Na_2Ca(CO_3)_2$ and gregoryite $(Na_2K_2Ca)CO_3$, surrounded by a quenched carbonatite groundmass (Fig. 1). Dispersed in the lava samples are silicate spheroids (<2 mm) characterised by a core kernel (>200 μm) enveloped in a cryptocrystalline assemblage composed of various silicate minerals. The lava has a low to moderate vesicularity (7–26% vesicles), with a size distribution from <50 μm to 10 mm. Small vesicles have subspherical shapes, whereas the large vesicles are irregular and elongated, often showing signs of coalescence.

4.1. Groundmass

The carbonatite groundmass accounts for around 20% of the lavas' volume (excluding vesicles) and is mainly composed of sodium carbonate, khanneshite $(NaCa)_3(Ba,Sr,Ce,Ca)_3(CO_3)_5$, salt aggregates and a CaF phase (Fig. 2). Scattered throughout the carbonatite groundmass are anhedral to subhedral crystals (<20 μm) of apatite, cuspidine $Ca_4(Si_2O_7)(F,OH)_2$, nepheline $(Na,K)AlSiO_4$ and sulphides.

The primary constituent of the groundmass is a sodium-rich carbonate phase (Figs. 2, 3) that has a similar chemical composition to the gregoryite phenocrysts but contains slightly more Na (32% and 31%, respectively) and less Ca (5% and 7%, respectively). Another groundmass carbonate is Ba-rich (38–41 wt.% BaO), similar to khanneshite, distributed sporadically in the lava and has irregular, angular shapes (Fig. 1b). The salt aggregates are composed of two chloride end-members: potassium and sodium chloride, with both phases containing minor Na and K, respectively. Potassium chloride (Na-sylvite) is the primary component with sodium chloride (K-halite) dispersed inside, although there are areas composed of pure halite. Irrespective of their composition, all salt aggregates have spherical to irregular shapes (Fig. 3). The CaF phase exhibits linear, globular, symplectic, and graphic textures (Fig. 3), similar textures have been observed by Church and Jones (1995) and Dawson et al. (1996). The texture of the CaF phase varies throughout the samples and appears to be dependent on the surrounding phases, the most prevalent is the linear intergrowth texture (Fig. 3b). There are several crystallographic orientations observed for a given CaF phase (Fig. 4c; d). The variation in colour in Fig. 4c and d indicates a difference in the orientation of the crystals, that is attributed to changes in the x, y and z axis. The stoichiometric composition is 44–47 wt.% F, 50–53 wt.% Ca and 1–4 wt.% Sr.

The sulphide minerals identified within the groundmass are pyrrhotite, Fe-alabandite MnS, Mn-sphalerite (Zn,Fe)S, djerfisherite $K_6Na(Fe,Cu,Ni)_{22}S_{26}Cl$ and galena. These sulphides mostly occur as small individual (<20 μm) anhedral crystals, as well as rare clusters (25–75 μm). The K-Fe-sulphide mineral has been identified as djerfisherite by the K:Fe:S ratio, despite the lack of Cu, Ni and Cl. The djerfisherite crystals occur as anhedral grains ranging in size from 5 μm to 100 μm, and contain 8–11% K and 38–44% Fe. K-Fe-sulphide minerals have been observed in other natrocarbonatite lavas at Oldoinyo Lengai (Dawson et al., 1995; Jago and Gittins, 1999; Mitchell, 1997; Mitchell, 2006). The irregular distribution of the sulphide minerals throughout the groundmass and in phenocrysts suggests that they were present in the magma prior to eruption, as supported by Mitchell (1997) in the case of the 1995 eruption.

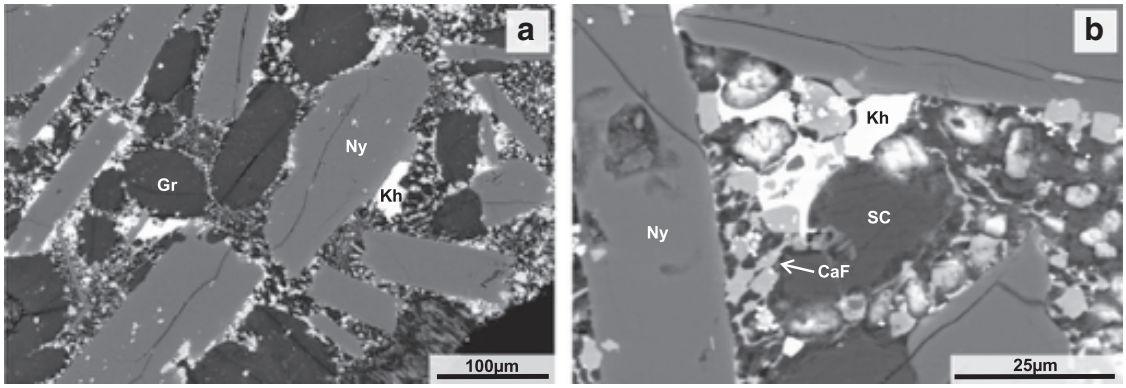

Fig. 1. (a) Back scattered electron (BSE) image of the 1993 lava, with nyerereite and gregoryite phenocrysts surrounded by the carbonatite groundmass. (b) BSE image of khanneshite in the carbonatite groundmass. Abbreviations: CaF – calcium fluoride, Gr – gregoryite, Kh – khanneshite, Ny – nyerereite, SC – sodium carbonate.

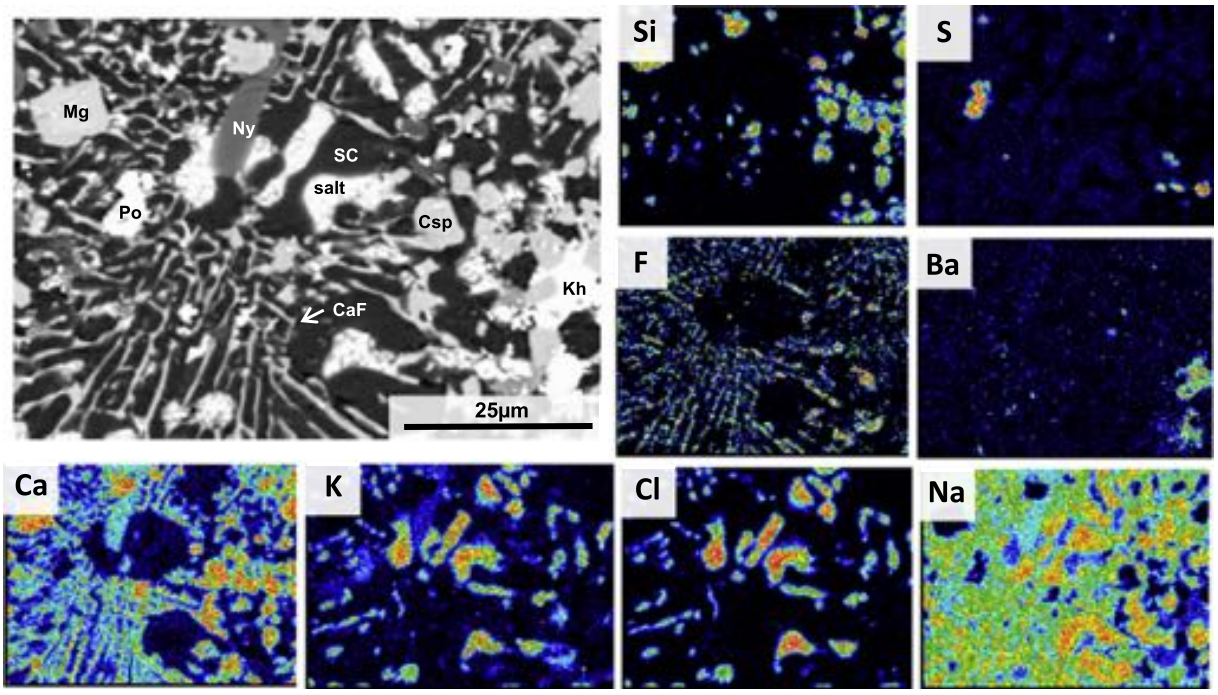

Fig. 2. BSE image and EDS element maps of the carbonatite groundmass. Abbreviations: CaF – calcium fluoride, Csp – cuspidine, Kh – khanneshite, Mg – magnetite, Ny – nyerereite, Po – pyrrhotite, salt – K-halite and Na-sylvite, SC – sodium carbonate.

Other accessory minerals found in the groundmass are euhedral to subhedral crystals of fluorapatite, nepheline, cuspidine, and magnetite with an elevated concentration of Mn (1–4 wt.%). The cuspidine crystals (<20 μm) exhibit oscillatory zoning and contain numerous inclusions of Mn-magnetite. Other rare minerals include a potentially water-bearing potassium sulphate (<10 um) and an unknown Ba-K-Na-Mg fluoride mineral that forms small (<10 μm) anhedral grains. A similar fluoride mineral was identified by Mitchell (1997) as an intermediate member between neighborite and its potassium analogue, identified as K-neighborite (Na,K)MgF_3.

4.2. Silicate spheroids

The silicate spheroids (<2 mm) feature a central kernel (<1 mm) surrounded by a cryptocrystalline assemblage of clinopyroxene, garnet, nepheline, wollastonite, fluorapatite, magnetite, cuspidine and various sulphides (<20 μm; Fig. 5). There is a distinct boundary between the spheroids and the surrounding carbonatite groundmass, with nyerereite phenocrysts oriented around the spheroids (Fig. 5a). The amount of the silicate material around kernels varies from a thin coating (Fig. 5d) to a much greater thickness that can fluctuate around the kernel (Fig. 5a, c). The kernel is usually a single euhedral crystal, or less commonly two or more crystal species either isolated or as a crystal aggregate (Fig. 5a-d). These grains are typically nepheline, clinopyroxene, garnet, wollastonite and fluorapatite. A subspherical carbonate phase is present within the silicate mineral assemblage, ranging in size from 10 to 150 μm (Fig. 5e, f). Some have separated into two carbonate compositions, a Na-rich phase (30–40 wt.% Na_2O), and a Ca-rich phase (23–28 wt.% CaO, 7–8 wt.% K_2O), both have irregular shapes, usually with the Ca-rich phase enveloped by the Na-rich phase.

4.2.1. Kernels

The majority of the nepheline grains have a homogeneous composition (Fig. 5b) with a small number exhibiting minor zonation with antithetic variations in FeO and K_2O concentrations (0.9–2.4 wt.% and 6–7.3 wt.%, respectively). The wollastonite grains are lath-shaped and have homogeneous compositions. Garnet grains belong to the andradite-schorlomite solid solution series and are identified as schorlomite end-members due to their high TiO_2 contents (10–15 wt.%; Fig. 5c). This mineral is referred to as Ti-andrandite by Dawson et al. (1996) and melanite by Church and Jones (1995). Clinopyroxene grains have predominantly low-Al, low-Ti compositions and display irregular oscillatory zoning with varying Mg and Fe contents that are readily observed in the BSE images (higher and lower Mg/Fe ratios correspond to darker and lighter areas, respectively; Fig. 5d). The fluorapatite grains have high F contents (2–3 wt.%) and are less common than the previously mentioned silicate minerals. All kernels contain inclusions (10–50 μm) of other minerals including wollastonite, schorlomite, nepheline, clinopyroxene, titanite, and pyrrhotite. The chemical compositions of the kernels are provided in Supplementary Table S1. Detailed descriptions of the kernels in the silicate spheroids are given in Church and Jones (1995), Dawson et al. (1994) and Dawson et al. (1996).

4.3. Alkali carbonate phenocrysts

The nyerereite phenocrysts are primarily euhedral lath-shaped crystals (Fig. 1) with homogeneous compositions and inclusions (<50 μm) of fluorapatite, unknown Ba-K-Na-Mg fluoride, and small clusters (<50 μm) of cuspidine and djerfisherite crystals (<10 μm). The gregoryite phenocrysts have mostly rounded shapes with no well-defined crystal faces (Fig. 1) and occasionally contain inclusions (5–20 μm) of nyerereite, magnetite and djerfisherite. These crystals differ in their degree of chemical and textural alteration, some phenocrysts have homogenous compositions, while others have perthitic textures with variation in the Na and K content across each phenocryst (4–39 wt.% and 14–33 wt.%, respectively). Some altered phenocrysts display simple lamellar textures, whereas irregular, patchy textures with disseminated halite or K-halite are dominant (Supplementary Figs. S35–40). The lamellar textures suggest the breakdown of the gregoryite solid solution (Dawson et al., 1995). Also, the rims of the chemically altered gregoryite phenocrysts are more texturally uneven than the homogeneous phenocrysts.

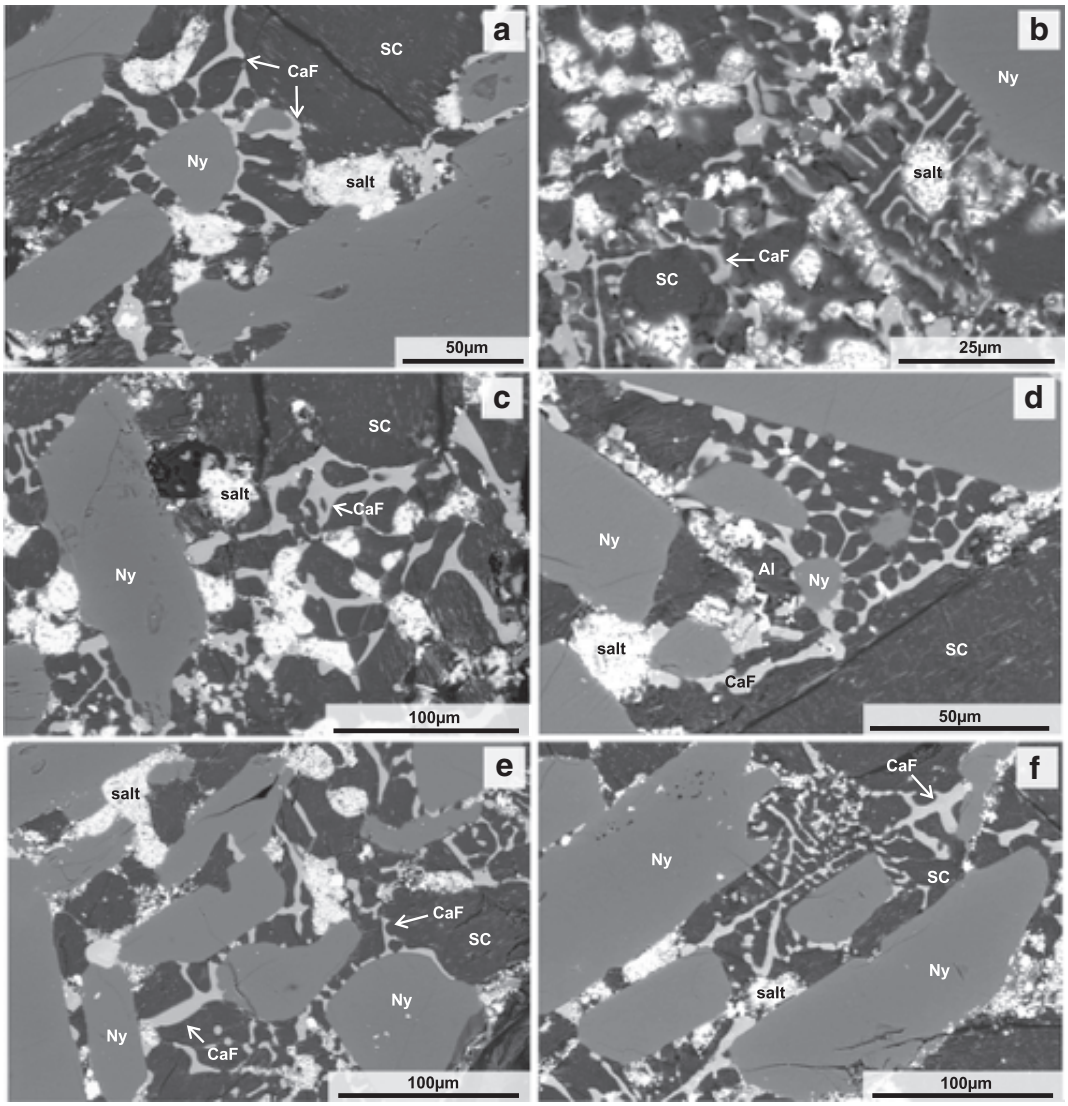

Fig. 3. BSE images of groundmass textures in the June 1993 lava. Abbreviations: Al – Fe-alabandite, CaF – calcium fluoride phase, Ny – nyerereite, salt – K-halite and Na-sylvite, SC – sodium carbonate.

The chemical compositions of the nyerereite and gregoryite phenocrysts do not differ significantly from those documented in other natrocarbonatite lavas, except for the nyerereite phenocrysts which have high BaO contents (up to 3 wt.%; Supplementary Table S2). More details on the composition and textures of nyerereite and gregoryite phenocrysts from other eruptions are described in Mitchell and Kamenetsky (2012), Peterson (1990) and Zaitsev et al. (2009).

4.4. Melt inclusions

The exposed silicate and carbonate melt inclusions have a negative crystallographic shape and are randomly distributed throughout the crystals (Fig. 6). These are primary melt inclusions and represent the melt composition at the time of entrapment, but may not represent the bulk composition as all phases may not have been observed.

4.4.1. Silicate spheroids

The silicate melt inclusions (10 to 50 μm) are identified in all the silicate kernel minerals (nepheline, wollastonite, clinopyroxene and schorlomite; Fig. 6a-e). The glasses are silica-undersaturated and highly enriched in alkali elements (Supplementary Table S3). The majority of the silicate melt inclusions contain small Na-rich carbonate globules (2–10 μm) and occasionally enclose small crystals (2–5 μm) of apatite, clinopyroxene, magnetite and pyrrhotite. The wollastonite-hosted melt inclusions are also characterised by the presence of annite (10 to 30 vol.%; Fig. 6c).

The clinopyroxene and schorlomite phenocrysts contain both silicate and silicate-carbonate melt inclusions. The silicate-carbonate melt inclusions contain Na-rich carbonate globules along with a polycrystalline carbonate globule (5–20 μm) composed of a fine-grained aggregate of Na-rich and Ca-rich carbonate phases, similar to the carbonate component in the silicate spheroids (Fig. 6d, e).

4.4.2. Alkali carbonate and fluorapatite phenocrysts

Primary carbonate melt inclusions (5–25 μm) have been identified in nyerereite, gregoryite and fluorapatite phenocrysts (Fig. 6f-i). These melt inclusions are scarce in comparison to the silicate melt inclusions as nyerereite and gregoryite typically lack melt inclusions. The carbonate melt inclusions have comparable chemical compositions to the carbonatite groundmass. The fluorapatite-hosted carbonate melt inclusions contain Na-rich carbonate and inclusions of apatite, magnetite and calcite (Fig. 6f). Some of the melt inclusions have separated into an alkali carbonate and khanneshite, with daughter phases of cuspidine, nepheline, and an unknown Ba-K-Na-Mg fluoride (Fig. 6g). Rare melt

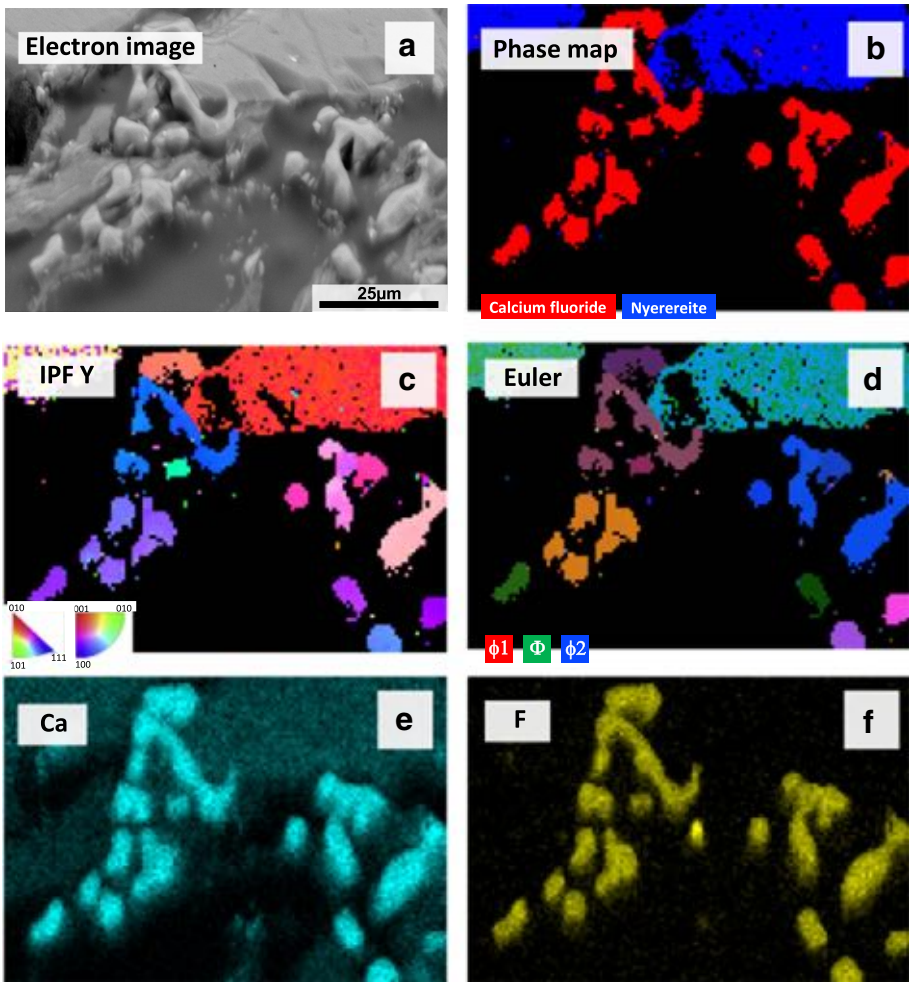

Fig. 4. (a) Electron image of the area mapped with a clear outline of the calcium fluoride (CaF) phase, (b) Phase map based on combined EDS and EBSD data showing the CaF phase, (c) Inverse pole figure (IPF) map in the Y direction showing varying crystal orientations in different colours, (d) Euler angle map using colours to denote the variety of crystal orientations in space using Euler angles: φ1-red φ-green, φ2-blue, (e-f) EDS compositional maps showing the uniform concentration of calcium and fluorine in the CaF phase.

inclusions hosted in gregoryite contain a single nyerereite crystal in a heterogeneous carbonate-Na-sylvite matrix (Fig. 6h). In contrast, the nyerereite phenocrysts contain abundant melt inclusions, composed of sodium carbonate, CaF and Na-sylvite with trapped crystals of cuspidine, apatite, and magnetite (Fig. 6i).

5. Discussion

5.1. Silicate-carbonate immiscibility

Occurrences of silicate-carbonate liquid immiscibility are widespread in nature and have been well documented in several alkaline carbonate-bearing complexes (Guzmics et al., 2011; Guzmics et al., 2012; Lloyd and Stoppa, 2003; Mitchell, 2009; Mitchell and Dawson, 2012; Nielsen et al., 1997; Panina, 2005; Sharygin et al., 2012; Zaitsev et al., 2009). In our study, textural features of the silicate spheroids, melt inclusions and carbonatite groundmass provide evidence of silicate-carbonate immiscibility. The main textural evidence that supports liquid immiscibility in the lava is the distinct boundaries between different compositions in the melt inclusions and groundmass.

As textural evidence for liquid immiscibility is rarely preserved in rocks, melt inclusions are fundamental for the identification of unmixing in natural systems. The onset of silicate-carbonate immiscibility in carbonate-rich magmatic systems is an area of ongoing research, and there have been several heating experiments on synthetic and natural samples to determine the temperature and pressure of unmixing (Freestone and Hamilton, 1980; Kjarsgaard et al., 1995; Koster van Groos and Wyllie, 1966; Sharygin et al., 2012).

The silicate spheroids are identified as immiscible droplets of nephelinitic composition, which is consistent with previous interpretations (Church and Jones, 1995; Dawson et al., 1994; Dawson et al., 1996). The distinct boundary between the spheroids and the surrounding carbonatite, the rounded shape of the spheroids, the orientation of the nyerereite phenocrysts around the spheroids and the absence of penetration by these phenocrysts (Fig. 5a, b), all support the idea that silicate-carbonate liquid immiscibility enabled the formation of the silicate spheroids. These textures also suggest that the silicate spheroids were molten when first enveloped by the carbonate melt, enabling a subspherical shape. The silicate spheroids subsequently cooled and solidified prior to the crystallisation of the surrounding carbonate melt preventing the carbonate melt from penetrating the spheroids, an interpretation first proposed by Dawson et al. (1996).

The presence of the carbonate component within the silicate mineral assemblage in the spheroids (Fig. 5e, f) suggests that silicate-carbonate immiscibility proceeds with changes in temperature and pressure in the magmatic system. The carbonate components have comparable chemical compositions, however, some have separated into Ca-rich and Na-rich phases similar to the carbonate globules in the silicate-carbonate melt inclusions (e.g. Fig. 6d), suggesting that the carbonate melt had a comparable chemical composition during unmixing. Dawson et al.

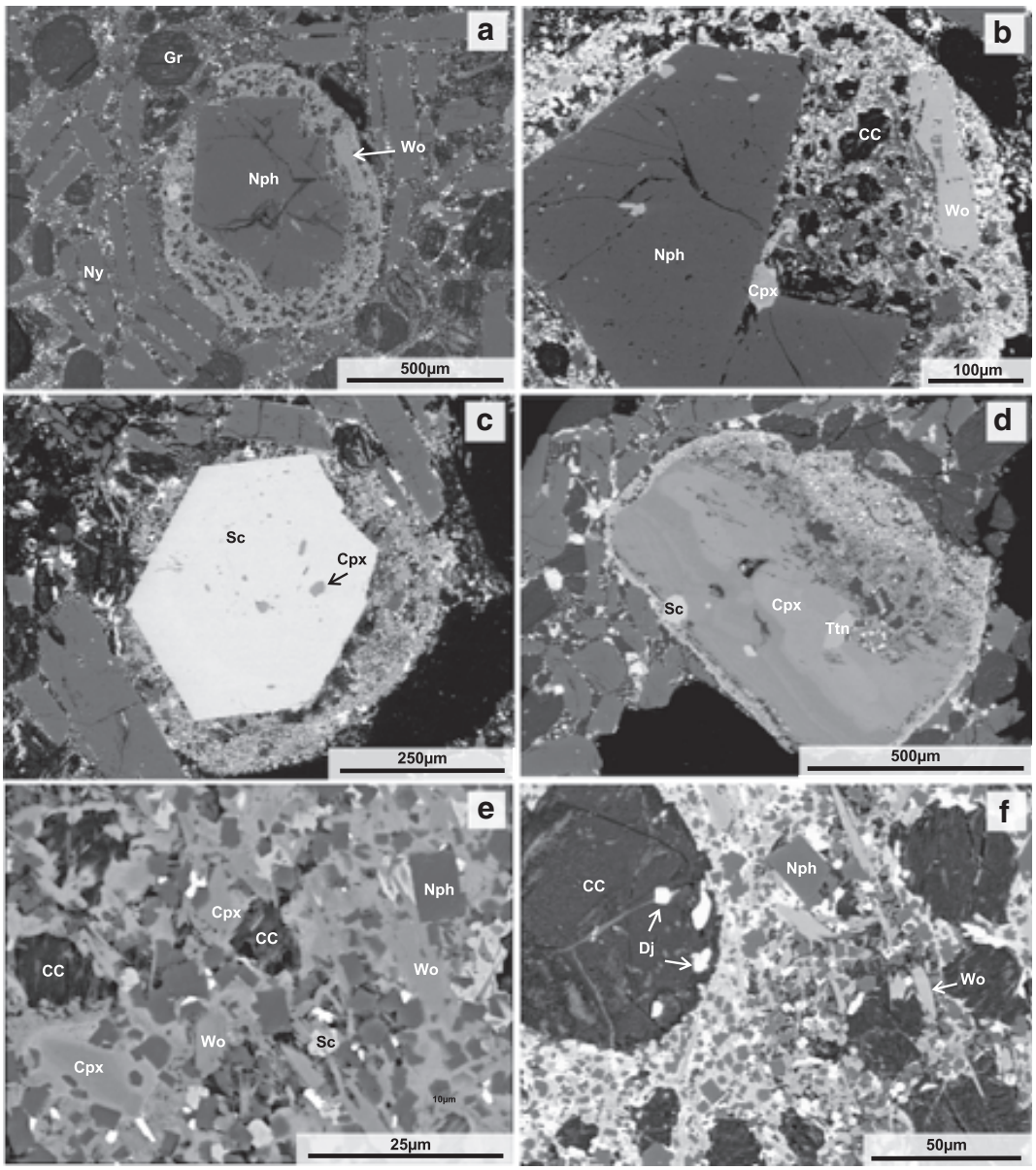

Fig. 5. BSE images of silicate spheroids in the June 1993 lava. (a, b) Nepheline kernel surrounded by a silicate mineral assemblage, (c) Schorlomite kernel surrounded by a silicate mineral assemblage, (d) Clinopyroxene kernel surrounded by a thin coating of the silicate mineral assemblage, (e, f) Close up of the silicate mineral assemblage within the silicate spheroids. Abbreviations: CC – carbonate component, Cpx – clinopyroxene, Dj – djerfisherite, Gr – gregoryite, Nph – nepheline, Ny – nyerereite, Sc – schorlomite, Ttn – titanate, Wo – wollastonite.

(1994) suggested "*the presence of carbonatite phases in the glasses entrapped in both the spheroid silicate phenocrysts and the spheroid matrix indicates that the spheroids are exhibiting multiple episodes of separation of carbonatite from a silicate melt*". The timing of separation of the carbonate component from the surrounding silicate melt remains unknown. However, we suggest that liquid immiscibility during magmatic ascent and cooling could have enabled the separation of the carbonate component from the surrounding silicate melt. Another possiblility could be that the carbonate component was trapped in the silicate melt when the silicate spheroids were first incorporated into the natrocarbonatite magma at the top of the magma chamber.

The kernels in the silicate spheroids do not represent phenocrysts in the natrocarbonatite magma, but they crystallised from the nephelinitic melt in the magma chamber. The kernels host silicate melt inclusions that are interpreted to represent the parental peralkaline nephelinitic magma in the magma chamber. The coexsistence of silicate and silicate-carbonate melt inclusions in the clinopyroxene and schorlomite kernels is the evidence for onset of silicate-carbonate liquid immiscibility, with the separation of the melt into two coexisting silicate and carbonate liquids.

The presence of cuspidine, nepheline and tilleyite in the groundmass is evidence that silica was present in the natrocarbonatite magma during crystallisation (Fig. 2; Dawson et al., 1996). The crystallisation of cuspidine is enabled by the significant concentration of fluorine in the natrocarbonatite magma.

5.1.1. Petrogenesis of silicate spheroids

The presence of silicate spheroids has not been reported in other natrocarbonatite lavas at Oldoinyo Lengai. The petrogenic model envisaged for the formation of these silicate spheroids in the 1993 lava is an adaptation of the processes suggested by Church and Jones (1995), Dawson et al. (1994) and Dawson et al. (1996), and is summarised here (Fig. 7). Prior to the 1993 eruption an injection of peralkaline nephelinitic magma intruded into the magma chamber (Fig. 7b). The intrusion disrupted the carbonate crystal mush at the top of the magma chamber that contains a high modal abundance of nyerereite and

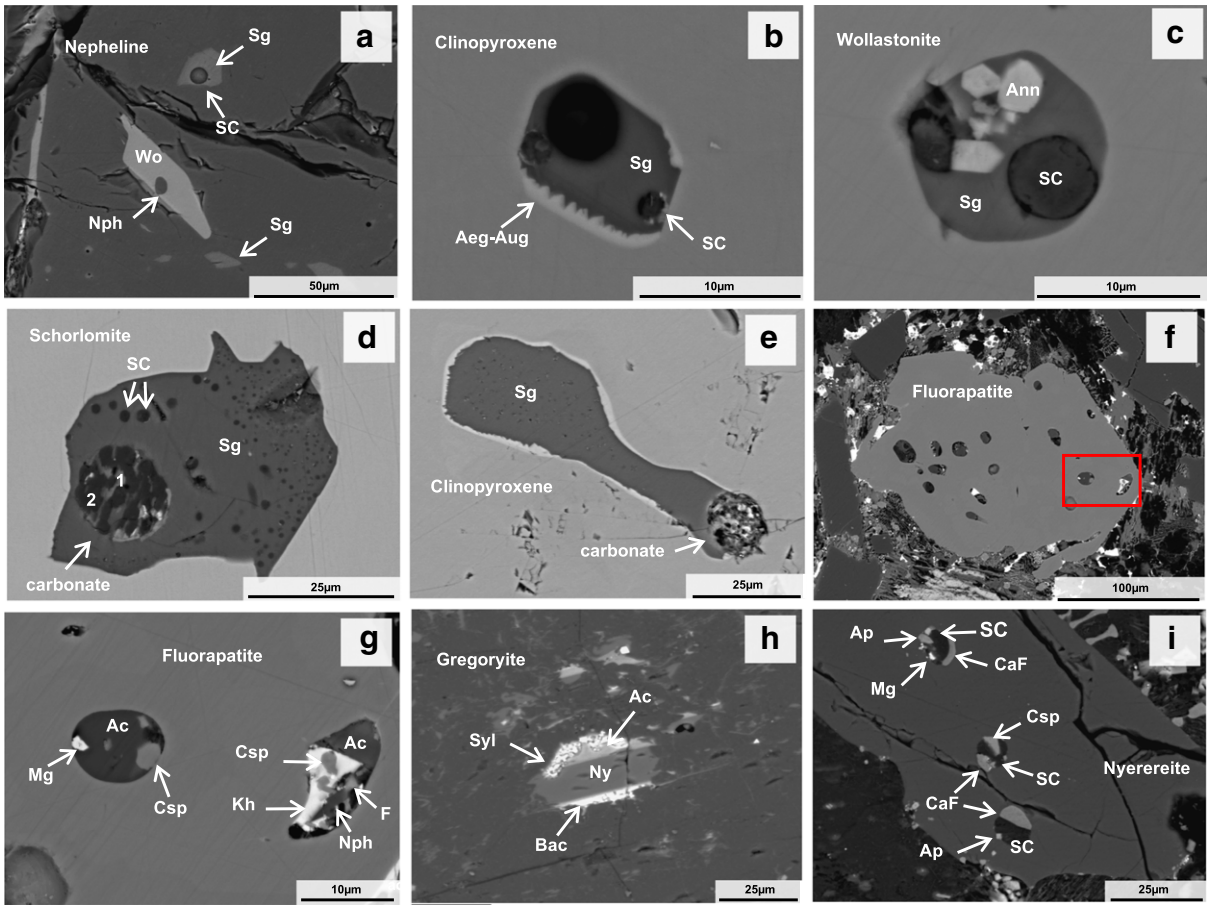

Fig. 6. BSE images of silicate and carbonate melt inclusions. (a) Nepheline kernel with silicate melt inclusions, (b) Clinopyroxene-hosted silicate melt inclusion with an intermediate reaction rim of aegirine-augite, (c) Wollastonite-hosted silicate melt inclusion, (d) Schorlomite-hosted silicate melt inclusion with a carbonate globule, (e) Clinopyroxene-hosted silicate melt inclusion with a carbonate globule, (f) Fluorapatite phenocryst in the carbonatite groundmass with numerous carbonate melt inclusions, (g) A close up of carbonate melt inclusions in the fig. 6f fluorapatite phenocryst, (h) Gregoryite-hosted carbonate melt inclusion, (i) Nyerereite-hosted carbonate melt inclusion. Abbreviations: Ac – alkali-carbonate, Aeg – aegirine, Ann – annite, Ap – apatite, Aug. – augite, Bac – barium-rich carbonate, CaF – calcium fluoride phase, Csp – cuspidine, F – unknown Ba-K-Na-Mg fluoride, Kh – khanneshite, Mg – magnetite, Nph – nepheline, Ny – nyerereite, SC – sodium carbonate, Sg – silicate glass, Syl – Na-sylvite, Wo – wollastonite, 1 – calcium-rich phase, 2 – sodium-rich phase.

gregoryite phenocrysts (Dawson et al., 1994; Dawson et al., 1996). This enabled the incorporation of silicate kernels into the natrocarbonatite magma, with a silicate melt surrounding the kernels (Fig. 7c). The elevated viscosity of the 1993 natrocarbonatite magma (i.e. nyerereite and gregoryite crystal mush; Dawson et al., 1994; Dawson et al., 1996) prevented the silicate spheroids from settling back into the nephelinitic magma (Fig. 7c).

5.2. Carbonate-carbonate immiscibility

Two carbonate phases have been identified within the groundmass of the June 1993 lava: sodium carbonate and khanneshite. Dawson et al. (1996) also identified two carbonate groundmass phases, a gregoryite-like phase and a Ba-rich carbonate phase referred to as witherite. The Ba-rich carbonate phase has a variety of compositions in other natrocarbonatite lavas, most likely caused by the different chemical compositions of the carbonate melt (Dawson et al., 1996; Mitchell, 1997; Mitchell, 2006; Peterson, 1990). The identification of two different carbonate phases in these natrocarbonatite lavas points to unmixing of carbonates as a common feature of lavas at Oldoinyo Lengai.

We suggest that carbonate-carbonate immiscibility occurred during quenching. The separation produced khanneshite and a homogeneous Na-K-rich carbonate phase containing fluorine and chlorine, which subsequently separates into sodium carbonate, CaF, and salt. The immiscible separation of these two carbonate phases was supported by Mitchell (1997), whereas Dawson et al. (1996) attributed the presence of two carbonate phases rather than one homogeneous carbonate phase (Phase X) and the coarser grain size of the "*sylvite and fluorite*" is due to slower cooling of the June 1993 lava.

5.3. Carbonate-halide immiscibility

We interpret the intergrown textures and chemical compositions of the groundmass phases: sodium carbonate, khanneshite, CaF and salt, and the presence of these same phases within the carbonate melt inclusions, to be evidence for carbonate-halide immiscibility in the June 1993 eruption at Oldoinyo Lengai. The presence of multiphase carbonate-halide immiscibility is identified by textural relationships between the carbonate, chloride, and fluoride phases in the groundmass and within the carbonate- and apatite-hosted melt inclusions. The melt inclusions have similar chemical compositions and textures as the carbonatite groundmass, which indicates that the same unmixing processes occurred on both macro- and micro-scales (Figs. 3, 6g-i). Subspherical to irregular shapes of the mixed Na-sylvite and K-halite aggregates are common in the groundmass of natrocarbonatites (Church and Jones, 1995; Dawson et al., 1995; Dawson et al., 1996; Keller and Krafft, 1990; Mitchell, 1997; Mitchell, 2006) and are most likely caused by sporadic unmixing of the chloride liquid (Fig. 3). The CaF phase has been identified in other natrocarbonatite lavas as "*intergrown fluorite with a gregoryite-like mineral*" (Church and Jones, 1995; Dawson et al., 1996; Mitchell, 1997; Mitchell, 2006). The EBSD data shows that the CaF phase has relatively homogeneous crystalline structures (Fig. 4), but

has a distinctive texture that is typical of a liquid occurring interstitially to solid phases (e.g. nyerereite in this case; Fig. 3). The high crystal content of the lava, and thus inferred high degree of crystallisation, could have led to high concentrations of fluorine and chlorine in the residual melt, prompting unmixing of halide liquids on quenching. The process of liquid immiscibility during quenching and related textures are best depicted in experimental works with carbonate-silicate compositions, where the melt components form 'immiscibility' textures, and bona fide crystallographic shapes do not have time to develop (Brooker and Kjarsgaard, 2011; Kamenetsky and Yaxley, 2015). Immiscible carbonate-halide intergrowths have been described in other natrocarbonatite lavas with different proportion and composition of the unmixed components (Mitchell, 1997; Mitchell, 2006; Peterson, 1990). The rapid quenching of the lava facilitated the preservation of the end products of these immiscibility processes within the groundmass.

5.4. Multistage immiscibility

The mineralogical and textural features of the studied samples support the following origin of the 1993 natrocarbonatite lava at Oldoinyo Lengai (Fig. 7). The unmixing of the silicate, carbonate, chloride and fluoride components can be separated into different stages of evolution in the magmatic system and represent both high- and low-pressure immiscibility.

The first stage of liquid immiscibility is recorded by the silicate spheroids and the silicate melt inclusions within the central kernels. The observation of sodium carbonate globules and fine-grained carbonate aggregates in the silicate melt inclusions indicates that the onset of silicate-carbonate liquid immiscibility happened prior to the crystallisation of the silicate minerals in the magma chamber. This immiscibility resulted in the spatial separation of the carbonate melt from the parental peralkaline nephelinitic melt in the magma chamber (Fig. 7a; Dawson et al., 1992; Mitchell, 1997; Sharygin et al., 2012). Our interpretations support that the separation happened at a shallow level within the magma plumbing system at Oldoinyo Lengai (Freestone and Hamilton, 1980; Keller and Zaitsev, 2012; Kervyn et al., 2008; Kjarsgaard et al., 1995).

The second stage of immiscibility occurred during eruption, as the decreasing temperature and pressure promotes unmixing in the carbonate melt, generating a heterogeneous mix of four immiscible phases. These fractions are represented by the two carbonate phases: sodium carbonate and khanneshite, and the two halide phases: CaF and Na-sylvite and K-halite salt aggregates.

6. Conclusions

1. The evidence presented suggests that liquid immiscibility occurred between silicate, carbonate, chloride, and fluoride melt phases in the June 1993 natrocarbonatite, and show that multi-stage liquid immiscibility is a major factor in the petrogenesis of this lava at Oldoinyo Lengai.
2. The identification of carbonate-carbonate and carbonate-halide immiscibility within the natrocarbonatite lava shows that different types of liquid immiscibility, other than silicate-silicate and silicate-carbonate, can occur in natural magmas. The identification of these

Fig. 7. (a) Stratified magma chamber with an emulsion of nephelinitic magma overlain by natrocarbonatite magma. The stratification is a result of silicate-carbonate immiscibility. The high modal abundance of gregoryite and nyerereite phenocrysts in the lava indicates that there was a high crystal content in the natrocarbonatite magma prior to eruption, identified as a carbonate crystal mush (Dawson et al., 1994; Dawson et al., 1996). (b) A new injection of nephelinitic magma intrudes into the magma chamber. As the intrusion rises and cools, it undergoes immiscibility and partially separates into carbonate and silicate melts, with the carbonate segregation accumulating at the top of the intrusion. (c) The carbonate head of the intrusion disrupts the carbonate crystal mush at the top of the magma chamber, and pushes silicate minerals into the carbonate crystal mush. The high density of crystals enabled these silicate spheroids to become trapped within the surrounding natrocarbonatite magma (Church and Jones, 1995; Dawson et al., 1994; Dawson et al., 1996). The intrusion of new ascending melt may also cause mixing within the surrounding magma. It cannot be specified whether the silicate spheroids came from the intrusion or the surrounding nephelinitic magma.

diverse unmixed phases at both the macro- and micro-scale presents clear evidence that several types of liquid immiscibility happen during evolution of a single melt, both in the magma plumbing system and during eruption.

3. Liquid immiscibility is rarely observed in the rock record due to masking effects of crystallisation and alteration, but can be observed in melt inclusion and experimental studies. The identification of unmixing in the lavas' groundmass has the potential to provide a new avenue for studying liquid immiscibility in natural magmas.

Acknowledgements

The samples of fresh natrocarbonatite lava from the Chaos Crags lava flow were collected by C. Shardy from the northern (active) crater floor of Oldoinyo Lengai on June 29, 1993. We would like to thank Aoife McFadden at Adelaide Microscopy for ion polishing. We are grateful to Adrian Jones, David Pyle, Matt Ferguson and the two anonymous reviewers for their helpful criticism and suggestions. This research was supported by the Australian Research Council (Discovery Grant DP130100257) to V. Kamenetsky.

Appendix A. Supplementary data

Supplementary data to this article can be found online at http://dx.doi.org/10.1016/j.chemgeo.2016.09.034.

References

Brooker, R.A., Kjarsgaard, B.A., 2011. Silicate-carbonate liquid immiscibility and phase relations in the system SiO_2-Na_2O-Al_2O_3-CaO-CO_2 at 0.1-2.5 GPa with applications to carbonatite genesis. J. Petrol. 52, 1281–1305.

Church, A.A., Jones, A.P., 1995. Silicate-carbonate immiscibility at Oldoinyo Lengai. J. Petrol. 36, 869–889.

Dawson, J.B., Pinkerton, H., Norton, G.E., Pyle, D.M., Browning, P., Jackson, D., Fallick, A.E., 1995. Petrology and geochemistry of Oldoinyo Lengai lavas extruded in November 1988: magma source, ascent and crystallization. In: Bell, K., Keller, J. (Eds.), Carbonatite Volcanism. Springer, pp. 47–69.

Dawson, J.B., Pinkerton, H., Pyle, D.M., Nyamweru, C., 1994. June 1993 eruption of Oldoinyo Lengai, Tanzania: exceptionally viscous and large carbonatite lava flows and evidence for coexisting silicate and carbonate magmas. Geology 22, 799–802.

Dawson, J.B., Pyle, D.M., Pinkerton, H., 1996. Evolution of natrocarbonatite from a wollastonite nephelinite parent: evidence from the June 1993 eruption of Oldoinyo Lengai, Tanzania. J. Geol. 41–54.

Dawson, J.B., Smith, J.V., Steele, I.M., 1992. 1966 ash eruption of the carbonatite volcano Oldoinyo Lengai: mineralogy of lapilli and mixing of silicate and carbonate magmas. Mineral. Mag. 56, 1–16.

Freestone, I.C., 1989. Liquid Immiscibility, Petrology. Springer, pp. 281–283.

Freestone, I.C., Hamilton, D.L., 1980. The role of liquid immiscibility in the genesis of carbonatites - an experimental study. Contrib. Mineral. Petrol. 73, 105–117.

Guzmics, T., Mitchell, R.H., Szabó, C., Berkesi, M., Milke, R., Abart, R., 2011. Carbonatite melt inclusions in coexisting magnetite, apatite and monticellite in Kerimasi calciocarbonatite, Tanzania: melt evolution and petrogenesis. Contrib. Mineral. Petrol. 161, 177–196.

Guzmics, T., Mitchell, R.H., Szabó, C., Berkesi, M., Milke, R., Ratter, K., 2012. Liquid immiscibility between silicate, carbonate and sulfide melts in melt inclusions hosted in co-precipitated minerals from Kerimasi volcano (Tanzania): evolution of carbonated nephelinitic magma. Contrib. Mineral. Petrol. 164, 101–122.

Jago, B.C., Gittins, J., 1999. Mn- and F-bearing rasvumite in natrocarbonatite at Oldoinyo Lengai volcano, Tanzania. Mineral. Mag. 63, 53–55.

Kamenetsky, V.S., Kamenetsky, M.B., 2010. Magmatic fluids immiscible with silicate melts: examples from inclusions in phenocrysts and glasses, and implications for magma evolution and metal transport. Geofluids 10, 293–311.

Kamenetsky, V.S., Yaxley, G.M., 2015. Carbonate–silicate liquid immiscibility in the mantle propels kimberlite magma ascent. Geochim. Cosmochim. Acta 158, 48–56.

Keller, J., Krafft, M., 1990. Effusive natrocarbonatite activity of Oldoinyo Lengai, June 1988. Bull. Volcanol. 52, 629–645.

Keller, J., Zaitsev, A.N., 2012. Geochemistry and petrogenetic significance of natrocarbonatites at Oldoinyo Lengai, Tanzania: Composition of lavas from 1988 to 2007. Lithos 148, 45–53.

Kervyn, M., Ernst, G.G.J., Klaudius, J., Keller, J., Kervyn, F., Mattsson, H.B., Belton, F., Mbede, E., Jacobs, P., 2008. Voluminous lava flows at Oldoinyo Lengai in 2006: chronology of events and insights into the shallow magmatic system. Bull. Volcanol. 70, 1069–1086.

Kjarsgaard, B., Peterson, T., 1991. Nephelinite-carbonatite liquid immiscibility at Shombole volcano, East Africa: petrographic and experimental evidence. Mineral. Petrol. 43, 293–314.

Kjarsgaard, B.A., Hamilton, D.L., Peterson, T.D., 1995. Peralkaline nephelinite/carbonatite liquid immiscibility: comparison of phase compositions in experiments and natural lavas from Oldoinyo Lengai. In: Bell, K., Keller, J. (Eds.), Carbonatite Volcanism. Springer, pp. 163–190.

Koster van Groos, A.F., Wyllie, P.J., 1966. Liquid immiscibility in the system Na_2O-Al_2O_3-SiO_2-CO_2 at pressures up to 1 kilobar. Am. J. Sci. 264, 234–235.

Lloyd, F.E., Stoppa, F., 2003. Pelletal lapilli in diatremes—some inspiration from the old masters. Geolines 15, 65–71.

Mitchell, R.H., 1997. Carbonate-carbonate immiscibility, neighborite and potassium iron sulphide in Oldoinyo Lengai natrocarbonatite. Mineral. Mag. 61, 779–789.

Mitchell, R.H., 2005. Carbonatites and carbonatites and carbonatites. Can. Mineral. 43, 2049–2068.

Mitchell, R.H., 2006. Sylvite and fluorite microcrysts, and fluorite-nyerereite intergrowths from natrocarbonatite, Oldoinyo Lengai, Tanzania. Mineral. Mag. 70, 103–114.

Mitchell, R.H., 2009. Peralkaline nephelinite–natrocarbonatite immiscibility and carbonatite assimilation at Oldoinyo Lengai, Tanzania. Contrib. Mineral. Petrol. 158, 589–598.

Mitchell, R.H., Dawson, J.B., 2012. Carbonate-silicate immiscibility and extremely peralkaline silicate glasses from Nasira cone and recent eruptions at Oldoinyo Lengai volcano, Tanzania. Lithos 152, 40–46.

Mitchell, R.H., Kamenetsky, V.S., 2012. Trace element geochemistry of nyerereite and gregoryite phenocrysts from natrocarbonatite lava, Oldoinyo Lengai, Tanzania: Implications for magma mixing. Lithos 152, 56–65.

Moore, K.R., 2012. Experimental study in the Na_2O–CaO–MgO–Al_2O_3–SiO_2–CO_2 system at 3 GPa: the effect of sodium on mantle melting to carbonate-rich liquids and implications for the petrogenesis of silicocarbonatites. Mineral. Mag. 76, 285–309.

Nielsen, T.F.D., Solovova, I.P., Veksler, I.V., 1997. Parental melts of melilitolite and origin of alkaline carbonatite: evidence from crystallised melt inclusions, Gardiner complex. Contrib. Mineral. Petrol. 126, 331–344.

Panina, L.I., 2005. Multiphase carbonate-salt immiscibility in carbonatite melts: data on melt inclusions from the Krestovskiy massif minerals (Polar Siberia). Contrib. Mineral. Petrol. 150, 19–36.

Panina, L.I., Motorina, I.V., 2008. Liquid immiscibility in deep-seated magmas and the generation of carbonatite melts. Geochem. Int. 46, 448–464.

Peterson, T.D., 1990. Petrology and genesis of natrocarbonatite. Contrib. Mineral. Petrol. 105, 143–155.

Sekisova, V.S., Sharygin, V.V., Zaitsev, A.N., Strekopytov, S., 2015. Liquid immiscibility during crystallization of forsterite-phlogopite ijolites at Oldoinyo Lengai volcano, Tanzania: study of melt inclusions. Russ. Geol. Geophys. 56, 1717–1737.

Sharygin, V.V., Kamenetsky, V.S., Zaitsev, A.N., Kamenetsky, M.B., 2012. Silicate–natrocarbonatite liquid immiscibility in 1917 eruption combeite–wollastonite nephelinite, Oldoinyo Lengai Volcano, Tanzania: Melt inclusion study. Lithos 152, 23–39.

Simonetti, A., Bell, K., Shrady, C., 1997. Trace-and rare-earth-element geochemistry of the June 1993 natrocarbonatite lavas, Oldoinyo Lengai (Tanzania): Implications for the origin of carbonatite magmas. J. Volcanol. Geotherm. Res. 75, 89–106.

Thompson, A.B., Aerts, M., Hack, A.C., 2007. Liquid immiscibility in silicate melts and related systems. Rev. Mineral. Geochem. 65, 99–127.

Veksler, I.V., Dorfman, A.M., Dulski, P., Kamenetsky, V.S., Danyushevsky, L.V., Jeffries, T., Dingwell, D.B., 2012. Partitioning of elements between silicate melt and immiscible fluoride, chloride, carbonate, phosphate and sulfate melts, with implications to the origin of natrocarbonatite. Geochim. Cosmochim. Acta 79, 20–40.

Woolley, A.R., 2003. Igneous silicate rocks associated with carbonatites: their diversity, relative abundances and implications for carbonatite genesis. Periodico di Mineralogia 72, 17.

Wyllie, P.J., Baker, M.B., White, B.S., 1990. Experimental boundaries for the origin and evolution of carbonatites. Lithos 26, 3–19.

Zaitsev, A.N., Keller, J., Spratt, J., Jeffries, T.E., Sharygin, V.V., 2009. Chemical composition of nyerereite and gregoryite from natrocarbonatites of Oldoinyo Lengai volcano, Tanzania. Geol. Ore Deposits 51, 608–616.

Contributions to Mineralogy and Petrology (2018) 173:100
https://doi.org/10.1007/s00410-018-1531-9

ORIGINAL PAPER

Textural evolution of perovskite in the Afrikanda alkaline–ultramafic complex, Kola Peninsula, Russia

Naomi J. Potter[1] · Matthew R. M. Ferguson[1] · Vadim S. Kamenetsky[1] · Anton R. Chakhmouradian[2] · Victor V. Sharygin[3,4] · Jay M. Thompson[1] · Karsten Goemann[5]

Received: 10 July 2018 / Accepted: 9 November 2018

Abstract

Perovskite is a common accessory mineral in a variety of mafic and ultramafic rocks, but perovskite deposits are rare and studies of perovskite ore deposits are correspondingly scarce. Perovskite is a key rock-forming mineral and reaches exceptionally high concentrations in olivinites, diverse clinopyroxenites and silicocarbonatites in the Afrikanda alkaline–ultramafic complex (Kola Peninsula, NW Russia). Across these lithologies, we classify perovskite into three types (T1–T3) based on crystal morphology, inclusion abundance, composition, and zonation. Perovskite in olivinites and some clinopyroxenites is represented by fine-grained, equigranular, monomineralic clusters and networks (T1). In contrast, perovskite in other clinopyroxenites and some silicocarbonatites has fine- to coarse-grained interlocked (T2) and massive (T3) textures. Electron backscatter diffraction reveals that some T1 and T2 perovskite grains in the olivinites and clinopyroxenites are composed of multiple subgrains and may represent stages of crystal rotation, coalescence and amalgamation. We propose that in the olivinites and clinopyroxenites, these processes result in the transformation of clusters and networks of fine-grained perovskite crystals (T1) to mosaics of more coarse-grained (T2) and massive perovskite (T3). This interpretation suggests that sub-solidus processes can lead to the development of coarse-grained and massive perovskite. A combination of characteristic features identified in the Afrikanda perovskite (equigranular crystal mosaics, interlocked irregular-shaped grains, and massive zones) is observed in other oxide ore deposits, particularly in layered intrusions of chromitites and intrusion-hosted magnetite deposits and suggests that the same amalgamation processes may be responsible for some of the coarse-grained and massive textures observed in oxide deposits worldwide.

Keywords Coalescence · Recrystallization · Perovskite · Afrikanda · U–Pb ages · Electron backscatter diffraction · Kola Peninsula · Re-equilibration · Oxide deposit

Communicated by Gordon Moore.

Electronic supplementary material The online version of this article (https://doi.org/10.1007/s00410-018-1531-9) contains supplementary material, which is available to authorized users.

✉ Naomi J. Potter
pottern@utas.edu.au

[1] Earth Sciences and CODES, University of Tasmania, Hobart, TAS 7001, Australia

[2] Department of Geological Sciences, University of Manitoba, Winnipeg, MB R3T 2N2, Canada

[3] V.S. Sobolev Institute of Geology and Mineralogy SB RAS, Koptyuga Prospect 3, Novosibirsk 630090, Russia

[4] Novosibirsk State University, Ul. Pirogova 2, Novosibirsk 630090, Russia

[5] Central Science Laboratory, University of Tasmania, Hobart, TAS 7001, Australia

Introduction

Oxide deposits formed by a range of magmatic, metamorphic and sedimentary processes (Borrok et al. 1998; Force 1991; Hou et al. 2017; Irvine 1977; Latypov et al. 2017) are important sources of economically critical elements, like Cr, Fe, V, Ti and platinum group metals. Perovskite ($CaTiO_3$) is not currently mined but could be a significant future titanium resource. This mineral is a typical accessory phase in a range of ultramafic and silica-undersaturated alkaline rocks, such as kimberlites, melilitolites, foidolites and carbonatites (Campbell et al. 1997; Chakhmouradian and Mitchell 1997; Nielsen 1980). In rare cases, perovskite is an abundant rock constituent, such as bebedourites in the Salitre alkaline complex, Brazil (Barbosa et al. 2012), dunites in the Gardiner carbonatite complex, Greenland (Campbell et al. 1997;

Published online: 17 November 2018

Nielsen et al. 1997), and Benfontein kimberlite sills in South Africa (Dawson and Hawthorn 1973). However, perovskite deposits of significant tonnage and grade are exceptionally rare; the few examples, where the economic potential of the perovskite mineralisation has been explored are structurally and texturally complex alkaline–ultramafic intrusions at Afrikanda in northwestern Russia (Herz 1976), Tapira in southeastern Brazil (Brod 1999), and Powderhorn in Colorado, USA (Armbrustmacher 1981). It remains uncertain how the perovskite accumulated to ore-grade levels in these settings.

Scarcity of perovskite ore deposits has not entailed many genetic studies. Several scenarios have been proposed to account for perovskite-rich zones, the most common involves magmatic layering due to gravitational settling (Brod 1999; Dawson and Hawthorn 1973). On the other hand, perovskite-rich segregations show textural similarities to other oxide deposits, so genetic models for oxide ores may be pertinent to the genesis of perovskite accumulations. Relevant models include in situ crystallisation (Charlier et al. 2006; Latypov et al. 2013; Pang et al. 2007; Vukmanovic et al. 2013), magma mixing (Eales et al. 1990; Irvine 1977; Kinnaird et al. 2002), liquid immiscibility (Kolker 1982; Lister 1966; McDonald 1965; Zhou et al. 2005), mobilization of cumulate suspension from staging magma reservoirs (Eales and Costin 2012; Mondal and Mathez 2006), and a range of post-magmatic ore-forming processes, including post-cumulus growth (Vidyashankar and Govindaiah 2009; Yudovskaya and Kinnaird 2010) and deposition from hydrothermal fluids (Cawthorn 2011; Harlov et al. 2016; Knipping et al. 2015; Pushkarev et al. 2015). The current array of contrasting genetic models for the formation of oxide deposits suggests that sources of metals and mechanisms of their accumulation are not exclusive and should not be pigeonholed.

Our study of perovskite from the Afrikanda alkaline–ultramafic complex targets the understanding of mechanisms responsible for the development of related massive ore textures. We describe the mineral assemblages and textures of the main Afrikanda lithologies and define three key perovskite textural types and associated chemical trends. We discuss the stages of perovskite textural development in the ultramafic rocks at Afrikanda, and the possibility of similar processes operating in other oxide deposits worldwide.

Geological background

The Afrikanda alkaline–ultramafic complex is one of the smallest intrusions in the Devonian (~ 380 Ma) Kola Alkaline Province that hosts more than twenty plutonic and subvolcanic bodies, including alkaline, ultramafic, carbonatite, and melilitolite suites (Kukharenko et al. 1965). The Afrikanda complex is a multiphase intrusion emplaced into Archaean gneisses of the Belomorian Mobile Belt during rifting of the Fennoscandian Shield (Chakhmouradian and Zaitsev 1999; Kramm et al. 1993). The complex has a ~ 11.5 km^2 circular shape at the current level of erosion, identified with gravimetric data as a 5 km thick ellipsoidal composite body with a NW-dipping conduit (Arzamastsev et al. 2000; Chakhmouradian and Zaitsev 2004). The complex has a concentric internal structure (Afanasyev 2011; Kukharenko et al. 1965) and hosts texturally and modally diverse olivinites and clinopyroxenites, cross-cut by minor intrusions of carbonatitic and foidolitic rocks (Chakhmouradian and Zaitsev 2004).

The olivinites and minor melilite-bearing olivinites are found as xenoliths (up to 7 m) in the clinopyroxenites, implying that the former rocks represent the earliest intrusive phase at Afrikanda (Chakhmouradian and Zaitsev 1999). The term "olivinites" is used to emphasize that magnetite and perovskite, not chromite, are the major opaque minerals and to maintain consistency with previously published work on Afrikanda and other complexes in the Kola Alkaline Province and petrogenetically similar igneous provinces elsewhere in Russia. Most of the intrusion is composed of texturally and compositionally diverse clinopyroxenites (Chakhmouradian and Zaitsev 2004). These clinopyroxenites are coarse-grained in the centre and transition outwards from fine-grained to nepheline-bearing along the margins, before grading to melteigites. The perovskite ore and perovskite-bearing rocks are hosted in the coarse-grained clinopyroxenites, referred to in the Russian literature as "ore pyroxenites", located in the central part of the complex. The ultramafic rocks often exhibit alternating oxide- and silicate-rich layers that are considered to represent igneous layering (Chakhmouradian and Zaitsev 2004). The oxide layers are primarily composed of perovskite and titanomagnetite and are enriched in rare earth elements (REE) (Chakhmouradian and Zaitsev 2004; Yudin and Zak 1971).

A carbonatitic suite, also known as calcite–amphibole–clinopyroxene rocks, occurs in the central part of the complex as branching veins (2 cm to 2 m thick) and seemingly irregular (in outcrop) bodies that cross-cut the ultramafic series (Chakhmouradian and Zaitsev 1999). According to the field, geochemical and mineralogical evidence, carbonatitic rocks are distinct from the clinopyroxenites, despite the abundance of diopside and perovskite in both. The carbonatitic rocks are mostly massive and coarse-grained to pegmatitic with modal proportions that change considerably over a short distance, producing a succession from silicocarbonatites to calcite carbonatites (Chakhmouradian et al. 2008; Chakhmouradian and Zaitsev 2004; Pekov et al. 1997). The silicocarbonatites show a widespread mineralogical variability on a small spatial scale (Chakhmouradian et al. 2008; Chakhmouradian and Zaitsev 1999, 2002, 2004; Zaitsev and Chakhmouradian 2002). Alkaline feldspathoidal

rocks appear to be the last intrusive phase and are principally represented by the melteigite–urtite series. The bulk of these rocks is associated with the nepheline-bearing clinopyroxenites in the eastern part of the complex, but pegmatoid ijolites comprising major nepheline, magnetite, perovskite and, locally, biotite also occur in the core as dikes cross-cutting the ultramafic and carbonatitic rocks (Chakhmouradian and Zaitsev 1999).

The Afrikanda perovskite-magnetite deposit is confined to the central part of the complex, dominated by coarse-grained clinopyroxenites (> 50%) that host blocks of olivinites and are cross-cut by carbonatitic and feldspathoidal rocks. The ore comprises 15–35 vol% Ti-rich magnetite and 10–36 vol% perovskite, and shows wide variations in the abundance of silicate minerals and calcite, reflecting extreme petrographic heterogeneity of this deposit. The measured reserves, delineated to a depth of 300 m, include 34.3 Mt of ore averaging 12.5 wt% Fe and 8.3 wt% TiO_2 (Afanasyev 2011).

Methodology

All instruments used for the characterisation of samples are housed at the University of Tasmania, Australia. Polished samples were analysed by backscattered electron (BSE) imaging, energy dispersive X-ray spectrometry (EDS) and electron backscatter diffraction (EBSD) using a Hitachi SU-70 field emission scanning electron microscope (SEM) in the Central Science Laboratory. The SEM is fitted with an Oxford XMax80 EDS detector and an HKL Nordlys Nano EBSD camera. Major and trace element and U–Pb isotope analyses of perovskite and titanite were conducted using an Agilent 7900 quadrupole ICPMS, coupled to a Coherent COMPex Pro 193 nm ArF excimer laser system equipped with a Laurin Technic (Resolution S155) constant geometry ablation cell at the School of Earth Sciences. Additional details are provided in the Appendix.

Petrography of rock units

Melilite-bearing olivinites

Melilite-bearing olivinites are fine- to medium-grained, inequigranular rocks composed of forsterite (0.3–2 mm), åkermanite (0.6–2.7 mm), perovskite (50–550 μm) and magnetite (0.2–1.5 mm), and cut by calcite and wollastonite veinlets. Inclusions of euhedral perovskite (30–200 μm) are also found in all other minerals. Perovskite grains are physically separated by serpentine. The preferential orientation of elongate forsterite and magnetite grains and ubiquitous serpentine in the same orientation defines a weak planar fabric in the rock. The interconnected networks and clusters of smaller euhedral perovskite grains enclose and distort the anhedral åkermanite, forsterite and magnetite grains generating intergrown, irregular and concave shapes (Fig. 1a). Åkermanite is sodium-rich (2–3 wt% Na_2O) with thin rims of monticellite (11–12 wt% FeO) surrounding some crystals. The

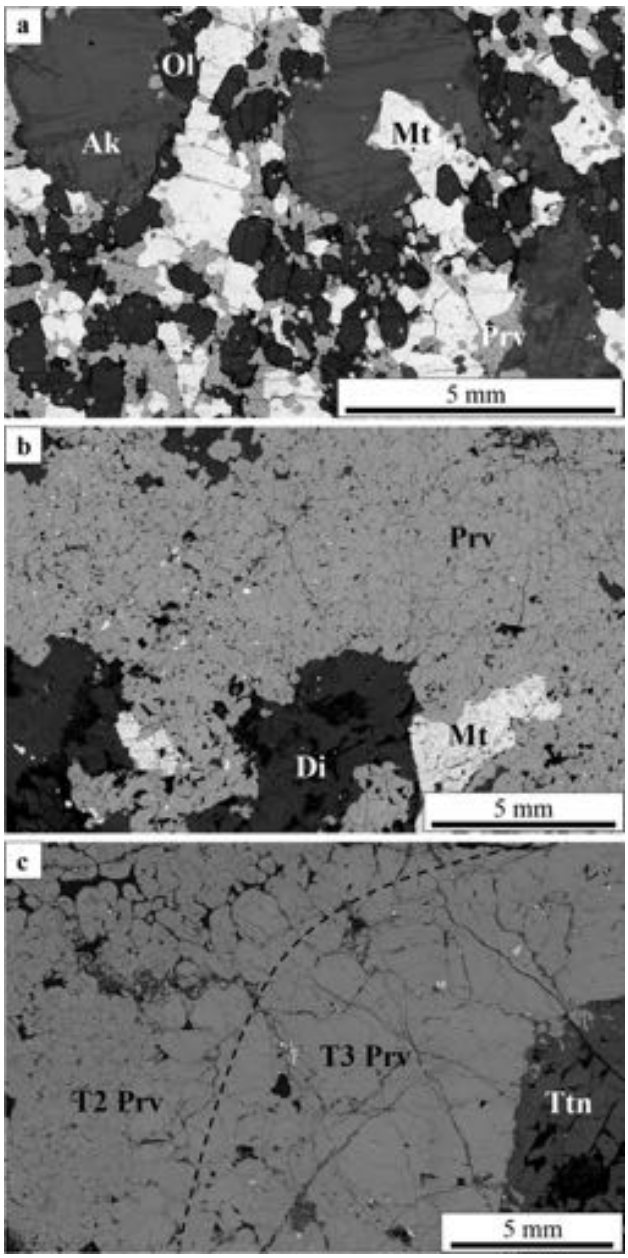

Fig. 1 Backscattered electron (BSE) images of characteristic textures and mineralogy of the three main Afrikanda rock types. **a** Olivinites composed of large akermanite, olivine and magnetite grains enclosed by smaller perovskite grains. **b** Clinopyroxenite composed of diopside, magnetite and smaller perovskite grains. **c** silicocarbonatite composed of perovskite, calcite and titanite. *Ak* akermanite, *Ttn* titanite, *Prv* perovskite, *Mt* magnetite, *Ol* olivine, *Di* diopside

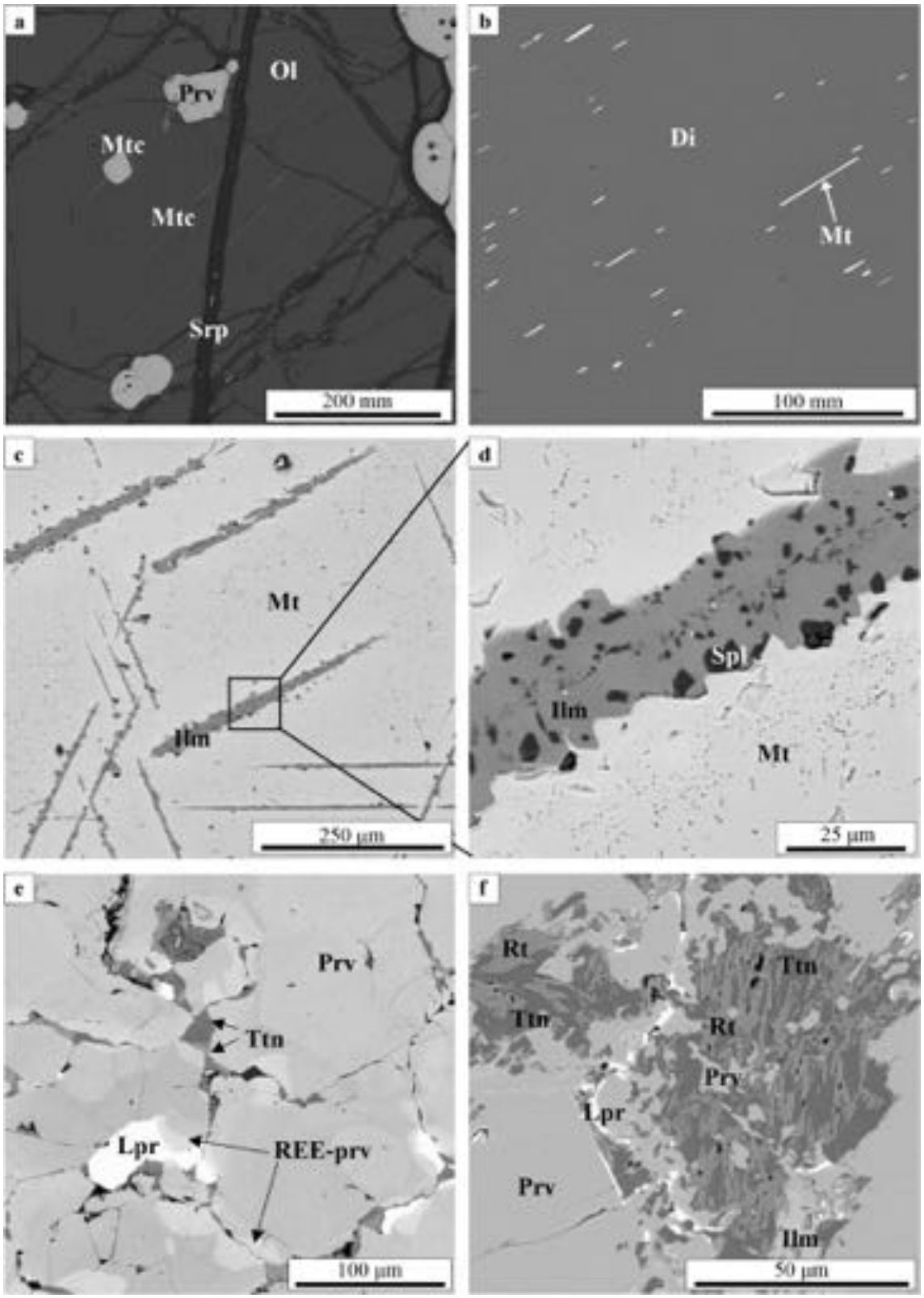

forsterite crystals (~ Fo_{86-88}) contain up to 1 wt.% CaO and are partially replaced and cross-cut by serpentine with magnetite infill. Ferroan monticellite lamellae are observed within a few olivine grains (Fig. 2a). Magnetite is compositionally homogeneous with high Ti, Mg and Al contents (4–7, 1–2 and 1–2 wt% respective oxides).

◂**Fig. 2** BSE images of textural features in the Afrikanda rocks. **a** Ferroan monticellite lamellae in olivine from olivinites. **b** Titanomagnetite lamellae in diopside from clinopyroxenite. **c** Mg-rich ilmenite lamellae in magnetite from clinopyroxenite. **d** Close up of **c** with small crystals of ferroan Ti-rich spinel and baddeleyite (white specs) in the Mg-rich ilmenite lamellae. **e** Titanite, REE-perovskite and loparite at T2 perovskite grain margins from clinopyroxenite. **f** Symplectite-like intergrowths of titanite, rutile and ilmenite in T2 perovskite from silicocarbonatite. *Ttn* titanite, *Lpr* loparite, *Prv* perovskite, *Ilm* ilmenite, *REE-prv* REE-rich perovskite, *Mt* magnetite, *Spl* spinel, *Di* diopside, *Mtc* monticellite, *Rt* rutile, *Srp* serpentine, *Ol* olivine

Clinopyroxenites

The examined clinopyroxenites are fine- to medium-grained, inequigranular rocks mainly composed of clinopyroxene, perovskite and magnetite with minor calcite, richterite, phlogopite, magnesiohastingsite, titanite, chlorite and various REE minerals (Fig. 1b). Diopside (0.2 to 1 mm) is zoned with titanomagnetite and magnesiohastingsite lamellae (Fig. 2b) and inclusions of calcite, phlogopite and titanite. Diopside is partially replaced by magnesiohastingsite, biotite and clinochlore. Perovskite shows a range in grain sizes (0.05 to more than 2 mm), shapes (rounded to irregular) and zonation (homogeneous to complexly zoned), and varies from chains of euhedral crystals to large areas of interlocking grains. Magnetite grains are rounded (0.3 to 1.3 mm, with rare grains up to 10 mm) and contain variable Ti, Mg and Al contents (< 4, 3 and 2 wt% respective oxides). Magnetite also contains lamellae of Mg-rich ilmenite (Fig. 2c), trellis-like and irregular patches of ferroan spinel (< 25 µm) and Mn- and Mg-rich ilmenite (< 50 µm). The Mg-rich ilmenite lamellae contain small crystals of ferroan Ti-rich spinel (1 to 3 µm) and baddeleyite (< 1 µm) (Fig. 2d). REE phases are observed as inclusions in other minerals, with ancylite-(Ce) in richterite, cerite-(Ce) in calcite, and ancylite-(Ce), cerite-(Ce) and loparite-(Ce) in titanite.

Silicocarbonatites

The examined silicocarbonatite samples are extremely inequigranular (fine- to coarse-grained) and predominantly composed of calcite, diopside, perovskite, magnetite, magnesiohastingsite and titanite. In perovskite-rich areas, calcite occurs as veinlets (up to 5 mm in width), euhedral crystals (0.3 to > 4 mm across) and interstitial to perovskite (0.3 to 2 mm), and is the most abundant mineral in the samples (up to 50 vol%). Titanite and cerite (less common) are observed at the peripheral areas of the calcite veinlets. Titanite is the most abundant interstitial mineral, with REE minerals such as cerite-(Ce), loparite-(Ce) and ancylite-(Ce) found enclosed in the titanite. Magnetite has low Ti, Mg and Al contents (less than 1 wt%, respectively) and contains lamellae of Mn- and Mg-rich ilmenite and irregular grains of Zn- and Fe-rich spinel. Perovskite shows a range of grain sizes (0.05 to more than 2 mm), shapes (rounded to irregular), and zonation (homogeneous to complexly zoned), and varies from small interlocking grains to large areas of massive perovskite (Fig. 1c). Perovskite also occurs as clusters with accessory titanite, calcite, loparite-(Ce) and rare fluorapatite. For more detailed descriptions of the mineralogy and textures of silicocarbonatites, the reader is referred to publications by Chakhmouradian and Zaitsev (1999, 2002, 2004) and Zaitsev and Chakhmouradian (2002).

Perovskite textures

Three distinct perovskite textures are identified in the three main rock types at Afrikanda. These types are defined by their morphology, composition, zoning patterns and abundance of multiphase inclusions (Fig. 3a–f).

Type one (T1) perovskite is observed in the olivinites and clinopyroxenites, characterised by interconnected polygonal crystal clusters and networks. The euhedral pseudo-octahedral perovskite grains (50–550 µm) have straight boundaries with widespread 120° triple-junctions (Fig. 3a). Multiphase inclusions are abundant in grain cores. The number of inclusions is dependent on grain size, with a general trend of more inclusions with increasing grain size. Most of the perovskite grains exhibit no detectable zoning in BSE images, while a small number of grains along the zone of contact with magnetite grains have a lower-AZ rim (AZ = average atomic number). Perovskite T1 in the clinopyroxenites has a greater number of grains with a low-AZ rim along their contact with both adjacent perovskite and magnetite grains. The perovskite grains neighboured by magnetite can also exhibit oscillatory zoning with multiple narrow bands along the grain boundaries (Fig. 3b). The grain boundaries between perovskite are straight, whereas boundaries with other minerals are curvilinear. The perovskite grain boundaries in the melilite olivinites and clinopyroxenites are clearly visible, however, EBSD revealed that some of these grains are a composite of several subgrains, each with slight deviations in crystal orientation (Fig. 4a_{iii}, b_{iii}).

Type two (T2) perovskite in the clinopyroxenites is represented by an intricate mosaic of interlocking anhedral grains (0.1 to 1 mm; Figs. 1b, 3c) and in the silicocarbonatites, by rounded grains (0.2 to > 2 mm) surrounded by interstitial material (Figs. 1c, 3d). Triple junctions are observed between adjacent perovskite grains in the clinopyroxenites, at approximately 120°. Multiphase and monomineralic inclusions of phlogopite, magnetite, loparite-(Ce), calcite, titanite and fluorapatite vary from rare to abundant among the examined samples. Perovskite in the silicocarbonatites contains a greater proportion of monomineralic inclusions and fewer multiphase inclusions than that in the clinopyroxenites. Zoning is prominent in all perovskite grains and

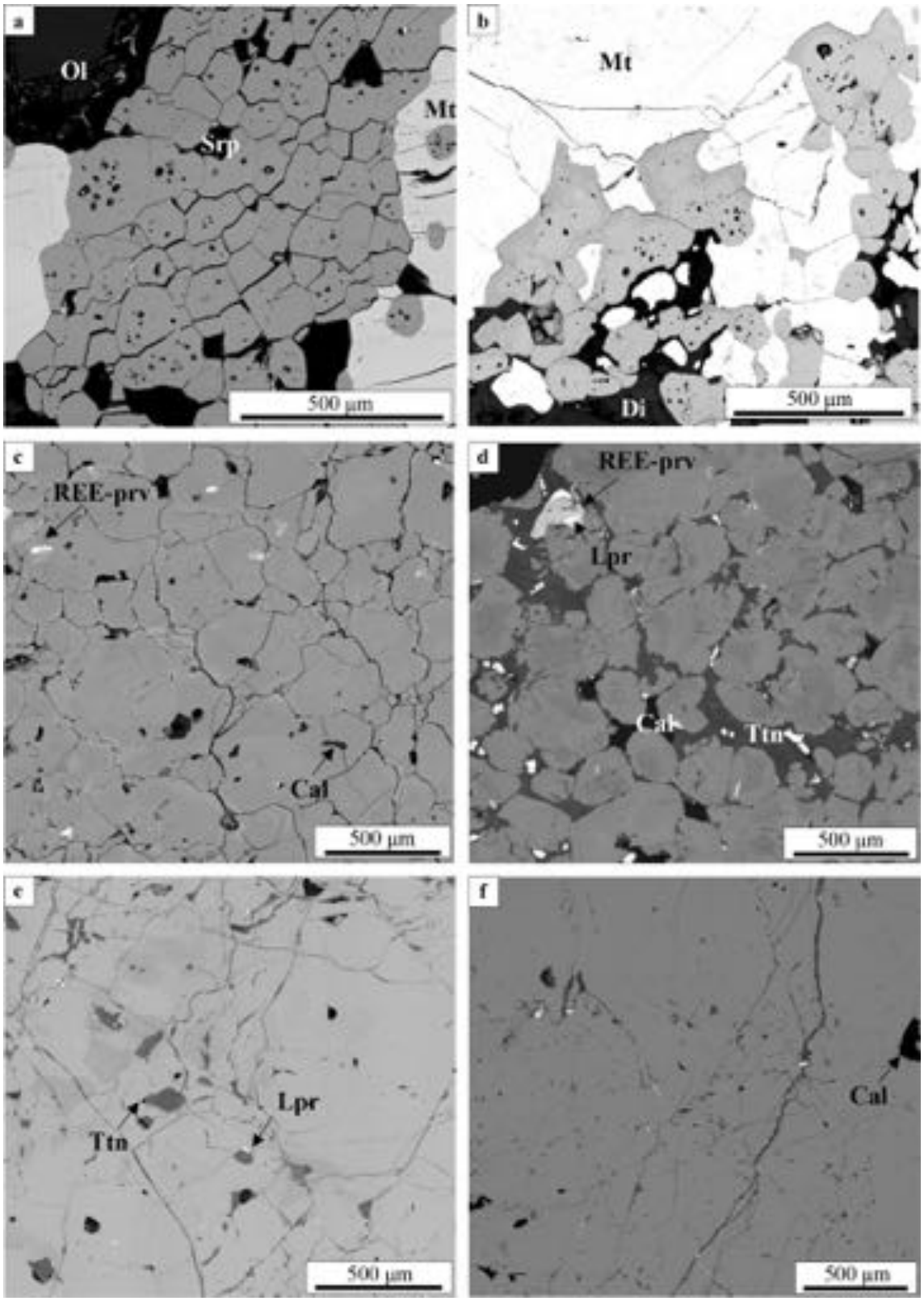

Fig. 3 Representative BSE images of the various perovskite textures. **a** T1 in olivinites. **b** T1 in clinopyroxenite. **c** T2 in clinopyroxenite. **d** T2 in silicocarbonatite. **e** T3 in clinopyroxenite. **f** T3 in silicocarbonatite. *Cal* calcite, *Di* diopside, *Lpr* loparite, *Mt* magnetite, *Ol* olivine, *Srp* serpentine, *REE-prv* REE-perovskite, *Ttn* titanite

can be highly complex in some areas or individual grains. Large grains commonly display less compositional complexity than the smaller grains. The zoning in the core is challenging to decipher due to compositional changes occurring along the grain boundaries and fractures (Figs. 3d, 5a). In BSE images, most grains have a darker core and comparatively lighter rim caused by differences in concentration of Na, light rare earth elements (LREE), and Nb (Fig. 5d). The changes in composition at the rims are not systematic, often showing irregular, embayed patterns (Fig. 5a). In some samples, perovskite has darker rim in areas where perovskite is in direct contact with magnetite or calcite (Fig. 5c).

Distinct areas of perovskite with elevated LREE contents (up to 20 wt%), reflected in their high AZ, are referred to here as REE-perovskite. The mineral ranges in size from 20 µm to 1.5 mm and can exhibit irregular zoning due to differences in Na, LREE and Nb contents (Fig. 3d). The REE-perovskite forms irregular, cuspate shapes as halos around loparite-(Ce) in perovskite and at perovskite rims that are commonly in contact with interstitial loparite-(Ce) and titanite (Fig. 2e). Type 2 perovskite coexists with titanite, calcite and loparite-(Ce); rare fluorapatite was also found in the silicocarbonatites. Titanite is zoned and forms irregular wedge-shaped crystals between perovskite, thin rims around perovskite and intergrown with interstitial ilmenite (0.2-1 mm). REE-perovskite and loparite-(Ce) associated with T2 perovskite are more abundant in the silicocarbonatites, which also contain a larger proportion of interstitial minerals. Perovskite grain boundaries can be difficult to distinguish in BSE images, especially in the silicocarbonatites, however, in the Euler images the boundaries are clearly visible (Fig. 4c_{ii}, d_{ii}). The Euler patterns also show that in the clinopyroxenites, most large irregularly shaped grains have only one crystallographic orientation, while the smaller more-rounded grains still have differences in orientation that indicate the presence of subgrains (Fig. 4c_{iii}). The irregular grain boundaries of large perovskite crystals suggest they developed from multiple smaller grains (Fig. 4c_{ii}). In the silicocarbonatites, the small and large perovskite grains have only one orientation (Fig. 4d_{iii}).

Type 3 (T3) in the clinopyroxenites and silicocarbonatites is represented by massive perovskite with patches of irregular zoning and rare multiphase inclusions. The intensity of the zoning varies across the samples, some areas are almost homogeneous and others exhibit complex patterns due to extreme variations in Na, LREE and Nb contents (Fig. 4b). Chakhmouradian and Zaitsev (1999) also reported small-scale order-of-magnitude variations in Th in REE-perovskite and loparite-(Ce) mantling T3. These authors also described oscillatory growth patterns truncated by Na-REE (±Nb,Th)-rich areas in euhedral cubo-octahedral crystals. Mineral inclusions of titanite, calcite, loparite-(Ce) and cerite are dispersed throughout massive perovskite and between perovskite grains. Generally, areas of perovskite with interstitial minerals contain fewer mineral inclusions, and vice versa. Interstitial titanite can be intergrown with ilmenite and form large patches up to 1 mm containing scattered ilmenite and perovskite. Symplectite-like intergrowths of titanite, rutile and ilmenite (200–500 µm) are typical in some silicocarbonatites (Fig. 2f). Type 3 perovskite lacks easily distinguishable grain boundaries. The Euler images show that perovskite is massive, with the same crystallographic orientation for large areas of perovskite (Fig. 4e_{ii}, f_{ii}).

Multiphase inclusions in perovskite

The perovskite-hosted multiphase inclusions in the three rock types show rounded, elongated and irregular shapes, and range from < 5 to 50 µm across. The inclusions are all identified as primary based on their random/unsystematic distribution within the grains and the lack of association with secondary features, such as healed fractures. The inclusions typically contain three to ten mineral phases and include anhydrous and water-bearing silicates, carbonates, oxides, sulphides and phosphates. The abundance of multiphase inclusions and their mineralogical complexity decrease from the olivinites to clinopyroxenites and then silicocarbonatites. A detailed analysis and discussion on these multiphase inclusions will be presented in a subsequent publication.

Perovskite compositions

The textural types of perovskite in the three rock types vary in major and trace element compositions. The substituent elements show a negative correlation with Ca and Ti and a positive correlation with each other (Fig. 6a–d). Type 1 perovskite has the lowest abundances of substituent elements and a limited range of compositions, notably up to 2 wt% REE and less than 1 wt% Fe (Fig. 6d). The range in element concentrations is greater in T2 and T3 perovskite due to their complex zoning patterns, with the most compositional scatter observed in T2 perovskite from the silicocarbonatites and T3 perovskite from the clinopyroxenites (Fig. 6). Type 2 perovskite contains 1–7 wt% REE and up to 1.5 wt% Nb and Fe, while T3 perovskite has 4–7 wt% REE, 1–2 wt% Nb, and up to 1.5 wt% Na and Fe.

The REE budget of perovskite is dominated by cerium with the abundance of other lanthanides decreasing with increasing atomic number [La > Nd > Pr > Sm; $(La/Yb)_{CN}$ = 140–2300]. Chondrite-normalised REE patterns for all textural types exhibit a negative slope (Fig. 7). Overall, the chondrite profiles show a relative enrichment in all REE from T1 to T3, with a greater increase in light REE for T2 and T3 compared to T1. The complete set of LA-ICPMS data is presented in the Appendix.

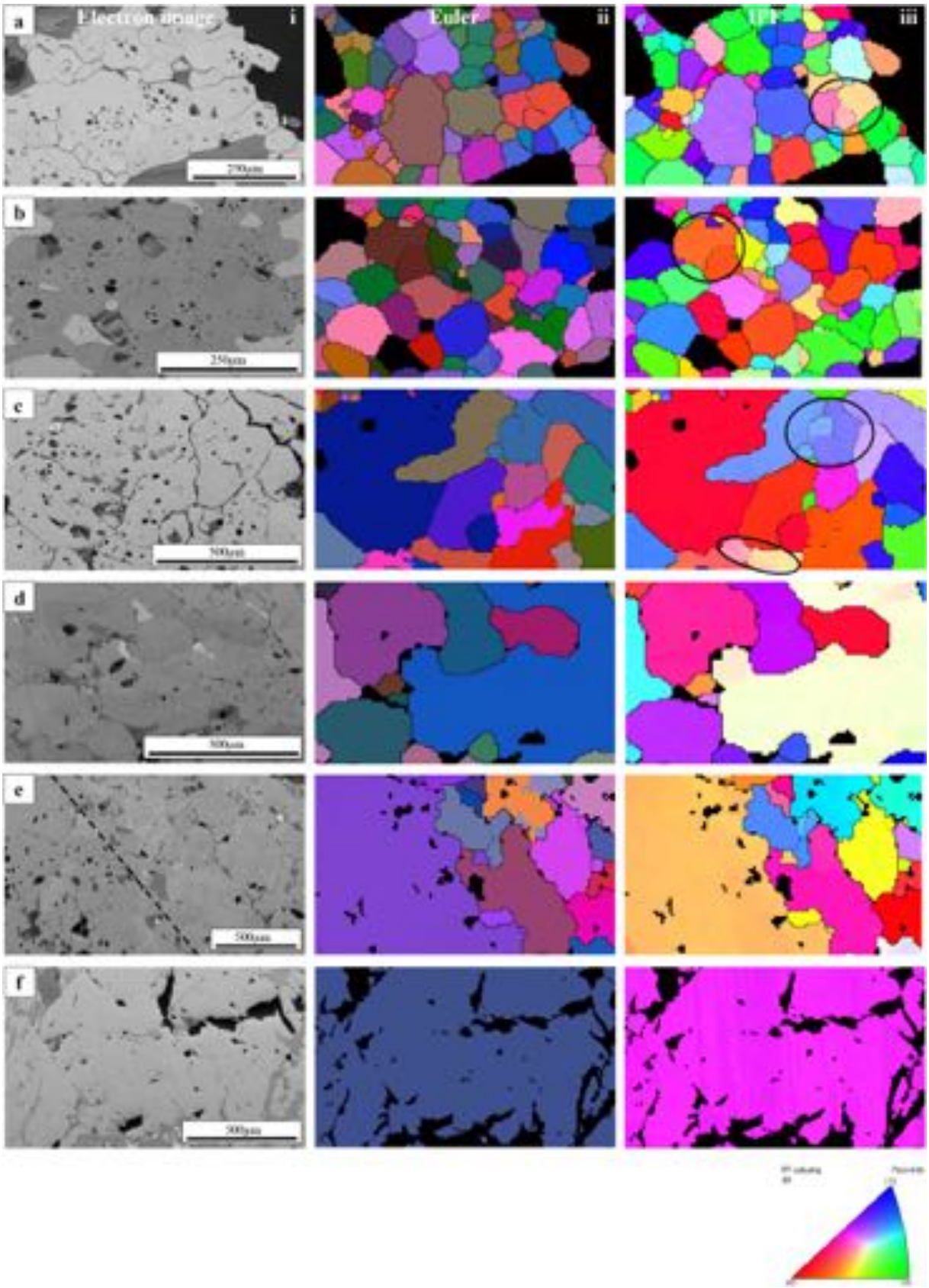
a
Electron image
i
Euler
ii
IPF
iii
b
c
d
e
f

◂**Fig. 4** Structural analysis and crystallographic orientation of perovskite grains in the different textures. **a** T1 in olivinites. **b** T1 in clinopyroxenite. **c** T2 in clinopyroxenite. **d** T2 in silicocarbonatite. **e** T2 (right) and T3 (left) in silicocarbonatite. **f** T3 in clinopyroxenite. **i** BSE image of the area mapped with EBSD shows perovskite grain boundaries. **ii** EBSD map representing the orientation of neighbouring perovskite grains in Euler space using colours to denote the variety of crystal orientations in space using Euler angles: φ1-red φ-green, φ2-blue. **iii** Inverse pole figure (IPF) map in the *X* or *Z* direction showing the variation in crystal orientation using colours. Black ovals show grains that are composed of subgrains with different crystallographic orientations

U–Pb geochronology

Fifteen in situ U–Pb isotopic measurements were obtained for perovskite from the olivinites, 45 from the clinopyroxenites and 124 from the silicocarbonatites. All but one analysis were used in age calculations. Perovskite contains abundant common Pb and so concordia intercept ages using the Tera–Wasserburg plot are reported. The Pb isotope composition of calcite was analysed and used as a common-Pb anchor for the concordia intercept ages because this mineral has high Pb/U ratios. The measured $^{207}Pb/^{206}Pb$ value of calcite is 0.8277 ± 0.0039 and, thus, differs from the two-stage Pb evolution model of Stacey and Kramers (1975) for 380 Ma. Perovskite from all lithologies gives a concordia intercept age of 368.3 ± 1.2 +/- 7.48 Ma (including systematic uncertainties) with an MSWD of 0.80 and a probability-of-fit of 0.98 (Fig. 8a). Perovskite ages for each of the analysed lithologies are reported in Table 1.

One hundred and eleven in situ U–Pb isotope analyses of titanite were obtained from the silicocarbonatites. Significant scatter and discordance in the U–Pb system are present. A concordia intercept age of 374.2 ± 5.3 Ma +/- 7.5 Ma (including systematic uncertainties) was calculated for data points, whose concordance was greater than 50%, using the calcite common-Pb anchor (see above; Fig. 8b). The complete set of U–Pb geochronology results is presented in the Appendix.

Discussion

Age of the Afrikanda complex

The Palaeozoic igneous complexes in the Kola Alkaline Province were emplaced during a relatively short time during the Late Devonian (380−360 Ma) with no reliably post-Devonian magmatic events recorded to date (Arzamastsev et al. 2000). The Afrikanda complex was emplaced at ~ 380 Ma with other alkaline–ultramafic complexes, including Kovdor, Turiy Mys, Lesnaya Varaka and Ozernaya Varaka (Arzamastsev and Wu 2014).

Our geochronological study of perovskite from the melilite olivinites, clinopyroxenites and silicocarbonatites yielded similar ages of 370.4 ± 5.4, 368.9 ± 2.9, 368.1 ± 1.3, respectively (Table 1). Our average perovskite age of 368.3 ± 1.2 Ma (Fig. 8a) is in good agreement with most of the previously published U–Pb ages for this intrusion (Fig. 9), including: 364 ± 3 Ma and 374 ± 10 for perovskite from clinopyroxenite (Kramm et al. 1993; Reguir et al. 2010), 371 ± 8 Ma for perovskite from silicocarbonatite (Reguir et al. 2010), and 377 ± 3 Ma for schorlomite from silicocarbonatite (Salnikova et al. 2018). Somewhat older ages were reported by Wu et al. (2010, 2013) for perovskite from clinopyroxenite, calcite-bearing perovskite ore and ijolite–melteigite (376–385 Ma, averaging 381 ± 2 Ma), and for calzirtite and zirconolite from clinopyroxenites (Wu et al. 2010). Several factors could be responsible for the slight age discrepancies between our data and the data of Wu et al. (2010, 2013), including the choice of U–Pb calibration material, susceptibility of some analytical techniques to matrix effects, and the choice of a common-Pb anchor. Our study supports the contemporaneous emplacement of the various rock types (olivinites, clinopyroxenites and silicocarbonatites) in the Afrikanda complex, as indicated by the identical ages of the perovskite from the different lithologies (Fig. 9). Evidence for the relatively rapid emplacement of the Afrikanda deposit comes primarily from the homogeneity of the perovskite U–Pb ages (MSWD of 0.80 for all perovskite analyses), at least at the precision attainable with the LA-ICPMS system used. Additionally, our study presents new insights into the common-Pb isotopic composition of the Afrikanda perovskite and shows that the initial Pb isotopic composition of its parental magma is significantly more radiogenic than predicted by the two-stage model of Stacey and Kramers (1975).

U–Pb age data have not been previously reported for titanite from the Afrikanda complex. Significant scatter in the U–Pb system for titanite is a result of either Pb movement within the titanite structure after crystallisation, or the incorporation of radiogenic and common Pb. Lead loss or partial re-setting of the U–Pb system during later recrystallisation events could also be responsible for some of the scatter (Fig. 8b). Using data whose concordance is better than 50%, an age of 374.2 ± 5.3 Ma was calculated and is consistent with the perovskite results discussed above (Table 1). However, a range of younger titanite ages that are more discordant due to Pb loss suggest there may have been a re-setting or titanite crystallisation event.

Development of perovskite textures

The detailed textural and chemical examination of perovskite in the olivinites, clinopyroxenites and silicocarbonatites

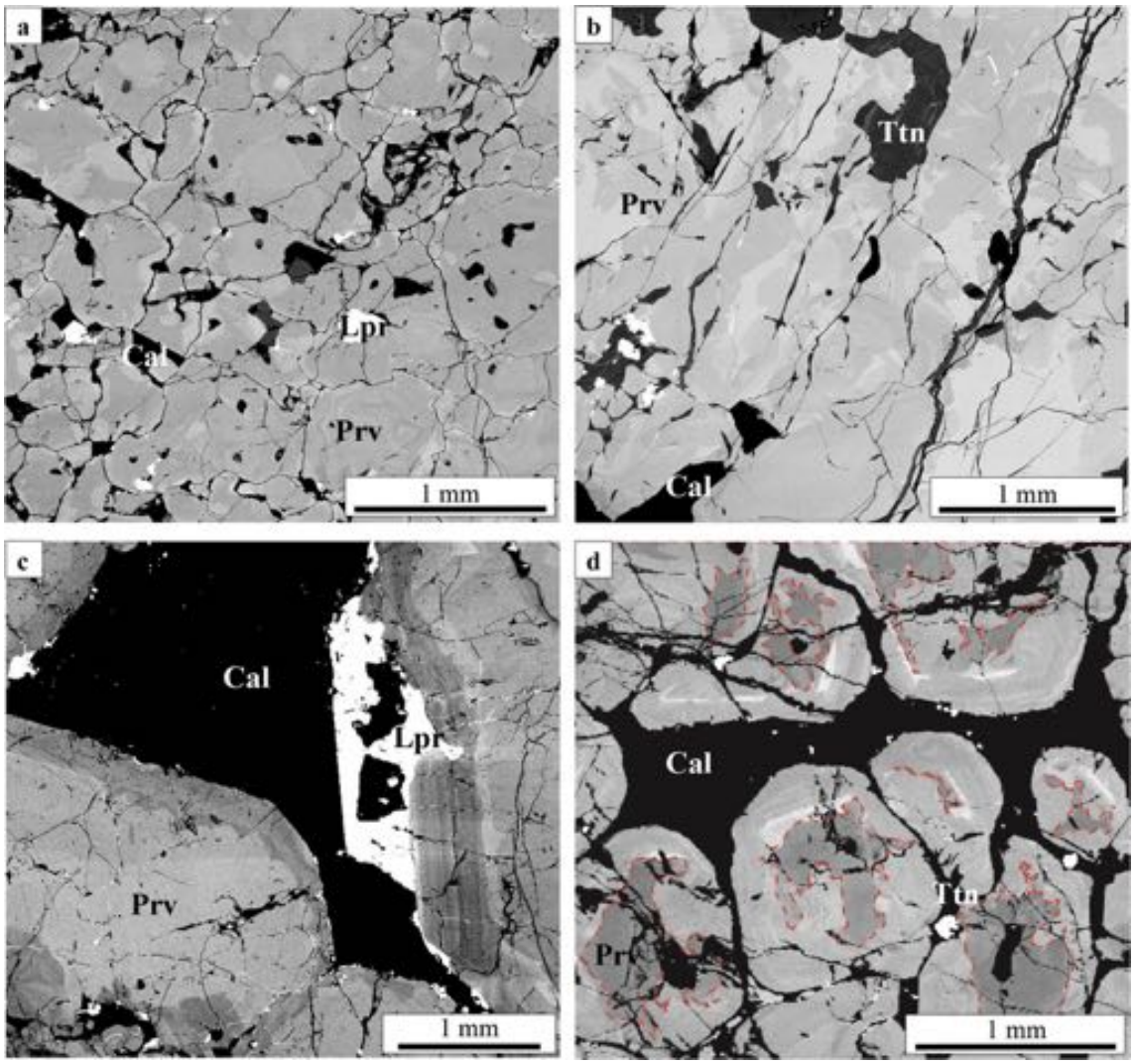

Fig. 5 BSE images of zoning patterns in T2 and T3 perovskite (enhanced contrast in **c, d**). **a** Complex zoning crossing grain boundaries in T2 clinopyroxenite. **b** Irregular zoning pattern in T3 clinopyroxenite. **c** The rims are enriched in REE (rare earth elements) and the cores are depleted in REEs in T2 perovskite in silicocarbonatites. The red dashed lines show the internal extent of zoning. **d** Dark rim (depleted in REE) in contact with calcite and loparite in silicocarbonatite. *Lpr* loparite, *Ttn* titanite, *Prv* perovskite, *Cal* calcite, *REE-prv* REE-perovskite

revealed three perovskite types distinguished by morphology, zonation, inclusion abundance and chemical composition. The olivinites host T1 perovskite (Figs. 1a, 3a), whereas the clinopyroxenites contain T1–3 perovskite (Figs. 1b, 3b–d) and similar T2 and T3 textures are observed in the silicocarbonatites. We have separated the geological interpretation of the ultramafic rocks (discussed below) from that of the silicocarbonatites. The focus here is primarily on the textural evolution of the olivinites and clinopyroxenites, because perovskite textures in the silicocarbonatites have been discussed previously by Chakhmouradian and Zaitsev (1999, 2004).

Olivinites and clinopyroxenites

Textures of rocks are the sum of all processes involved from the initial formation through maturation, and can be used to understand the sequence and nature of each of the evolutionary stages. However, the process of textural equilibration can effectively obscure features related to earlier developmental phases, so we can only speculate from the existing textures about the nature of a rock prior to recrystallization (Pike and Schwarzman 1977). In the case of the Afrikanda rocks, T1 perovskite forms chains and clusters and may suggest that at some point in the early history of the rock individual euhedral grains of perovskite were disseminated and then clumped together to form clusters and chains (Figs. 1a, 3a,

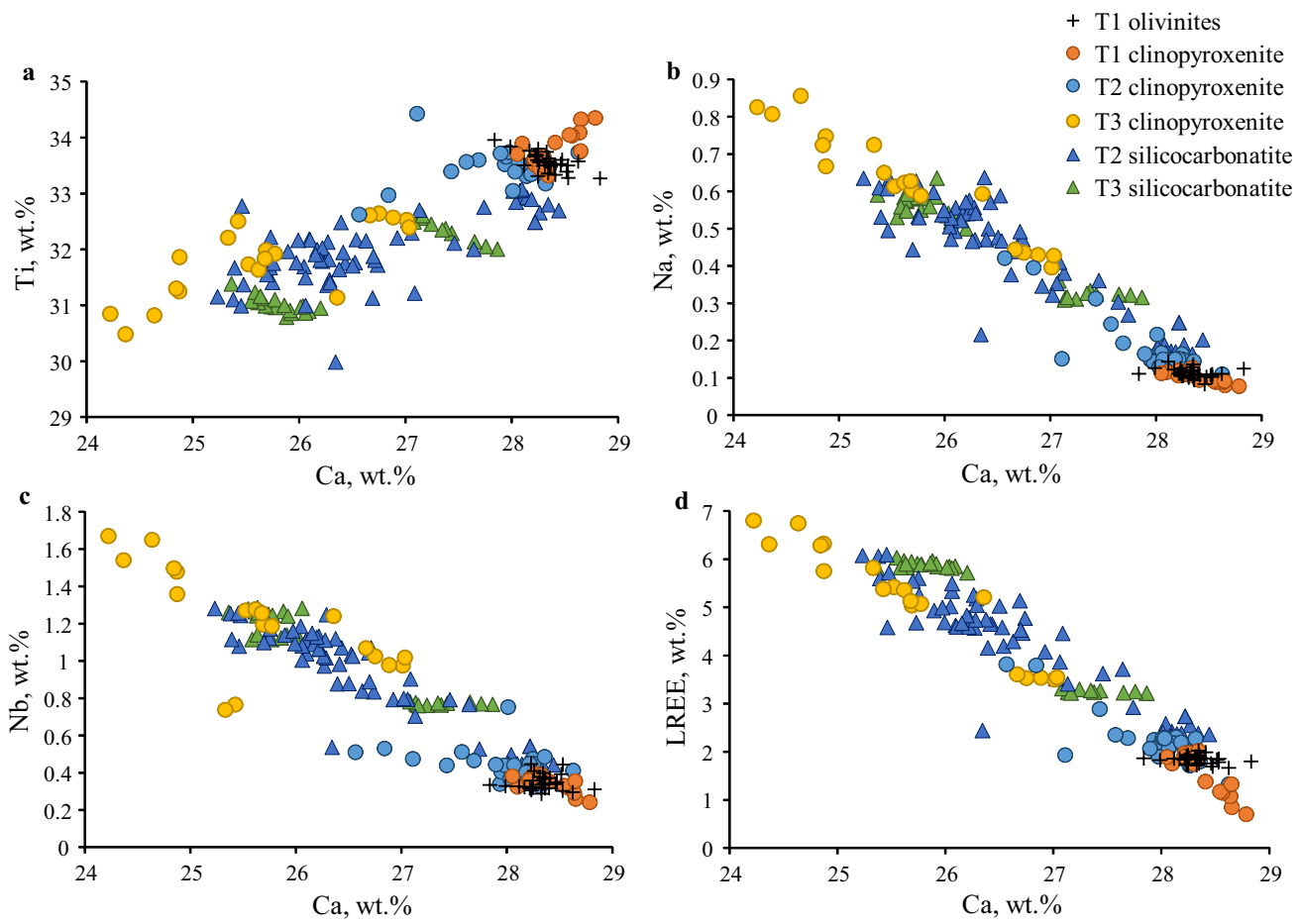

Fig. 6 Bivariate plots of LA-ICPMS major- and trace-element chemistry of the perovskites. Symbols correspond to the four perovskite textures found in the Afrikanda rock types: olivinites (crosses), clinopyroxenites (circles) and silicocarbonatites (triangles)

b). However, we cannot provide clues on the origin of these individual perovskite grains due to the subsequent overprinting events. Therefore, we focus here on development of the Afrikanda perovskite ore by reconstructing the later stages of mineral amalgamation and recrystallization.

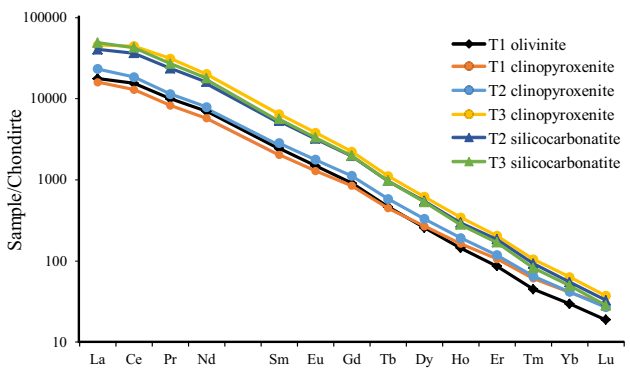

Fig. 7 Chondrite-normalised REE diagram of the average composition of T1 to T3 perovskite in the Afrikanda complex

Textural equilibration

The T1 perovskite aggregates consist of closely packed equigranular crystals with pseudo-octahedral shapes, forming straight boundaries that converge at ~120° triple junctions. This arrangement resembles granoblastic-polygonal textures (Figs. 3a, 10a), as observed in monomineralic cumulates, mantle-derived ultramafics and massive metamorphic rocks such as granofelses (Fig. 10a, b) (Higgins 2011; Holness et al. 2005, 2006; Hunter 1987; Kretz 1966; Wandji et al. 2009). Therefore, we suggest the granoblastic-polygonal texture of T1 perovskite indicates that the host rocks have experienced dynamic textural equilibration. The granoblastic-polygonal texture of T1 perovskite in olivinites and clinopyroxenites differs marginally due to the variable abundance and distribution of the surrounding minerals, with perovskite in

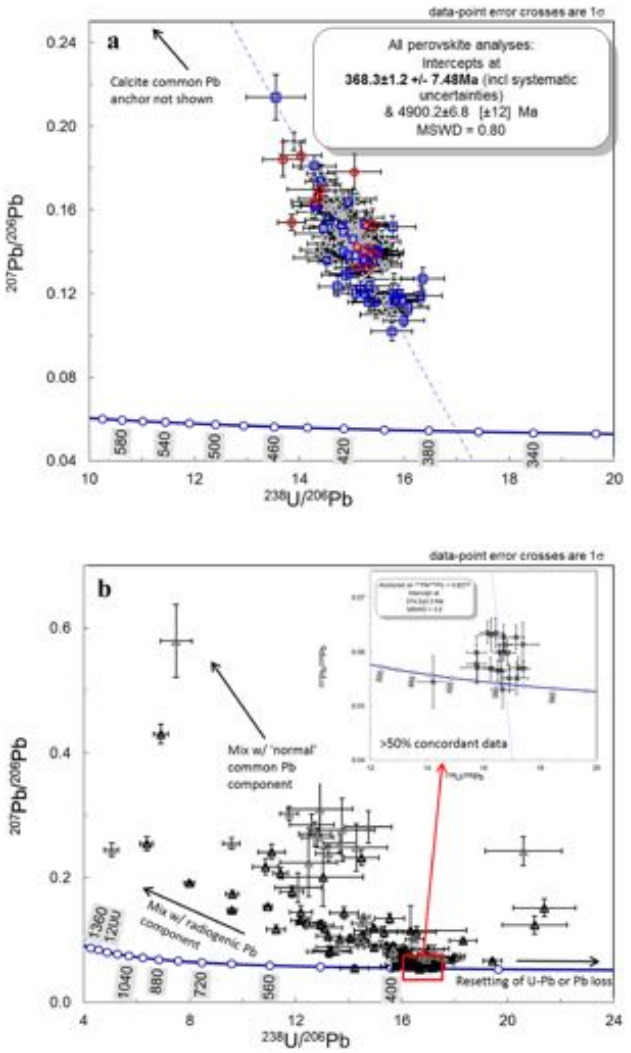

Fig. 8 Tera–Wasserburg concordia plot for **a** perovskite and **b** titanite analyses. Symbols: **a** red circles are olivinites, blue squares are clinopyroxenites, grey diamonds are silicocarbonatites **b** grey and black triangles represent titanite around perovskite in the T3 and T4 silicocarbonatites, respectively. Error crosses are 1 sigma, while concordia intercept ages are 2 sigma. Systematic error component includes uncertainty in decay constants, uncertainty in primary calibration material and excess uncertainty factor of Horstwood et al. (2016)

Table 1 Summary of U–Pb ages of perovskite and titanite from samples of olivinites, clinopyroxenites and silicocarbonatites

Rock type	Mineral	Age (Ma)	MSWD	POF
Olivinite	Perovskite	370.4 ± 5.4/ ± 9.8	1.3	0.19
Clinopyroxenite	Perovskite	368.9 ± 2.9/ ± 7.9	0.84	0.76
Silicocarbonatite	Perovskite	368.1 ± 1.3/ ± 7.5	0.74	0.98
Silicocarbonatite	Titanite	374.2 ± 5.3/ ± 7.5	3.2	0

Uncertainties are 2 sigma absolute and include uncertainties derived from random sources followed by uncertainties from random plus systematic sources of uncertainty calculated according to Horstwood et al. (2016)

POF probability-of-fit

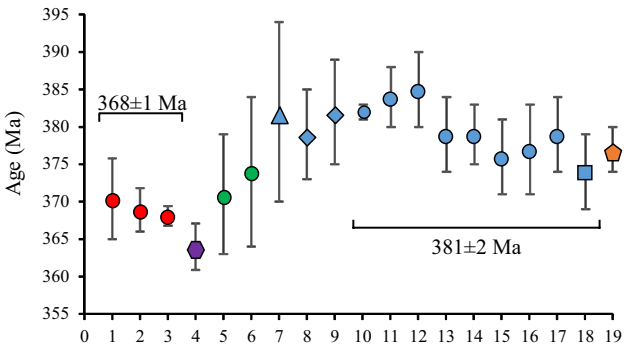

Fig. 9 Age summary of the alkaline ultramafic rocks in the Afrikanda complex. **1–3** Perovskite (circles) analysed in this paper. **4** Whole rock analysis (hexagon) in Kramm et al. (1993). **5–6** Perovskite data in Reguir et al. (2010). **7–9** Calzirtite (triangle) and zirconolite (diamond) data in Wu et al. (2010). **10–18** Perovskite and baddeleyite (square) data in Wu et al. (2013). **19** Schorlomite (pentagon) analysis in Salnikova et al. (2018)

the olivinites clumped together forming aggregates, but dispersed in clinopyroxenites forming chains. Textural equilibration is a well-known phenomenon in natural systems (e.g., Higgins 2015, 2017; Holness et al. 2006), but the bulk of empirical data, computer simulations and models comes from materials research, especially alloys, ceramics and thin films (e.g., Holm et al. 2016). Thus, our current understanding of textural equilibration is limited to relatively simple systems (from a geologist's standpoint) that differ both chemically and mechanically from oxide-silicate assemblages described in the present work. Another challenge in adopting materials science theories to rocks is terminology; for example, their use of the term "recrystallization" is essentially restricted to deformation-induced phenomena, whereas processes addressed in this paper would be described as "grain growth due to annealing" [e.g., Chap. 11 in Humphreys and Hatherly (2004)]. According to previously published experimental evidence, the degree and style of textural equilibration depend on many parameters, notably temperature, pressure, grain distribution, modal homogeneity of the precursor, high-temperature phase transitions, the presence of structural defects, and such kinetic factors as cooling rate (Clark et al. 1977; Humphreys and Hatherly 2004; Kreitcberg et al. 2017; McCloy et al. 2009; Syrenko and Klinishev 1973). Because we observe no evidence for postmagmatic metamorphism at Afrikanda, and the subsolidus mineral assemblages common in the silicocarbonatites record a temperature range of 200–400 °C (Chakhmouradian and Williams 2004; Chakhmouradian and Zaitsev 2004), we assume the documented textural changes arose during cooling. The process involved grain boundary migration, boundary-angle adjustment, dislocation movement, loss of inclusions, and ultimately, coarsening of the grains

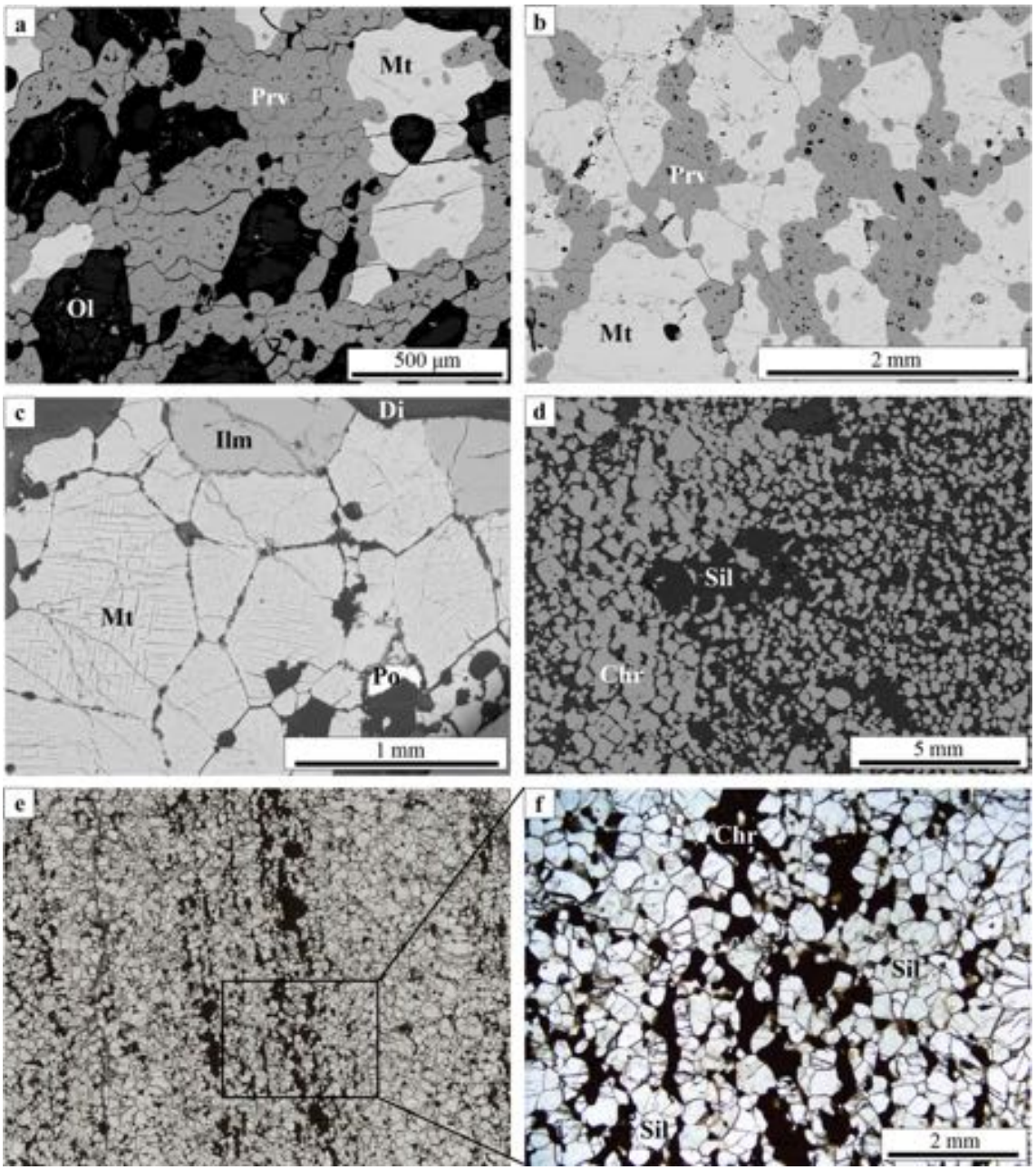

Fig. 10 BSE images of granoblastic textures (**a–d**) SEM (**e, f**) Plane-polarized light. **a** Equigranular mosaic of T1 perovskite from olivinite in the Afrikanda complex with straight boundaries and 120° triple junctions. **b** Perovskite chains of T1 perovskite from clinopyroxenite in the Afrikanda complex. **c** Polygonal grains of Ti-magnetite in an Fe–Ti oxide ore layer at Panzhihua, China. **d** Disseminated equigranular euhedral chromite, with some chains and aggregates from Merensky Reef, South Africa. **e** Chains of chromite grains in a xenolith hosted in a tertiary basalt from the Snowy Mountains, Australia. **f** Close up of (**e**). *Chr* chromite, *Sil* silicate minerals, *Prv* perovskite, *Ilm* ilmenite, *Mt* magnetite, *Di* diopside, *Po* pyrrhotite

to minimise their internal and surface energies (Hunter 1987). We suggest that after perovskite accumulation, slow cooling of the ultramafic rocks enabled the transformation of many small, randomly oriented and possibly irregularly fitted perovskite grains into the observed polygonal mosaics (Figs. 1a, 3a, 10a).

Perovskite coalescence and coarsening

Grain coalescence and coarsening are important processes in the late stages of textural equilibration (Doherty et al. 1997; Hunter 1987). In this section, we discuss grain growth during subsolidus evolution of the ultramafic rocks at Afrikanda as a continuation of the previously recognised textural equilibration. The development of larger grains can either occur by grain boundary migration, i.e., through the dissolution of small crystals and simultaneous growth of larger crystals, or by grain coalescence, where adjacent grain boundaries are eliminated as similarly oriented crystals coalesce (Higgins 2011; Li 1962). The application of EBSD in our study of perovskite enables us to identify and differentiate between these two types of grain growth (Humphreys 2001). Some large grains in T1 and T2 perovskite are composed of subgrains with slightly different crystallographic orientations (circled in Fig. 4a–c). These subgrains within larger perovskite grains suggest the dominant mechanism of grain growth was grain rotation and coalescence. Experimental evidence has shown that coalescence is favoured over grain boundary migration at lower temperatures (Rios et al. 2005; Sandström et al. 1978; Varma and Willits 1984; Walter and Koch 1963). This further supports that the observed perovskite textures and their inferred transformation represent a postmagmatic environment.

The process of grain coarsening occurs via diffusion of vacancies in the crystal lattice, in an effort to eliminate or homogenise high angle, irregular, and large area boundaries (Li 1962). These disequilibrium features are removed as adjacent crystals adopt similar crystallographic orientations and grain boundaries are eliminated as similarly oriented grains coalesce into one larger crystal; this process is exemplified by T1 and T2 perovskite (circled in Fig. 4a–c) (Jones et al. 1979; Li 1962; Rios et al. 2005). These larger grains can continue to grow at low-angle boundaries with neighbouring small grains (Li 1962). Also during coalescence, the new grain boundaries straighten, removing 120° triple junctions by adjusting the dihedral angles of the adjacent grains. This process alters the morphology of the newly coalesced grain and neighbouring grains (see Fig. 4 in Rios et al. (2005)). Triple junctions are typical in T1 perovskite, while less common triple junctions in T2 are no longer strictly at 120° due to the boundary migration associated with grain coalescence (Fig. 3c; Vernon 1970). Type 2 perovskite shows the best examples of grain coalescence, with EBSD images capturing grain coalescence "in progress" (like T1) and at completion. Larger T2 perovskite grains in the clinopyroxenites have some remaining triple junctions and are composed of multiple misoriented subgrains of similar sizes to T1 perovskite (Fig. 4c_{iii}). We suggest the large grains initially resembled T1 perovskite clusters prior to coalescence and have not completely adopted a uniform orientation. Further, we interpret the textural equilibration in the Afrikanda perovskite samples to indicate that coalescence and coarsening of small equilibrated polygonal clusters (T1) enabled the development of a mosaic of larger T2 polycrystalline grains with interlocking grain boundaries and smaller areas of massive T3 perovskite.

Effects of recrystallization

The coarsening of accumulated perovskite during recrystallization in the Afrikanda complex is supported by the complex chemical zoning patterns in perovskite and exsolution lamellae in the associated minerals.

Perovskite chemical zoning

Perovskite-group minerals serve as sensitive indicators to changes in parental environments through complex substitutions of multiple elements in their structure (Chakhmouradian et al. 2013; Mitchell et al. 2017). The variation in the composition and zoning of perovskite from T1 to T3 records the chemical evolution of its crystallisation environment under open- or closed-system conditions. Zoning patterns can be caused by chemical fluctuations in the parental medium, changes in the physical conditions during crystal growth, or solid-state redistribution of elements (Dowty 1976a, b).

Perovskite in T1 is distinguished from T2 and T3 perovskite by the state of textural equilibration and significant differences in chemical composition. Importantly, T1 grains have no internal zoning, consistently low REE values and minor compositional variation localized to the rims of some grains in contact with magnetite (Figs. 3b, 6a–d). Perovskite in the clinopyroxenite shows far more compositional variation, with simple zoning along perovskite grain contacts and oscillatory patterns at the contacts adjacent to magnetite (Fig. 3b). We interpret the internal compositional homogeneity to record textural equilibration of perovskite grains, and the minor zoning to arise from later metasomatic processes.

In contrast, T2 and T3 perovskite are significantly more complex with non-systematic and discontinuous zoning (Fig. 5a, b). Their composition is highly variable, particularly with respect to REE contents (Fig. 6d) and is linked with the irregular and complex zoning patterns. Zoning in T2 and T3 perovskite could be associated with the development of local chemical gradients during grain coalescence, where the differential diffusion of cations creates compositional complexity and irregularity superposed over the existing grain morphology (Fig. 6d). Perovskite in T3 is massive and most of T3 is relatively homogeneous, with some areas still displaying convoluted zoning with no clear pattern (Fig. 3e, f). We suggest these homogeneous areas re-equilibrated through solid-state diffusion removing the

complex zoning and physical impurities such as multiphase inclusions. Areas that are texturally heterogeneous underwent limited textural re-equilibration; however, the zoning is still less complex or abundant than in T2 perovskite.

Controls on perovskite compositions

The composition of T1 perovskite is fairly homogeneous, while T2 and T3 vary significantly, reflecting changes in the availability of such elements as REE, Nb and Th (Fig. 6c, d). In T2 perovskite, these elements are primarily concentrated at the rims and along the grain boundaries (Fig. 2e, 5a, c, d). This type of zoning can be produced by selective cation diffusion during re-equilibration of perovskite with a fluid phase. This process has been invoked to explain perovskite zoning in some kimberlites (Chakhmouradian et al. 2013) and loparite-(Ce) replacement by cation-deficient phases in some alkaline rocks (Chakhmouradian et al. 1999). We suggest the high-REE rims in the Afrikanda T2 perovskite are probably associated with the progressive infiltration of REE and other substituent elements into perovskite from a fluid percolating along grain boundaries and fractures (Fig. 2e). The formation of T3 perovskite was a continuation from T2 polycrystalline grains, and resulted in higher levels of REE (on average) in T3 relative to T2 perovskite from the same rock type (Fig. 7). This enrichment in REE possibly required input of these elements from an external source (e.g., carbonatitic or alkaline magma; Chakhmouradian and Mitchell 1997). We envisage that continuous flux of REE through the ultramafic intrusion under open-system conditions produced the compositional variations.

The presence of REE-perovskite and loparite-(Ce) as discontinuous rims and overgrowths on T2 and T3 perovskite (Figs. 2e, 5a, b) is also undoubtedly linked to the infiltration of a REE-rich fluid in an open system. We agree with Chakhmouradian and Mitchell (1997) that these minerals developed due to infiltration of REE-rich CO_2-rich fluid, which facilitated both fracturing and the uptake of REE ($\pm$ Th $\pm$ Nb) in the perovskite structure. The infiltration of REE into the crystal structure produces a diffuse marginal zone of REE-perovskite (Fig. 2e), whose width is controlled by the kinetics of diffusion and the relative diffusivity of differently charged cations (Chakhmouradian et al. 2013). Similar perovskite–loparite-(Ce) reaction rims and mantles have been reported in other carbonatite complexes and, less commonly, in evolved kimberlites (Chakhmouradian et al. 1999; Chakhmouradian and Mitchell 1997, 2000).

Exsolution lamellae

Exsolution lamellae are a common feature in minerals that have undergone re-equilibration to rid their crystal structure of impurities through solid-state diffusion (Putnis 2009). Exsolution textures in the olivinites and clinopyroxenites include monticellite lamellae in forsterite (Fig. 2a), magnetite and magnesiohastingsite lamellae in diopside (Fig. 2b), and inclusions of spinel and ilmenite in Ti-rich magnetite (Fig. 2c, d).

Calcium is generally a minor constituent in forsterite, with concentrations lower than 1 wt% (Jurewicz and Watson 1988; Simkin and Smith 1970). The rare occurrence of Ca-rich exsolution phases, such as diopside and monticellite-kirschsteinite, have been reported as a product of postmagmatic transformation of olivine in terrestrial rocks (Gaeta 1996; Markl et al. 2001; Xiong et al. 2017; Yufeng et al. 2008) and meteorites (McKay et al. 1998; Mikouchi et al. 1995). We interpret the textures in the Afrikanda samples to have formed by exsolution of Fe-rich monticellite during postmagmatic equilibration of Ca-rich forsterite. Elongate lamellae of oxide phases in pyroxenes are observed in mafic igneous and metamorphic rocks (Fleet et al. 1980; Garrison and Taylor 1981). Based on petrographic evidence, we suggest that exsolution of Ti-rich magnetite and magnesiohastingsite from the diopside host at Afrikanda also occurred during subsolidus equilibration.

Magnetite is observed in both rock types, but the composition and homogeneity (i.e., the nature and relative abundance of exsolution lamellae) differs between the examined olivinite and clinopyroxenite samples. Exsolution textures in Ti-rich magnetite are common in mafic plutonic rocks and have been the subject of many researches (Haggerty 1991; Price 1980; Ramdohr 2013). Exsolution textures reflect the chemical composition and cooling history of the precursor magnetite (Buddington and Lindsley 1964; Howarth et al. 2013; Von Gruenewaldt et al. 1985). The magnetite in the olivinites has the highest concentrations of Ti, Mg and Al and does not exhibit any exsolution lamellae. Magnetite in the clinopyroxenite samples has much lower levels of these elements due to preferential partitioning of Ti and Mg into ilmenite, and Mg and Al into spinel inclusions (Fig. 2d). The variation in magnetite texture between the two rock types supports the suggestion that they underwent different degrees of subsolidus re-equilibration.

Perovskite textures in the silicocarbonatites

Chemical composition and zoning

Perovskite zoning in the silicocarbonatites is more complex than in the clinopyroxenites. The T2 perovskite has oscillatory zoning in the cores and irregular zoning at the rims (Fig. 5d) and in T3 massive perovskite has areas with oscillatory or irregular zoning, as well as homogeneous areas. The oscillatory zoning in T2 and T3 perovskite is a primary magmatic feature. The irregular complex zoning juxtaposed over primary growth patterns in these perovskite

varieties was caused by progressive infiltration of REE, Na and locally also Nb and Th into the structure during post-magmatic fluid-driven alteration (Chakhmouradian and Zaitsev 1999). This process culminated with the deposition of REE-perovskite and loparite-(Ce) locally along the margin of, and fractures within, perovskite crystals (Figs. 3d, 5c, d). Titanite crystallised after these minerals, indicating either an increase in silica activity, or a decrease in fluid temperature (Chakhmouradian 2004). The formation of symplectitic intergrowths of titanite with rutile and ilmenite (Fig. 2f) implies increasing fluid acidity or, more likely, a further decrease in temperature, which would expand the stability fields of both rutile and ilmenite at a given pH, $p(CO_2)$ and $a(Fe^{2+})$ (Chakhmouradian 2004; Chakhmouradian and Mitchell 2002).

Occasional grains of T2 perovskite rimmed by low-REE material are much less common and could be produced by the inverse process, i.e., extraction of REEs from perovskite by percolating fluids (Fig. 5c). The compositionally homogeneous sections in T3 perovskite probably re-equilibrated through solid-state diffusion, which erased such primary textural characteristics as growth zoning and multiphase inclusions.

Textural development

In the silicocarbonatites, we observe irregularly shaped crystals with continuous crystallographic orientation, similar to the clinopyroxenites; however, the small perovskite grains also have a single crystallographic orientation and are not a composite of subgrains (Fig. 4d_{iii}). The absence of EBSD evidence of subgrain coalescence and the preservation of oscillatory zoning in T2 and T3 perovskite suggests that the coarse-grained perovskite did not undergo the same coalescence and amalgamation processes as those observed in the ultramafic rocks. However, the similarities in chemical composition, zoning patterns and associated minerals [e.g., titanite, REE-perovskite and loparite-(Ce)] indicate that the perovskite from both the ultramafic rocks and silicocarbonatites experienced the same fluid-driven alteration. We propose that the silicocarbonatites did not undergo perovskite recrystallization due to the lower solidus temperature of the silicocarbonatites compared to the ultramafic rocks. Also, the perovskite was initially fine-grained in the olivinites and clinopyroxenites but coarse-grained in the silicocarbonatites, so the difference in initial grain size may have impeded perovskite re-crystallisation in the silicocarbonatites.

Textural similarities with other oxide deposits

Several textural features that support the process of perovskite amalgamation and re-equilibration in the Afrikanda complex are observed in other oxide-rich igneous systems, namely chromite and magnetite deposits (Charlier et al. 2006; Dill 2010; Mungall 2014), as well as mantle-derived lherzolites and dunites (Wandji et al. 2009), apatite in carbonatites (Chakhmouradian et al. 2017; Kamenetsky et al. 2015), recrystallized nepheline syenites (Chakrabarty et al. 2016; Ulbrich 1993) and magnesian-ilmenite xenolith/xenocrysts in kimberlites and basanites (Mitchell 1973; Leblanc et al. 1982). These features include granoblastic mosaics, massive textures, grain coarsening and the transition from inclusion-rich to inclusion-free grains (Christiansen 1985; Ghisler 1976; Yudovskaya and Kinnaird 2010). Understanding the mechanisms responsible for the development of these features in disseminated and massive ore bodies within chromitite and magnetitite layers remains ambiguous.

Granoblastic mosaics and massive textures

For comparison, we have chosen typical examples of ophiolite dunites, podiform chromitites and ultramafic xenoliths. Chains of connected euhedral chromite crystals observed in ultramafic xenoliths, igneous complexes like Bushveld (South Africa) and Fiskenaesset (Greenland) and the Oman ophiolite resemble networks of T1 perovskite (Fig. 10e). Granoblastic textures in peridotitic xenoliths from the subcontinental lithospheric mantle are highlighted by the equigranular, euhedral olivine with interspersed linear chromite chains (Fig. 10e, f). The latter are similar to the T1 perovskite chains at Afrikanda (Fig. 10b). The xenolith textures reflect metamorphic stresses that caused mineral grains to recrystallize into granoblastic mosaic textures with straight margins and 120° triple junctions (Pike and Schwarzman 1977). At Bushveld and Fisknaesset, small chromite grains are generally euhedral to subhedral and form elongate chains, also reminiscent of T1 perovskite (Ghisler 1970; Sampson 1932; Yudovskaya and Kinnaird 2010). Silicate mineral inclusions are common and mostly restricted to grain cores.

Chromitites in the Oman ophiolite belt demonstrate an increasing grain size with deformation (Christiansen 1986). Christiansen (1985) described three morphological types of chromite (A, B and C) that are comparable to the three textural types of perovskite (T1, T2 and T3), respectively, in the present study. Type A consists of closely packed subhedral to euhedral chromite grains that mostly range between 0.5 and 1 mm across and regularly host silicate inclusions. Type B is closely packed, subhedral to anhedral chromite grains between 0.1 mm and 4.5 mm in size with occasional silicate inclusions. Type C is composed of massive, closely packed and interlocking anhedral chromite grains with indiscernible boundaries and an estimated size larger than A- and B-type grains. Christiansen (1985, 1986) proposed that the coarsening of chromite occurred during recrystallization and

was driven by strain-induced grain boundary migration and/or grain growth driven by interfacial energy gradient. We suggest that a similar mechanism was responsible for the textural evolution of perovskite in the Afrikanda ultramafic rocks.

Chains of connected crystals with granoblastic-polygonal textures are also observed in disseminated magnetite ore from the Panzhihua layered mafic intrusion, China. In this intrusion, magnetite mostly forms net textures with densely packed clusters of polygonal grains with straight boundaries and 120° interfacial angles (Fig. 10c) that resemble the granoblastic texture of T1 perovskite (Figs. 1a, 3a, 10a; Pang et al. 2007; Zhou et al. 2005).

The presence of both inclusion-rich euhedral grains and inclusion-poor anhedral grains is also observed in chromitite layers from the Oman ophiolite belt and the Fiskenaesset and Bushveld complexes (Christiansen 1985; Ghisler 1976; Yudovskaya and Kinnaird 2010). The transition between these textures can be associated with late post-magmatic processes including re-equilibration, post-cumulus growth and contact metamorphism. The development of these inclusion-free grains and the associated massive textures at Afrikanda and other oxide deposits will be discussed in a subsequent publication.

No conclusive and/or unifying model has been proposed to explain the ore distributions and textural transformations observed in the aforementioned mineral deposits. Traditionally, the formation of oxide-rich seams, bands, stringers and layers has been linked to magmatic processes. Perovskite, chromite and magnetite deposits share textural features that could imply that their development involved similar mechanisms. As we suggest for perovskite in the Afrikanda alkaline–ultramafic complex, the initial crystallisation of oxide minerals (whether magmatic or not) is followed by their textural re-equilibration at subsolidus temperatures. This re-equilibration produces perceptible changes in the morphology, size, orientation and compositional homogeneity of oxide mineral grains. From an exploration standpoint, the most important outcome of these processes is the accumulation of early-formed crystals into high-density oxide-rich zones and their coarsening and "purification" to form high-grade mineralized zones.

Conclusions

The textural and chemical examination of perovskite from the olivinites, clinopyroxenites and silicocarbonatites in the Afrikanda alkaline–ultramafic complex revealed three types of perovskite (T1 to T3) and lead to the following conclusions:

1. Perovskite from olivinites, clinopyroxenite and silicocarbonatite yielded similar ages, with an average of 368.3 ± 1.2 Ma. The perovskite and titanite ages support the contemporaneous emplacement of these lithologies at Afrikanda. The ages are slightly younger than previously published ages and could be due to discrepancies associated with the technique or reflect the timing of recrystallization.
2. In ultramafic rocks (olivinites and clinopyroxenites), the progressive coarsening of perovskite from small, euhedral, disseminated grains into large anhedral and massive grains, and the various textures and zoning patterns is evidence of post-magmatic recrystallization and textural re-equilibration. We propose the post-magmatic development of perovskite involved three stages: (1) textural equilibration enabling the development of perovskite clusters and chains after initial perovskite crystallisation; (2) grain rotation and coalescence of the small equilibrated polygonal clusters to form larger anhedral polycrystalline mosaics; (3) in some areas the continued consolidation and coarsening transform the large polycrystalline perovskite into massive perovskite.
3. The textural similarities between perovskite from Afrikanda and chromite and magnetite layers in various igneous complexes suggest similar post-magmatic coarsening processes are also involved in the development of other oxide ore deposits with monomineralic layers.

Acknowledgements We thank the Geological Institute (the Kola Science Center of the Russian Academy of Sciences) in Apatity for donating Afrikanda samples for our study. We are grateful to Peter Downes and an anonymous reviewer, for their constructive comments and suggestions. Editorial handling by Ramya Murali is acknowledged. Financial support was provided by the Australian Research Council (Discovery Grant DP130100257, 2013–2015) and University of Tasmania (New Star Professorship, 2010–2014) to V. Kamenetsky.

References

Afanasyev BV (2011) Mineral resources of the alkaline–ultramafic massifs of the Kola Peninsula. Roza Vetrov, St. Petersburg, p 224 (in Russian)

Armbrustmacher TJ (1981) The Complex of Alkaline Rocks at Iron Hill, Powderhorn district, Gunnison County, Colorado. New Mexico Geological Society, New Mexico

Arzamastsev A, Wu F-Y (2014) U–Pb geochronology and Sr-Nd isotopic systematics of minerals from the ultrabasic-alkaline massifs of the Kola province. Petrology 22:462–479

Arzamastsev A, Glaznev V, Raevsky A, Arzamastseva L (2000) Morphology and internal structure of the Kola Alkaline intrusions, NE Fennoscandian shield: 3D density modelling and geological implications. J Asian Earth Sci 18:213–228

Barbosa ESR, Brod JA, Junqueira-Brod TC, Dantas EL, de Oliveira Cordeiro PF, Gomide CS (2012) Bebedourite from its type area

(Salitre I complex): a key petrogenetic series in the Late-Cretaceous Alto Paranaíba Kamafugite–Carbonatite–Phoscorite association. Cent Br Lithos 144:56–72
Borrok DM, Kelser SE, Boer RH, Essene EJ (1998) The Vergenoeg magnetite-fluorite deposit, South Africa; support for a hydrothermal model for massive iron oxide deposits. Econ Geol 93:564–586
Brod JA (1999) Petrology and geochemistry of the Tapira alkaline complex, Minas Gerais State, Brazil. Durham University, Durham
Buddington A, Lindsley D (1964) Iron-titanium oxide minerals and synthetic equivalents. J Petrol 5:310–357
Campbell LS, Henderson P, Wall F, Nielsen TF (1997) Rare earth chemistry of perovskite group minerals from the Gardiner complex. East Greenl Mineral Mag 61:197–212
Cawthorn R (2011) Geological interpretations from the PGE distribution in the Bushveld Merensky and UG2 chromitite reefs. J S Afr Inst Min Metall 111:67–79
Chakhmouradian AR (2004) Crystal chemistry and paragenesis of compositionally unique (Al-, Fe-, Nb-, and Zr-rich) titanite from Afrikanda, Russia. Am Mineral 89:1752–1762
Chakhmouradian AR, Mitchell RH (1997) Compositional variation of perovskite-group minerals from the carbonatite complexes of the Kola Alkaline Province, Russia. Can Mineral 35:1293–1310
Chakhmouradian AR, Mitchell RH (2000) Occurrence, alteration patterns and compositional variation of perovskite in kimberlites. Can Mineral 38:975–994
Chakhmouradian AR, Mitchell RH (2002) New data on pyrochlore-and perovskite-group minerals from the Lovozero alkaline complex, Russia. Eur J Mineral 14:821–836
Chakhmouradian A, Williams C (2004) Mineralogy of high-field-strength elements (Ti, Nb, Zr, Ta, Hf) in phoscoritic and carbonatitic rocks of the Kola Peninsula, Russia. Phoscorites Carbon Mantle Mine Key Example Kola Alkaline Province 10:293–340
Chakhmouradian AR, Zaitsev AN (1999) Calcite-amphibole-clinopyroxene rock from the Afrikanda complex, Kola Peninsula, Russia: mineralogy and a possible link to carbonatites. I Oxide minerals. Can Mineral 37:177–198
Chakhmouradian AR, Zaitsev AN (2002) Calcite–amphibole–clinopyroxene rock from the Afrikanda complex, Kola Peninsula, Russia: mineralogy and a possible link to carbonatites. III Silicate minerals. Can Mineral 40:1347–1374
Chakhmouradian AR, Zaitsev AN (2004) Afrikanda: an association of ultramafic, alkaline and alkali-silica-rich carbonatitic rocks from mantle-derived melts Phoscorites and carbonatites from mantle to mine: the key example of the Kola Alkaline Province. Mineral Soc UK Ser 10:247–291
Chakhmouradian A, Mitchell R, Pankov A, Chukanov N (1999) Loparite and 'metaloparite' from the Burpala alkaline complex, Baikal Alkaline Province (Russia). Mineral Mag 63:519–519
Chakhmouradian AR, Cooper MA, Medici L, Hawthorne FC, Adar F (2008) Fluorine-rich hibschite from silicocarbonatite, Afrikanda complex, Russia: crystal chemistry and conditions of crystallization. Can Mineral 46:1033–1042
Chakhmouradian AR, Reguir EP, Kamenetsky VS, Sharygin VV, Golovin AV (2013) Trace-element partitioning in perovskite: implications for the geochemistry of kimberlites and other mantle-derived undersaturated. Rocks Chem Geol 353:112–131
Chakhmouradian AR et al (2017) Apatite in carbonatitic rocks: compositional variation, zoning, element partitioning and petrogenetic significance. Lithos 274:188–213
Chakrabarty A, Mitchell R, Ren M, Saha P, Pal S, Pruseth K, Sen A (2016) Magmatic, hydrothermal and subsolidus evolution of the agpaitic nepheline syenites of the Sushina Hill Complex, India: implications for the metamorphism of peralkaline syenites. Mineral Mag 80:1161–1193
Charlier B, Duchesne J-C, Vander Auwera J (2006) Magma chamber processes in the Tellnes ilmenite deposit (Rogaland Anorthosite Province, SW Norway) and the formation of Fe–Ti ores in massif-type anorthosites. Chem Geol 234:264–290
Christiansen F (1985) Deformation fabric and microstructures in ophiolitic chromitites and host ultramafics, Sultanate of Oman. Geologische Rundschau 74:61–76
Christiansen FG (1986) Deformation of chromite: SEM investigations. Tectonophysics 121:175–196
Clark BR, Price FR, Kelly WC (1977) Effects of annealing on deformation textures in galena. Contrib Miner Petrol 64:149–165
Dawson J, Hawthorn J (1973) Magmatic sedimentation and carbonatitic differentiation in kimberlite sills at Benfontein, South Africa. J Geol Soc 129:61–85
Dill HG (2010) The "chessboard" classification scheme of mineral deposits: Mineralogy and geology from aluminum to zirconium. Earth Sci Rev 100:1–420
Doherty R et al (1997) Current issues in recrystallization: a review. Mater Sci Eng A 238:219–274
Dowty E (1976a) Crystal structure and crystal growth: I. The influence of internal structure on morphology. Am Miner 61:448–459
Dowty E (1976b) Crystal structure and crystal growth: II. Sect Zon Miner Am Mineral 61:460–469
Eales H, Costin G (2012) Crustally contaminated komatiite: primary source of the chromitites and Marginal, Lower, and Critical Zone magmas in a staging chamber beneath the Bushveld. Complex Econ Geol 107:645–665
Eales H, De Klerk W, Teigler B (1990) Evidence for magma mixing processes within the Critical and Lower Zones of the northwestern Bushveld Complex. S Afr Chem Geol 88:261–278
Fleet M, Bilcox GA, Barnett RL (1980) Oriented magnetite inclusions in pyroxenes from the Grenville Province. Can Mineral 18:89–99
Force ER (1991) Geology of titanium-mineral deposits, vol 259. Geological Society of America, New York
Gaeta M (1996) Ca–Fe-rich exsolution lamellae from olivine in a wehrlitic xenolith, Monti Vulsini Volcanic District, Central Italy. Mineral Petrol Acta 39:159–167
Garrison JR, Taylor LA (1981) Petrogenesis of pyroxene-oxide intergrowths from kimberlite and cumulate rocks; co-precipitation or exsolution? Am Miner 66:723–740
Ghisler M (1970) Pre-metamorphic folded chromite deposits of stratiform type in the early Precambrian of West, Greenland. Mineral Depos 5:223–236
Ghisler M (1976) The geology, mineralogy and geochemistry of the-Pre-Orogenic Archaean stratiform chromite deposits at-Fiskenaesset, West Greenland
Haggerty SE (1991) Oxide textures; a mini-atlas. Rev Mineral Geochem 25:129–219
Harlov DE, Meighan CJ, Kerr ID, Samson IM (2016) Mineralogy, chemistry, and fluid-aided evolution of the Pea Ridge Fe oxide-(Y + REE) deposit, southeast Missouri, USA. Econ Geol 111:1963–1984
Herz N (1976) Titanium deposits in alkalic igneous rocks. US Department of the Interior, Geological Survey, New York
Higgins MD (2011) Textural coarsening in igneous rocks. Int Geol Rev 53:354–376
Higgins MD (2015) Quantitative textural analysis of rocks in layered mafic intrusions. In: Layered Intrusions. Springer, pp 153–181
Higgins MD (2017) Quantitative investigation of felsic rock textures using cathodoluminescence images and other techniques. Lithos 277:259–268
Holm E, Farjami S, Manohar P, Rohrer G, Rollett A, Srolovitz D, Weiland H (2016) Proceedings of the 6th International Conference on Recrystallization and Grain Growth (ReX&GG 2016). Springer

Holness MB, Cheadle MJ, McKenzie D (2005) On the use of changes in dihedral angle to decode late-stage textural evolution in cumulates. J Petrol 46:1565–1583

Holness MB, Nielsen TF, Tegner C (2006) Textural maturity of cumulates: a record of chamber filling, liquidus assemblage, cooling rate and large-scale convection in mafic layered intrusions. J Petrol 48:141–157

Horstwood MS et al (2016) Community-derived standards for LA-ICP-MS U-(Th-) Pb geochronology–uncertainty propagation, age interpretation and data reporting. Geostand Geoanal Res 40:311–332

Hou B, Keeling J, Van Gosen BS (2017) Geological and exploration models of beach placer deposits, integrated from case-studies of Southern Australia. Ore Geol Rev 80:437–459

Howarth GH, Prevec SA, Zhou M-F (2013) Timing of Ti-magnetite crystallisation and silicate disequilibrium in the Panzhihua mafic layered intrusion: Implications for ore-forming processes. Lithos 170:73–89

Humphreys F (2001) Review grain and subgrain characterisation by electron backscatter diffraction. J Mater Sci 36:3833–3854

Humphreys FJ, Hatherly M (2004) Recrystallization and related annealing phenomena. Elsevier, Amsterdam

Hunter RH (1987) Textural equilibrium in layered igneous rocks. In: Origins of igneous layering. Springer, pp 473–503

Irvine T (1977) Origin of chromitite layers in the Muskox intrusion and other stratiform intrusions: a new interpretation. Geology 5:273–277

Jones A, Ralph B, Hansen N (1979) Subgrain coalescence and the nucleation of recrystallization at grain boundaries in aluminium. Proc R Soc Lond 368:345–357

Jurewicz AJ, Watson EB (1988) Cations in olivine, Part 1: Calcium partitioning and calcium-magnesium distribution between olivines and coexisting melts, with petrologic applications. Contrib Mineral Petrol 99:176–185

Kamenetsky VS, Mitchell RH, Maas R, Giuliani A, Gaboury D, Zhitova L (2015) Chlorine in mantle-derived carbonatite melts revealed by halite in the St.-Honoré intrusion (Québec, Canada). Geology 43:687–690

Kinnaird J, Kruger F, Nex P, Cawthorn R (2002) Chromitite formation—a key to understanding processes of platinum enrichment. Appl Earth Sci 111:23–35

Knipping JL et al (2015) Trace elements in magnetite from massive iron oxide-apatite deposits indicate a combined formation by igneous and magmatic-hydrothermal processes. Geochim Cosmochim Acta 171:15–38

Kolker A (1982) Mineralogy and geochemistry of Fe–Ti oxide and apatite (nelsonite) deposits and evaluation of the liquid immiscibility hypothesis. Econ Geol 77:1146–1158

Kramm U, Kogarko L, Kononova V, Vartiainen H (1993) The Kola Alkaline province of the CIS and Finland: Precise Rb-Sr ages define 380–360 Ma age range for all magmatism. Lithos 30:33–44

Kreitcberg A, Brailovski V, Turenne S (2017) Effect of heat treatment and hot isostatic pressing on the microstructure and mechanical properties of Inconel 625 alloy processed by laser powder bed fusion. Mater Sci Eng A 689:1–10

Kretz R (1966) Interpretation of the shape of mineral grains in metamorphic rocks. J Petrol 7:68–94

Kukharenko AA et al (1965) The Caledonian complex of ultrabasic and alkaline rocks and carbonatites of the Kola Peninsula and Northern Karelia. Nedra, Leningrad

Latypov R, O'Driscoll B, Lavrenchuk A (2013) Towards a model for the in situ origin of PGE reefs in layered intrusions: insights from chromitite seams of the Rum Eastern Layered Intrusion, Scotland. Contrib Mineral Petrol 166:309–327

Latypov R, Chistyakova S, Mukherjee R (2017) A novel hypothesis for origin of massive Chromitites in the bushveld igneous complex. J Petrol 1:41

Leblanc M, Dautria J-M, Girod M (1982) Magnesian ilmenitite xenoliths in a basanite from Tahalra, Ahaggar (Southern Algeria). Contrib Miner Petrol 79:347–354

Li JC (1962) Possibility of subgrain rotation during recrystallization. J Appl Phys 33:2958–2965

Lister GF (1966) The composition and origin of selected iron-titanium deposits. Econ Geol 61:275–310

Markl G, Marks M, Wirth R (2001) The influence of T, $aSiO_2$, and fO_2 on exsolution textures in Fe–Mg olivine: an example from augite syenites of the Ilimaussaq Intrusion, South Greenland. Am Mineral 86:36–46

McCloy J, Korenstein R, Zelinski B (2009) Effects of temperature, pressure, and metal promoter on the recrystallized structure and optical transmission of chemical vapor deposited zinc sulfide. J Am Ceram Soc 92:1725–1731

McDonald JA (1965) Liquid immiscibility as one factor in chromitite seam formation in the Bushveld Igneous complex. Econ Geol 60:1674–1685

McKay G, Miyamoto M, Mikouchi T, Ogawa T (1998) The cooling history of the Lewis Cliff 86010 angrite as inferred from kirschsteinite lamellae in olivine. Meteorit Planet Sci 33:977–983

Mikouchi T, Takeda H, Miyamoto M, Ohsumi K, McKay GA (1995) Exsolution lamellae of kirschsteinite in magnesium-iron olivine from an angrite meteorite. Am Mineral 80:585–592

Mitchell RH (1973) Magnesian ilmenite and its role in kimberlite petrogenesis. J Geol 81:301–311

Mitchell RH, Welch MD, Chakhmouradian AR (2017) Nomenclature of the perovskite supergroup: a hierarchical system of classification based on crystal structure and composition. Mineral Mag 81:411–462

Mondal SK, Mathez EA (2006) Origin of the UG2 chromitite layer Bushveld Complex. J Petrol 48:495–510

Mungall J (2014) Geochemistry of magmatic ore deposits. In: Treatise on geohemistry, vol 13. 2 edn, pp 195–218

Nielsen T (1980) The petrology of a melilitolite, melteigite, carbonatite and syenite ring dike system, in the Gardiner complex, East Greenland Lithos 13:181–197

Nielsen TFD, Solovova IP, Veksler IV (1997) Parental melts of melilitolite and origin of alkaline carbonatite: evidence from crystallised melt inclusions Gardiner complex. Contrib Mineral Petrol 126:331–344

Pang K-N, Zhou M-F, Lindsley D, Zhao D, Malpas J (2007) Origin of Fe–Ti oxide ores in mafic intrusions: evidence from the Panzhihua intrusion SW China. J Petrol 49:295–313

Pekov I, Petersen OV, Voloshin A (1997) Calcio-ancylite-(Ce) from Ilímaussaq and Narssârssuk, Greenland, Kola Peninsula and Polar Urals, Russia, ancylite-(Ce)-calcio-ancylite-(Ce) an isomorphous series. Neues Jahrbuch für Minerologie, Abhandlungen 171(3):309–322

Pike JN, Schwarzman E (1977) Classification of textures in ultramafic xenoliths. J Geol 85:49–61

Price G (1980) Exsolution microstructures in titanomagnetites and their magnetic significance. Phys Earth Planet Int 23:2–12

Pushkarev E, Kamenetsky V, Morozova A, Khiller V, Glavatskykh S, Rodemann T (2015) Ontogeny of ore Cr-spinel and composition of inclusions as indicators of the pneumatolytic–hydrothermal origin of PGM-bearing chromitites from Kondyor massif, the Aldan Shield. Geol Ore Deposit 57:352–380

Putnis A (2009) Mineral replacement reactions. Rev Mineral Geochem 70:87–124

Ramdohr P (2013) The ore minerals and their intergrowths. Elsevier, Amsterdam

Reguir EP, Camacho A, Yang P, Chakhmouradian AR, Kamenetsky VS, Halden NM (2010) Trace-element study and uranium-lead dating of perovskite from the Afrikanda plutonic complex, Kola Peninsula (Russia) using LA-ICP-MS. Miner Petrol 100:95–103

Rios PR, Siciliano F Jr, Sandim HRZ, Plaut RL, Padilha AF (2005) Nucleation and growth during recrystallization. Mater Res 8:225–238

Salnikova E, Stifeeva M, Chakhmouradian A, Glebovitsky V, Reguir E (2018) The U–Pb system in schorlomite from calcite–amphobole–pyroxene Pegmatite of the Afrikanda Complex (Kola Peninsula). Dokl Earth Sci 478:148–151

Sampson E (1932) Magmatic chromite deposits in southern Africa. Econ Geol 27:113–144

Sandström R, Lehtinen B, Hedman E, Groza I, Karlsson S (1978) Subgrain growth in Al and Al-1% Mn during annealing. J Mater Sci 13:1229–1242

Simkin T, Smith J (1970) Minor-element distribution in olivine. J Geol 78:304–325

Stacey JS, Kramers JD (1975) Approximation of terrestrial lead isotope evolution by a two-stage model. Earth Planet Sci Lett 26:207–221

Syrenko A, Klinishev G (1973) Recrystallization of copper under hydrostatic pressure up to 15 kbar. J Mater Sci 8:765–769

Ulbrich MN (1993) Mineralogy of nepheline syenites from the Poços de Caldas alkaline massif SE Brazil: chemistry, X-ray data and microtextures of feldspars. Revista Brasileira de Geociências 23:388–399

Varma S, Willits BL (1984) Subgrain growth in aluminum during static annealing. Metal Trans A 15:1502–1503

Vernon R (1970) Comparative grain-boundary studies of some basic and ultrabasic granulites, nodules and cumulates Scottish. J Geol 6:337–351

Vidyashankar H, Govindaiah S (2009) Ore petrology of the V-Ti magnetite (lodestone) layers of the Kurihundi area of Sargur schist belt, Dharwar craton. J Geol Soc India 74:58–68

Von Gruenewaldt G, Klemm D, Henckel J, Dehm R (1985) Exsolution features in titanomagnetites from massive magnetite layers and their host rocks of the Upper Zone, Eastern Bushveld Complex. Econ Geol 80:1049–1061

Vukmanovic Z, Barnes SJ, Reddy SM, Godel B, Fiorentini ML (2013) Morphology and microstructure of chromite crystals in chromitites from the Merensky Reef (Bushveld Complex, South Africa). Contrib Miner Petrol 165:1031–1050

Walter J, Koch E (1963) Substructures and recrystallization of deformed (100)[001]-oriented crystals of high-purity silicon-iron. Acta Metall 11:923–938

Wandji P, Tsafack J, Bardintzeff J, Nkouathio D, Dongmo AK, Bellon H, Guillou H (2009) Xenoliths of dunites, wehrlites and clinopyroxenites in the basanites from Batoke volcanic cone (Mount Cameroon, Central Africa): petrogenetic implications. Miner Petrol 96:81–98

Wu F-Y, Yang Y-H, Mitchell RH, Bellatreccia F, Li Q-L, Zhao Z-F (2010) In situ U–Pb and Nd–Hf–(Sr) isotopic investigations of zirconolite and calzirtite. Chem Geol 277:178–195

Wu F-Y, Arzamastsev AA, Mitchell RH, Li Q-L, Sun J, Yang Y-H, Wang R-C (2013) Emplacement age and Sr–Nd isotopic compositions of the Afrikanda alkaline ultramafic complex, Kola Peninsula, Russia. Chem Geol 353:210–229

Xiong F, Yang J, Dilek Y, Wang C (2017) Nanoscale diopside and spinel exsolution in olivine from dunite of the tethyan ophiolites, Southwestern Turkey: implications for the multi-stage process. J Nanosci Nanotechnol 17:6587–6596

Yudin B, Zak S (1971) Titanium deposits of northwestern USSR (eastern part of Baltic Shield). Int Geol Rev 13:864–872

Yudovskaya MA, Kinnaird JA (2010) Chromite in the Platreef (Bushveld Complex, South Africa): occurrence and evolution of its chemical composition. Miner Depos 45:369–391

Yufeng R, Fangyuan C, Jingsui Y, Yuanhong G (2008) Exsolutions of diopside and magnetite in olivine from mantle dunite, Luobusa ophiolite, Tibet, China. Acta Geol Sin English Ed 82:377–384

Zaitsev AN, Chakhmouradian AR (2002) Calcite–amphibole–clinopyroxene rock from the Afrikanda complex, Kola Peninsula, Russia: mineralogy and a possible link to carbonatites. II Oxysalt minerals. Can Mineral 40:103–120

Zhou M-F, Robinson PT, Lesher CM, Keays RR, Zhang C-J, Malpas J (2005) Geochemistry, petrogenesis and metallogenesis of the Panzhihua gabbroic layered intrusion and associated Fe–Ti–V oxide deposits, Sichuan Province, SW China. J Petrol 46:2253–2280